

A Feasibility Study of A Neutrino Factory in Japan

Version 1.0

NufactJ Working Group

May 24, 2001

Contents

1	Overview	9
1.1	What is a Neutrino Factory ?	9
1.1.1	Advantages of neutrino factory	10
1.1.2	Beam intensity and rates	10
1.2	Oscillation Physics at Neutrino Factory	11
1.2.1	Oscillation event rates	12
1.2.2	CP violation	13
1.2.3	T violation	14
1.3	The KEK/JAERI Joint Project of High-Intensity Proton Ac- celerator	14
1.3.1	Neutrino Factory Layout	15
1.4	Staging Approach	15
1.4.1	Full-size Neutrino Factory	15
1.4.2	PRISM	16
2	Accelerator	20
2.1	Overview of FFAG based neutrino factory	20
2.2	Scheme	24
2.2.1	Proton Driver	24
2.2.2	Capture	31
2.2.3	Acceleration	35
2.2.4	Constraints	36
2.2.5	Storage Ring	53
2.2.6	Muon Cooling	53
2.3	Hardware	56
2.3.1	RF system	56
2.3.2	Magnet	66
3	Physics	72
3.1	Theory	72
3.1.1	Introduction	72
3.1.2	Sensitivity to θ_{13}	74
3.1.3	Determination of the sign of Δm_{32}^2	80

3.1.4	Precise measurements of the oscillation parameters . . .	80
3.1.5	The measurement of δ	87
3.1.6	Statistical Evaluation	114
3.1.7	Possibility of Search for T violation	121
3.1.8	The dependence of polarization pattern	129
A	PRISM	131
A.1	PRISM Overview	131
A.2	Solenoid Pion Capture	133
A.3	Phase Rotation	135
A.4	Time Structure	136
A.5	PRISM at the 50-GeV PS Experimental Hall	137
B	FFAG Principle	140
B.1	FFAG and Other Accelerators	140
B.2	Zero Chromaticity	141
B.3	Large Acceptance	142
B.4	Radial and Spiral Type	142
B.5	Historical Background	143
C	R&D Status of POP FFAG	144
C.1	Overview	144
C.2	Experimental status	146
C.2.1	Beam acceleration	146
C.2.2	Tune survey	147
C.2.3	Beam position	148
C.3	Aperture survey	148
C.4	Summary of POP FFAG R&D	151
D	R&D Status of 150 MeV FFAG	152
D.1	Overview	152
D.2	Main Features of 150-MeV FFAG	152
D.3	R&D status and Construction Schedule	154

Preface

This is a report on Japanese studies of a neutrino factory to produce high-intensity energetic neutrino sources, either electron- and muon-neutrinos and their anti-neutrinos.

The Japanese scheme of a neutrino factory that is given in this report has unique features, compared with the other designs in U.S. and Europe. It is based on muon acceleration by a series of fixed-field alternating gradient synchrotrons (FFAG). It has, we believe, several advantages which are discussed in this report. Our study on this novel FFAG scheme has just begun recently. And therefore all the machine parameters are not yet completed, and may be inconsistent through this draft version of the report. But, it will be studied further in the final version.

Another important emphasis, which has happened timely, is the approval of construction of the 50-GeV proton synchrotron of about 1 Mega watt beam power. This high-intensity proton machine will be constructed by year 2006. It would provide a great opportunity to construct a neutrino factory in Japan in future. And it would be useful for all the scientists in the world to carry out necessary R&D works for a neutrino factory and a $\mu^+\mu^-$ collider, with this high intensity beam.

may 22nd, 2001

Yoshitaka Kuno (Osaka University)
Yoshiharu Mori (KEK)

Contributors

Yoshihisa Iwashita	Kyoto University
Yoshitaka Kuno	Osaka Univeristy
Shinji Machida	KEK
Yoshiharu Mori	KEK
Joe Sato	Kyushu University
Osamu Yasuda	Tokyo Metropolitan University
Takeichiro Yokoi	KEK

Executive Summary

Physics Motivation : A high-intensity accelerator-based neutrino source is definitely a next-generation facility of particle physics. It is required in order to push neutrino physics forward into an unexplored territory. One of the physics motivations at neutrino factories is to study the 3×3 neutrino mixing matrix, which is called Maki-Nakagawa-Sakata (MNS) mixing matrix [1]. This is a completely new field in the lepton sector that must be pursued from now on, after many years of studies on the Kobayashi-Maskawa mixing matrix in the quark sector. The potential topics are

1. determination of θ_{13} ,
2. determination of the sign of Δm_{32}^2 , and most-importantly
3. the discovery of CP violation in the lepton sector.

Parameters of a Neutrino Factory : The number of muon decays in the muon storage ring is aimed to be about 1×10^{20} muon decay/one straight section/year. The energy of muons is at most 20 GeV in the first phase (Phase-I), and will be improved to be 4.4×10^{20} muon decay/one straight section/year by increasing the primary proton beam intensity in Phase-II. The muon energy could be increased to 50 GeV if necessary. The determination of muon energy and intensity in the muon storage ring will be subject to physics demands and cost optimization. They are listed in Table 1.

	A number of Muon Decays (/straight section/year)	Maximum Muon Energy	Proton Beam Power
Phase-I	1×10^{20}	20 GeV	1 MW
Phase-II	4.4×10^{20}	50 GeV	4.4 MW

Table 1: Parameters of Neutrino Factory Scenario

Proton Driver : The KEK/JAERI Joint project to construct a high-intensity proton synchrotron (previously called JHF) has been *approved*. The accelerator complex includes a 50-GeV proton machine with about 3×10^{14} proton per pulse with 0.4 Hz, providing about 1 Mega watt beam power. It is sufficient for the initial stage of a neutrino factory. The construction will start from April, 2001 and will complete by year 2006. The existence

of a proton driver would give a great opportunity to realize the future case of a neutrino factory in Japan. It would also provide various opportunities to carry out necessary R&D studies for a neutrino factory and even for a muon collider and open for scientists world-wide. Furthermore, there has been discussion on the upgrade path towards 4.4 Mega-watt beam power by installing more rf cavities and power supplies.

Accelerator Scheme : The accelerator complex of the neutrino factory considered in Japan has significantly different aspect from the others in U.S. [2] and in Europe [3]. One of the major differences that should be stressed is to adopt *fix-field alternating gradient synchrotron* (FFAG) for muon acceleration. FFAG is known to have wide longitudinal (momentum) acceptance, and wide geometrical acceptance (vertical and horizontal), compared with ordinary synchrotrons. It allows us to accelerate directly a muon beam of broad emittance, without involving any phase rotation and muon cooling.

In consequences, the use of FFAG will give the major advantages as follows:

- a *simplicity* of the accelerator complex,
- significant *cost saving* (because of adoption of circular rings instead of linear accelerator),
- *earlier readiness* of technology necessary (because of less R&D items, in particular the muon cooling is not involved),

The initial idea of FFAG originated from a Japanese physicist a long time ago. Since then, except for electron FFAG accelerator built in U.S. in the mid 60's, no attempt has been made by the most recent year when the KEK accelerator group constructed the small POP (=proof of principle) machine in year 2000. This machine was successfully operated. A larger prototype (of 150 MeV) is now being constructed. The completion will be in year 2003.

Physics Sensitivity : After the completion of the 50-GeV PS of about 1 Mega-watt beam power, it is natural to start an experiment with the conventional neutrino beam to Super-Kamiokande. (The conventional beam with a Mega-watt proton beam is used to be referred to as "superbeam"). The study group (*JHF neutrino group*) has already submitted the Letter of Intent [4].

It is necessary to identify the physics reaches with the superbeam and with a neutrino factory. In general, if one of the mixing angle, $\sin 2\theta_{13} < 0.01$, the conventional beam with a water Cerenkov detector has difficulty to discover $\nu_\mu \rightarrow \nu_e$ oscillation. It would not be improved even if the detector size becomes larger mostly because of backgrounds from π^0 . Therefore, in the

FFAG based neutrino factory in Japan

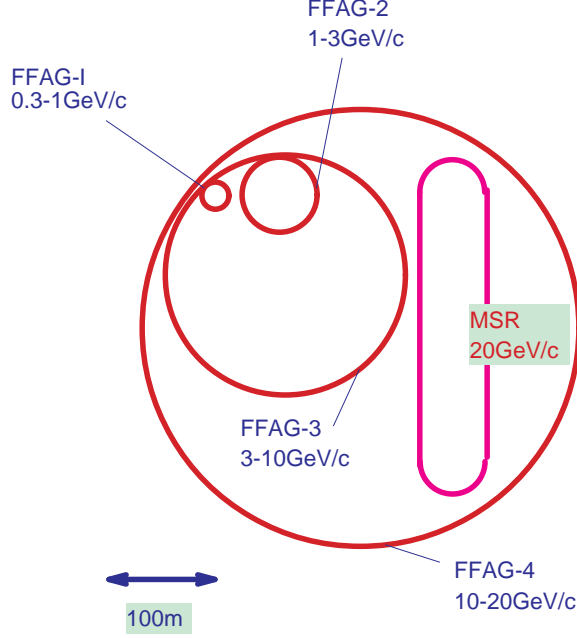


Figure 1: Schematic layout of a neutrino factory based on FFAG acceleration. A total of four FFAG rings accelerate muons from 0.3 GeV/c to 20 GeV/c.

case of small $\sin 2\theta_{13}$, a neutrino factory is the only possibility to explore the physics potentials [5].

The physics goals of both (1) determination of θ_{13} and (2) determination of the sign of the Δm_{32}^2 need an energetic neutrino beam (\sim a few 10 GeV) with a long oscillation distance (\sim a few 1000 km). However, (3) search for CP (or T) violation requires some optimization on them. The CP asymmetry A_{CP} is known to scale with (L/E) , where L and E are the baseline length and the energy of a neutrino beam, suggesting that having a long baseline length and a low energy is better. However, a figure of merit of the sensitivity is given by $A_{CP} \times \sqrt{N_{osc}}$ where N_{osc} is a number of the oscillating events and it is proportional to the energy of neutrino. It becomes clear that the search for CP violation at very low energy become difficult because statistics is simply not enough. At a long distance, the matter effect dominates over the intrinsic CP violation, and therefore it has to be discriminated. The other issues in the search for CP violation is whether we like to see the CP asymmetry or we just determine the imaginary phase in the MNS matrix. This two different approaches give two different optimization. For the latter, 50 GeV and 3000 km gives the best solution, and the former gives lower energy and

shorter distance. For further studies, more inputs on the MNS mixing matrix elements are needed. Also the possibility of search for T-violation must be pursued.



Chapter 1

Overview

Japan has been taking a major leading role in neutrino physics at present. To keep this high level of physics contributions from Japan and go steps further, it is definitely required to have neutrino sources with higher intensity. To achieve this, a neutrino beam based on a muon storage ring has been considered extensively [2, 3].

1.1 What is a Neutrino Factory ?

A neutrino factory is a high-intensity neutrino source based on muon storage ring. The neutrino beam energy ranges from a few GeV to several 10 GeV. The beam intensity anticipated at a neutrino factory is about 100 times the present intensity of conventional beams based on pion decays in the corresponding energy region. It is firmly believed that a neutrino factory would open great opportunities for significant progress in neutrino physics. Historically, it was considered based on the R&D works of a $\mu^+\mu^-$ collider. Therefore, all the efforts towards a neutrino factory could have potentials leading the realization of future energy-frontier $\mu^+\mu^-$ colliders at TeV energy range.

In the design of a neutrino factory, muons of 20-50 GeV are injected into a storage ring. Muon decays in the long straight section of the muon storage ring would provide a high intensity beam of neutrinos. A number of neutrinos of about $10^{20} - 10^{21}$ ν s/year/straight section is aimed. Both μ^+ s and μ^- s are used to produce four different flavors of neutrinos, ν_e , $\bar{\nu}_e$, ν_μ and $\bar{\nu}_\mu$ from $\mu^+ \rightarrow e^+ + \bar{\nu}_\mu + \nu_e$ and $\mu^- \rightarrow e^- + \nu_\mu + \bar{\nu}_e$ decays. To identify neutrino or anti-neutrino events at the detector, the charge discrimination is required at detection.

1.1.1 Advantages of neutrino factory

A neutrino factory is needed to make precision measurement of neutrino oscillation at a long baseline. The precision of 10^{-3} or better will be needed to determine all of the physics parameters in the lepton sector. To achieve, a high intensity beam of neutrinos with full understanding of beam characteristic is required. To meet all the requirements, a neutrino beam from muon decays must be the best candidate in the following reasons:

1. higher neutrino-beam intensity at high energy, of $10^{20} - 10^{21}$ neutrinos/year, which is about 100 times intensity at a few 10 GeV energy range. In particular, energetic ν_e ($\bar{\nu}_e$) beams can be available at only a neutrino factory,
2. lower background of $10^{-4} - 10^{-3}$ level (which is compared with a few % level at the pion source), and
3. precise knowledge on neutrino intensity and emittance.

Thus, a neutrino factory is suitable for precision measurements. At the neutrino factory, the oscillation signature is determined by a wrong-signed lepton. In practice, the discrimination of e^+ and e^- is more difficult than that of μ^+ and μ^- . And therefore, $\nu_e \rightarrow \nu_\mu$ ($\bar{\nu}_e \rightarrow \bar{\nu}_\mu$) are looked at at a neutrino factory.

1.1.2 Beam intensity and rates

The neutrino flux from a neutrino factory can be estimated [6, 8]. First of all, at the muon-rest frame, the distributions of neutrinos (anti-neutrinos) from (unpolarized) muon decays are given as follows.

$$\begin{aligned}\frac{d^2\sigma_{\nu_\mu, \bar{\nu}_\mu}}{dxdt} &= x^2(3 - 2x), \\ \frac{d^2\sigma_{\nu_e, \bar{\nu}_e}}{dxdt} &= 6x^2(1 - x),\end{aligned}\tag{1.1}$$

where $x = 2E_\nu/m_\mu$. At the laboratory frame where muons are accelerated, the neutrino flux at a distance, L , along the forward direction of muon momentum are given by

$$\begin{aligned}\Phi_{\nu_\mu, \bar{\nu}_\mu} &= \gamma^2 \frac{n_\mu}{\pi L^2} \left\{ 2y^2(3 - 2y) \right\}, \\ \Phi_{\nu_e, \bar{\nu}_e} &= \gamma^2 \frac{n_\mu}{\pi L^2} \left\{ 12y^2(1 - y) \right\},\end{aligned}\tag{1.2}$$

where n_μ is a number of decaying muons, $\gamma = E_\mu/m_\mu$ and $y = E_\nu/E_\mu$. It should be noted that the total neutrino flux increases with E_μ^2 .

The charged-current rates, which arises as neutrino-nucleon scattering, can be estimated. For high-energy neutrinos (\sim tens of GeV), the deep inelastic scattering ($\nu + A \rightarrow l + X$). The cross section (of deep inelastic scattering) are proportional to the neutrino energy, E_ν , and are given by

$$\begin{aligned}\sigma_{\nu N} &\sim 0.67 \times 10^{-38} \times E_\nu [\text{GeV}] \text{ (cm}^2\text{)}, \\ \sigma_{\bar{\nu} N} &\sim 0.34 \times 10^{-38} \times E_\nu [\text{GeV}] \text{ (cm}^2\text{)}.\end{aligned}\tag{1.3}$$

From Eq.(1.2) and (1.3), the rates of charged-current events (in the case of no oscillation) can be estimated.

$$\begin{aligned}N_{\nu_\mu} &\sim 8 \times \frac{n_\mu [10^{21}] E_\mu^3 [\text{GeV}] N_k [\text{kt}]}{L^2 [1000\text{km}]}, \\ N_{\nu_e} &\sim 7 \times \frac{n_\mu [10^{21}] E_\mu^3 [\text{GeV}] N_k [\text{kt}]}{L^2 [1000\text{km}]},\end{aligned}\tag{1.4}$$

$$\begin{aligned}N_{\bar{\nu}_\mu} &\sim 4 \times \frac{n_\mu [10^{21}] E_\mu^3 [\text{GeV}] N_k [\text{kt}]}{L^2 [1000\text{km}]}, \\ N_{\bar{\nu}_e} &\sim 3.5 \times \frac{n_\mu [10^{21}] E_\mu^3 [\text{GeV}] N_k [\text{kt}]}{L^2 [1000\text{km}]}.\end{aligned}\tag{1.5}$$

1.2 Oscillation Physics at Neutrino Factory

One of the major physics topics at the neutrino factory is to measure and determine the neutrino mixing matrix, which is now called the Maki-Nakagawa-Sakata (MNS) matrix [1]. It is given by

$$\begin{pmatrix} \nu_e \\ \nu_\mu \\ \nu_\tau \end{pmatrix} = U_{MNS} \cdot \begin{pmatrix} \nu_1 \\ \nu_2 \\ \nu_3 \end{pmatrix},\tag{1.6}$$

where the MNS matrix is

$$U_{MNS} = \begin{pmatrix} c_{12}c_{13} & s_{12}c_{13} & s_{13}e^{-i\delta} \\ -s_{12}c_{23} - c_{12}s_{13}s_{23}e^{-i\delta} & c_{12}c_{23} - s_{12}s_{13}s_{23}e^{i\delta} & c_{13}s_{23} \\ s_{12}c_{23} - c_{12}s_{13}c_{23}e^{i\delta} & -c_{12}s_{23} - s_{12}s_{13}c_{23}e^{i\delta} & c_{13}c_{23} \end{pmatrix}\tag{1.7}$$

where $c_{ij} = \cos \theta_{ij}$ and $s_{ij} = \sin \theta_{ij}$. θ_{12} , θ_{13} , and θ_{23} are three mixing angles, and δ is a CP-violating phase. Other parameters are the mass squared difference, Δm_{21}^2 and Δm_{32}^2 . The current knowledge on these parameters are

Table 1.1: Current knowledge on the MNS mixing parameters

Parameters	Comments
$\Delta m_{32}^2 \sim 3 \times 10^{-3} \text{ eV}^2$ $\sin^2 \theta_{23} \sim (0.9 - 1.0)$	from atmospheric neutrinos
$\Delta m_{13}^2 < 0.1$	from CHOOZ
$\Delta m_{21}^2 = \Delta m_{solar}^2$ $\sin^2 \theta_{12}$	from solar neutrinos (large angle MSW solution) (small angle MSW solution) (vacuum oscillation solution)
δ	unknown

obtained in Table 1.1. These parameters will be determined more precisely in the measurements of long-baseline neutrino oscillations at a neutrino factory.

Major goals of the oscillation physics program are such as

- determination of θ_{13} ,
- determination of the sign of Δm_{32}^2 , and
- search for CP violation in the neutrino sector.

1.2.1 Oscillation event rates

In the three-generation neutrino mixing, when $|\Delta m_{21}^2| \ll |\Delta m_{32}^2|$, the oscillation probabilities in vacuum are given by

$$\begin{aligned}
 P(\nu_e \rightarrow \nu_\mu) &\approx \sin^2(2\theta_{13}) \sin^2(\theta_{23}) \sin^2\left(\frac{1.27\Delta m_{32}^2 L}{E_\nu}\right), \\
 P(\nu_e \rightarrow \nu_\tau) &\approx \sin^2(2\theta_{13}) \cos^2(\theta_{23}) \sin^2\left(\frac{1.27\Delta m_{32}^2 L}{E_\nu}\right), \\
 P(\nu_\mu \rightarrow \nu_\tau) &\approx \cos^4(\theta_{13}) \sin^2(2\theta_{23}) \sin^2\left(\frac{1.27\Delta m_{32}^2 L}{E_\nu}\right). \quad (1.8)
 \end{aligned}$$

From Eq.(1.8), it is seen that the measurement of $P(\nu_e \rightarrow \nu_\mu)$ will determine for instance θ_{13} . In the currently-proposed scheme of a neutrino factory, E_ν is relatively high (of 20 – 50 GeV), yielding $(\Delta m_{32}^2 \cdot L/E_\nu)$ is small. And thereby the oscillation probability is not terribly large but high statistics would give a good figure of merit in observing the oscillation phenomena. It will be shown below.

The charged neutrino current rate is given by

$$N_{cc}(\nu_e \rightarrow e^-) \propto \theta_\nu^2 \cdot \sigma_{inela}(E_\mu) \propto \frac{E_\mu^2}{L^2} \cdot E_\mu = \frac{E_\mu^3}{L^2}, \quad (1.9)$$

where θ_ν is an opening angle of the neutrino beam, and the fact that the neutrino inelastic interaction (σ_{inela}) is proportional to a neutrino energy (E_μ) is used. Typically, at 1500 km with the muon energy of 30 GeV, 0.5 M events can be expected for a 10 kton detector.

The oscillation event rate is then given by

$$N_{osc}(\nu_e \rightarrow \mu^-) \propto \theta_\nu^2 \cdot \sigma_{inela}(E_\mu) \cdot P(\nu_e \rightarrow \nu_\mu) \propto \frac{E_\mu^3}{L^2} \cdot \frac{L^2}{E_\mu^2} = E_\mu \quad (1.10)$$

where the oscillation probability is assumed to be proportional to $P(\nu_e \rightarrow \nu_\mu) \propto L^2/E_\mu^2$ since $\Delta m^2 \cdot L^2/E_\mu^2$ is sufficiently small. Therefore, to observe more neutrino-oscillation events, a higher energy is better.

1.2.2 CP violation

The CP-odd oscillation probability is given by

$$P_{CPodd}(\nu_e \rightarrow \nu_\mu) \sim -4J \frac{\delta m_{21}^2 L}{2E_\nu} \sin^2\left(\frac{\delta m_{31}^2 L}{4E_\nu}\right) \propto \left(\frac{L^3}{E_\nu^3}\right), \quad (1.11)$$

where J is the Jarlskog parameter given by

$$J = c_{12}c_{13}^2c_{23}s_{12}s_{13}s_{23}\sin(\delta). \quad (1.12)$$

The observable of the CP-odd asymmetry is defined by

$$A_{CP-odd} \equiv \frac{P(\nu_e \rightarrow \nu_\mu) - P(\bar{\nu}_e \rightarrow \bar{\nu}_\mu)}{P(\nu_e \rightarrow \nu_\mu) + P(\bar{\nu}_e \rightarrow \bar{\nu}_\mu)} \propto \frac{L}{E_\nu} \quad (1.13)$$

The CP-odd asymmetry is proportional to L/E_ν . Since the number of the oscillation events is given by Eq.(1.10). The figure of merit is given by

$$A_{CP-odd}^2 \cdot N_{osc} \propto \frac{L^2}{E_\nu}. \quad (1.14)$$

To search for CP violation in neutrino sector, it cannot be simply concluded that a higher energy is better, rather a lower energy might be more preferable. But, if the neutrino energy is too low, the neutrino intensity is definitely not sufficient. To reduce the matter effect, it is also desirable to have a shorter distance. A study of all the optimization is underway.

1.2.3 T violation

The comparison of the time-reversed oscillation processes would give a good test of T-violation as follows,

$$A_T = \frac{P(\nu_\alpha \rightarrow \nu_\beta) - P(\nu_\beta \rightarrow \nu_\alpha)}{P(\nu_\alpha \rightarrow \nu_\beta) + P(\nu_\beta \rightarrow \nu_\alpha)} \quad (1.15)$$

The T-violating asymmetry defined the above is known to have smaller contribution from the matter effect. It is also discussed that the intrinsic T-violating asymmetry can be modified slightly by the matter effects[7]. To observe T-violation, the detection of $\nu_\mu \rightarrow \nu_e$ oscillation is needed, where the naive charge identification of e^\pm is believed to be difficult. Some consideration is underway to overcome this difficulty. But, if it become doable, the search for T-violation would give the best sensitivity to measure the CP-violating imaginary phase in the MNS matrix.

1.3 The KEK/JAERI Joint Project of High-Intensity Proton Accelerator

In Japan, the project of constructing a high-intensity proton accelerator complex has been recently approved. It is the KEK/JAERI Joint Project. It would be possible to serve, if a neutrino factory is built in Japan in future, as its proton driver, providing a Mega-Watt proton beam. It is in fact sufficient enough for the neutrino factory studies presently considered in the world. Now, the realization in Japan could become more realistic. It could supply a proton beam (and a muon beam) to the world-wide scientists to carry out R&D works necessary for a neutrino factory and muon collider.

The KEK/JAERI joint project is originally to pursue broad frontier science ranging from particle and nuclear physics, materials science, life science to nuclear technology [9]. It has been proposed jointly by the High Energy Accelerator Research Organization (KEK) under the Ministry of Education, Science, Sports and Culture (Monbu-sho) and the Japan Atomic Energy Research Institute (JAERI) under that Science and Technology Agency (STA). Previously, these institutions proposed the Japan Hadron Facility (JHF) at KEK and the Neutron Science Project (NSP) at JAERI, respectively. The present new joint plan, which is temporarily called the “Joint Project”, is based on these two past proposals. It is also proposed that the accelerator complex of this Joint Project can be constructed at the JAERI Tokai campus.

The accelerator complex in the Joint Project composes three parts:

- a 400-MeV proton linac,
- a 3-GeV rapid cycle synchrotron (3-GeV PS), and

- a 50-GeV proton synchrotron (50-GeV PS).

The schematic layout of the accelerator complex is shown in Fig.1.1. The linac system consists of a 400 MeV normal-conducting linac with 50 mA and 25 Hz repetition and a super-conducting linac from 400 MeV to 600 MeV. The 3-GeV PS will provide 330 μA average beam current. The beam intensity of the 50-GeV PS is 3.2×10^{14} proton per pulse with a repetition rate of about 0.4 Hz at fast beam extraction. (The repetition rate is about 0.3 Hz for slow beam extraction.) The total beam power becomes about 1.0 MW. The total cost of the project is about 1800 billion US dollars. The phase 1 of the project has been approved, the total cost of which is about 1300 billion US dollars. The phase 2 will be requested as the phase 1 construction is going on. The construction will start from Japanese fiscal year of 2001 and will complete by year 2006.

The upgrade path of the proton beam intensity has been also considered. It will be achieved by installing more RF cavities and their power supplies into the 50-GeV PS ring. The expected proton beam intensity will be about 4.4 times the beam intensity considered now, providing 4.4 MW beam power. The details of the proton accelerator will be discussed in the following chapter.

1.3.1 Neutrino Factory Layout

As shown in the subsequent sections, our neutrino factory is based on the scheme of FFAG (Fixed-Field Alternating Synchrotron) acceleration, where after the muon capture, a series of FFAG rings are used to accelerate muons with large emittance. For this scheme, the total accelerator complex is simple and compact. A preliminary layout of the neutrino factory of the FFAG version at the 50-GeV PS at the Tokai campus is also shown in Fig.1.1. The accelerators must be located deep underground.

1.4 Staging Approach

1.4.1 Full-size Neutrino Factory

A staging approach should be seriously considered to construct a neutrino factory. This staging approach is needed in two folds. One is that to establish technology will require long term, whereas physics activities had better kept high even in the R&D period. It could be possibly done. The second is to maintain the budget profile to a reasonable size at different stages to get the funding easier. This is, we believe, essential to accomplish a large Mega-science project such as a neutrino factory.

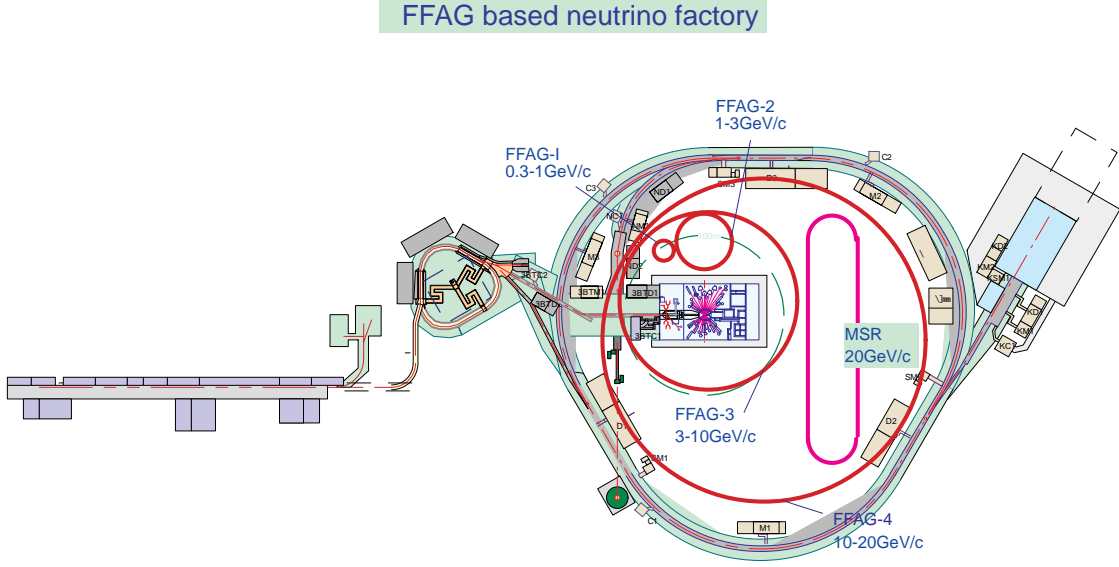


Figure 1.1: Schematic layout of a FFAG-based neutrino factory at the Tokai campus

Possible staging approach towards full-size neutrino factories that we consider is the following.

- **Phase I:** 1.0×10^{20} muon decays/year at the one straight section. The initial beam power of the 50-GeV PS is 1 MW. The muon energy in the muon storage ring is 20 MeV.
- **Phase II:** 4.4×10^{20} muon decays/year at the one straight section. The beam power of the 50-GeV PS is upgraded to 4.4 MW by installing more rf cavities in the 50-GeV PS ring. The muon energy in the muon storage ring is from 20-50 GeV.

It is shown in Fig.1.3.

The staging approach at the R&D period leads some specialized approach, which is shown in Fig.1.2. Since we are considering the scheme of FFAG-based acceleration, it is conceivable to start with a small-size FFAG at upstream, and add downstream FFAG's in the later stage.

1.4.2 PRISM


In particular, at a very early stage, we consider to have a very small FFAG ring for stopped muon experiments, where searches for muon lepton flavor

violation can be carried out. It is noted that the search for muon lepton flavor violation has attracted much interest as good testing ground of supersymmetric grand unification [21]. The project is called *PRISM*, which stands for Phase Rotated Intense Muon beam. In PRISM, the FFAG ring of about 10 m diameter will be used to do phase rotation, not acceleration. The phase rotation is necessary to make an energy spread of muon beam narrower. it is known to be crucial for stopped-muon experiments. PRISM has many common technical challenges with R&D for neutrino factories. They are such as a large-solid angle pion capture with high-field solenoid magnet, phase rotation, high-gradient rf cavity, and a FFAG ring itself. The details of PRISM are shown in Appendix.

Pre-Neutrino Factory



PRISM

- 
- High-intensity low-energy muon source (**for rar muon decays**)
 - » 10T pion capture
 - » Phase rotation at PRISM-FFAG
 - **P=68 MeV/c** (KE=20 MeV)
 - Injection momentum: $dp/p = 50\%$
 - **10^{19} muons/(10^7 sec)** in the ring
 - Based on 1-MW 50-GeV PS

PRISM-II


- 
- Acceleration with an additional accelerator (FFAG)
 - **10^{20} muons/(10^7 sec)** in the ring
 - Give a modest neutrino source

Figure 1.2: Possible staging scenario before full-size neutrino factories. PRISM is the project for stopped muon experiments and PRISM-II will provide more energetic muons together with low-energy neutrinos of about 1 GeV/c

Accelerator Scenario



Neutrino Factory



- **1×10^{20} muon decays/year** at one straight section
- Based on 1-MW 50-GeV PS
- Muon energy: **20 GeV**
 - » Energy is determined by cost and physics topics.
- Location: JAERI Tokai campus

Neutrino Factory-II



- **4.4×10^{20} muon decays/year** at one straight section
- Based on upgraded **4.4-MW** 50-GeV PS
- Muon energy: **50 GeV**

Figure 1.3: Possible staging scenario of full-size neutrino factories: Phase I uses 1 Mega-watt proton beam power and Phase II uses upgraded 4.4 Mega-watt proton beam power.

Chapter 2

Accelerator

2.1 Overview of FFAG based neutrino factory

The requested total number of muon decays in one straight section of the muon storage ring at the first stage of the neutrino factory is more than 1×10^{20} muon decays per year and the goal intensity is to get about 5×10^{20} muon decays per year. A high accelerating gradient and small total length of the accelerator minimize beam loss caused by muon decay, but require that the rf frequency used in the linear accelerator system becomes relatively high. The typical rf frequency range utilized in this scheme is several 100MHz. Moreover, a small total length of the linear accelerator system also helps to reduce the cost of the accelerator. The muon survival for various accelerating field gradients when the muons are accelerated from 300MeV/c to 20 GeV/c is shown in Fig.2.1.

The conventional neutrino factory scheme, so called "PJK" scenario, which is based on the linear accelerators and muon storage ring, has been proposed[11]. In the linear accelerator based neutrino factory scenario, the accelerating field gradient should be more than 5MV/m. This is not only to increase muon survival rates, but also because the total distance during the acceleration becomes tremendously large in the linear accelerator system if the accelerating field gradient is less than 5MV/m.

In order to achieve such a high accelerating field gradient in an rf system, it is inevitable to adopt an rf system using relatively high frequency rf cavities where the frequency range is several 100 MHz. For such a high frequency rf accelerating system, the beam aperture size is limited to keep the shunt impedance of the rf cavity large enough. This limits the transverse acceptance of the system. Thus, transverse muon beam cooling before acceleration becomes essential in the high frequency rf accelerating system.

Any ordinary beam cooling such as stochastic cooling can obviously be

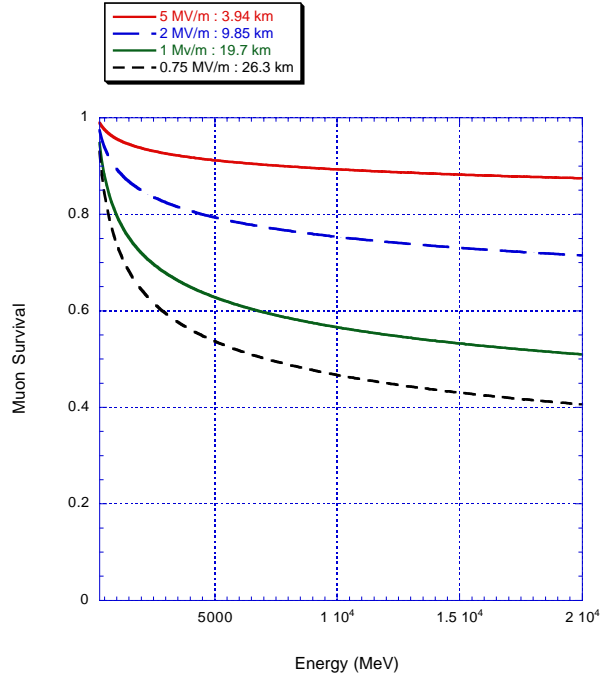


Figure 2.1: Muon survival during acceleration from 300MeV/c to 20GeV/c for various accelerating gradients and fractional distances along the machine

useless since the cooling time is much longer than the muon lifetime. Ionization cooling consists of a number of energy degrading media between the rf accelerating cavities, and seems to be a possible solution. To make cooling efficient, the accelerating field gradient of the rf cavity has to be large and also a high frequency rf system whose frequency range is more than 100MHz is unavoidable.

The initial pions and the product muons, however, have a large energy spread, which is much larger than the acceptance of the ionization cooling system. Phase rotation before cooling is also required to decrease the energy spread. Total beam loss in the cooling channel seems to be very large. According to detailed work done by the FNAL group, the muon beam intensity after cooling could drop substantially.

If a ring accelerator can be adopted to muon acceleration, this limitation becomes modest. Many turns for acceleration in the same ring using the same accelerating system help to reduce the total size of the accelerator and the total construction cost. As can be seen in Fig.2.1, even when the accelerating gradient is only 1MV/m, the muon survival during acceleration up to 20GeV/c is still more than 50 %, which should not be so painful.

Such a low accelerating field gradient can be realized with a rather low frequency rf accelerating system. For example, in the anti-proton decelerator (AD) at CERN, the 9.5MHz rf cavity has achieved a field gradi-

ent of about 0.35MV/m with a modest rf peak power of 0.19MW in burst mode operation[19]. If the rf power increases, the field gradient could reach 1MV/m. One of the advantages in using a low frequency rf system is its large longitudinal acceptance. The typical longitudinal acceptance with such a low frequency rf system would be several eV.s or more. The particle distribution of the initial pions and the product muons in the longitudinal phase space after the captured solenoid when the 50 GeV proton driver described above is used are shown in Fig.2.2. In this case, the bunch length of the primary proton beam from the 50 GeV proton driver is assumed to be 6 nsec in rms value.

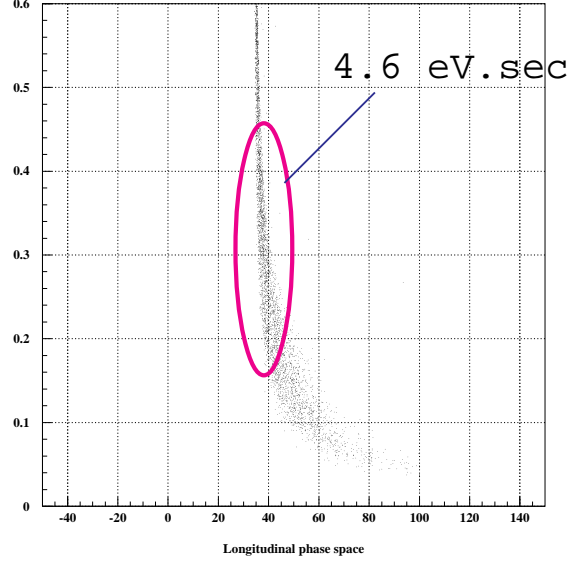


Figure 2.2: The particle distribution of the initial pions, and the product muons generated by a short bunched 50 GeV proton beam in the longitudinal phase space. (Horizontal axis: time of flight(ns) Vertical axis:total momentum(GeV/c))

As can be seen in the figure, the particles having central momentum and momentum spread of 300MeV/c and $\pm 50\%$, respectively, are well within the area of 4.6 eV.s.

This size of longitudinal acceptance can be realized by a low frequency rf accelerating system having an accelerating field gradient of 1MV/m. Obviously, a linear accelerator with such a low frequency rf system is not suitable for accelerating muons to high energy because the total distance becomes too long. Thus, a ring accelerator is practically the only scheme possible for muon acceleration with a low frequency rf system.

The ordinary synchrotron is obviously inadequate for accelerating muons. The magnetic field in an ordinary synchrotron must increase during acceleration and the ramping rate cannot be fast enough to compete with the muon

lifetime. The maximum magnetic field ramping rate for a conventional steel electro-magnet is limited by eddy current loss to less than about 200T/sec. At least, time of the order of msec to reach the high magnetic field is needed, which is too long for accelerating muons within their lifetimes. A ferrite magnet has a 100 times larger maximum magnetic field ramping rate, but the maximum attainable magnetic field strength is about 0.1 T or less, making the ring size very big. Thus, we consider that a static magnetic field must be used in ring accelerators for muon acceleration.

The cyclotron is inadequate for accelerating muons to high energy. Keeping isochronous in this type of accelerator becomes rather difficult when accelerating relativistic particles. The FFAG (fixed-field alternating gradient) accelerator should be ideal for accelerating muons to high energy.

The FFAG is a strong focusing type of synchrotron having a static magnetic field. The concept of the FFAG accelerator was proposed by Ohkawa in 1953.[12] In the early 1960s, this type of accelerator was widely studied and small electron models were developed mostly in North America under the MURA project.[13] However, no practical FFAG had ever been built until recently.

In 1999, development of the proton model of the FFAG accelerator (POP model) was started at KEK and the first proton beam acceleration was successfully achieved in June of 2000[14].

A big advantage of the FFAG accelerator for accelerating short lived particles such as muons is that the beam guiding magnetic field is static. The acceleration time can be short enough to eliminate the particle decay if the rf voltage is large enough. Contrary to electron acceleration, acceleration of a heavy particle such as the proton in an FFAG accelerator is rather difficult, because the rf accelerating system must have a frequency modulation that matches the varying beam revolution time. In order to produce frequency modulation, a low frequency rf cavity inductive material such as ferrite has been used in the ordinary proton synchrotron. Since the bandwidth of ferrite is, however, rather small and the rf loss caused by hysteresis becomes very large at a field more than several hundred gauss, the ferrite loaded type of cavity is totally inadequate for the FFAG accelerator.

A new type of broadband rf cavity using a soft magnetic alloy (MA cavity) has been developed at KEK. The bandwidth of this type of rf cavity is very broad because of its small Q-value ($Q < 1$). The attainable rf field strength becomes very large compared with that of ferrite which has been widely used as the inductive material for the proton synchrotron

Another advantage of the FFAG accelerator is that it has a large acceptance for both transverse and longitudinal directions. The horizontal acceptance of the FFAG accelerator is very large and normally exceeds $10000\pi\text{mm}\cdot\text{mrad}$ in real phase space. The momentum acceptance is also very large and a beam having a large momentum spread of more than $\pm 50\%$ can be acceler-

ated. Thus, both muon cooling and, accordingly, phase rotation should not be necessary. That should be a straightforward option for muon acceleration in the neutrino factory.

In the FFAG accelerators, there are two different types from the beam dynamics point of view; one is the scaling type and the other the non-scaling type. In the scaling type of FFAG accelerator, the beam orbit scales for different energies, which means that the betatron tunes for both horizontal and vertical directions are always constant during acceleration. This is the so-called "zero-chromaticity" condition.

In Fig. 1.1, a conceptual schematic layout of the FFAG based neutrino factory with the 50 GeV proton driver at JAERI Tokai site is presented. Since the practical momentum range from injection to extraction in the FFAG accelerator is about 3 to 4 times, there are four FFAG rings for each ring will be described later but the basic beam parameters for each one are summarized in Table 2.1.

Table 2.1: Main parameters of FFAG accelerator complex.

momentum (GeV/c)	0.3 to 1 (normal)	0.3 to 1 (super)	1 to 3 (normal)	1 to 3 (super)	3 to 10	10 to 20
average radius (m)	21	10	80	30	90	200
number of sector	32	16	64	32	64	120
k value	50	15	190	63	220	280
beam size at extraction(mm)	170×55	143×55	146×41	115×25	93×17	104×34

In this FFAG based neutrino factory, the expected muon intensity after acceleration exceeds more than 3×10^{20} muons/year with the 50 GeV and 1MW proton driver and about 1×10^{20} muon/decays/year/straight in the muon storage ring can be realized. If the 50 GeV proton driver is upgraded to reach the beam power of 4 MW as described below, the more than 4×10^{20} muon decays/year/straight becomes possible.

2.2 Scheme

2.2.1 Proton Driver

2.2.1.1 General

The 50 GeV proton synchrotron of the joint project between KEK and JAERI, which will begin construction in April, 2001 as a 6-year term project,

is considered to be the proton driver for the future neutrino factory. The planned 50-GeV proton synchrotron consist of a 400-MeV proton linear accelerator (400-MeV linac) as an injector, a 3-GeV rapid cycling synchrotron as a booster and a 50-GeV proton synchrotron (main ring).[15] The accelerators will be constructed at the south site of JAERI-Tokai, as shown in Fig.2.3.

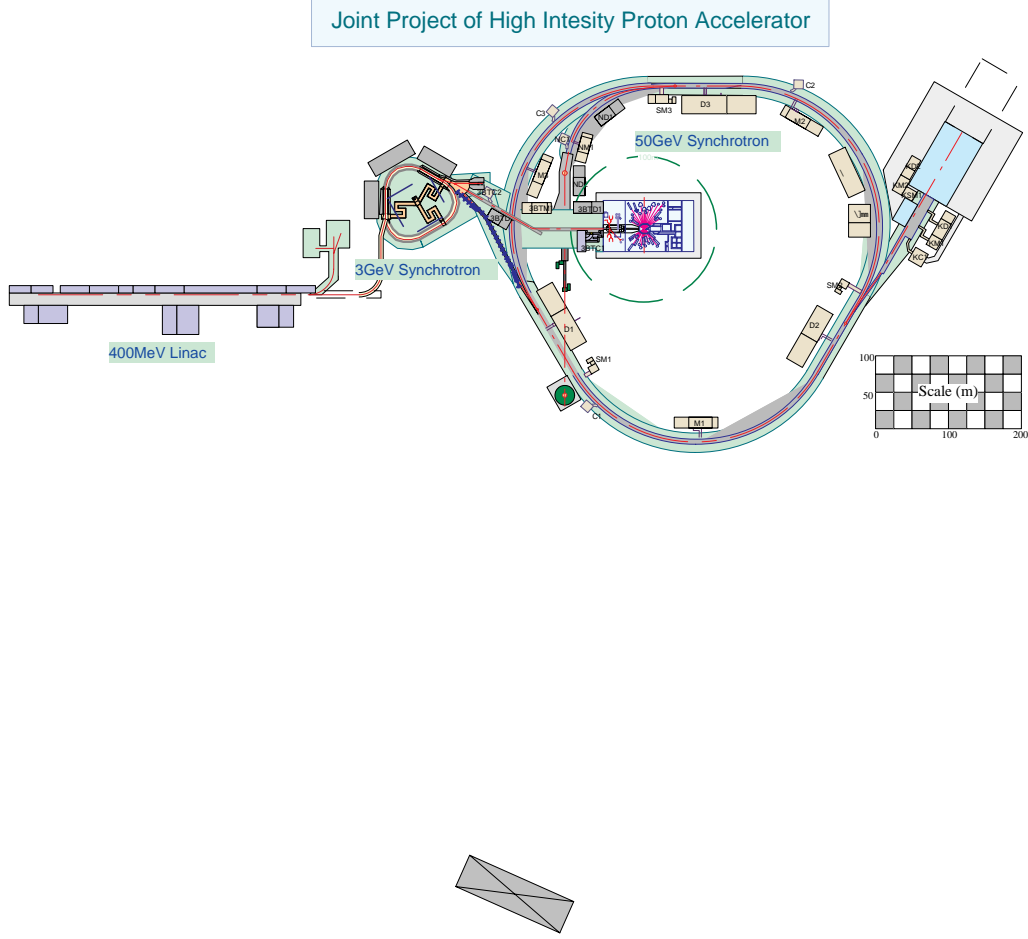


Figure 2.3: Schematic layout of the accelerator complex of the joint project at the JAERI Tokai site.

The main ring is to accelerate protons from 3 GeV to 50 GeV. The expected beam intensity in the main ring is 3.3×10^{14} ppp and the repetition rate is about 0.3 Hz. The 50-GeV protons are extracted by slow and fast extraction schemes into two experimental areas: one is for experiments using secondary beams (K, antiproton, etc.) and primary beams by slow extraction, and the other is for the neutrino oscillation experiments by fast extraction. When operated in a slow extraction mode, the average current and duty factor, which is defined as the fraction of a cycle when a beam is

available, are $15 \mu\text{A}$ and 0.20, respectively.

2.2.1.2 Beam Parameters

The typical machine cycle structure is illustrated in Fig.2.4 Four batches from the booster are injected into the main ring when the main ring stays at a low field. Then, 8 buckets out of 10 are filled with beams, and the main ring starts acceleration while three other facilities start to use 3-GeV beams directly from the booster. Table 2.2 gives the main parameters of the main ring.[1]

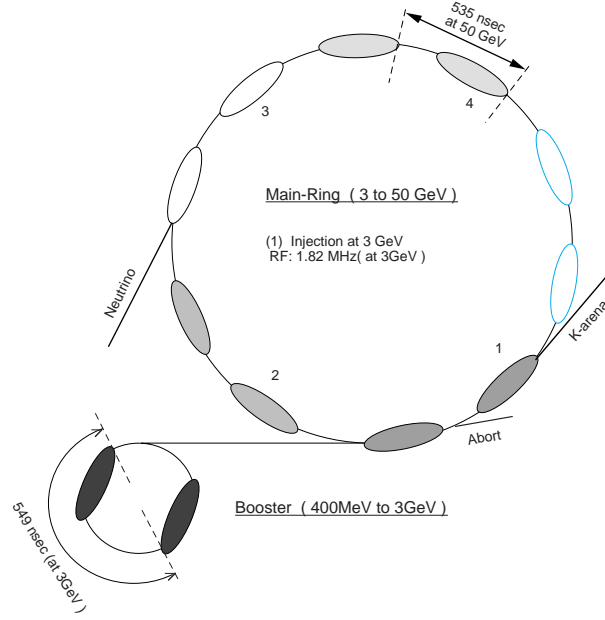


Figure 2.4: Typical machine cycle structure

2.2.1.3 Imaginary Transition γ Lattice

Protons are accelerated from 3 GeV to 50 GeV in the main ring. At the top energy of the 50-GeV main ring, γ is 54.3. In a conventional way of designing a lattice using a regular FODO cell, the transition γ approximately equals to the horizontal betatron tune (ν_x). In a machine of this scale, because ν_x is about 20-30, it is difficult to avoid the transition energy in the regular FODO lattice. Although transition energy crossing techniques have been developed in many operational proton synchrotrons, it is favorable to place the transition energy, where the phase focusing becomes zero, well above the maximum energy, avoiding the instabilities and associated beam losses. Thus, an imaginary transition γ lattice, in which the momentum compaction

Table 2.2: Main parameters of 50 GeV PS synchrotron as a proton driver.

Parameter	present	upgraded
Proton energy	50 GeV	50 GeV
Protons/pulse	3.3×10^{14}	8.2×10^{14}
Pulse rate	0.37 Hz	0.66 Hz
Beam Power	1.0 MW	4.4 MW
μ -acceptance (μ/p)	0.21	0.21
μ -survival (N_μ/N_{source})	0.52	0.52

factor is negative, is employed. The momentum compaction factor is given by

$$\alpha = \frac{1}{\gamma_t^2} = \frac{1}{C} \oint_C \frac{\eta(s)}{\rho(s)} ds = \frac{\nu_x^3}{R} \sum_{n=-\infty}^{\infty} \frac{|a_n|^2}{\nu_x^2 - n^2} \quad (2.1)$$

$$a_n = \frac{1}{2\pi} \int_0^{2\pi} \frac{\beta_x(\phi)^{3/2}}{\rho(\phi)} \exp(-in\phi) d\phi \quad (2.2)$$

Here, η the dispersion function, ρ the radius at the orbit position of s in the ring, C the circumference of the ring, and R the average radius of the ring. β_x and ρ are the horizontal beta function and curvature, respectively. To make the momentum compaction factor negative, either β_x or ρ should be modulated properly. In order to avoid a bigger beam size, ρ modulation while invoking the missing bend sections in each arc of the ring is better than β_x modulation, although the ring circumference becomes slightly large. In the ρ modulation scheme, the momentum compaction factor and the dispersion function can be estimated analytically. [2] If each arc of the ring comprises periodic modules and each module consists of several FODO lattices, a negative momentum compaction factor can be obtained by choosing the total phase advance of the module as

$$\phi > 2\pi \sqrt{1 / \left\{ 1 + \frac{2 \sin^2 \xi}{\pi^2} \left(\frac{1}{1 - \xi} \right)^2 \right\}} \quad (2.3)$$

Here, ξ is the ratio of the missing bend length to the total module length. If ξ is 1/3, for example, the momentum compaction factor becomes negative when the total phase advance (ϕ) is $> 0.83 \times 2\pi$. In the 50-GeV main ring, the superperiodicity is three and each arc section consists of eight modules. Each module has three FODO cells starting from a defocusing quadrupole. In the center cell of the module, there are no bending magnets (missing bend cell). Thus, ξ is about 1/3.

2.2.1.4 RF System

A large rf voltage is required for the accelerating system in a high-intensity medium-energy proton synchrotron because of its large ring radius and fast rate of change of the dipole magnetic field. Since space for the rf cavity in the ring is normally limited, it is desired that the rf voltage per unit length, the so-called effective rf field gradient, should be raised as high as possible. When the total length of the cavities becomes short, the impedance seen by the beams also becomes small. This is good for stable operation under heavy beam loading. The conventional ferrite-loaded accelerating cavity suffers from several points: (1) high loss effect, (2) small B_{rf} , (3) low Curie temperature and (4) coupled bunch instabilities caused by the parasitic mode. Recently, high-permeability soft magnetic alloys, such as FINEMET and Metglas, have become available for application in the rf cavity. Compared with ferrite, these materials have the following characteristics:

1. The μQf -value remains constant at a high rf magnetic field. In the case of the FINEMET, the μQf -value is still constant, even at an rf magnetic field of 2 kG. Therefore, the rf power density in the material is still marginal ($\sim 2.5 \text{ W/cm}^3$) at a relatively high effective rf field gradient ($\sim 70 \text{ kV/m}$), as shown in Fig. 1.5.
2. A high Curie temperature, typically 570°C for FINEMET, makes the cavity possible to operate at a high effective field gradient.
3. Because of its low Q-value ($Q \sim 1$), no frequency tuning loop is necessary in the cavity control system. This substantially widens the stable operating region of the cavity loading phase angle under heavy beam loading.
4. The longitudinal coupled-bunch instability may be reduced, since the Q-value of the cavity is low.
5. Fabrication of a large core is possible because the core is formed by winding very thin tapes.

A high-power test cavity using FINEMET has been developed in order to clarify the above-mentioned characteristics. There are 8 pieces of FINEMET cores in the cavity, and the length of the cavity is about 0.4 m. An rf voltage of more than 20-kV, and therefore an effective rf field gradient of more than 50-kV/m, was obtained under cw operation. The maximum rf voltage is only limited by the rf power source, not by any defects in the cavity. This type of cavity may also open up many possibilities in rf gymnastics, because of its ability to generate a high field gradient and to allow broadband operation, such as beam stacking with an rf barrier bucket, a higher harmonics cavity for reducing the space charge effect, and so on.

2.2.1.5 Main Ring Upgrading

The average beam current of $15.6 \mu\text{A}$ for slow extraction and $19.6 \mu\text{A}$ for fast extraction at the first stage will be increased in future. There are several upgrading options. Roughly speaking, two major paths should be taken: one is increase of repetition rate and the other is increase of particles per pulse. Although the repetition rate of the main ring at the beginning is 0.29 Hz for slow extraction mode and 0.37 Hz for fast extraction mode, the lattice magnets themselves are designed so that a higher repetition rate such as 0.51 Hz operation for slow extraction and 0.79 Hz for fast extraction will be possible. That pushes up the average current to roughly $26.8 \mu\text{A}$ and $41.6 \mu\text{A}$, respectively. In this case, the electric power required for exciting the lattice magnets increases and becomes almost doubled. Although the main ring is not a space charge limited synchrotron at the design particles per pulse in terms of space charge tune shift, special care is necessary if we need to increase the number of particles. One of the options to increase the number of particles is to use barrier buckets at injection. Capturing with barrier buckets decreases the local line density at injection so that the tune shift becomes less. Another advantage of using barrier buckets for injection is that we can inject as many booster batches as we want in contrast with bunch to bucket transfer. The number of batch is rather limited by transverse space charge effects or longitudinal momentum spread.

If a higher repetition rate and barrier bucket injection with 10 beam batches are adopted simultaneously in future operation, the average current increases up to $59.4 \mu\text{A}$ for slow extraction mode and $86.9 \mu\text{A}$ for fast extraction mode.

Table 2.3: Upgrade path for 50-GeV main ring

	beam current slow/fast	repetition rate slow/fast	duty factor	intensity
design	$15.6 \mu\text{A}/19.6 \mu\text{A}$	$0.29 \text{ Hz}/0.37 \text{ Hz}$	20%	$3.3 \times 10^{14} \text{ ppp}$
ramping rate	$26.8 \mu\text{A}/41.6 \mu\text{A}$	$0.51 \text{ Hz}/0.79 \text{ Hz}$	36%	$3.3 \times 10^{14} \text{ ppp}$
barrier bucket	$59.4 \mu\text{A}/86.9 \mu\text{A}$	$0.45 \text{ Hz}/0.66 \text{ Hz}$	32%	$8.2 \times 10^{14} \text{ ppp}$

2.2.1.6 Bunch structure for the FFAG based neutrino factory

In the linac based neutrino factory, in order to reduce the beam emittance efficiently by ionization cooling, phase rotation in longitudinal phase space to decrease the momentum spread of the muon beams becomes essential. Thus, the bunch length of the beam from the proton driver should be rather short in the linac based neutrino factory. The required bunch length in this case is

about 3ns or less in rms size. On the other hand, in the FFAG based scenario, the requirement of the bunch length is much more modest compared with this because the longitudinal acceptance of the FFAG using a low frequency rf system is relatively large. The expected bunch width from the proton beam is 6 ns or more in rms size. In fact, the rf frequency at 50 GeV is about 2 MHz and the bunching factor at 50 GeV becomes about 0.038. Thus, the rms bunch length at 50 GeV is approximately 6 ns in ordinary operation, which is exactly the same as required in the FFAG based neutrino factory. This means that no special treatment to the bunch shortening is necessary for the 50GeV proton driver in our FFAG based neutrino factory. If we need in future a bunch shortening for some reasons such as muon polarization, we may take the several schemes for this purpose as described below.

1. Double harmonic number

The peak beam current at 50 GeV reaches almost 200 A, This is not an easy value to compensate for its beam loading effects on the rf system. It is preferable not to exceed the peak beam current from 200A, which means that the bunching factor should be around 0.038 even when we shorten the bunch width to half of the ordinary one. To shorten a bunch width of less than 6 ns in rms size while keeping the same bunching factor, we increase the harmonic number twice at the top energy of the 50 GeV ring. It is rather hard to change all of the harmonic numbers from the 3-GeV booster to 50-GeV main ring. The new harmonic number becomes 20. In order to realize this, a second harmonic rf system at the top energy of the 50 GeV ring should be introduced, and bunch manipulation with de- bunching and re-bunching could be applied.

As described in section 2.2.1, broadband rf cavities with soft magnetic alloy (MA cavity) are used for acceleration in the 50 GeV ring. The Q-value of this type of cavity can be rather low and controllable by cutting cores. In case of the 50 GeV ring, any Q values between 1 and 10 can be set by varying the core spacing. The second harmonic rf cavities using the same material are installed in the 50 GeV ring for increasing the bunching factor at beam injection to reduce the transverse space charge effect. These rf cavities may also be used for the bunch shortening. The main items to be examined from the beam dynamics view in this scheme are microwave instability during the debunching and coupled bunch instability after rebunching. As for the microwave instability, the stability condition would be the same as that of the ordinary operation, which is $Z/n < 2\Omega$, because the bunching factor and $\Delta p/p$ is the same. Low Q cavities are used in the rf acceleration of the 50 GeV ring. Provided the low Q cavities are also utilized for doubling the harmonic number, the coupled-bunch instability can be avoided.

2. Other scheme

There are a couple of other methods to achieve a short bunch as shown in ref.[2]: (1) rf amplitude jump, (2) rf phase jump, and (3) Γ t manipulation. Method (1) is a common one, however, very high gradient and low frequency rf cavities are necessary and transient beam loading effect has to be cured carefully. Methods (2) and (3) has been preliminarily tried at the HIMAC synchrotron[3] and the KEK 12-GeV PS[4], respectively. It seems to work at the intensity level of 10^{12} ppp for the method (3), however, further intensive studies including simulations and experiments should be done.

2.2.2 Capture

The proton beam extracted from the proton driver is lead to the targetry and capture section. In the present design of the capture section, solenoid capture with superconducting solenoid magnets is employed. In this scheme, issues to be considered in FFAG scenario are typically the following two points.

1. Momentum region to be captured
Which momentum region should be captured ?
2. Hardware issues
 - How large and strong field can be generated under the strong radiation environment
 - How to realize a long production target to stand for huge energy dissipation ? ¹

The second one is common among different neutrino factory scenarios[2, 3]. On the other hand, the first one is a proper issue for individual neutrino factory scenario. Thus, this note concentrates on the beam characteristics.

2.2.2.1 Simulation setup

The hadron interaction in the production target was simulated by MARS14(00) which was developed by FNAL .The particle transport in the solenoid channel was simulated by GEANT3.14 with with the generated events by MARS. Fig. 2.5 shows the setup used in the capture simulation.

In that study, as a typical capture field configuration, the field strength of 20T(inner bore radius: 8cm) was taken for the capture solenoid. For the transport channel, 5T(inner bore radius: 16cm) solenoid was assumed.

As a typical target material, tungsten is employed. The dimension of the target is 0.5cm(radius) \times 20cm(length). Here, the target length is 20cm,

¹typical power dissipation in the target is about 10~15% of beam energy

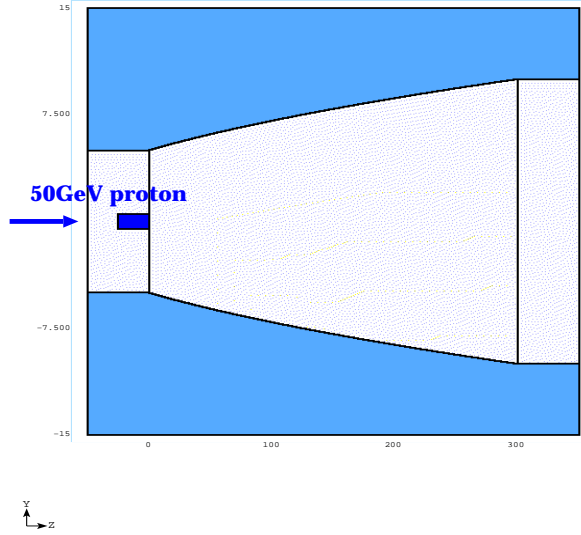


Figure 2.5: Schematic view of the setup for the pion capture simulation

which corresponds to 2 nuclear interaction length of tungsten. The secondary particles yield reaches its maximum at the almost center of the target. It should be noted that the target material species do not affect the spectrum of secondary particles so much but change the absolute yield. Considering the heat load in the production target, lighter and more tolerable material such as carbon seems to be realistic. In the case of a carbon target, the only major difference is absolute yield. The yield reduces about 40% of that with tungsten target.

Thus, except the absolute yield, the following discussion with a typical target material(tungsten) is valid.

2.2.2.2 Distributions of secondary particles

Before going to the detail of the capture scheme, initial distribution at the exit of solenoid capture channel is presented.

Fig. 2.6 shows a typical pion and muon distribution at the point 15m downstream of the production target. The setup used to obtain the figure is described in the previous section. The maximum transverse momentum captured in the channel is $0.24 \text{ GeV}/c (= 0.3 \times 20(\text{T}) \times 0.08(\text{m})/2)$. The momentum is peaked around $150 \text{ MeV}/c$. The peak mainly consists of relatively low energy muons and undecayed pions are peaked around $250 \text{ MeV}/c$. In the setup, the yield of captured pion is about 1.2 /one 50GeV proton.

Compared to the momentum spectrum captured by the solenoid field with that without solenoid field, the solenoid capture somehow gains pion yield up to about 1GeV. Above the momentum region, there is no apparent difference

compared to the case of without solenoidal field.

In the beam momentum region higher than 1GeV/c, the conventional horn magnet will be more effective.

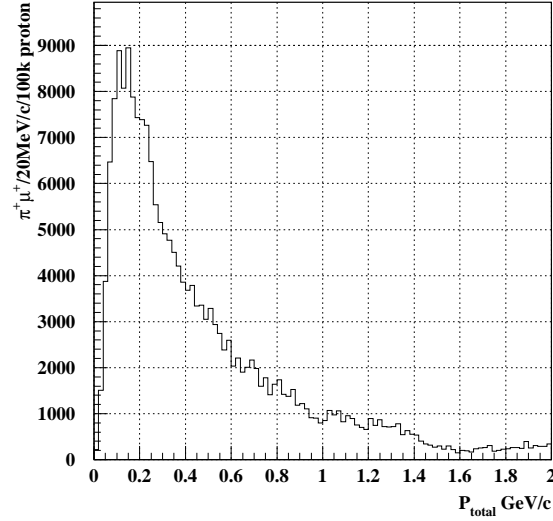


Figure 2.6: μ^+, π^+ momentum distribution at the exit of the capture magnet(10m downstream from the production target)

2.2.2.3 High energy capture

In the FFAG scenario, making use of FFAG's large horizontal acceptance, muons are accelerated without applying phase rotation and cooling. In addition, with the FFAG scenario, momentum width that can be captured by RF bucket could be as large as $\pm 50\%$ in dp/p .

Under such a situation, the configuration and requirement of the capture stage might be changed compared to that with phase rotation and cooling channel. Firstly, the long drift space for the generation of longitudinal distribution, which is indispensable for phase rotation, is also omitted. Secondly, the initial energy at which muon acceleration starts is arbitrary, due to the energy loss behavior of muon in a material is no more a problem. Thus, the initial energy can be determined only from the point of view of muon yield.

If the momentum acceptance of dp/p (typically $\sim 50\%$) is fixed, the absolute momentum width gets larger as the central momentum gets higher. In result, even if the muon is distributed in rather low energy region, $\sim 200\text{MeV}/c$ (see Fig. 2.6), muon acceleration with higher initial energy, which is called "high energy capture, might increase the muon yield.

With the above motivation, muon yield was estimated with fixed momentum acceptance ($dp/p=0.5$). Fig. 2.7 shows the change of muon yield as a

function of central muon momentum. Here, the transverse phase space cut was applied at $10000 \pi\text{mm}\cdot\text{mrad}$. Here, unnormalized emittance was employed for the emittance cut. With the emittance cut, the horizontal space was varied to find out the optimum point. In this figure, the muon yield reaches its maximum around the central energy of $0.9\text{GeV}/c$. The optimum energy tends to get lower, as the emittance cut point gets larger. For example, in the case of emittance cut of $20000\pi\text{mm}\cdot\text{mrad}$., the optimum central momentum is about $0.6\text{GeV}/c$.

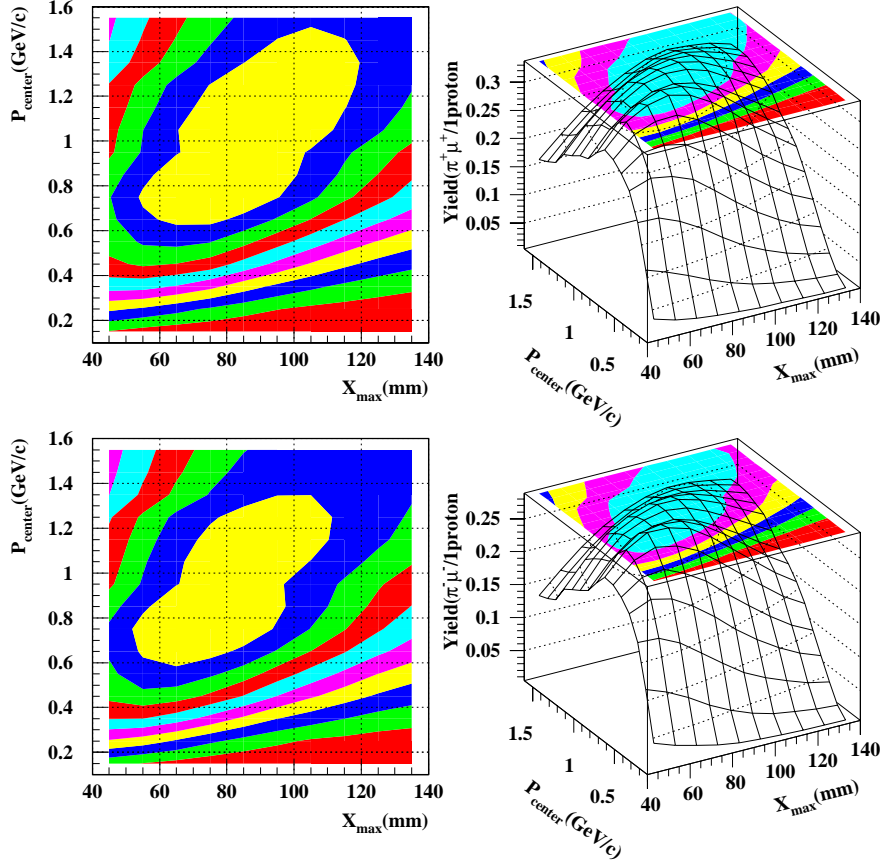


Figure 2.7: Muon and pion yield with fixed transverse acceptance, The top two figures : $\mu^+ + \pi^+$, the bottom two figures : $\mu^- + \pi^-$

In the setup used in the study, the muon yields per one 50GeV proton incident are ~ 0.3 , ~ 0.5 for the case of emittance cut of $10000 \pi\text{mm}\cdot\text{mrad}$, and $20000\pi\text{mm}\cdot\text{mrad}$., respectively. It is sufficiently a high yield.

Therefore, if the phase rotation and muon cooling stages can be skipped, the high energy capture might be an option. Another merit of the high energy capture is that the phase-slip due to the wide momentum spread

is less serious compared to the lower energy case, since the velocity of the particles of interest is nearly c , the speed of light. As shown in Fig.2.2, in high energy capture, the longitudinal emittance is about 4.6eV·sec.

From the point of view of the beam characteristics, one of the potential problems in the case of high energy capture is muon polarization. The key to obtain a highly polarized muon beam is to get a monochromatic pion beam². Without it, after pion decay, the polarization of muon is mixed up and diluted. Ordinal pion capture with solenoidal field is the case. The FFAG scenario with high energy capture is a straight forward scheme. Thus, there is no handling knobs to control the muon polarization. In result, it might be difficult to obtain a highly polarized muon beam in the FFAG scenario. However, the muon polarization offers fruitful physics potentials for a neutrino factory. Therefore, it is too early to make a negative conclusion, and it needs further investigation.

2.2.3 Acceleration

2.2.3.1 Requirements

Quick acceleration of muon beams becomes possible with a Fixed Field Alternating Gradient (FFAG) synchrotron (See Appendix) and high voltage rf cavity such as 1MV/m on average with very low frequency. We plan to capture muons with the central momentum of 0.3 GeV/c as discussed in the previous section. Large momentum acceptance of a FFAG ring makes it possible to accommodate the momentum spread of $\pm 50\%$ and to accelerate a beam up to the final momentum without any beam cooling.

There are several arguments what the optimized momentum is from the physics point of view. Nevertheless, 20 GeV/c is the upper bound if the whole accelerator complex should be fit in the area enclosed with 50 GeV PS in JAERI site. The final momentum is rather arbitrary within the range of 10 to 50 GeV/c. There are several arguments what the optimized momentum is from the physics point of view. Nevertheless, 20 GeV/c is the upper bound if the whole accelerator complex should be fit in the area enclosed with 50 GeV PS in JAERI site.

In order to accelerate muon beams from 0.3 GeV/c to 20 GeV/c, we have designed four FFAG rings, which are connected in cascade. The first ring accelerates muons from 0.3 GeV/c to 1 GeV/c, followed by the second one of 1 GeV/c to 3 GeV/c, the third one of 3 GeV/c to 10 GeV/c, and the final one of 10 GeV/c to 20 GeV/c. The momentum ratio of each injection and extraction is about 3 except for the final ring. That is a moderate design and gives small orbit excursion, say 0.5m.

²A typical example is the surface muon beam.

2.2.4 Constraints

The design constraints of the four FFAG rings are summarized in the following. First, the machine size should be as small as possible. Presumably, the whole muon accelerator complex will be constructed inside the area enclosed with the 50GeV PS, whose average radius is around 250m. Secondly, the magnetic field strength should be either below 1.8T in order to use normal conducting magnet or higher than that but definitely below 6T for superconducting magnet option. Thirdly, orbit excursion should be less than 1m or possibly around 0.5m. Therefore, the size of a magnet will be reasonable. Fourthly, longitudinal packing factor should be less than 0.5, meaning that the total magnet length compared with the circumference is less than a half. That is required to install rf accelerating cavity as much as possible and obtain average field gradient of more than 1MV/m.

2.2.4.1 Triplet radial sector

We adopted a scaled radial sector type FFAG with a triplet focusing. Compared with a spiral sector type FFAG, the radial one tends to have larger circumference ratio, which is the ratio of bending radius and average machine radius. However, easiness of magnet fabrication and better quality of fringing field of the triplet magnet is attractive enough to discard the spiral option. The triplet configuration has several advantages to other radial and spiral types. One is the field crump effects that is expected between adjacent focusing and defocusing magnets. Secondly, the length of each straight section becomes almost doubled because one focusing and two half defocusing magnets are combined together to make one multi function magnet. A minimum magnet unit has both focusing and defocusing. Therefore, the number of magnets is reduced. Finally, the lattice functions has mirror symmetry at the center of a straight section even though that may not be essential. An injection optics design is eased and diagnostics at that position produce better signal to be interpreted.

There is another argument whether we need to make the machine scaled, in other words, zero chromaticity. In each ring, the acceleration is completed within a few turns and it seems to be not enough time to develop any resonance behavior. We try to design a scaled machine in any case and later ease that requirement according to the further beam dynamics study and tolerance of magnet fabrication.

2.2.4.2 Design procedure

In order to simplify the FFAG model and quickly estimate optical property, the following steps are taken. First, we assume that the FFAG consists of N identical sector. Thus, the total bending angle in each sector is $2\pi/N$.

Each sector consists of a normal bending magnet at the center and reversed bends on both sides. Those have nonlinear gradient. We name the normal bend at the center F magnet and the reversed bends on both sides D magnet. There are straight sections between adjacent sectors, not between F and D magnets.

In each kind of bending magnet, we assume that the bending radius is constant, which is not the case in reality. If we take the bending angle in F magnet as θ_F and that in D magnet as θ_D , the following relation is satisfied; $\theta_F - 2\theta_D = 2\pi/N$. Once a closed orbit at a certain energy is fixed in that way, the focusing property is determined according to the linear field gradient derived nearby the closed orbit. Fig. 2.8 shows one half of a sector, and Table 2.2.4.2 explains the definition of symbols. All the nonlinear components at the large amplitude area are ignored. Again, we assume that the linear field gradient is constant along the closed orbit as we assumed the constant bending radius. In order to estimate the linear field gradient, we take average radius and expand the field with respect to it.

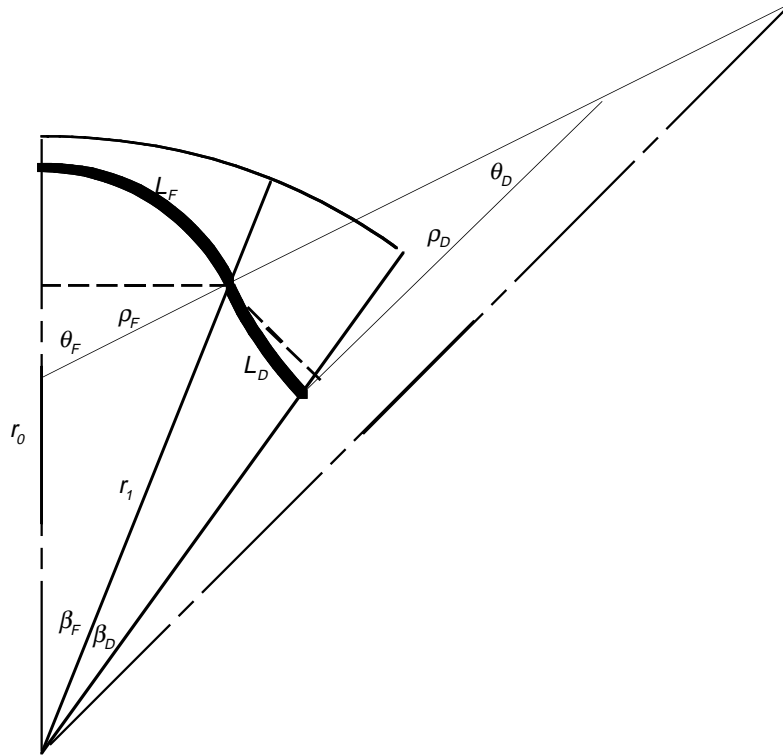


Figure 2.8: One half of a triplet radial sector FFAG and its approximated orbit.

Now we know the path length in each magnet, bending angle, and gradient near the closed orbit, we can calculate linear lattice functions. That is done

Table 2.4: Definition of symbols.

symbol	definition
N	number of cell
k	field index
β_F	opening angle of F/2 with respect to machine center
β_D	opening angle of D with respect to machine center
θ_F	bending angle of F/2
θ_D	bending angle of D
ρ_F	bending radius of F
ρ_D	bending radius of D
L_F	path length of F/2
L_D	path length of D
r_0	orbit radius of F center
r_1	orbit radius of F exit

with an ordinary synchrotron design code SAD. We will explain the design parameters in each FFAG ring.

2.2.4.3 0.3 to 1GeV/c FFAG

The first (and second) FFAG accelerator can be either normal conducting magnet FFAG or superconducting one. The main difference is bending strength and average radius; 1.8T and 21m, respectively, for normal conducting and 2.8T and 10m for superconducting. Fig. 2.9 and 2.10 show a footprint of the normal conducting version and its lattice functions in one sector and those for superconducting one, respectively. Table 2.5 summarizes main parameters.

Obviously the normal conducting one has more cell, twice as much, although the length of each cell is about the same for two versions, that is 4m, resulting in the similar maximum value of beta functions. The dispersion function of the superconducting version is 50% more.

2.2.4.4 1 to 3GeV/c FFAG

The second FFAG can be also either normal or superconducting magnet. The field strength of the normal conducting magnet is 1.8T and that of superconducting one is 3.6T. The number of sector in the normal one is twice as much compared with superconducting one. Fig. 2.11 and 2.12 show a footprint of the normal conducting version and its lattice functions in one sector and those for superconducting one, respectively. Table 2.6 summarizes main parameters.

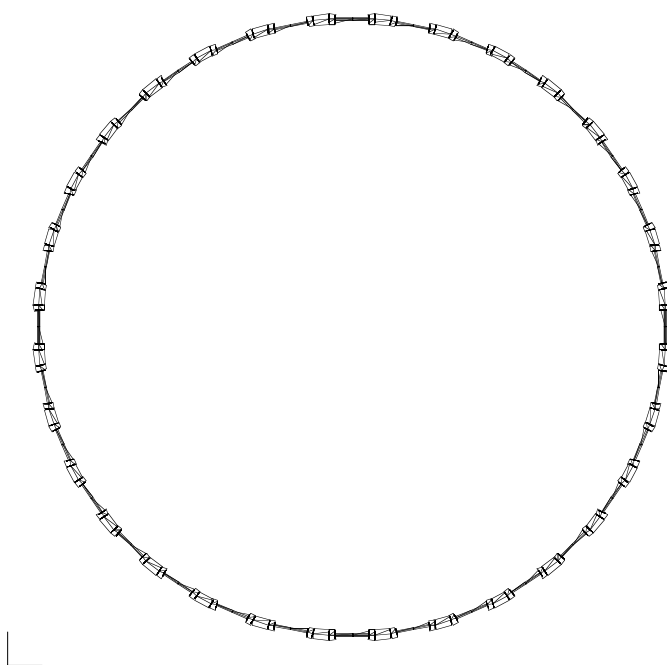
Table 2.5: Main parameters of 0.3 to 1 GeV/c FFAG.

	normal conducting	superconducting
number of sector	32	16
k value	50	15
transition gamma	7.1	4
orbit excursion	0.50 m	0.77 m
average radius	21 m	10 m
B@F/D	1.8 T	2.8 T
F/2 angle	0.026 rad	0.052 rad
D angle	0.018 rad	0.036 rad
F/2 bend angle	17 degree	26 degree
packing f	0.45	0.46
phase advance(H/V)	120/61 deg.	131/103 deg.
drift length	2.060 m	2.120 m
BF length	1.104 m	1.065 m
BD length	0.382 m	0.367 m

Table 2.6: Main parameters of 1 to 3 GeV/c FFAG.

	normal conducting	superconducting
number of sector	64	32
k value	190	63
transition gamma	13.8	8
orbit excursion	0.46 m	0.52 m
average radius	80 m	30 m
B@F/D	1.8 T	3.6 T
F/2 angle	0.0127 rad	0.026 rad
D angle	0.0093 rad	0.018 rad
F/2 bend angle	10.5 degree	16 degree
packing f	0.45	0.45
phase advance(H/V)	132/33 deg.	154/46 deg.
drift length	4.325 m	3.229 m
BF length	2.041 m	1.575 m
BD length	0.747 m	0.544 m

11:26:11 Thursday 12/28/2000



11:23:39 Thursday 12/28/2000

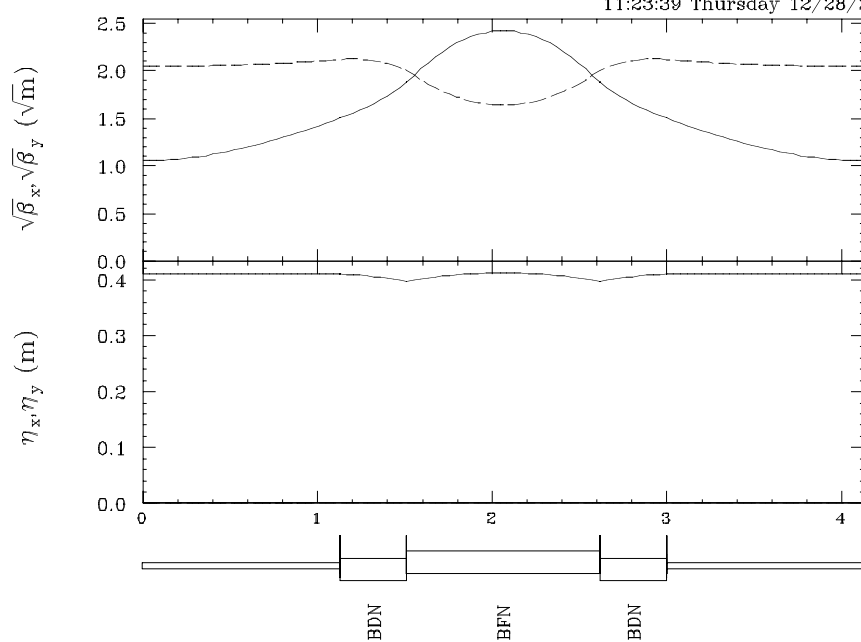


Figure 2.9: 0.3 to 1 GeV/c FFAG accelerator with normal conducting magnets.

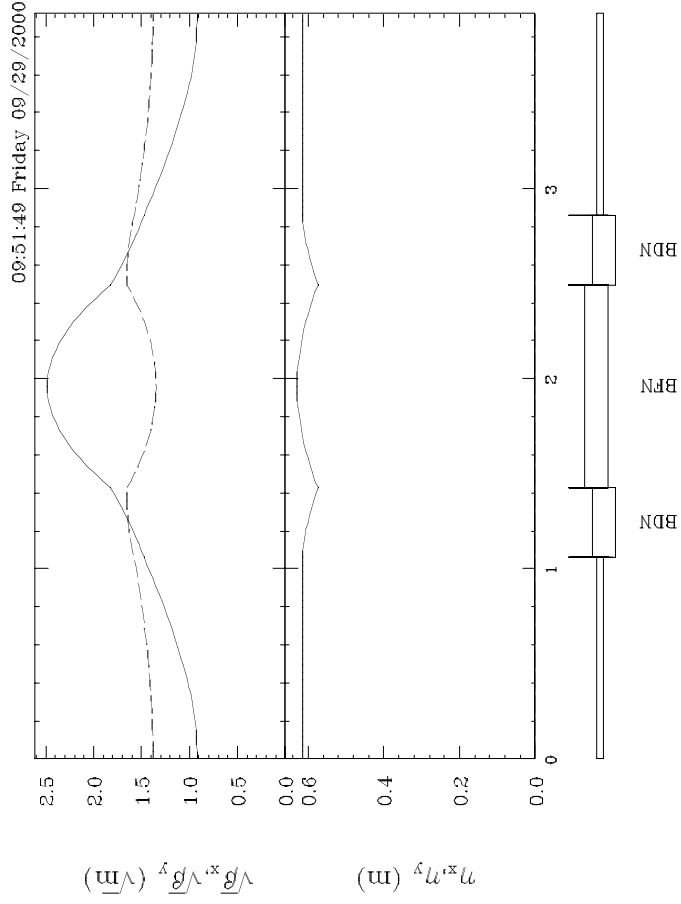
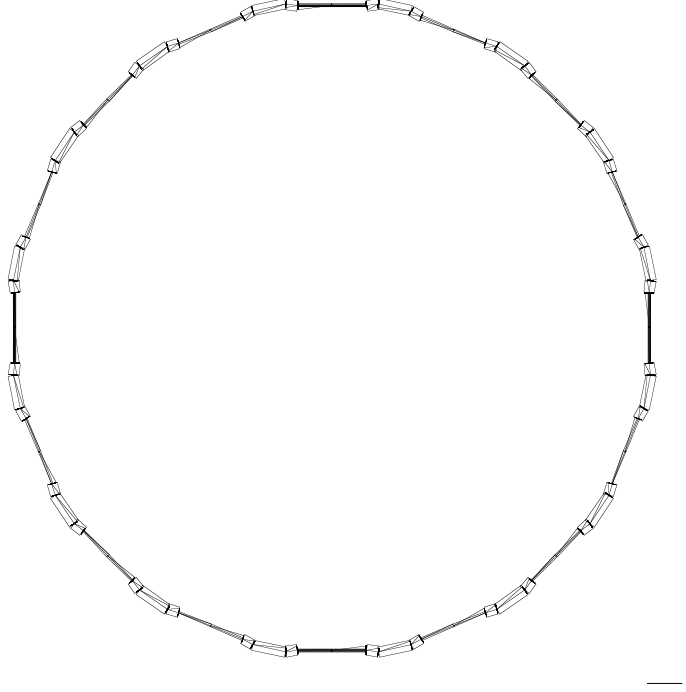
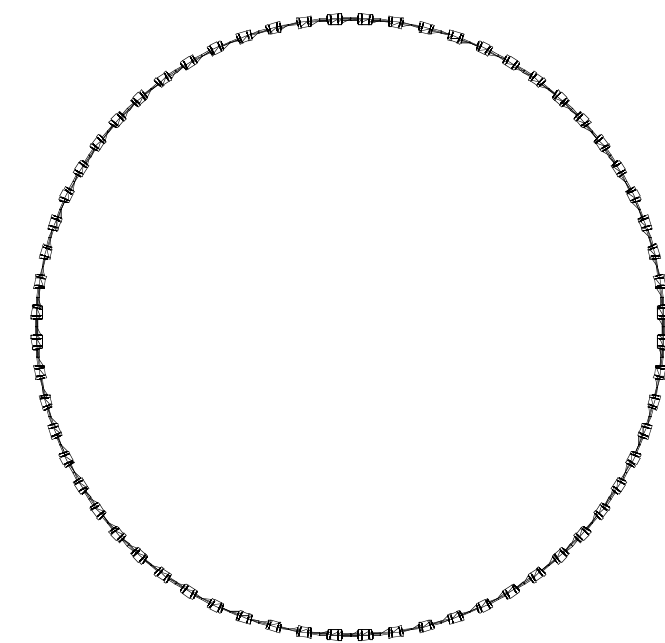


Figure 2.10: 0.3 to 1 GeV/c FFAG accelerator with superconducting magnets.

12:20:36 Thursday 12/28/2000



12:18:32 Thursday 12/28/2000

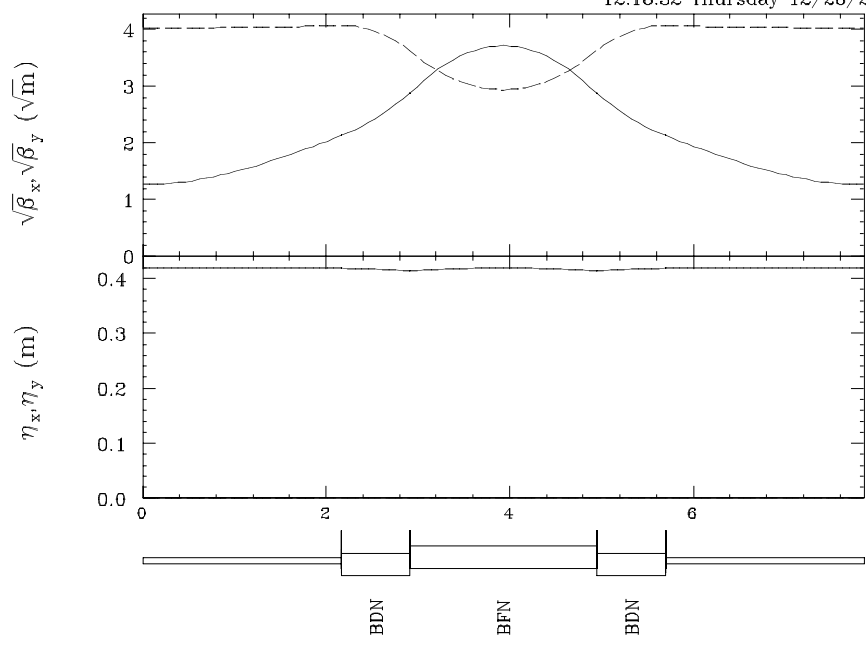


Figure 2.11: 1 to 3 GeV/c FFAG accelerator with normal conducting magnets.

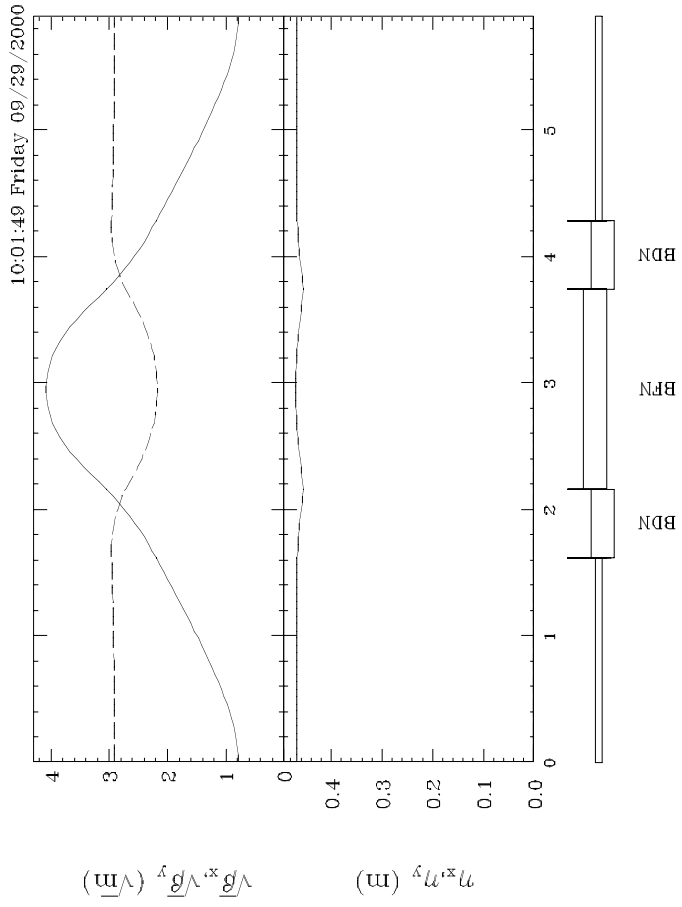
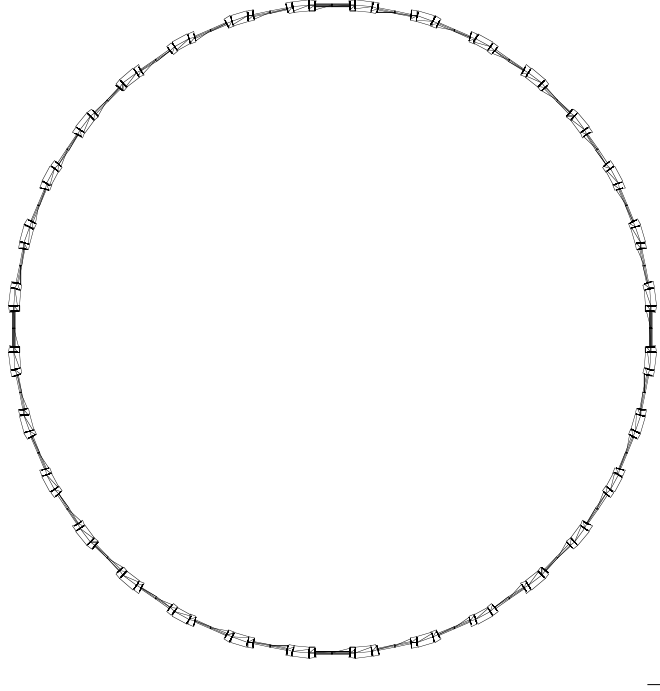


Figure 2.12: 1 to 3 GeV/c FFAG accelerator with superconducting magnets.

2.2.4.5 3 to 10GeV/c FFAG

The third one will be superconducting magnet FFAG because the normal conducting version becomes too large to fit in the area enclosed with 50GeV PS. Fig. 2.13 shows a footprint of the superconducting version and its lattice functions in one sector. Table 2.7 summarizes main parameters.

Table 2.7: Main parameters of 3 to 10 GeV/c FFAG.

	superconducting
number of sector	64
k value	220
transition gamma	14.9
orbit excursion	0.49 m
average radius	90 m
B@F/D	5.4 T
F/2 angle	0.012 rad
D angle	0.009 rad
F/2 bend angle	10 degree
packing f	0.43
phase advance(H/V)	157/23 deg.
drift length	5.046 m
BF length	2.169 m
BD length	0.813 m

2.2.4.6 10 to 20 GeV/c FFAG

By the same reason of the preceding ring, the final FFAG will use superconducting magnet. Furthermore, the 20GeV/c is the maximum available energy if we set a limit on the magnet strength of 6.0T and average radius of 150m, which is the requirement to locate the machine in the area inside the 50GeV PS. Fig. 2.14 show a footprint of the superconducting version and its lattice functions in one sector. Table 2.8 summarizes main parameters.

2.2.4.7 Transverse dynamics

Limitation of SAD design

The zeroth order design of the FFAG accelerators is described in the previous section. There are several missing items which should be taken into account to complete more detailed design. First, no fringing fields are taken into account. Since the vertical focusing comes mainly from the edge

16:37:13 Tuesday 01/30/2001

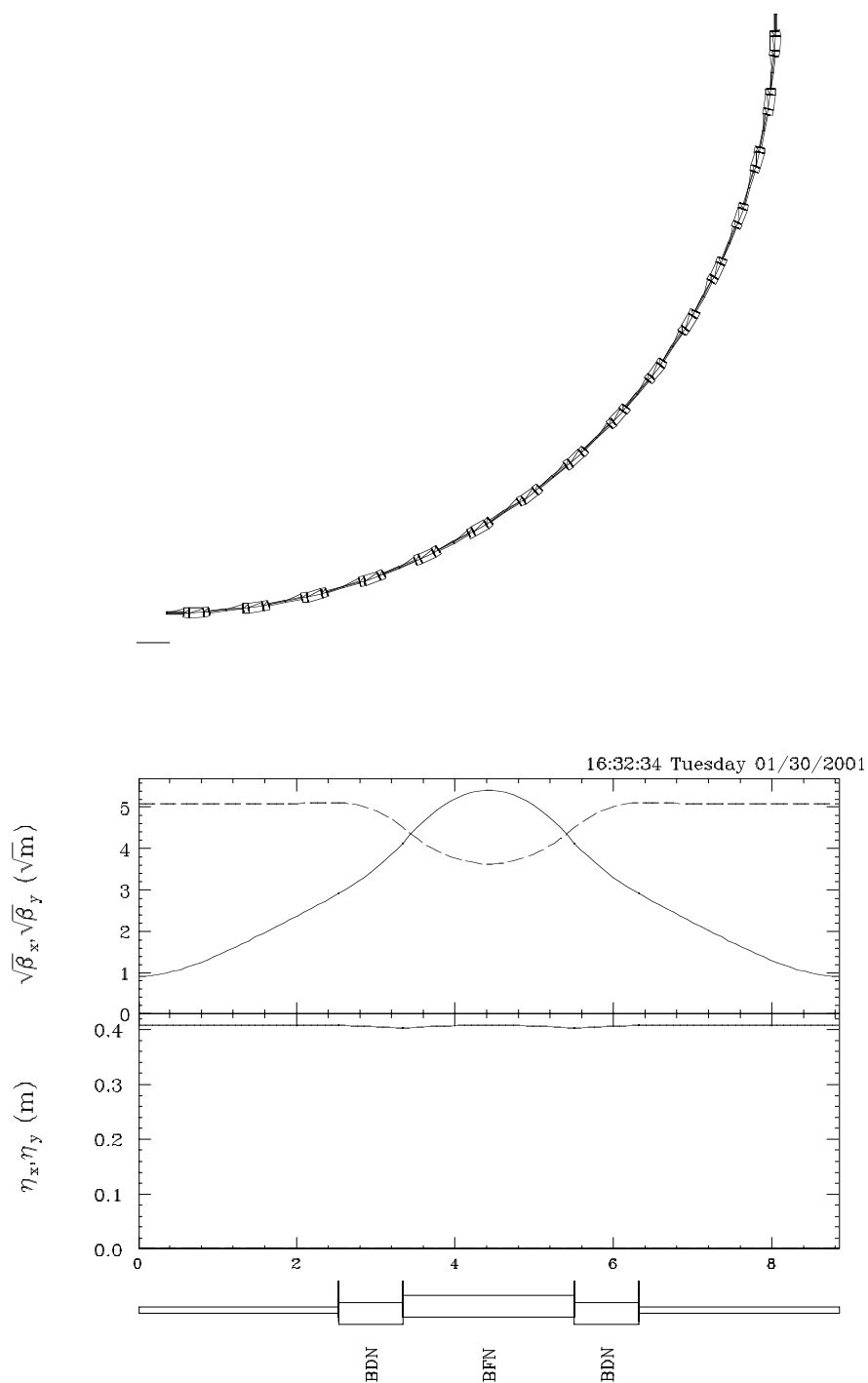
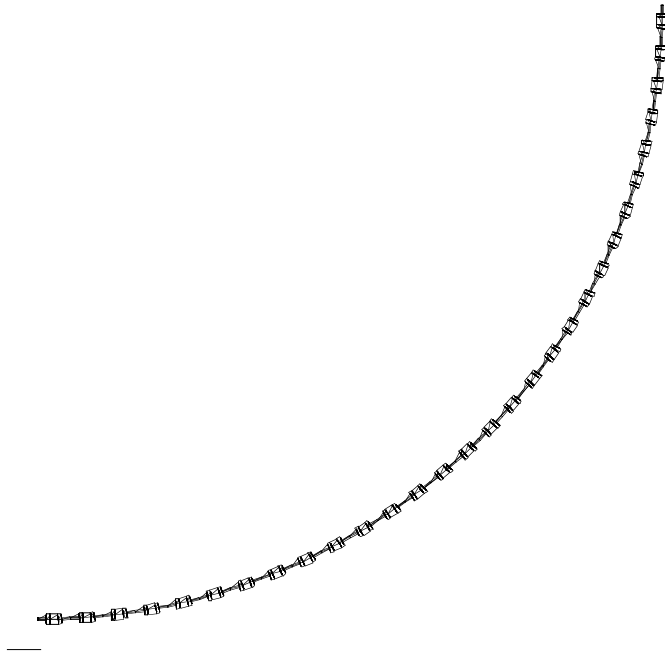


Figure 2.13: 3 to 10 GeV/c FFAG accelerator with superconducting magnets.

16:19:31 Tuesday 01/30/2001



15:53:46 Tuesday 01/30/2001

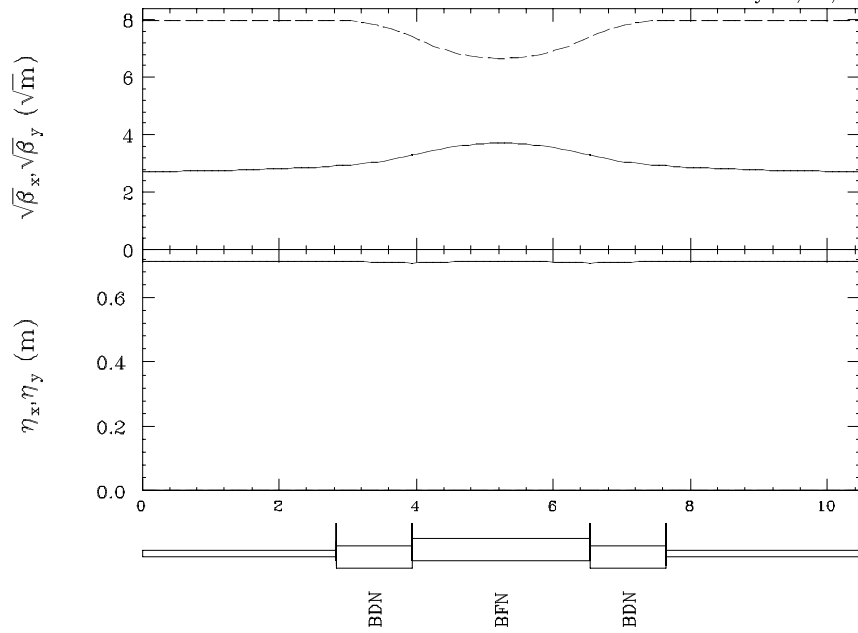


Figure 2.14: 10 to 20 GeV/c FFAG accelerator with superconducting magnets.

Table 2.8: Main parameters of 10 to 20 GeV/c FFAG.

	superconducting
number of sector	120
k value	280
transition gamma	16.8
orbit excursion	0.49 m
average radius	200 m
B@F/D	6.0 T
F/2 angle	0.0067 rad
D angle	0.0053 rad
F/2 bend angle	6.8 degree
packing f	0.46
phase advance(H/V)	67/19 deg.
drift length	5.668 m
BF length	2.685 m
BD length	1.062 m

focusing, detailed modeling of fringing field, especially in the region between D and straight section, is essential to the first order optics, such that the closed orbit and linear lattice functions.

Secondly, the orbit in F and D magnet, respectively, are not the arc of a circle. The constant field contour line exists at the equi-distance from the machine center, the field strength along the orbit is not constant. The only way to find a closed orbit is to track a particle and find out the initial condition in the phase space where the particle comes back. In the same manner, the gradient along the orbit is not the same. An integrated focusing force, in other words, effective field index n which a beam feels is different from the one of magnet. There is an approximated formula, but the exact value is estimated with particle tracking.

Thirdly, SAD approximation is based on the orbit of constant momentum. Either the dynamics of off-momentum particles or a particle which is accelerated cannot be simulated. Off-momentum matching at injection cannot be handled.

Finally, in a FFAG accelerator, nonlinearity is inherent, not inevitable due to fabrication errors in an ordinary synchrotron. In fact, those nonlinear force can be included in SAD design as a field expansion up to some multipoles. However, estimate of dynamic aperture and nonlinear coupling effects are only studied with more direct tracking in an actual magnetic field.

Step by step integration

In order to design beyond the linearized model with SAD, the magnetic field calculation based on actual magnetic shape is necessary. Either field measurement or 3D calculation code is used. At the moment, no design on the neutrino factory beyond SAD model is completed. However, a design on similar type of machine has been done. That is a machine in PRISM project, which capture muons with very short pulse, say 10 ns, and rotate it in longitudinal phase space to obtain monochromatic beams. We expect that the PRISM project will be a pre-neutrino factory scenario. In any case, we will discuss the design procedure taken for PRISM project in the following to demonstrate transverse dynamics study.

Parameters

The energy of muons which are capture in a PRISM FFAG ring is about 100 MeV, much less than that of the neutrino factory design. Nevertheless, the unnormalized emittance and initial momentum spread assumed are about the same, that is $10,000 \pi mm - mrad$ in horizontal and $3,000 \pi mm - mrad$ in vertical direction. The momentum spread at the injection is $\pm 20\%$. Other parameters are listed in Table 2.9.

Table 2.9: Main parameters of PRISM FFAG.

	normal conducting
number of sector	8
k value	5
transition gamma	2.4
orbit excursion	0.44 m
average radius	5 m
B@F/D	0.54 T
F/2 angle	0.05 rad
D angle	0.02 rad
F/2 bend angle	25 degree
packing f	0.19
phase advance(H/V)	107/37 deg.
drift length	3.117 m
BF length	0.511 m
BD length	0.105 m

We assume the magnetic field at 3D grid points in configuration space

according to the following function.

$$B_z = B_0 \left(\frac{r}{r_0} \right)^k, \quad (2.4)$$

in a region of magnets and zero elsewhere. B_r has only linear components which satisfy

$$\frac{\partial B_z}{\partial r} - \frac{\partial B_r}{\partial z} = 0. \quad (2.5)$$

B_θ is zero at the all grid points, but edge focusing is taken into account at the edge.

A particle tracking with step by step integration using Runge-Kutta method is carried out. Fig. 2.15 (a) and 2.15 (b) show the initial particle distribution in longitudinal and transverse phase space, respectively.

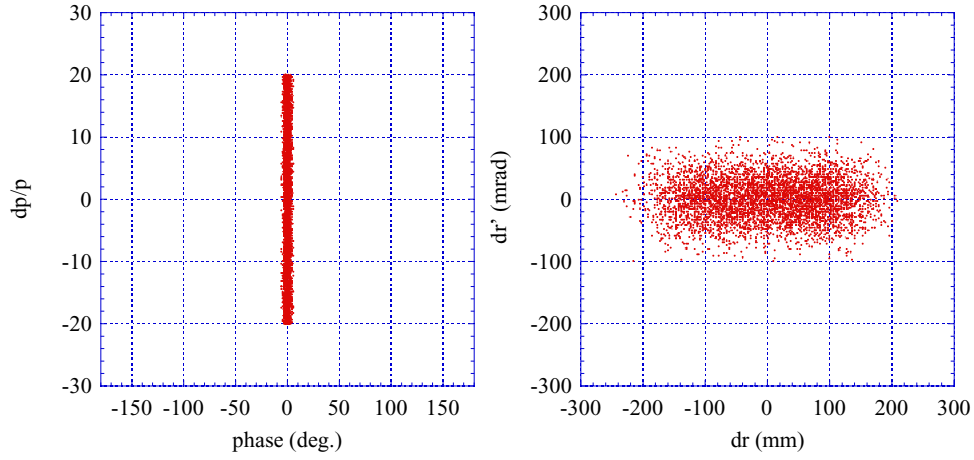


Figure 2.15: Longitudinal (a) and horizontal (b) particle distribution at injection in PRISM FFAG.

At injection, dispersion matching is done based on linear dispersion estimated. Fig. 2.16 (a) and 2.16 (b) show phase space after 6 turns in PRISM FFAG. From those figures, we show that FFAG can provide large transverse acceptance, here it is $10,000 \pi mm - mrad$, and longitudinal momentum acceptance, $\pm 20\%$.

2.2.4.8 Longitudinal motion in FFAG accelerator

The magnetic field of a scaling type of FFAG accelerator can be expressed in Eq.2.4. Thus, a phase shift $\Delta\phi_p$ between the synchronous particle (ϕ_s) and the other particle (ϕ_n) can be written as follows.

$$\Delta\phi = 2\pi h \left\{ \left(\frac{P}{P_s} \right)^{\frac{1}{k+1}} \frac{\beta_s}{\beta} - 1 \right\}, \quad (2.6)$$

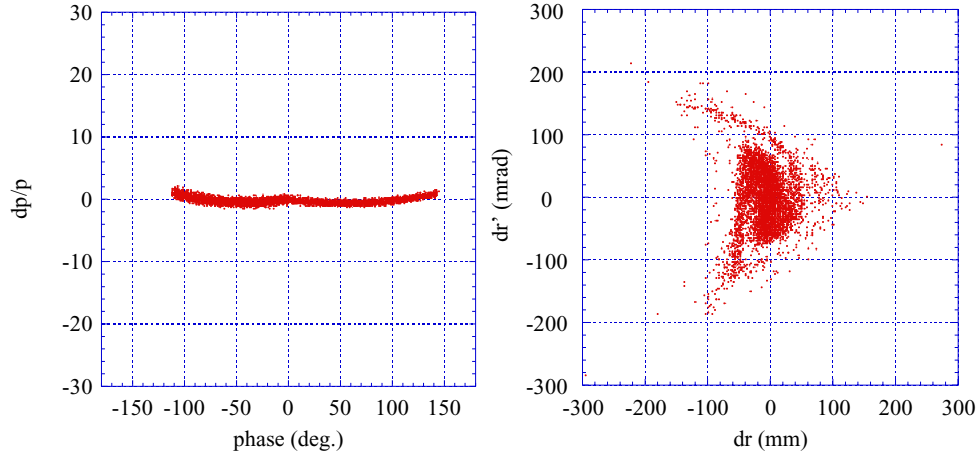


Figure 2.16: Longitudinal (a) and horizontal (b) particle distribution after 6 turns in PRISM FFAG.

where h is the harmonic number, P is the momentum and β is Lorentz factor. Thus, the longitudinal particle motion can be obtained by simulating the two difference equations numerically.

$$\phi_n = \phi_{n-1} + 2\pi h \left\{ \left(\frac{P}{P_s} \right)^{\frac{1}{k+1}} \frac{\beta_s}{\beta} - 1 \right\}, \quad (2.7)$$

$$\Delta E_n = \Delta E_{n-1} + eV_{rf}(\sin \phi_n - \sin \phi_s). \quad (2.8)$$

Here, ΔE_s is the difference in the energy between the synchronous particle and the other particle, and V_{rf} is the peak rf voltage. In our FFAG based neutrino factory, muons are accelerated thorough four FFAG rings from the momentum of 0.3GeV/c to 20GeV/c as described above. In order to examine the longitudinal particle motions in the beam acceleration through these four FFAG rings using superconducting magnets, particle tracking simulation using Eqs. (3) and (4) has been carried out. The assumed initial longitudinal emittance and the maximum momentum spread at injection are 4.6 eV·sec and $\pm 50\%$, respectively. In this simulation, the averaged rf accelerating field strength of about 1 MV/m is assumed for all of the rings. The simulation results are summarized in Fig 2.17

As can be seen from these results, the particles are accelerated up to the final energy without having serious problems and the RMS momentum spread is reduced to about $\pm 1\%$.

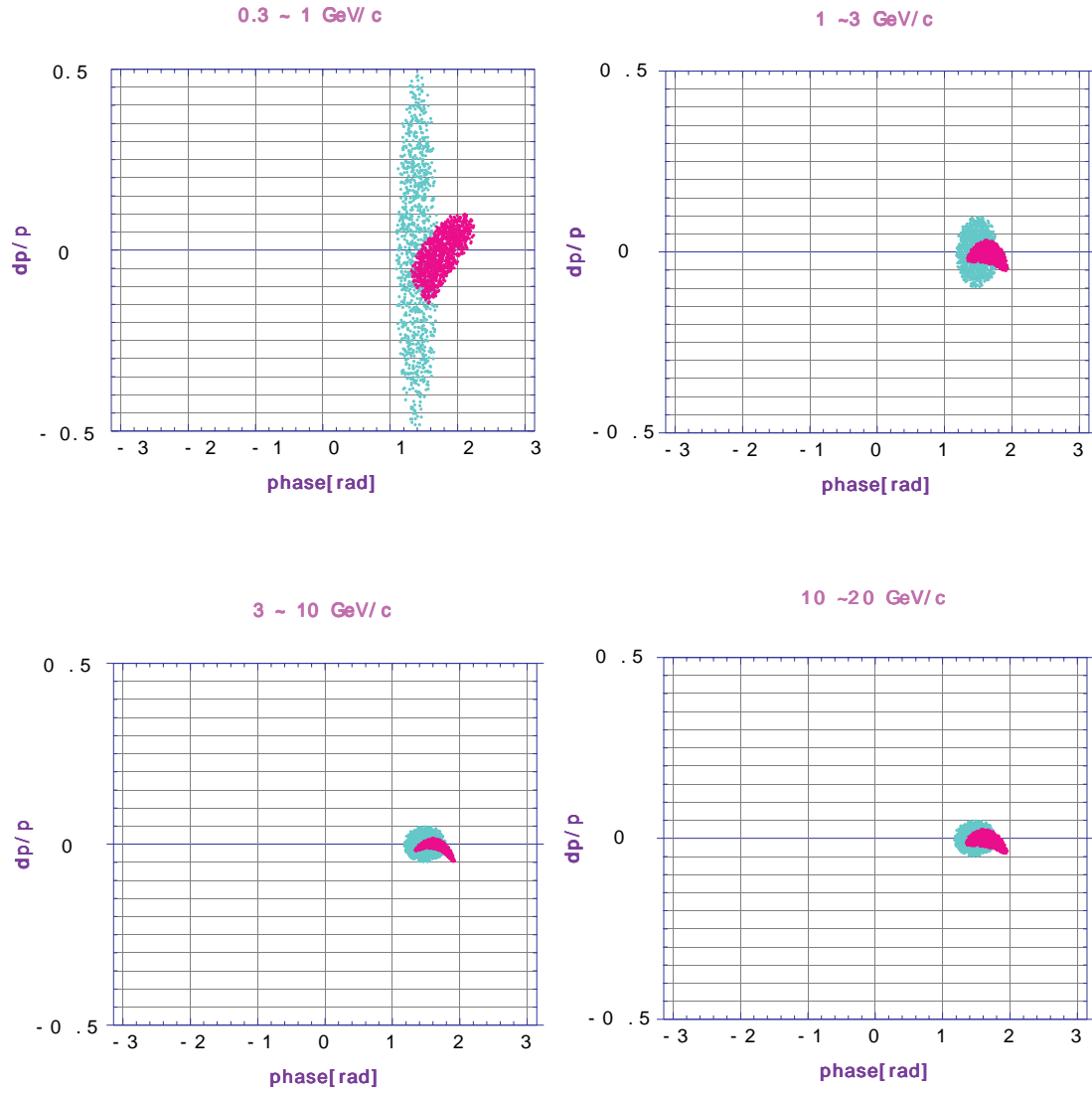


Figure 2.17: Longitudinal motions in the FFAF rings

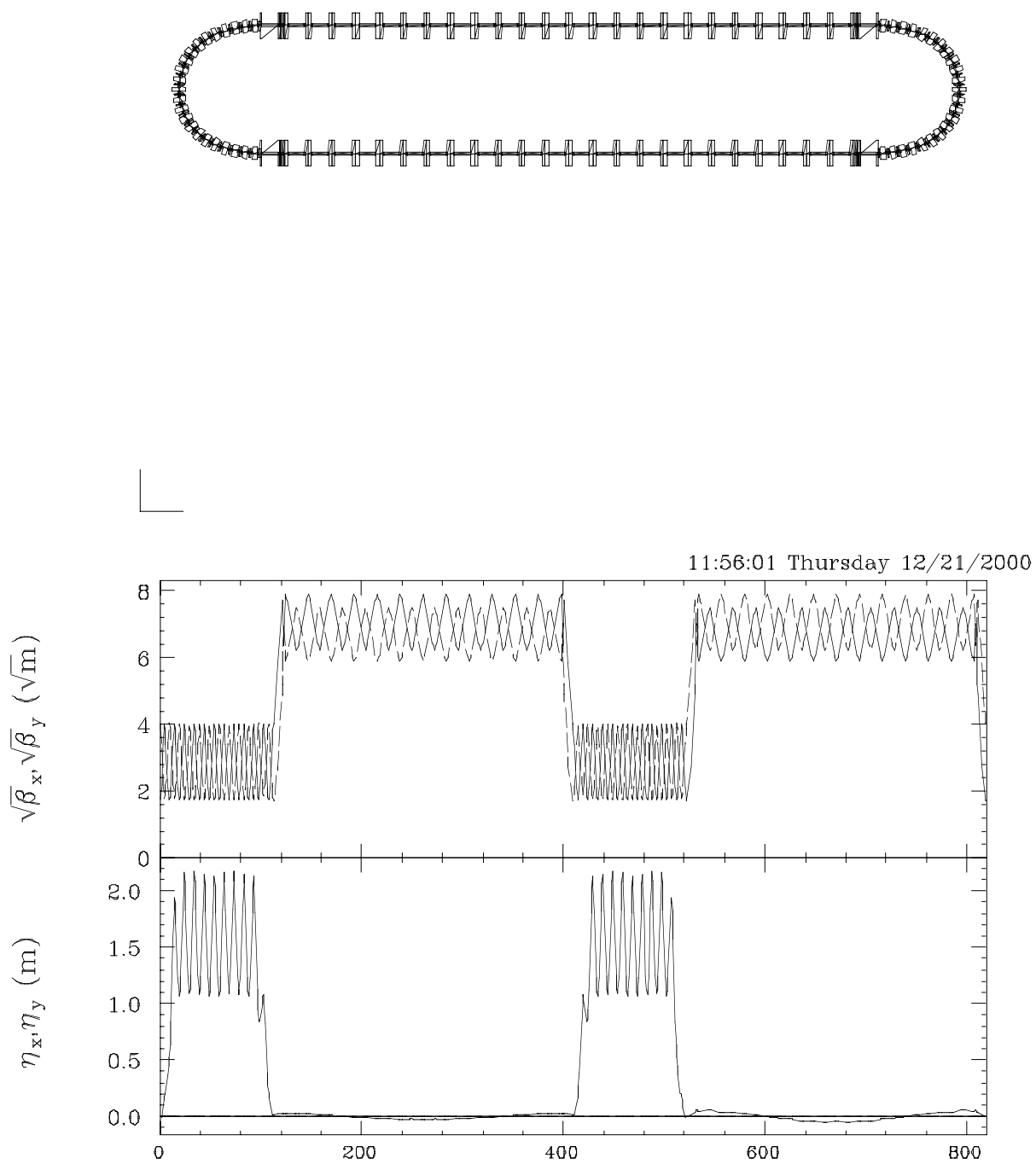


Figure 2.18: Muon storage ring design.

2.2.5 Storage Ring

A storage ring is designed and main parameters are listed in Table 2.10. It has two of approximately 300 m straight sections. At the straight section, beam size is enlarged and the rms divergence of beams becomes 0.92. That satisfies the condition of

$$D_{beam} < \frac{1}{5\gamma}, \quad (2.9)$$

where γ is a relativistic Lorentz factor.

Table 2.10: Muon Storage Ring Design Parameters and Constraints

Storage Ring Geometry		racetrack
Storage Ring Energy	GeV	20
$\epsilon(100\%)$ (normalized)	mm·mrad	30,000 π
dp/p (%)	%	1
maximum poletip field	T	<5.0
arc cell phase advance	deg	90

2.2.6 Muon Cooling

In the FFAG based neutrino factory, muon cooling is not necessarily constituent because of their large beam acceptance of the FFAG accelerators. Nevertheless, it would be helpful to reduce the technical difficulties of making the large aperture superconducting magnets for the high energy rings and the storage ring and also the initial investment cost for them if the muon cooling works effectively, in particular, at low energy. The FFAG ring scenario, contrary to the linac based scenario, can work without longitudinal cooling because of its large momentum acceptance.

The potential of transverse ionization cooling in the FFAG ring scenario has been examined by Shonauer.[16] Transverse ionization cooling process is expressed by the following differential equation. [2]

$$\frac{d\epsilon_n}{\epsilon_n ds} = -\frac{1}{\beta^2 E} \frac{dE}{ds} + \frac{(13.6 MeV)^2}{2\beta^3 m_\mu c^2 L_R} \frac{\beta_T}{E \epsilon_n} \quad (2.10)$$

Here, L_R is the radiation length of the absorber material and β_T the average transverse beta function at absorber, respectively. In the transverse ionization cooling in the FFAG ring scenario, a absorber with pressurized gas filling the beam pipe is distributed in the ring. The effect of the main parameters, such as transverse beta functions and rf accelerating field gradient, on cooling and transmission can be examined by solving the above

Table 2.11: Parameters of the large-momentum acceptance arc cells for a 20-GeV muon storage ring

<u>General:</u> tungsten shield thickness	cm	1.0
beam-stay clear	cm	1.0
inter-magnet spacing	m	0.75
<u>Dipoles:</u>		
dipole length	m	2.4
dipole bend	rad	0.1654
dipole field	T	4.6
beam size (6σ , max), W×H	cm	12.8×5.3
dipole full aperture**, W×H	cm	14.8×9.3
sagitta	cm	2.67
<u>Quadrupoles:</u>		
quadrupole length	m	1
arc quadrupole strength	m^{-2}	.3
arc quadrupole poletip field	T	1.8
beam size (6σ), W×H		
F quad	cm	13.2×4.3
D quad	cm	6.2×5.0
arc quadrupole bore**	cm	18
<u>Sextupoles (overlay on quad field)</u>		
horiz. sextupole strength	m^{-2}	0.26
vert. sextupole strength	m^{-2}	0.51
horiz. sextupole poletip field	T	0.14
vert. sextupole poletip field	T	0.27
<u>Arc FODO cell parameters:</u>		
cell length	m	9.8
cell phase advance	deg	90
β_{max}	m	16.2
$D_x(max)$	m	2.2
total number arc cells		15
total number disp. sup. cells		8

Table 2.12: Parameters of the high-beta cells for neutrino production in a 20-GeV muon storage ring

drift length	m	7.4
quadrupole length	m	3
quadrupole strength	m^{-2}	0.016
quadrupole poletip field	T	0.12
quadrupole bore	cm	24
total cell length	m	22.8
cell phase advance	deg	$\approx 4 - 5$
β_{max}	m	62.6
rms divergence	mr	0.92
number of high-beta cells		12

Table 2.13: Storage Ring Parameters at 20-GeV

Circumference	m	819.0
Neutrino decay fraction		33.4%
Production region:		
matching	m	23.2
High- β FODO straight	m	273.6
$\beta_{xmax}/\beta_{ymax}$	m	62.6/56.2
ν_x/ν_y		8.26/8.17
natural chromaticity		-10.4/-10.5

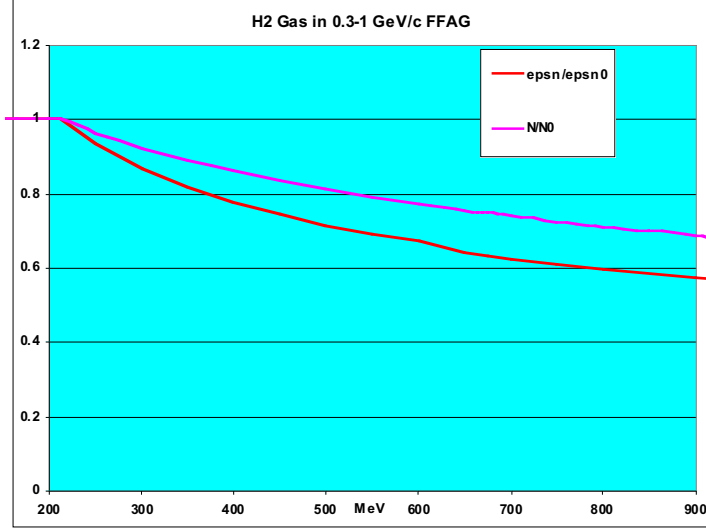


Figure 2.19: Cooling factor and transmission as function of muon energy for 0.3-1 GeV/c FFAG ring. The H₂ gas pressure is 25 bar

equation. The cooling effect depends strongly on the transverse beta function values. The heating caused by multiple scattering becomes dominant at lower energy for larger beta function values and the emittance blows up. According to Shonauer, when the H₂ gas of 25 bar is filled into the 0.3-1GeV/c FFAG ring where the average beta function value is 2m, the cooling factor becomes 0.57 and the transmission is 83% of its no- cooling value as shown in Fig. 2.19. He is also claiming that, in order to gain additional cooling, it is preferable to insert cooling sections or rings between the FFAG's at energies between 1 and 3GeV/c.

2.3 Hardware

2.3.1 RF system

A high gradient and low frequency rf system is very important to realize the muon beam acceleration in the FFAG based neutrino factory. As we described above, a field gradient of more than 1 MV/m at a relatively low frequency such as 5 MHz is requested especially for the low energy rings. Since the FFAG ring has a large or almost infinite momentum acceptance,[1] the accelerating time and acceptable momentum spread are solely limited by

the rf voltage. As possible candidates for the high gradient and low frequency rf cavities, we have been developing three types: (1) the inductive material loaded rf cavity using a new type of ferrite [2], (2) the capacitive material loaded rf cavity using high grain ceramic and (3) the air gap rf cavity.

2.3.1.1 Ferrite loaded rf cavity

A new type of NiZn based ferrite, SY20, which includes a large amount of cobalt oxide, has been developed at the TDK company. Unlike the ordinary NiZn type of ferrite, this ferrite has relatively large Q value, and its μQf -product is large. However, μQf values decrease when the strength of the rf magnetic field induced in the ferrite core, B_{rf} , increases. This is because this type of ferrite is easily affected by a high loss effect caused by a spin wave excitation. Once the high loss effect occurs, the Q-value of the material drops steeply a few milliseconds after the rf field is excited, as shown in Fig. 2.20, and the rf power loss becomes unacceptably large. This type of ferrite is obviously inadequate for long pulse or cw mode operation.

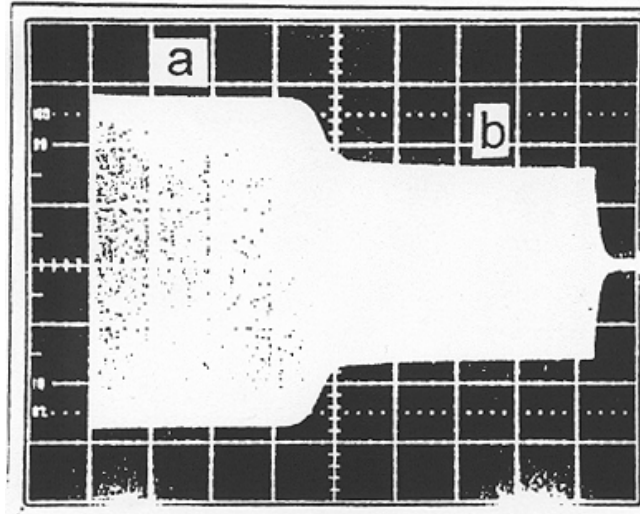


Figure 2.20: High loss effect in the ferrite core. About 1.2 msec after the rf is excited, the rf voltage drops to almost 60% of the initial value.

Fortunately, in the case of the neutrino factory, operation is in a burst mode, because the total acceleration time should be much less than 1 msec even for the highest energy FFAG ring and the repetition rate is about a couple of Hz. Thus, the high loss effect is not seen in the rf cavity of the FFAG accelerator in the neutrino factory. The μQf value corresponding to the shunt impedance of SY-20 was measured as a function of input rf voltage

in burst mode. The measured μQ_f values are plotted as a function of B_{rf} in Fig. 2.21.

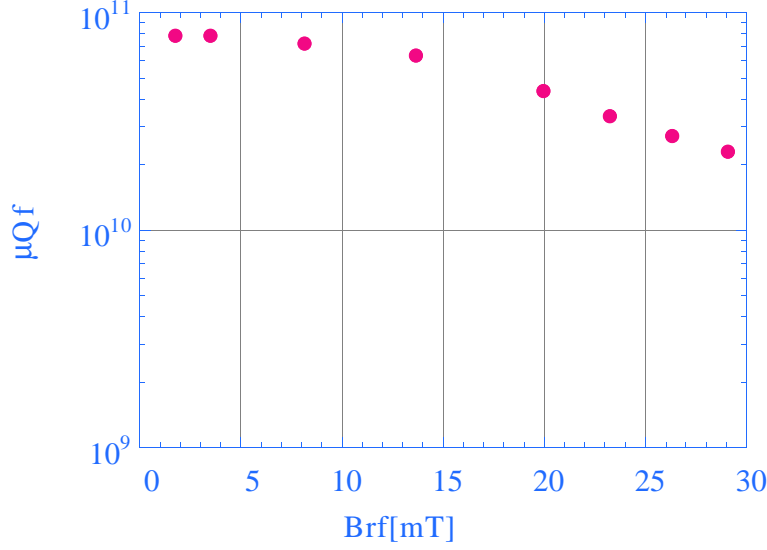


Figure 2.21: The measured μQ_f values of the SY-20 ferrite as a function of B_{rf} .

The Q-value was obtained from the measurement of rise or fall time response behavior in burst mode operation. A typical result of the SY-20 ferrite is shown in Fig. 2.22. The Q-value of SY-20 from these measurements at an rf frequency of 5MHz was about 10, which was small enough for covering the frequency shift during acceleration in the FFAG rings.

Using the μQ_f value obtained from the measurement, the rf power to achieve an average field gradient of 1MV/m in the FFAG ring can be estimated. Assuming that the length of a single rf cavity is 1m and 60% of the ring is occupied by the rf cavities, the peak rf power which is necessary to generate a peak voltage of 1.6 MV for the cavity would be about 3 MW or more. In order to get such a high peak rf power in burst mode operation, an rf tetrode having an anode dissipation of more than 1.2 MW can be utilized with positive voltage grid biasing. One should note that even for such a high peak rf power, the average rf power is rather small, only 3 kW, because the duty factor is about 0.1% or less. Thus, the investment cost for the rf system caused by the anode dissipation is relatively cheap. Even for the highest energy (20GeV/c) FFAG ring, for example, the required average rf power is only 1.8 MW in total.

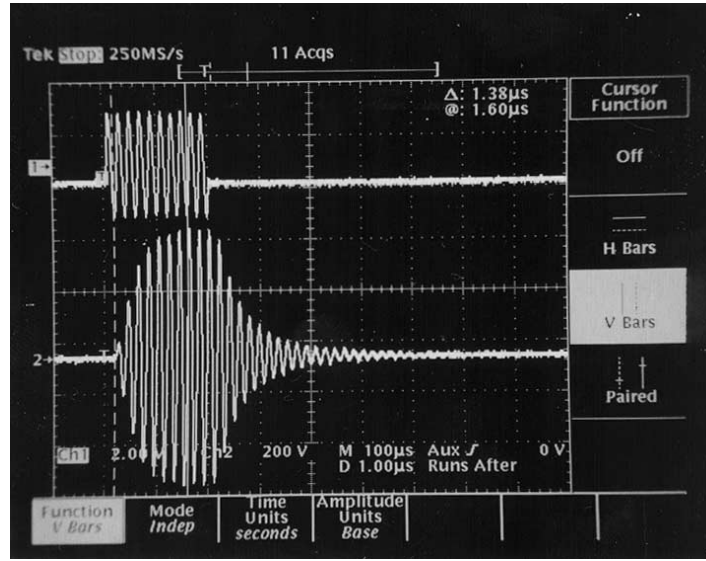


Figure 2.22: Typical time response for the rf burst in SY-20 ferrite.

2.3.1.2 Ceramic Gap Loaded High Gradient RF Cavity

A rf cavity capable of developing 0.5 to 1 MV/m at 7.5 MHz has been proposed. In order to reduce the physical size, it is proposed to store a large fraction of the electrical stored energy in high dielectric constant ceramic with very low loss factor. This design is subject to criticism on two basic counts. Because of the very large voltage gradient at the accelerating gap, there is concern regarding sparking breakdown due to high electric field gradient at "triple points," where the dielectric material, the metal conductor, and the vacuum meet. In addition, because it is required that the entire accelerating gradient be sustained across the cylindrical ceramic capacitor, there is concern that the material may not have sufficient dielectric strength to prevent failure due to internal dielectric breakdown. In order to check the feasibility of this type of rf cavity, various studies for the following items are going on at FNAL.

1. Bulk ceramic properties
 - (a) Is alumina the right dielectric? Consult manufacturers regarding properties.
 - (b) Are cylinders of required dimensions available?
 - (c) Are there methods of joining adjacent cylinders with high dielectric strength adhesive?
 - (d) Build 800 pF cylindrical capacitors (similar to the Booster coupling capacitor) using old MR ceramic. Test dielectric strength using standard commercial method, i.e., 60 Hz high-pot.

- (e) Test with burst-mode high power rf at 5 MHz, using the Proton Driver power amplifier in resonant cavity mode.
- 2. Gap corona roll study
 - (a) Use Superfish to do extensive study of triple point geometry.
 - (b) Try to test results using corona roll on modified MR seal
- 3. Power amplifier design study:
 - (a) Analyze Y567B properties for use in high peak current burst-mode.
 - (b) Consider required Proton Driver rf system modification for this use.
- 4. Scale model:
 - (a) Using several recovered MR seals, build scale model of the proposed cavity. (22.5 and 30 MHz)
 - (b) Operate entire system at low and then high rf power.
- 5. Electric breakdown experiment
 - (a) Test the bulk ceramic as well as the triple point in vacuum.
 - (b) The same test in sulfurhexafluoride (SF6), which has 3 time the breakdown strength of air at atmospheric

2.3.1.3 Oil Loaded Cavity

As mentioned in the later section, the large capacitive electrode surface tends to degrade the shunt impedance, because of the long electric current path. Although the small gap distance is preferable in this context, the sparking problem inhibits it. The Kilpatrick's criterion, however, is applicable only to a vacuum surface. Hence, the gap area can be filled with insulating oil that has dielectric strength higher than the vacuum. In addition to the relative permittivity of larger than one, the smaller gap distance will make the cavity size small. For silicone oil, the dielectric strength and loss can be 100kV/mm and 10^{-4} , respectively. The liquid insulator may be durable against a sparking than solid insulator, because it will not be broken but make dissolved gas bubbles and impurities to the oil, that can be removed by oil circulation. A schematic view of an oil cavity is shown in Fig. 2.24. Because the aperture for the beam should be evacuated for the muon beam, a solid insulator separates the vacuum and the oil area at the low electric field gradient region. Outer area can also be filled with the oil, but too much oil

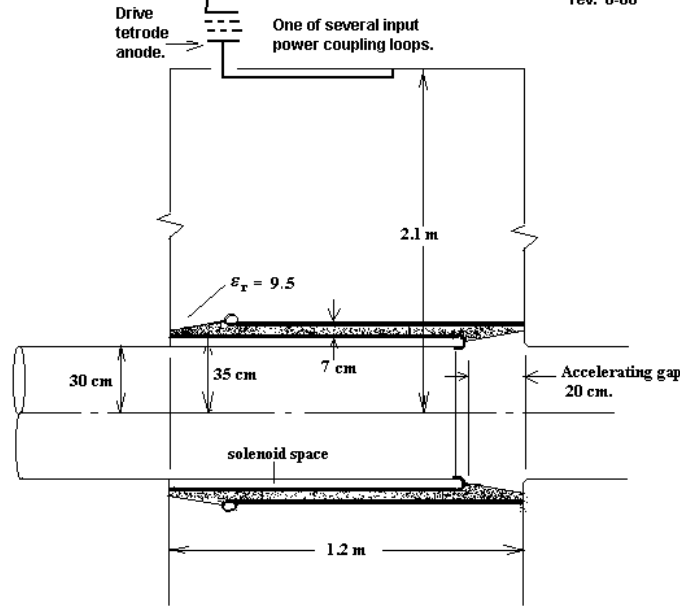


Figure 2.23: Conceptual design of a ceramic loaded rf cavity

may cause some trouble in handling. Oil cavity will require much peak power than the vacuum cavity. This type of cavity also needs R&D in selecting the material and its structure.

2.3.1.4 Air-core RF cavity

In order to lower the resonant frequency, the inductance L and the capacitance C have to be increased. The capacitance can be increased without any inflation of outer dimension by narrowing the gap distance and/or spreading the electrode area, while it decreases the shunt impedance. The gap should have enough distance to keep less field gradient or small sparking probability for a stable operation. In terms of the criterion for the sparking problem, well known Kilpatrick's sparking criterion [17] has been used:

$$f[\text{MHz}] = 1.64(E[\text{MV/c}])^2 \exp\left(\frac{-8.5}{E[\text{MV/m}]}\right) \quad (2.11)$$

Fig. 2.25 shows the electric field gradient as a function of the frequency in the range from 1MHz to 100MHz. According to the criterion, the electric field E_{Kp} is 4.8MV/m at 6.5MHz. The original Kilpatrick's model was based on the two-electrodes-model, and the above equation is the asymptotic limit of large gap[18] (see Fig. 2.26). Some low frequency RFQ linacs with very short gaps seem to exceed the criterion nearly three times, where the gap length is not in the asymptotic region. Unfortunately, the 6.5MHz cavity whose gap

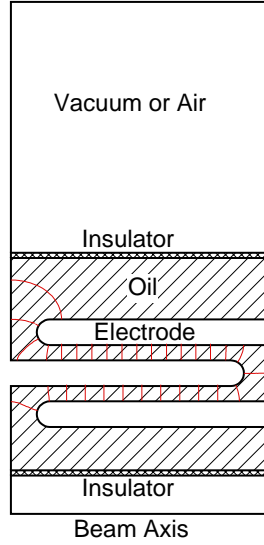


Figure 2.24: A schematic view of an oil cavity

length should be kept large against sparking and thus is in the asymptotic region, will suffer from the surface electric field limitation suggested by the Kilpatrick's criterion.

A real example for such a low frequency cavity was the 9.5MHz 1MV generator for antiproton accumulator ring at CERN[19]. The directly scaled size to the frequency of 6.5MHz is a length of 3m and a diameter of $\phi 3.2\text{m}$, while the E_{Kp} decreases 10%. Because the small outer radius of the drift tube (the aperture seems about $\phi 150\text{mm}$) contributed to enhance the cavity inductance, the resonant frequency was able to be reduced as a cavity with a wave length of 30m. Because an FFAG ring has a large orbit excursion, its aperture or outer size of the drift tube has to be large in the horizontal plane and thus the inductance decreases. Consequently, a possible cavity size for an FFAG RF has to be large.

It consists of two of 2m cavities with diameter of $\phi 2.2\text{m}$ where the field gradient and the shunt impedance were reported as 325kV/m and 275k Ω /m, respectively. The peak surface field seems to be about 1.4 E_{Kp} at 650kV of gap voltage (325kV/m), which should be moderate in conventional design.

Fig. 2.27 shows cross sections of some 6.5MHz cavities with 3m in length and various radii. Because of the symmetries, only the upper right quarter parts are shown. The gap lengths of the left two cavities are 30cm (20% of the cavity length), and those of the right two cavities are 15cm (10% of the cavity length). Cavities with large gap can have higher averaged electric field gradient E_{ave} . The large diameter cavities have the higher shunt impedances, and simple shaped electrodes. The complex shape electrode makes the electric current path long and thus influences the shunt impedance.

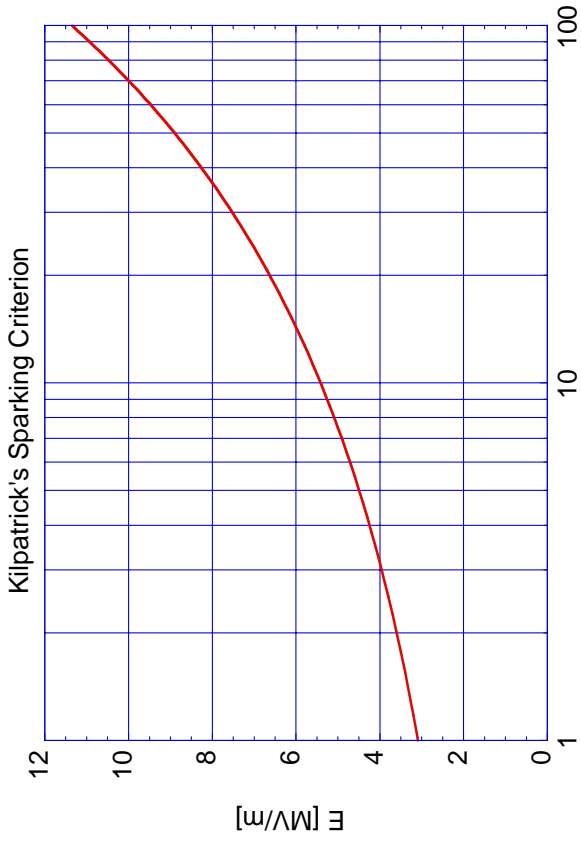


Figure 2.25: Kilpatrick's sparking criterion of RF in the asymptotic region

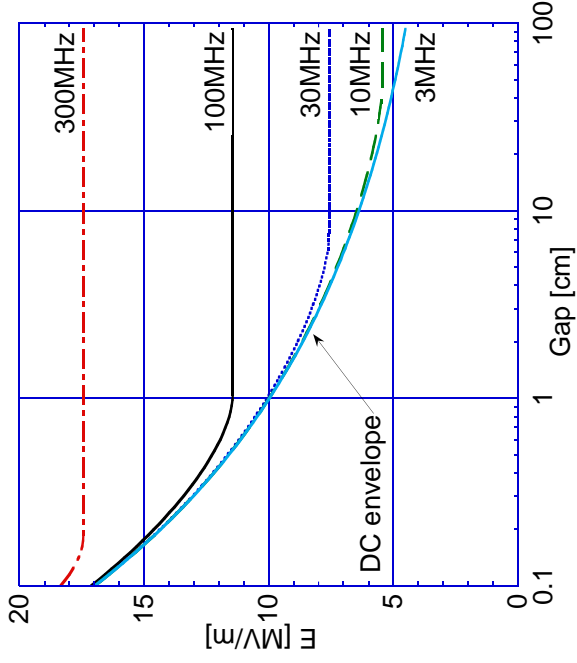


Figure 2.26: Kilpatrick's sparking criterion not in the asymptotic region

The stored energy becomes large in the small diameter cavity, which may cause a damage on the cavity surface in case of a sparking. Because these cavities are operated in pulsed mode, the averaged power consumption is not significant. Considering the filling time of about 1ms and repetition rate of about 0.3Hz of 50GeV ring, the duty factor is only $10^{-3.5}$. For a $1\text{M}\Omega/\text{m}$ cavity with length of 3m, RF power of 3MW peak has to be fed during the 1ms. The number of turns in an FFAG ring is of the order of ten and it takes less than $100\mu\text{s}$. Thus the averaged power consumption is about 1kW per cavity. Because of the huge sizes of the $\phi 9\text{m}$ and $\phi 6\text{m}$ cavities, their construction requires a civil engineering technique and R&D for the fabrication.

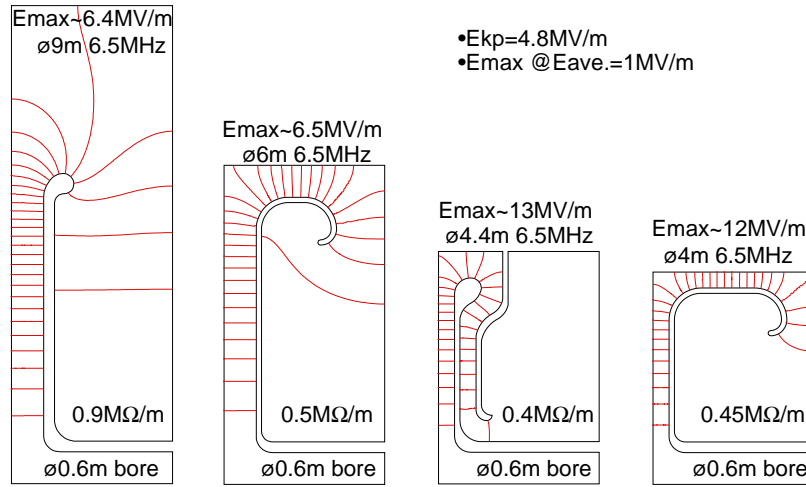


Figure 2.27: 6.5MHz cavities with various radii.

If the large option in the cavity diameter can be adopted, magnets may be pushed into a cavity region that has a drift tube of a large diameter (see Fig. 2.28). A magnet with its diagonal size of less than 1.5m (maybe a little more?) can be installed in the drift tube area. This scheme can reduce the spacing factor between the magnets or can raise the averaged accelerating field gradient. In order to endure the vacuum pressure, the end walls of the cavity can be connected to those of the next cavities. Because each gap voltage should have corresponding RF phase, each cavity has to be driven by individual RF power amplifier. There may be a technical problem on the connection between the flat vacuum beam tubes installed in the magnets and those of the cavities in the drift tube.

26MHz high gradient cavity As seen in Fig. 2.1, the high field gradient has less importance in the higher energy rings, compared with that in the lower part. The Kilpatrick's criterion E_{Kp} at the frequency of 26MHz

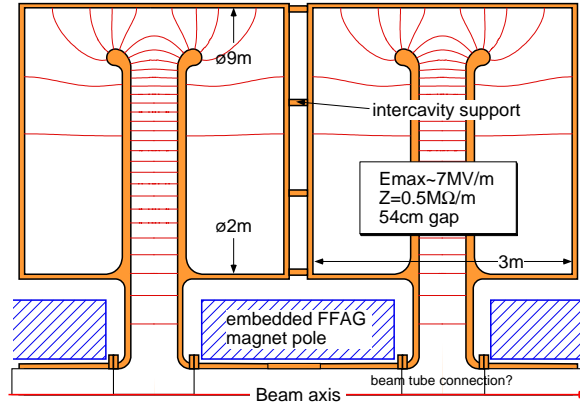


Figure 2.28: $\phi 9\text{m}$ cavity with embedded FFAG magnet.

is 7.2MV/m . Because of the higher frequency, higher E_{kp} and the less requirement for the high field gradient, the design of the 26MHz cavity can be straightforward. Fig.2.29 shows a 26MHz simple reentrant cavity. The asymmetric aperture size makes the capacitive electrode shape oval. Because the shape itself is not so important, just a circular shape electrode with the same capacitance may be sufficient.

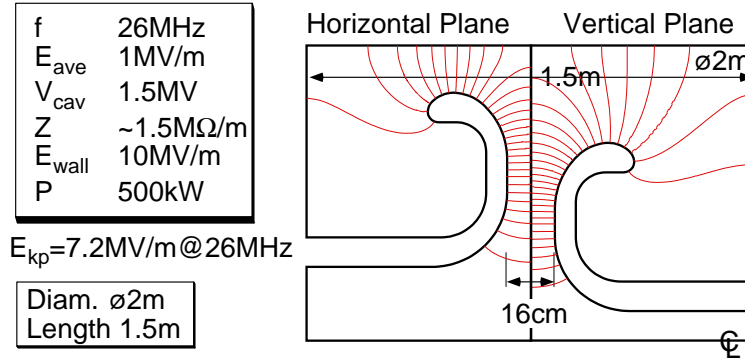


Figure 2.29: 26MHz high gradient cavity

When a higher average gradient and a higher shunt impedance are required, a cavity with large drift tubes can take bending magnets in the drift tubes (see Fig. 2.30). Because of the large diameter of the drift tube, the asymmetry of the aperture does not affect the frequency, and thus the cavity can easily be designed with two dimensional code such as SUPERFISH. This

scheme can reduce the spacing factor between the magnets and thus will help to reduce the FFAG ring size.

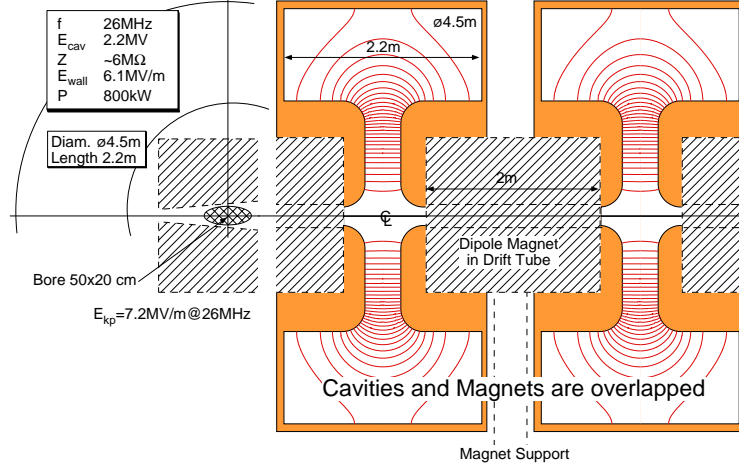


Figure 2.30: 26MHz high gradient cavity with large drift tubes where magnets can be overlapped.

If a magnet density on a ring needs to be increased further, the acceleration gap may be moved into the magnet region. Because the quarter wave length $1/4$ at 26MHz is about 3m, a bending magnet whose length is 3m or 6m can cover a whole quarter or half wave length cavity(see Fig. 2.31). Because of the orbit excursion, the cavity should be wide in horizontal direction and thus has a flat shape. Although the magnet's gap height has to be large enough, the magnet population on the ring would come close to 100%. A sparking problem due to the high field gradient between the inner and the outer conductor has to be considered, which may be cured by use of ceramic insulators. Sparking problem in a high magnetic field may cause a problem, while this configuration is usually seen in cyclotrons with lower voltage though.

2.3.2 Magnet

2.3.2.1 Yoke free design of FFAG magnet

One of the problems of the conventional radial sector type of FFAG is that the sector magnets occupy most of the ring circumference. It results in the lack of free space for beam injection and extraction.

Up to now, the FFAG triplet magnet developed in KEK employs the conventional H-type magnet, such that the field flux returns through the side yoke attached to its pole. The triplet magnet used in KEK POP FFAG synchrotron is a complex of three independent H-type sector magnets(see Appendix C).

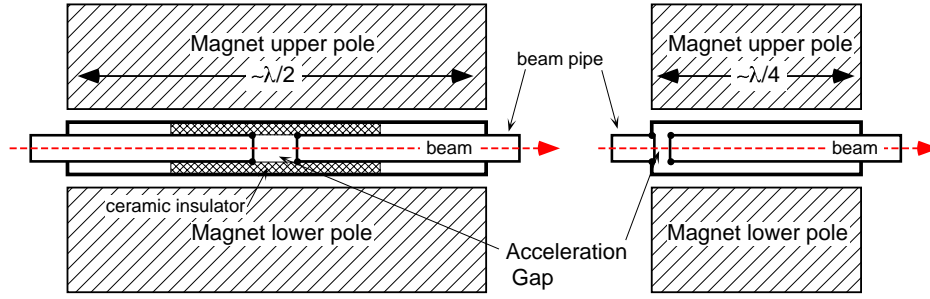


Figure 2.31: a 26MHz flat cavity inserted between a dipole magnet. Left: $\lambda/2$ unit with ceramic insulator. Right: $\lambda/4$ unit where magnets can be overlapped.

However, considering the field direction of the F-magnet and D-magnet of the triplet magnet, it is reversed each other. Thus, if the return yokes of F and D-magnets are removed, the flux circulates through the F-pole and the D-pole. Such flux generates the reversed field in F-pole and D-pole(see Fig. 2.32). This is a rough explanation of the idea of a new type FFAG magnet, so called 'yoke-free magnet'.

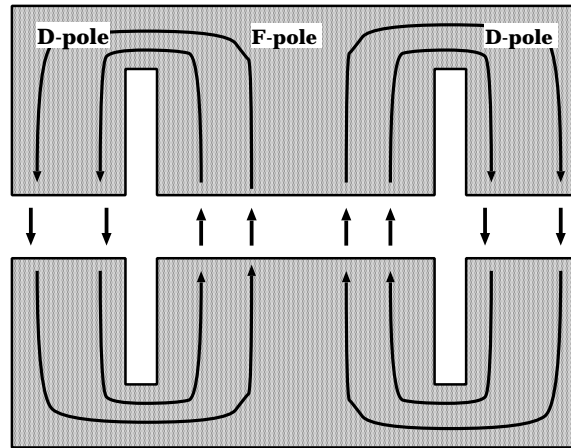


Figure 2.32: Schematic view of the field flux in the yoke-free magnet

In fact, if the return yoke is completely removed, the net flux of F-pole and D-pole should be equal. It is unsuitable for FFAG ring, since the field of D-pole should be weaker than that of F-pole. In order to reduce the flux

in the D-pole, shunt yokes are installed at the side of D-pole. In addition, so as to apply fine tuning of the field strength, tuning coils are installed around D-pole.

Schematic view of the typical yoke free magnet is shown in Fig. 2.33. The return yoke of F-pole is completely removed. This structure is favorable for the beam extraction, since the beam radius becomes the maximum at the center of the F-pole. The beam could be extracted at that point.

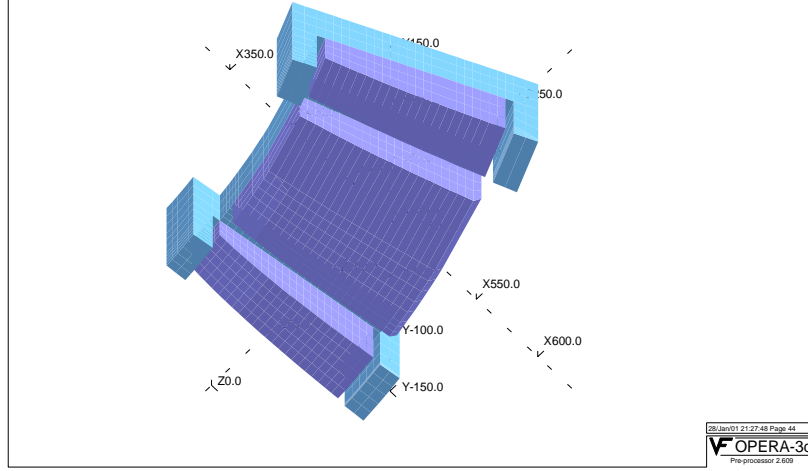


Figure 2.33: View of a half pole of a typical yoke-free magnet

Up to now, a prototype yoke free magnet was made (see. Fig. 2.34) by modifying the prototype magnet of POP FFAG, and the field measurement was carried out. The result shown in Fig. 2.35 indicates good agreement with the numerical calculation by TOSCA.

It should be mentioned that a new project to demonstrate the yoke-free magnet is under development(see appendix D).

2.3.2.2 superconducting magnet

In order to reduce the total circumference and the orbit excursion, superconducting magnets becomes surely an option of the FFAG gradient magnets. Here we will show one example of the magnet design.

One of crucial issues in making the FFAG magnets superconducting is a way of field shaping. The FFAG magnet has the field strength in the following form,

$$B = B_0 \left(\frac{r}{r_0} \right)^k \quad (2.12)$$



Figure 2.34: Prototype yoke free magnet

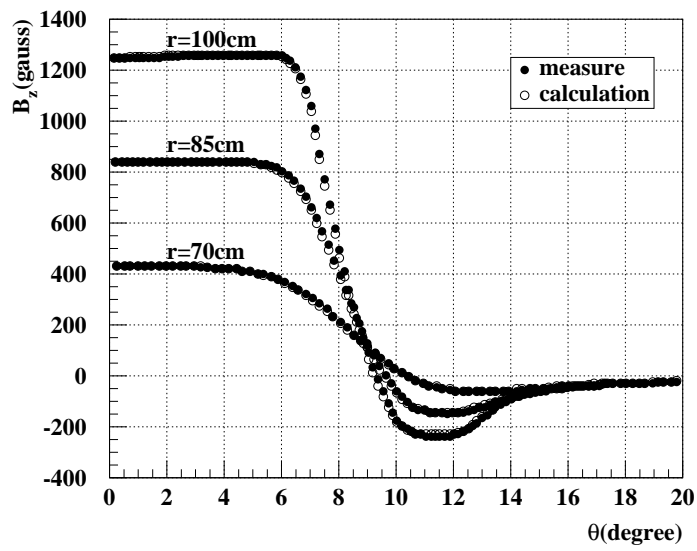


Figure 2.35: Result of field measurement of the prototype yoke-free magnet

where r is a radius from the machine center and k is a field index. The subscript 0 means the value at a reference point.

In a small machine like POP-FFAG described in Appendix, the maximum field strength of gradient magnets are 1 T or so. The gradient of Eq. 2.12 is made by the pole shape. That can be no longer available in a superconducting magnet, where the pole of iron is saturated and the pole shape does not impose any boundary conditions.

The magnetic field distribution along the radial axis can be created with distributed coil windings. For example, evenly distributed coils in the beam region with their returns at one point are considered. In addition, current of each coil can be different to further trim the field.

Fig. 2.36 shows the coil configuration in our design. That magnet has a single pole for simple FODO radial sector FFAG. However, it can be also a model of center pole of a triplet magnet with “yoke-free” scheme because the yokes are attached in azimuthal direction. The size of the magnet is 400mm×400mm×470mm (length×width× height). Each coils are separated in 40 mm.

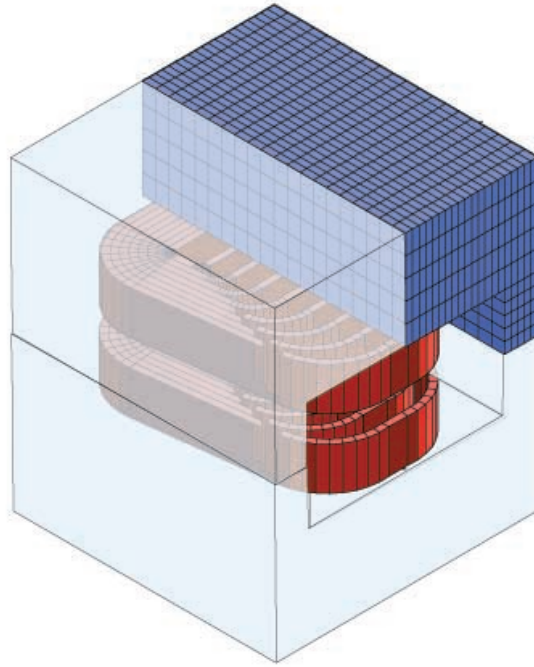


Figure 2.36: Coil configuration of the model superconducting magnet

Fig. 2.37 shows the vertical field strength on the medium plane calculated with TOSCA. The obtained field has a field index of 6.1 in the region of $r = 200$ mm to 350 mm and the maximum field is 3.5 T as expected.

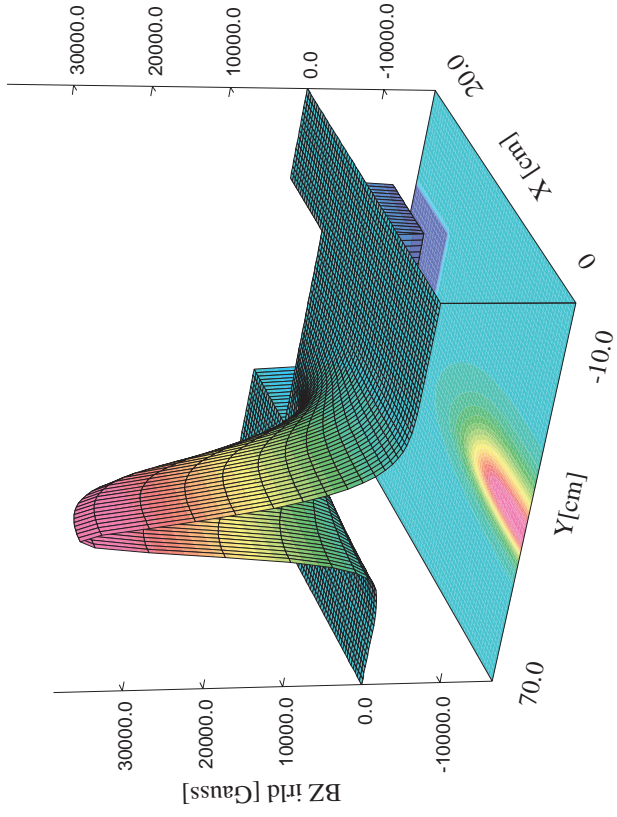


Figure 2.37: Field distribution of the model superconducting magnet

Chapter 3

Physics

3.1 Theory

3.1.1 Introduction

There have been several experiments [22, 23, 24, 25, 26, 27, 28, 29, 30, 31, 32, 33] which suggest neutrino oscillations [34, 35]. It has been shown in the two flavor framework that the solar neutrino deficit can be explained by neutrino oscillation with the set of parameters $(\Delta m_{\odot}^2, \sin^2 2\theta_{\odot}) \simeq (\mathcal{O}(10^{-5}\text{eV}^2), \mathcal{O}(10^{-2}))$ (SMA (small mixing angle) MSW solution), $(\mathcal{O}(10^{-5}\text{eV}^2), \mathcal{O}(1))$ (LMA (large mixing angle) MSW solution), $(\mathcal{O}(10^{-7}\text{eV}^2), \mathcal{O}(1))$ (LOW solution) or $(\mathcal{O}(10^{-10}\text{eV}^2), \mathcal{O}(1))$ (VO (vacuum oscillation) solution), and among these the LMA MSW solution gives the best fit to the data [36]. On the other hand, the atmospheric neutrino anomaly can be accounted for by dominant $\nu_{\mu} \leftrightarrow \nu_{\tau}$ oscillations with $(\Delta m_{\text{atm}}^2, \sin^2 2\theta_{\text{atm}}) \simeq (10^{-2.5}\text{eV}^2, 1.0)$. In the three flavor framework there are two independent mass squared differences and it is usually assumed that these two mass differences correspond to Δm_{\odot}^2 and Δm_{atm}^2 . Throughout this report we will assume three neutrino species which can account for only the solar neutrino deficit and the atmospheric neutrino anomaly¹. Without loss of generality we assume $|\Delta m_{21}^2| < |\Delta m_{32}^2| < |\Delta m_{31}^2|$ where $\Delta m_{ij}^2 \equiv m_i^2 - m_j^2$. The flavor eigenstates are related to the mass eigenstates by $U_{\alpha j}$ ($\alpha = e, \mu, \tau$), where $U_{\alpha j}$ are the elements of the MNS mixing matrix U [35]:

$$\begin{pmatrix} \nu_e \\ \nu_{\mu} \\ \nu_{\tau} \end{pmatrix} = U \begin{pmatrix} \nu_1 \\ \nu_2 \\ \nu_3 \end{pmatrix},$$

¹To explain the LSND anomaly [33] one would need at least four neutrino species.

$$\begin{aligned}
U &\equiv \begin{pmatrix} U_{e1} & U_{e2} & U_{e3} \\ U_{\mu 1} & U_{\mu 2} & U_{\mu 3} \\ U_{\tau 1} & U_{\tau 2} & U_{\tau 3} \end{pmatrix} \\
&= \begin{pmatrix} c_{12}c_{13} & s_{12}c_{13} & s_{13}e^{-i\delta} \\ -s_{12}c_{23} - c_{12}s_{23}s_{13}e^{i\delta} & c_{12}c_{23} - s_{12}s_{23}s_{13}e^{i\delta} & s_{23}c_{13} \\ s_{12}s_{23} - c_{12}c_{23}s_{13}e^{i\delta} & -c_{12}s_{23} - s_{12}c_{23}s_{13}e^{i\delta} & c_{23}c_{13} \end{pmatrix}.
\end{aligned}$$

With the mass hierarchy $|\Delta m_{21}^2| \ll |\Delta m_{32}^2|$ there are two possible mass patterns which are depicted in Fig. 3.1, depending on whether Δm_{32}^2 is positive or negative.

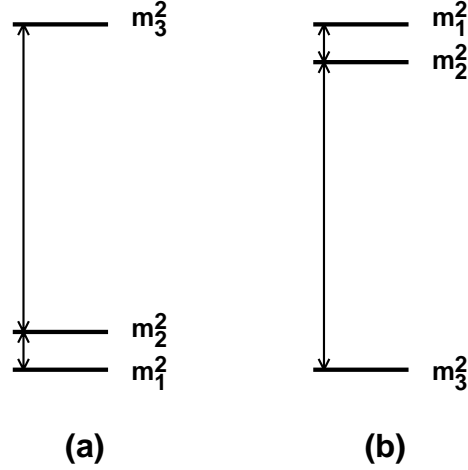


Figure 3.1: Two mass patterns. (a), (b) correspond to $\Delta m_{32}^2 > 0$, $\Delta m_{32}^2 < 0$, respectively.

It has been shown in the three flavor framework [37, 38, 39] that combination of the CHOOZ reactor data [40] and the atmospheric neutrino data implies small θ_{13} , i.e., $\sin^2 2\theta_{13} < 0.1$ which is essentially the result of the CHOOZ data ². When $|\theta_{13}|$ is small, the MNS matrix looks like

$$U \simeq \begin{pmatrix} c_{\odot} & s_{\odot} & \epsilon \\ -s_{\odot}c_{\text{atm}} & c_{\odot}c_{\text{atm}} & s_{\text{atm}} \\ s_{\odot}s_{\text{atm}} & -c_{\odot}s_{\text{atm}} & c_{\text{atm}} \end{pmatrix},$$

where θ_{12} , θ_{23} have been replaced by θ_{\odot} and θ_{atm} , respectively. According to the most up-to-date analysis [42, 43, 44, 45] (See Figs. 3.2 and 3.3), assuming the LMA MSW solution is the right one for the solar neutrino problem [36], these mixing angles and the mass squared differences satisfy at 90%CL

$$0.57 \leq \sin^2 2\theta_{\odot} \leq 0.98,$$

²If one does not include the constraint of the Kamiokande data then one get milder bound on θ_{13} , i.e., $\sin^2 2\theta_{13} \lesssim 0.25$ [41].

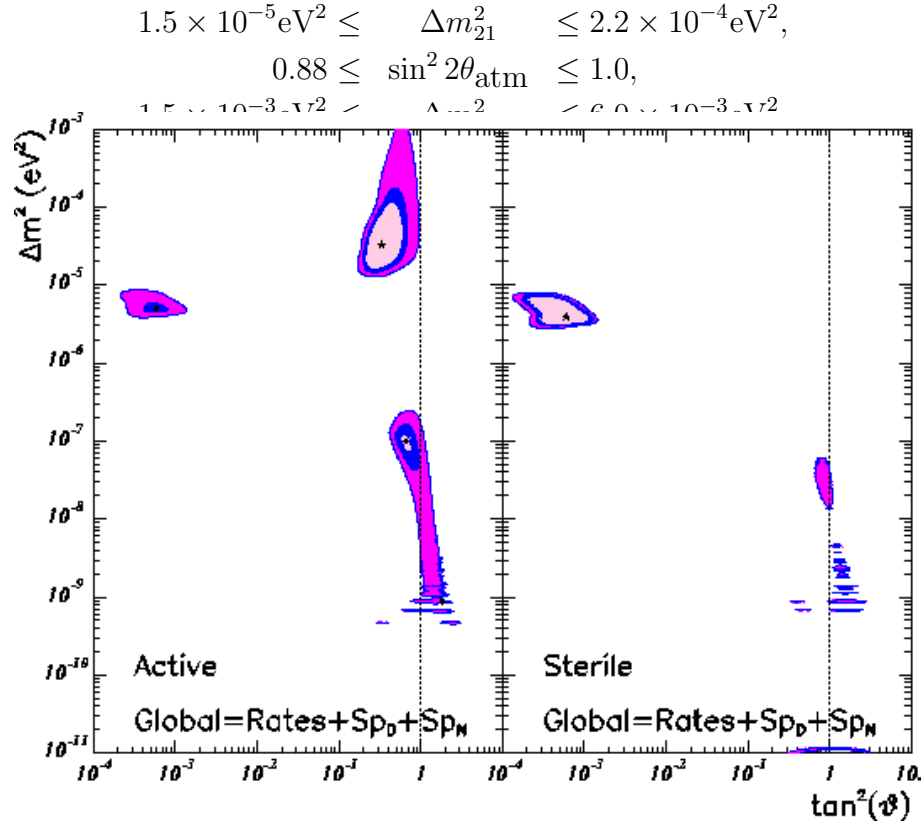


Figure 3.2: Results of recent analysis on solar neutrinos [42], which almost agrees with [43] and [44].

The measurement of $\theta_{\odot} \equiv \theta_{12}$ and $\theta_{\text{atm}} \equiv \theta_{23}$ is expected to be greatly improved in the future experiments on solar and atmospheric neutrinos, so the remaining problems in the three flavor framework are to determine (1) the sign of Δm_{32}^2 , (2) the magnitude of θ_{13} , (3) the magnitude of the CP phase δ . Recently a lot of research have been done on neutrino factories, [46, 6, 89, 47, 48, 49, 50, 51, 52, 53, 54, 55, 56, 57, 58, 59, 60, 61] and the three problems mentioned above may be solved at neutrino factories. In the following, we discuss these three topics.

3.1.2 Sensitivity to θ_{13}

The main channels which are supposed to be measurable at neutrino factories are $\nu_e \rightarrow \nu_\mu$ and $\bar{\nu}_e \rightarrow \bar{\nu}_\mu$. When contributions from Δm_{21}^2 are negligible, the appearance probabilities $P(\nu_e \rightarrow \nu_\mu)$ and $P(\bar{\nu}_e \rightarrow \bar{\nu}_\mu)$ are given by (on the assumption of constant density of the matter)

$$P(\nu_e \rightarrow \nu_\mu) = s_{23}^2 \sin^2 2\theta_{13}^{M^{(-)}} \sin^2 \left(\frac{B^{(-)}L}{2} \right)$$

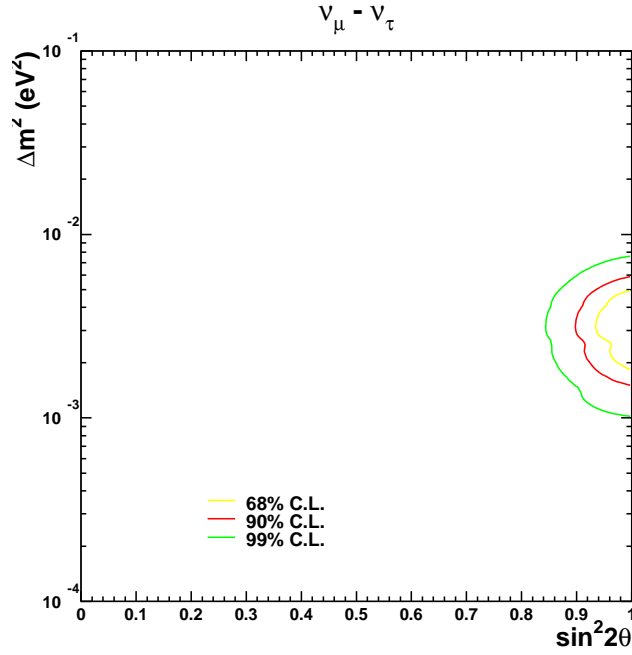


Figure 3.3: Allowed region from Superkamiokande contained and partially contained event for $\nu_\mu - \nu_\tau$ oscillations. The figure is from [45].

$$P(\bar{\nu}_e \rightarrow \bar{\nu}_\mu) = s_{23}^2 \sin^2 2\theta_{13}^{M(+)} \sin^2 \left(\frac{B^{(+)}L}{2} \right), \quad (3.1)$$

where $A \equiv \sqrt{2}G_F N_e$ stands for the matter effect of the Earth, $\theta_{13}^{M(\pm)}$ is the effective mixing angle in matter given by

$$\tan 2\theta_{13}^{M(\pm)} \equiv \frac{\Delta E_{32} \sin 2\theta_{13}}{\Delta E_{32} \cos 2\theta_{13} \pm A},$$

and

$$B^{(\pm)} \equiv \sqrt{(\Delta E_{32} \cos 2\theta_{13} \pm A)^2 + (\Delta E_{32} \sin 2\theta_{13})^2}.$$

The number of muon decays needed to observe 10 $\nu_e \rightarrow \nu_\mu$ events is shown in Fig. 3.4 as a function of E_μ for a few solar neutrino scenarios [47]. As can be seen from Fig. 3.4, the sub-leading contributions from Δm_{21}^2 may be observed in a high intensity muon source even if $\theta_{13} = 0$. In the following discussions on the magnitude of θ_{13} , this sub-leading contributions will not be taken into account.

The asymptotic sensitivities to θ_{13} has been studied by taking into account realistic background and efficiencies as well as the spectral information for detectors, or without consideration of backgrounds and systematic errors [60]. [89] studied the sensitivity for a 40KTon magnetized iron calorimeter at $L=732\text{km}$, 3500km , 7332 km , $E_\mu=50\text{ GeV}$ with 10^{21} useful muon decays (See Fig. 3.5), and [54] did for a liquid argon detector at $L=7400\text{ km}$,

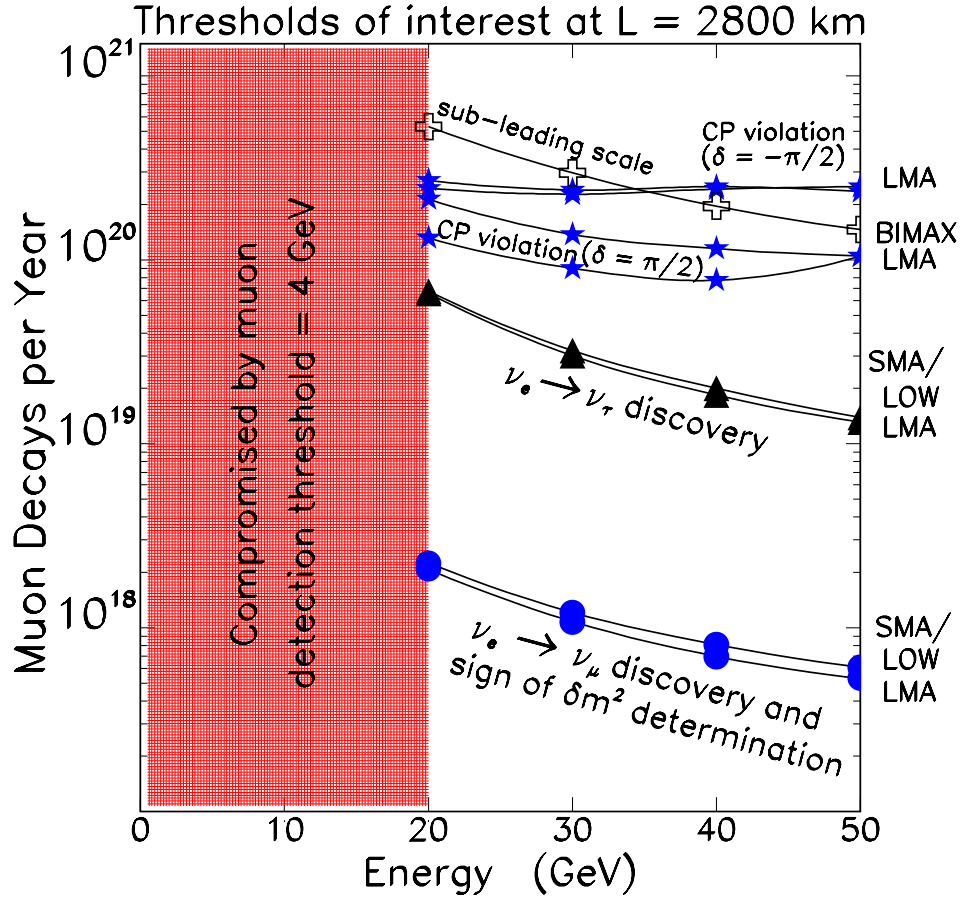


Figure 3.4: The required number of muon decays needed in the beam for the LMA scenario, SMA scenario, LOW scenario, and a bimaximal mixing scenario BIMAX for a 50 kt detector (a 5 kt detector in the case of $\nu_e \rightarrow \nu_\tau$ appearance) at $L=2800$ km with a muon detection threshold of 4 GeV [47].

$E_\mu=30$ GeV with 10^{20} and 10^{21} useful muon decays (See Fig. 3.6). [60] studied the sensitivity for the case $N_\mu = 2 \times 10^{21} \text{kt}\cdot\text{yr}$ with correlation of all errors and without the background effect and the systematic errors taken into account. When only statistical errors are considered, the asymptotic sensitivity to the angle is naively expected to improve at shorter baselines, but it has been shown [89] that background contamination makes sensitivity poorer at shorter baselines.

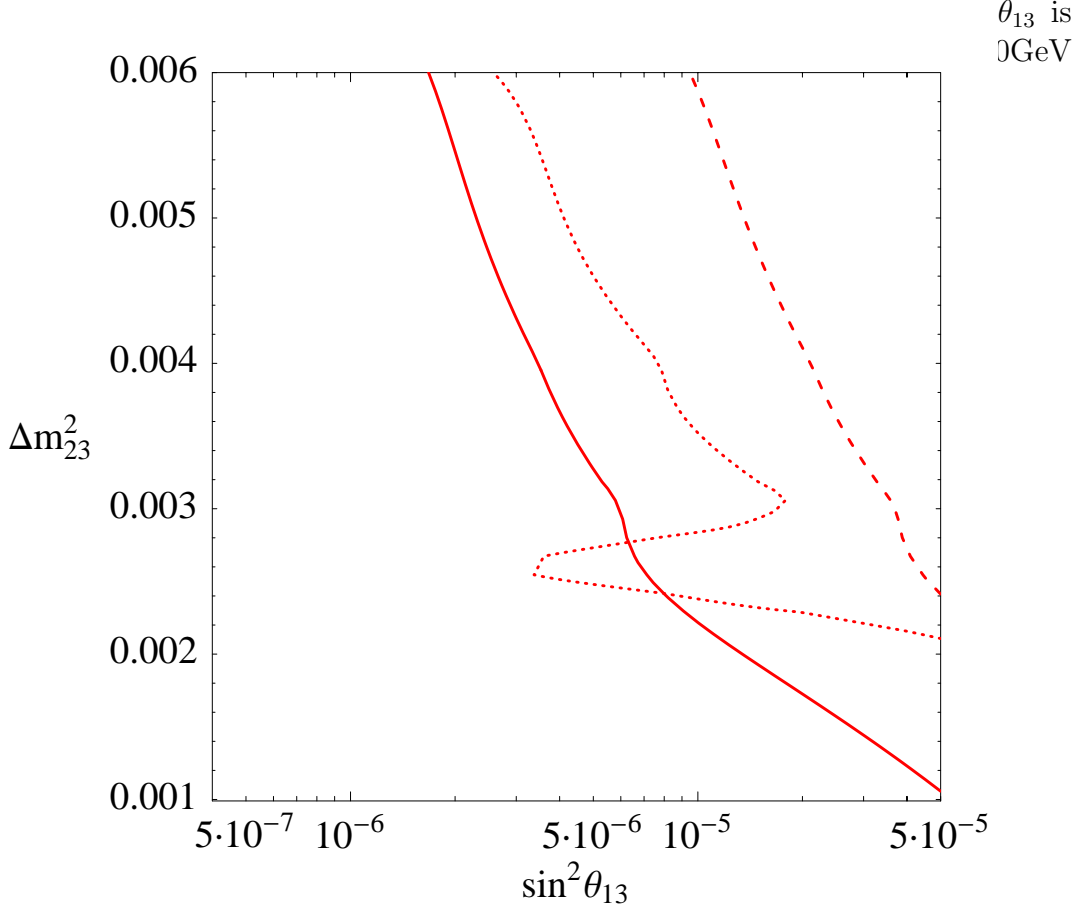


Figure 3.5: The asymptotic sensitivity to $\sin^2 \theta_{13}$ as a function of Δm_{23}^2 at 90% CL for a 40KTon magnetized iron calorimeter at $L=732\text{km}$ (dashed lines), 3500km (solid lines), 7332 km (dotted lines), $E_\mu=50$ GeV with 10^{21} useful muon decays [89]. The SMA MSW solution ($\Delta m_{21}^2 = 6 \times 10^{-6} \text{eV}^2$, $\sin^2 2\theta_{12}=0.006$) is assumed. Backgrounds and detection efficiencies are included.

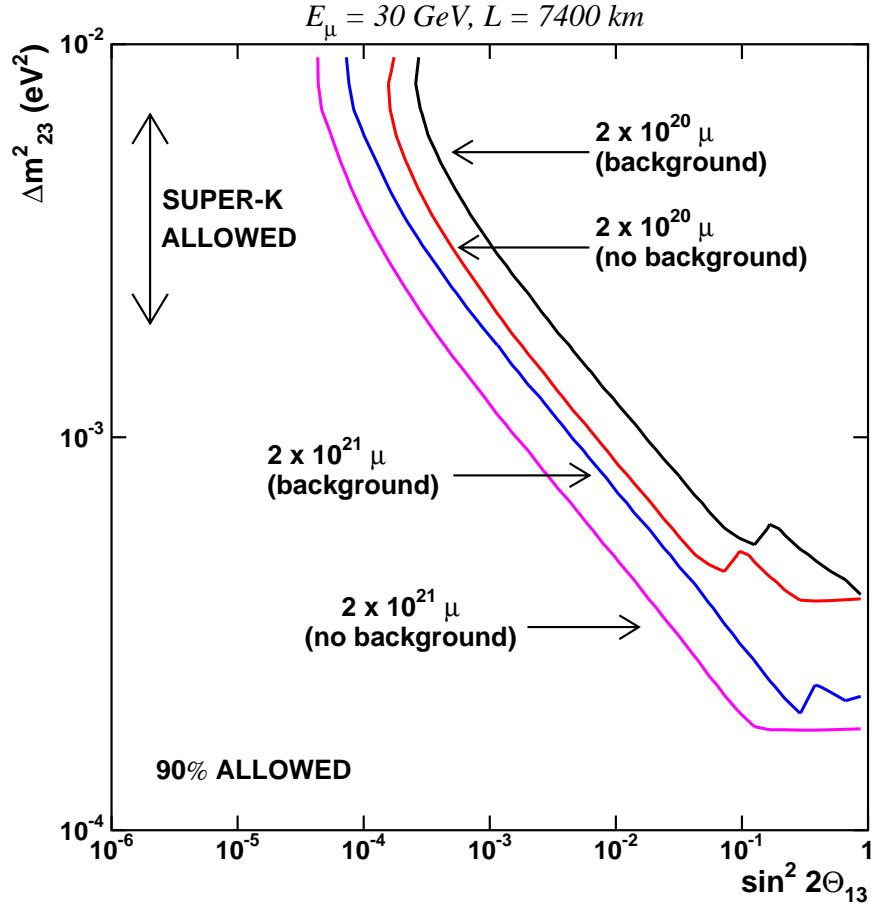


Figure 3.6: The asymptotic sensitivity to θ_{13} for a 10kt ICANOE-type detector at $L=7400$ km, $E_\mu=30$ GeV with 10^{20} and 10^{21} useful muon decays [54]. Backgrounds and detection efficiencies are included.

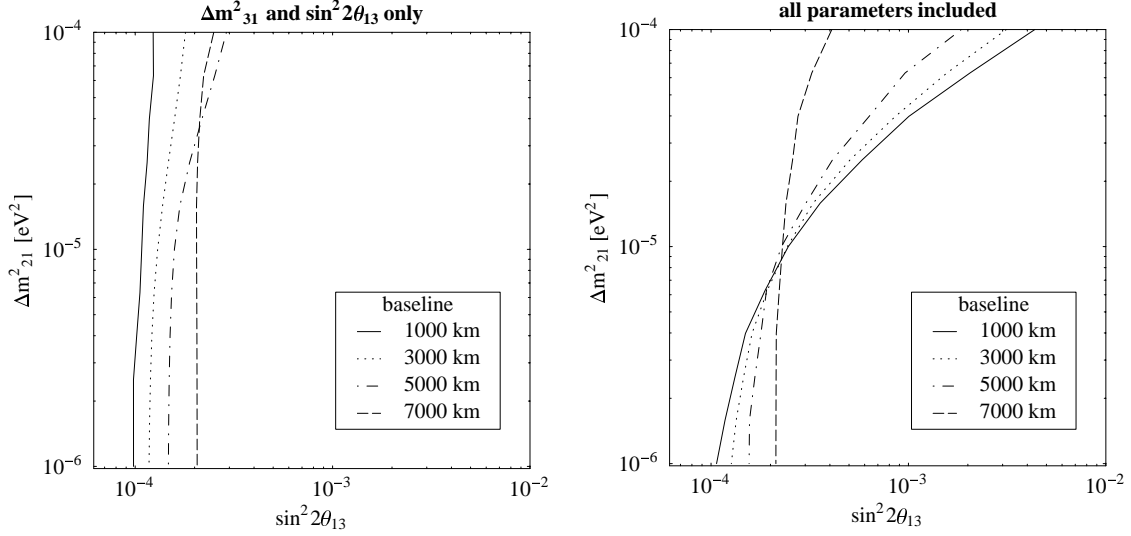


Figure 3.7: Sensitivity reach for measurements of $\sin^2 2\theta_{13}$ [60]. The area to the left of the lines indicates the parameter range where measurements are compatible with $\sin^2 2\theta_{13} = 0$ at 99% C.L. The calculation was performed with a beam energy of 50 GeV. The different line types are for different baseline as explained in the legend. For comparison to older studies, the left panel displays the result obtained from a two parameter fit of only $\sin^2 2\theta_{13}$ and Δm_{31}^2 . Backgrounds and experimental uncertainties are not taken into account. The right panel displays the result of [60] with all parameters taken into account.

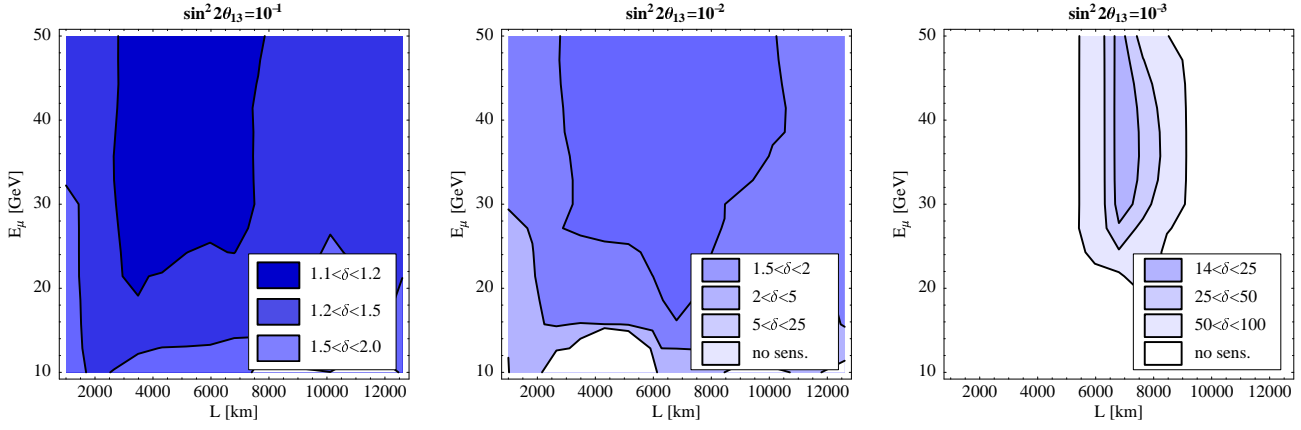


Figure 3.8: Statistical error of the quantity $\sin^2 2\theta_{13}$ as function of the baseline L and the muon energy E_μ for $\Delta m_{31}^2 = 3.5 \cdot 10^{-3} \text{eV}^2$, $\sin^2 2\theta_{23} = 1$, $N_\mu m_{\text{kt}} = 2 \cdot 10^{21} \text{ kt year}$ and three values of $\sin^2 2\theta_{13}$ (10^{-1} , 10^{-2} , 10^{-3}) [60]. Backgrounds and experimental uncertainties are not taken into account. Dark shading indicates the preferred regions. The parameters Δm_{21}^2 and δ_{cp} play a role mainly for small values of θ_{13} . Here, they are assumed as unknown.

3.1.3 Determination of the sign of Δm_{32}^2

As was mentioned earlier, in the three flavor framework the mass pattern corresponds to either Fig. 3.1 (a) or (b), depending on whether Δm_{32}^2 is positive or negative. Determination of this mass pattern is important, since Figs. 3.1 (a) and (b) correspond to one and two massive states, assuming that the lowest mass is almost zero. As we can see from (3.1), if $\Delta m_{32}^2 > 0$ then the effective mixing angle $\theta_{13}^{M(-)}$ is enhanced and $P(\nu_e \rightarrow \nu_\mu)$ increases. On the other hand, if $\Delta m_{32}^2 < 0$ then $\theta_{13}^{M(+)}$ is enhanced and $P(\bar{\nu}_e \rightarrow \bar{\nu}_\mu)$ increases. So, at neutrino factories where baseline is relatively large and therefore the matter effect plays an important role, the sign of Δm_{32}^2 can be determined by looking at the difference between neutrino and anti-neutrino events which should reflect the difference between $P(\nu_e \rightarrow \nu_\mu)$ and $P(\bar{\nu}_e \rightarrow \bar{\nu}_\mu)$. The ratio $N(\bar{\nu}_e \rightarrow \bar{\nu}_\mu)/N(\nu_e \rightarrow \nu_\mu)$ is plotted as a function of the baseline L in Fig. 3.9 for $E_\mu = 20 \text{ GeV}$ [47]. From Fig. 3.9 we observe that we can determine the sign of Δm_{32}^2 for $L \gtrsim 2000 \text{ km}$.

3.1.4 Precise measurements of the oscillation parameters

Once wrong sign muons are observed, the next thing to do is to determine the precise values of the mixing angles and the mass squared differences. Correlations of errors in the mixing angles and the mass squared differences

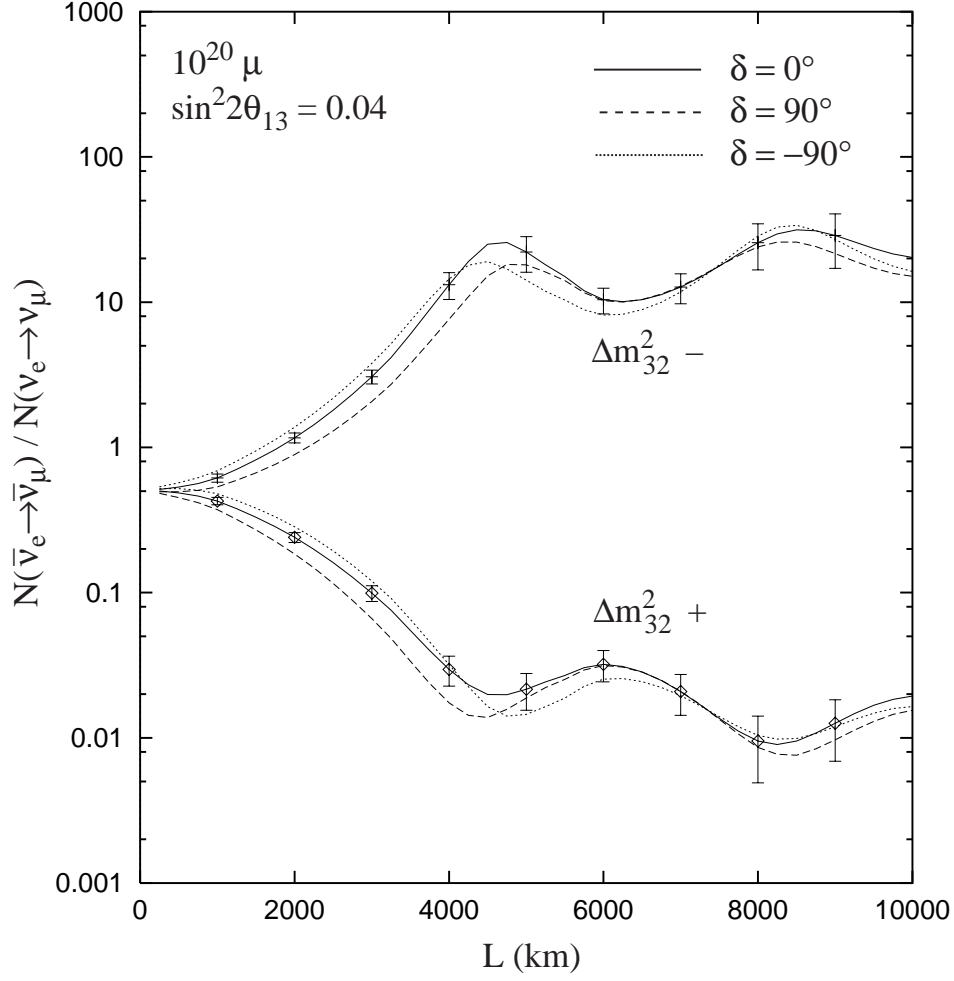


Figure 3.9: The ratio of $\bar{\nu}_e \rightarrow \bar{\nu}_\mu$ to $\nu_e \rightarrow \nu_\mu$ event rates at $E_\mu=20\text{GeV}$ for $\delta = 0, \pm\pi/2$ [47]. The upper (lower) group of curves is for $\Delta m_{32}^2 < 0$ ($\Delta m_{32}^2 > 0$), and the statistical errors correspond to 10^{20} muon decays of each sign and a 50 kt detector. The oscillation parameters correspond to the LAM solar solution with $|\Delta m_{32}^2| = 3.5 \times 10^{-3} \text{ eV}^2$ and $\sin^2 2\theta_{13} = 0.04$.

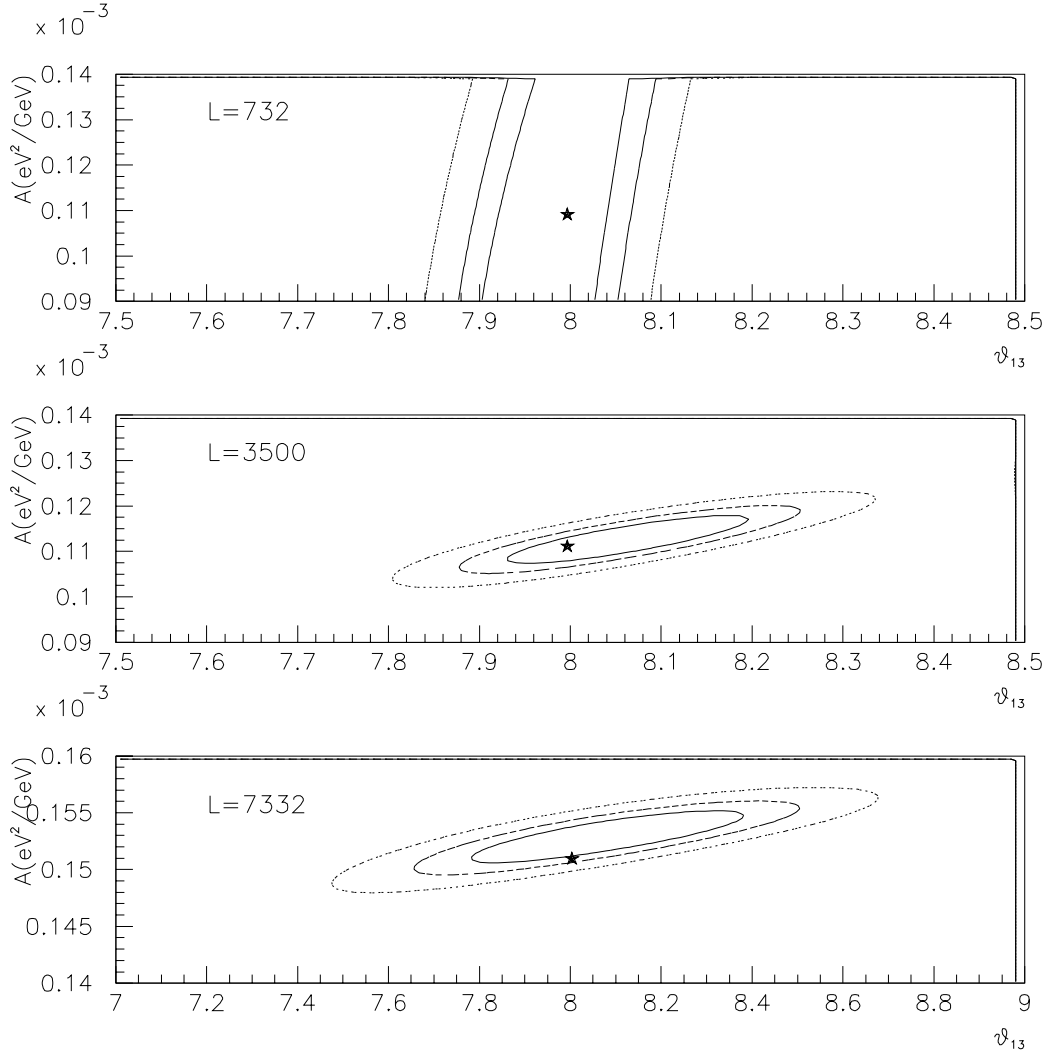


Figure 3.10: 68.5, 90, 99 % CL resulting from a simultaneous fit of θ_{13} and the matter effect A for a 40Kton magnetized iron calorimeter at $L=732$ km, 3500km, 7332 km, $E_\mu=50$ GeV with 10^{21} useful muon decays including backgrounds and efficiencies [89]. The star indicates the parameters used to generate the “data”.

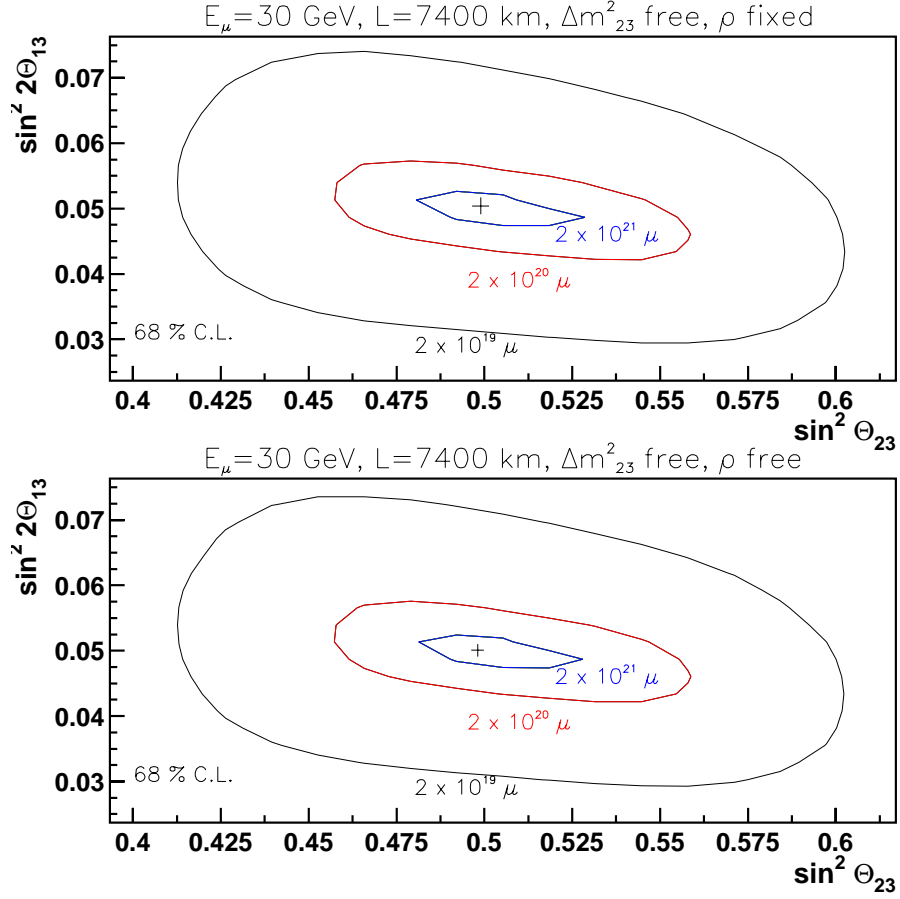


Figure 3.11: 68%C.L. two-dimensional contours for $\sin^2 2\theta_{13}$ and $\sin^2 \theta_{23}$ for a 10kt ICANOE-type detector at $L=7400$ km, $E_\mu=30$ GeV with 10^{20} and 10^{21} useful muon decays [54]. Backgrounds and detection efficiencies are included. In the upper plot ρ is fixed during the fit, while in the lower one is taken as a free parameter. Influence of the density ρ in the determination of the mixing angles is not large for three different muon normalizations and for $E_\mu=30$ GeV at $L=7400$ km.

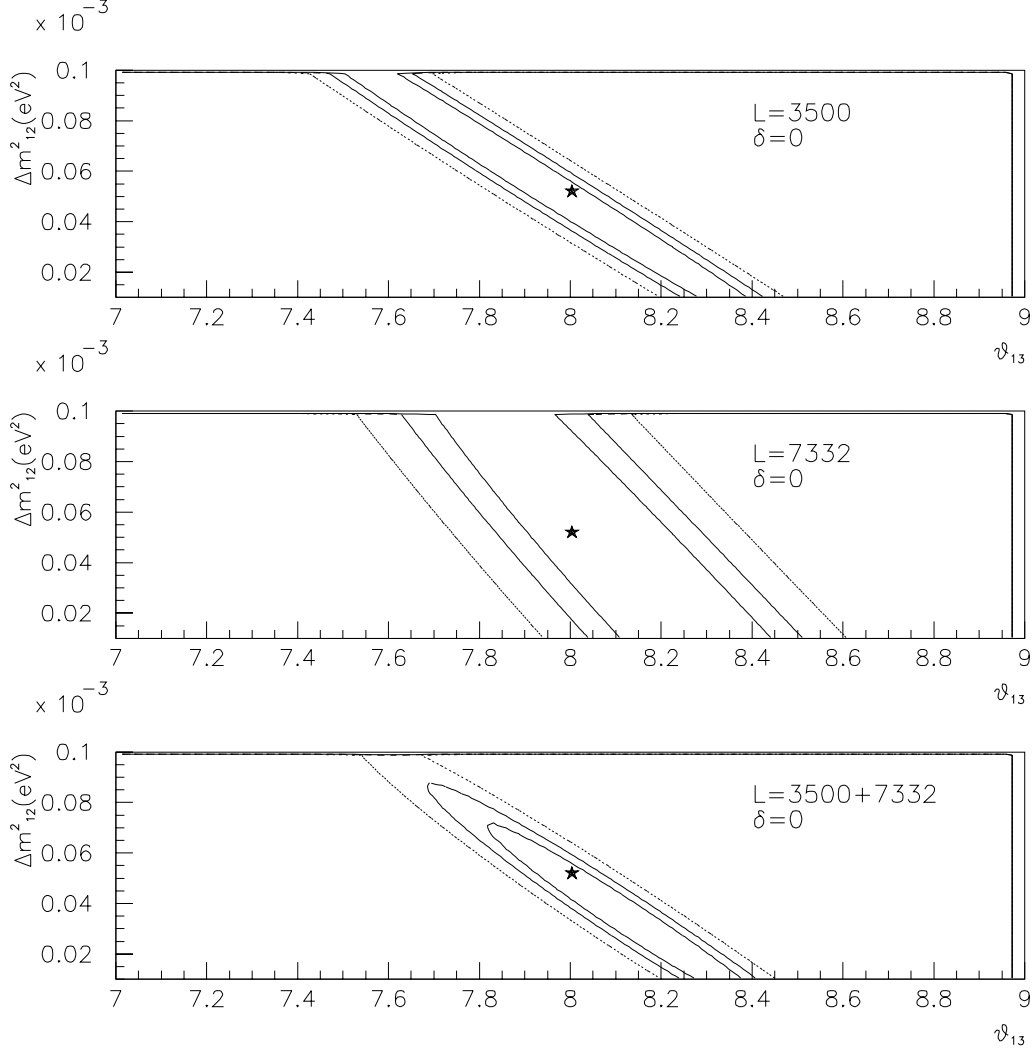


Figure 3.12: Simultaneous fit to θ_{13} and Δm^2_{12} for a 40K Ton magnetized iron calorimeter at $L= 3500\text{km}$, 7332 km , $3500\text{km} + 7332 \text{ km}$, $E_\mu=50 \text{ GeV}$ with 10^{21} useful muon decays [89]. The range shown in the vertical axis is the presently allowed LMA-MSW range. The star indicates the parameters used to generate the “data” and the CP-odd phase is set to zero. Backgrounds and detection efficiencies are included.

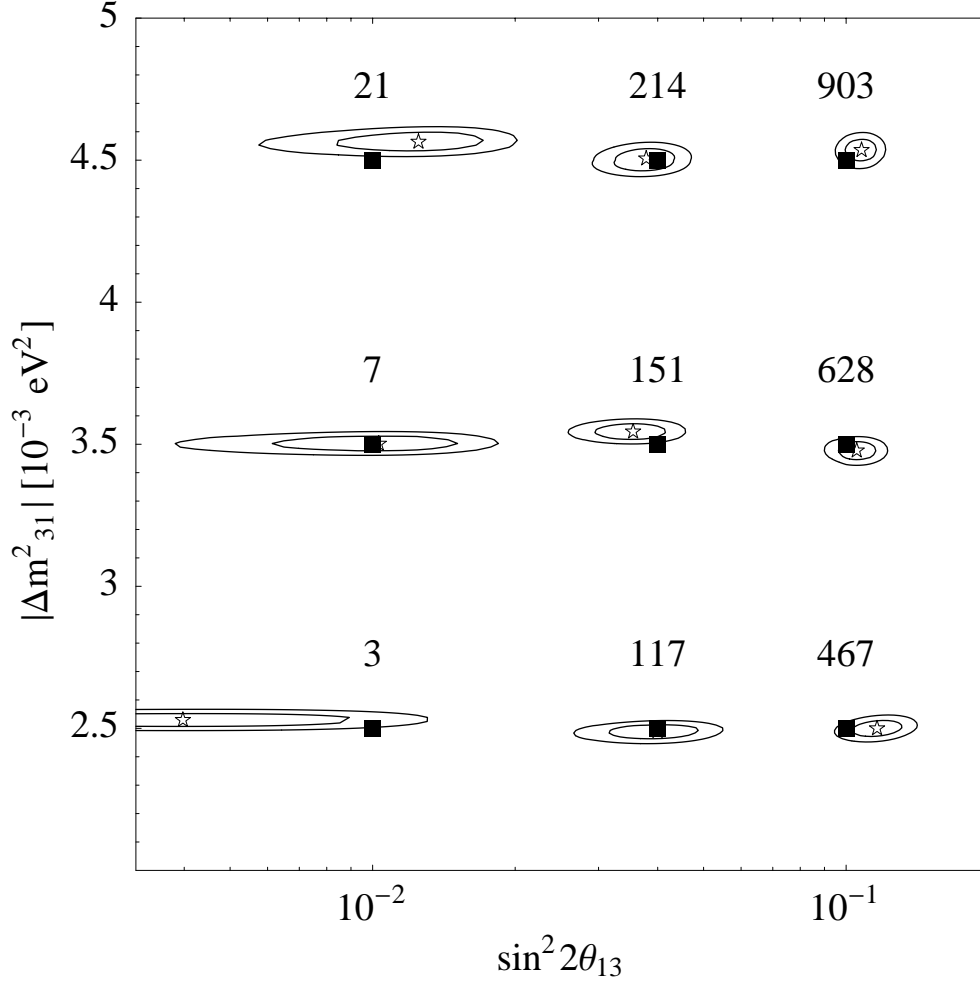


Figure 3.13: The 1σ and 2σ contours in the $(\sin^2 \theta_{13}, \Delta m^2_{23})$ plane which can be achieved without charge identification (i.e., the sum of the total muons) for $E_\mu=30$ GeV at $L=7332\text{km}$ with 2×10^{21} useful μ^+ and μ^- decays [55]. The rectangles denote the parameter pair for which the data were generated and the stars denote the obtained best fit. The numbers printed next to each case are the values of χ^2 per 2 d.o.f for the best fit with the wrong sign of Δm^2_{31} .

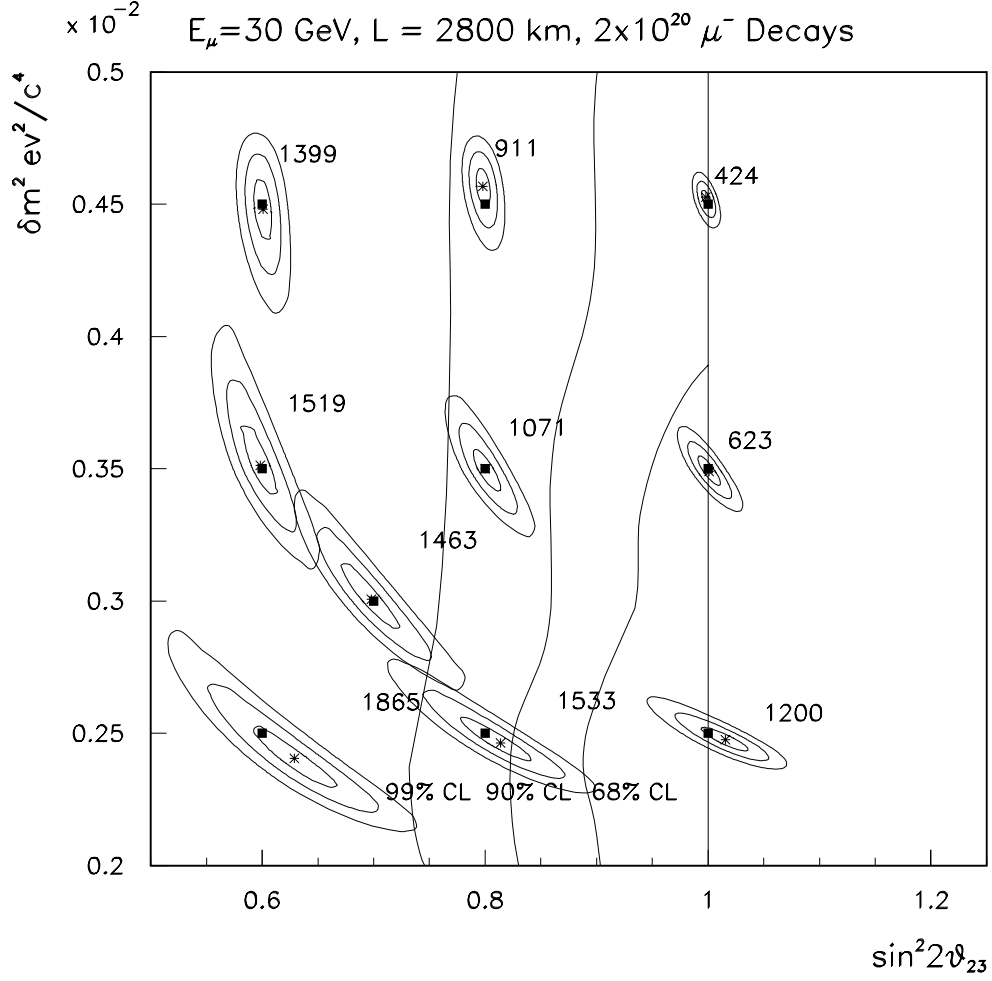


Figure 3.14: Fit results for simulated ν_μ disappearance measurements with a 10 kt MINOS-type detector 2800 km downstream of a 30 GeV neutrino factory in which there are $2 \times 10^{20} \mu^-$ decays. For each trial point the 1σ , 2σ , and 3σ contours are shown for a perfect detector (no backgrounds) and no systematic uncertainty on the beam flux. The 68%, 90% and 95% SuperK regions are indicated. Results are from Ref. [47].

have been studied by several groups.

The correlation of θ_{13} and the matter effect is given in Fig. 3.10 for a 40 kt Fe-scintillator detector at a distance $L = 732\text{km}, 3500\text{km}, 7332\text{km}$, $E_\mu = 50\text{ GeV}$, 10^{21} muon decays in the case of the SMA MSW solution ($\Delta m_{21}^2 = 6 \times 10^{-6} \text{eV}^2$, $\sin^2 2\theta_{12} = 0.006$) [89]. At 732 km there is no sensitivity to the matter term. At the larger baseline, while the precision in A improves, the precision in θ_{13} gets worse due to the loss in statistics.

The correlation of θ_{13} and θ_{23} is given in Fig. 3.11 for a 10kt ICANOE-type detector at $L=7400\text{km}$ with $10^{19}, 10^{20}, 10^{21}$ μ^+ decays followed by the same number of μ^- decays [54]. In Fig. 3.11 the density ρ is either considered as a free parameter (lower plot) or fixed (upper plot) in a fit but there is no much difference.

The correlation of θ_{13} and Δm_{21}^2 is shown in Fig. 3.12 [89]. This correlation is potentially large, but the authors of [89] assume that Δm_{21}^2 and θ_{12} are known by the time the neutrino factory will be operational. In fact KamLAND is expected to measure Δm_{21}^2 and θ_{12} with certain precision within a few years after it starts running in 2001. Even if the errors in these two parameters of solar neutrino oscillation are as large as 50 %, the effect on the precision in θ_{13} is not so serious and the precision 5 % in θ_{13} can be expected from the analysis of [89].

It was shown [55] that if θ_{13} turns out to be relatively large ($\sin^2 2\theta_{13} \gtrsim 0.01$), by the total number of muons without charge identification, a similar precision in the determination of θ_{13} is obtained as using the wrong-sign muon signal (cf. Fig. 3.13).

The correlation of θ_{23} and Δm_{32}^2 is given in Fig. 3.9 using disappearance of right-sign muons for $E_\mu=30\text{GeV}$, $L=2800\text{km}$, 2×10^{20} muon decays [47]. The precision for the Δm_{32}^2 and $\sin^2 2\theta_{23}$ measurements is a few %, which is one order of magnitude better than that expected at MINOS and OPERA.

3.1.5 The measurement of δ

3.1.5.1 CP violation at neutrino factories

For two of the solar neutrino solutions (SMA MSW and VO) it has been known that measurements of CP violation is practically impossible. For the LMA MSW solution, however, CP violation may be large enough to be measured and recent report from the Superkamiokande group [36] gives us a hope for measurements of CP violation. Hereafter we assume that the LMA MSW is the correct solution.

There have been a lot of works on CP violation at neutrino factories [46, 6, 89, 47, 48, 49, 50, 51, 52, 53, 54, 56, 57, 58, 59, 60, 61]. Some of earlier works [49, 50, 51] used an asymmetry parameter between ν and $\bar{\nu}$ after subtracting the matter effect, and some [56, 57] discussed T violation. Most of these works concluded that the baseline $L \sim 3000\text{km}$ and the muon

energy $E_\mu \sim 50\text{GeV}$ optimizes the signal.

On the other hand, there have been works [56, 62, 63, 64] which advocated the advantage of conventional low energy neutrino beams over neutrino factories with high energy, and there does not seem to be consensus among the community of neutrino physicists about the optimum neutrino energy and the baseline. One of the purposes of this subsection is to show that neutrino factories with high or medium muon energy ($20\text{GeV} \lesssim E_\mu \lesssim 50\text{GeV}$) are more advantageous over experiments with low energy ($E_\mu \ll 10\text{GeV}$). In the present report we use the result of [61] in which correlations of errors of δ and all the oscillations parameters as well as the matter effect have been taken into account and the data size to reject a hypothesis $\delta = 0$ has been obtained. The statistical significance of possible CP violation in neutrino factory type experiments is evaluated for a range of the muon energy $0.5\text{GeV} \leq E_\mu \leq 50\text{GeV}$ and the baseline $10\text{km} \leq L \leq 10^4\text{km}$ and it is shown that the case $E_\mu \lesssim$ a few GeV is always inferior to the option with higher energy. It is also shown analytically that the two kinds of $\Delta\chi^2$ which will be used, one of which is defined through the difference of $\delta \neq 0$ and $\delta = 0$ and the other of which through T violation, decrease for large muon energy $E_\mu \gg 50\text{GeV}$.

3.1.5.2 Definition of $\Delta\chi^2$

Our strategy here is to examine whether a hypothesis with a vanishing CP phase is rejected or not by taking into consideration all channels $\nu_e \rightarrow \nu_\mu$, $\bar{\nu}_e \rightarrow \bar{\nu}_\mu$, $\nu_\mu \rightarrow \nu_\mu$ and $\bar{\nu}_\mu \rightarrow \bar{\nu}_\mu$. For this purpose we define $\Delta\chi^2$ to test a hypothesis that a CP phase is given by $\bar{\delta}$ in the case where the true value is δ :

$$\begin{aligned}
& \Delta\chi^2(\theta_{k\ell}, \Delta m_{k\ell}^2, \delta, C; \bar{\theta}_{k\ell}, \overline{\Delta m_{k\ell}^2}, \bar{\delta}, \bar{C}) \\
& \equiv \sum_j \frac{[N_j^{\text{wrong}}(\mu^-; \theta_{k\ell}, \Delta m_{k\ell}^2, \delta, C) - N_j^{\text{wrong}}(\mu^-; \bar{\theta}_{k\ell}, \overline{\Delta m_{k\ell}^2}, \bar{\delta}, \bar{C})]^2}{N_j^{\text{wrong}}(\mu^-; \theta_{k\ell}, \Delta m_{k\ell}^2, \delta, C)} \\
& + \sum_j \frac{[N_j^{\text{wrong}}(\mu^+; \theta_{k\ell}, \Delta m_{k\ell}^2, \delta, C) - N_j^{\text{wrong}}(\mu^+; \bar{\theta}_{k\ell}, \overline{\Delta m_{k\ell}^2}, \bar{\delta}, \bar{C})]^2}{N_j^{\text{wrong}}(\mu^+; \theta_{k\ell}, \Delta m_{k\ell}^2, \delta, C)} \\
& + \sum_j \frac{[N_j^{\text{right}}(\mu^-; \theta_{k\ell}, \Delta m_{k\ell}^2, \delta, C) - N_j^{\text{right}}(\mu^-; \bar{\theta}_{k\ell}, \overline{\Delta m_{k\ell}^2}, \bar{\delta}, \bar{C})]^2}{N_j^{\text{right}}(\mu^-; \theta_{k\ell}, \Delta m_{k\ell}^2, \delta, C)} \\
& + \sum_j \frac{[N_j^{\text{right}}(\mu^+; \theta_{k\ell}, \Delta m_{k\ell}^2, \delta, C) - N_j^{\text{right}}(\mu^+; \bar{\theta}_{k\ell}, \overline{\Delta m_{k\ell}^2}, \bar{\delta}, \bar{C})]^2}{N_j^{\text{right}}(\mu^+; \theta_{k\ell}, \Delta m_{k\ell}^2, \delta, C)} \quad (3.2)
\end{aligned}$$

where j runs over energy bins and the numbers of events are given by

$$\begin{aligned}
& N_j^{\text{wrong}}(\mu^-; \theta_{k\ell}, \Delta m_{k\ell}^2, \delta, C) \\
&= \frac{12N_0 E_\mu}{\pi L^2 m_\mu^2} \int_{E_j}^{E_{j+1}} dE_\nu \left(\frac{E_\nu}{E_\mu} \right)^2 \left(1 - \frac{E_\nu}{E_\mu} \right) \sigma_{\nu N}(E_\nu) P(\nu_e \rightarrow \nu_\mu; \theta_{k\ell}, \Delta m_{k\ell}^2, \delta, C) \\
& N_j^{\text{wrong}}(\mu^+; \theta_{k\ell}, \Delta m_{k\ell}^2, \delta, C) \\
&= \frac{12N_0 E_\mu}{\pi L^2 m_\mu^2} \int_{E_j}^{E_{j+1}} dE_{\bar{\nu}} \left(\frac{E_{\bar{\nu}}}{E_\mu} \right)^2 \left(1 - \frac{E_{\bar{\nu}}}{E_\mu} \right) \sigma_{\bar{\nu} N}(E_{\bar{\nu}}) P(\bar{\nu}_e \rightarrow \bar{\nu}_\mu; \theta_{k\ell}, \Delta m_{k\ell}^2, \delta, C) \\
& N_j^{\text{right}}(\mu^-; \theta_{k\ell}, \Delta m_{k\ell}^2, \delta, C) \\
&= \frac{2N_0 E_\mu}{\pi L^2 m_\mu^2} \int_{E_j}^{E_{j+1}} dE_\nu \left(\frac{E_\nu}{E_\mu} \right)^2 \left(3 - 2 \frac{E_\nu}{E_\mu} \right) \sigma_{\nu N}(E_\nu) P(\nu_\mu \rightarrow \nu_\mu; \theta_{k\ell}, \Delta m_{k\ell}^2, \delta, C) \\
& N_j^{\text{right}}(\mu^+; \theta_{k\ell}, \Delta m_{k\ell}^2, \delta, C) \\
&= \frac{2N_0 E_\mu}{\pi L^2 m_\mu^2} \int_{E_j}^{E_{j+1}} dE_{\bar{\nu}} \left(\frac{E_{\bar{\nu}}}{E_\mu} \right)^2 \left(3 - 2 \frac{E_{\bar{\nu}}}{E_\mu} \right) \sigma_{\bar{\nu} N}(E_{\bar{\nu}}) P(\bar{\nu}_\mu \rightarrow \bar{\nu}_\mu; \theta_{k\ell}, \Delta m_{k\ell}^2, \delta, C),
\end{aligned}$$

where E_μ is the muon energy, L is the length of the neutrino path, N_0 is the number of the target nucleons times the number of useful decays of muons, $\sigma_{\nu N}(E_\nu)$ and $\sigma_{\bar{\nu} N}(E_{\bar{\nu}})$ are the (anti-)neutrino nucleon cross sections. We adopt the cross section which is the sum of those [65] of the quasi elastic scattering, one pion production, and inelastic scattering, where double counting of the latter two is suitably subtracted [66]. Throughout this section the threshold energy is assumed to be 0.1 GeV which is close to what has been assumed for liquid argon detectors [54] and which may be realized in possible mega ton water Cherenkov detectors [67, 68].

The number of the free parameters in the present case is six ($\delta, \theta_{12}, \theta_{13}, \theta_{23}, \Delta m_{21}^2, \Delta m_{32}^2$), but the density $N_e(x) = Y_e(x)\rho(x)$ of electrons is not known exactly ($Y_e(x)$ is the ratio of the number of electrons to that of protons and neutrons, and $\rho(x)$ is the density of the Earth at a distance x from the beam production point), so we have to vary $N_e(x)$ also. Here for simplicity we assume the PREM (Preliminary Reference Earth Model) [69] and vary the overall normalization of the PREM:

$$A(x) = C A_0(x) = \sqrt{2} C G_F Y_e(x) N_e(x),$$

where $C = 1$ corresponds to the PREM. We have to consider correlations of errors of the CP phase and six other quantities and taking into account all these errors we obtain the probability of rejecting a hypothesis $\bar{\delta} = 0$. To do that we look for the minimum value of $\Delta\chi^2(\theta_{k\ell}, \Delta m_{k\ell}^2, \delta, C; \bar{\theta}_{k\ell}, \overline{\Delta m_{k\ell}^2}, \bar{\delta}, \bar{C})$ by varying the six parameters ($\bar{\theta}_{12}, \bar{\theta}_{13}, \bar{\theta}_{23}, \overline{\Delta m_{21}^2}, \overline{\Delta m_{32}^2}, \bar{C}$):

$$\Delta\chi_{\min}^2 \equiv \min_{\bar{\theta}_{k\ell}, \overline{\Delta m_{k\ell}^2}, \bar{C}} \Delta\chi^2(\theta_{k\ell}, \Delta m_{k\ell}^2, \delta, C; \bar{\theta}_{k\ell}, \overline{\Delta m_{k\ell}^2}, \bar{\delta} = 0, \bar{C}),$$

where C stands for the overall normalization of the electron density.

3.1.5.3 Correlations of errors of δ and other parameters

Let us first discuss correlations of two variables $(\bar{\delta}, \bar{X})$ where a parameter X stands for $C, \theta_{13}, \theta_{12}, \theta_{23}, \Delta m_{21}^2$ and Δm_{32}^2 .

We have studied numerically correlations of errors between δ and the other oscillation parameters $(\theta_{k\ell}, \Delta m_{k\ell}^2)$ as well as the normalization C of the matter effect for the case where the central values for these parameters are those of the best fit point, i.e., $\sin^2 2\theta_{12} = 0.75$, $\Delta m_{21}^2 = 3.2 \times 10^{-5} \text{eV}^2$; $\sin^2 2\theta_{23} = 1.0$, $\Delta m_{32}^2 = 3.2 \times 10^{-3} \text{eV}^2$, $C=1.0$ and we have used a reference value 8° . The values of

$$\begin{aligned} &\Delta\chi^2(\theta_{12}, \theta_{13}, \theta_{23}, \Delta m_{21}^2, \Delta m_{32}^2, \delta, C; \theta_{12}, \theta_{13}, \theta_{23}, \Delta m_{21}^2, \Delta m_{32}^2, \bar{\delta}, \bar{C}), \\ &\Delta\chi^2(\theta_{12}, \theta_{13}, \theta_{23}, \Delta m_{21}^2, \Delta m_{32}^2, \delta, C; \theta_{12}, \bar{\theta}_{13}, \theta_{23}, \Delta m_{21}^2, \Delta m_{32}^2, \bar{\delta}, \bar{C}), \\ &\Delta\chi^2(\theta_{12}, \theta_{13}, \theta_{23}, \Delta m_{21}^2, \Delta m_{32}^2, \delta, C; \bar{\theta}_{12}, \theta_{13}, \theta_{23}, \Delta m_{21}^2, \Delta m_{32}^2, \bar{\delta}, \bar{C}), \\ &\Delta\chi^2(\theta_{12}, \theta_{13}, \theta_{23}, \Delta m_{21}^2, \Delta m_{32}^2, \delta, C; \theta_{12}, \theta_{13}, \bar{\theta}_{23}, \Delta m_{21}^2, \Delta m_{32}^2, \bar{\delta}, \bar{C}), \\ &\Delta\chi^2(\theta_{12}, \theta_{13}, \theta_{23}, \Delta m_{21}^2, \Delta m_{32}^2, \delta, C; \theta_{12}, \theta_{13}, \theta_{23}, \bar{\Delta m}_{21}^2, \Delta m_{32}^2, \bar{\delta}, \bar{C}), \\ &\Delta\chi^2(\theta_{12}, \theta_{13}, \theta_{23}, \Delta m_{21}^2, \Delta m_{32}^2, \delta, C; \theta_{12}, \theta_{13}, \theta_{23}, \Delta m_{21}^2, \bar{\Delta m}_{32}^2, \bar{\delta}, \bar{C}) \end{aligned}$$

are plotted in Fig. 3.15 – 3.21 in the case of $\delta = \pi/2$ for $E_\mu=3, 20, 50$ GeV, $L=100\text{km}, 1000\text{km}, 2500\text{km}, 6300\text{km}$, where the data size $10^{21}\mu\cdot 10\text{kt}$ is used as a reference value and no backgrounds are assumed. Since the number of degrees of freedom is 2, $\Delta\chi^2=0.18, 0.34, 0.73$ correspond to $1\sigma, 90\%, 99\%$ confidence level to reject a hypothesis with $\bar{\delta} = 0$.

As can be seen in Fig. 3.15, the correlation $(\bar{\delta}, \bar{C})$ for $L \sim 3000\text{km}$ is strong for $\theta_{13} = 8^\circ$. The correlation $(\bar{\delta}, \bar{C})$ turns out to be small for larger values of Δm_{21}^2 or for smaller value of θ_{13} (i.e., $\theta_{13} \lesssim 3^\circ$; See Fig. 3.15b), as the gradient of the ellipse in the $(\bar{\delta}, \bar{C})$ plane becomes smaller for larger values of Δm_{21}^2 . This is why strong correlations were not found in [54] where the set of parameters ($\sin^2 2\theta_{12} = 1.0$, $\Delta m_{21}^2 = 1.0 \times 10^{-4} \text{eV}^2$; $\sin^2 2\theta_{23} = 1.0$, $\Delta m_{32}^2 = 3.5(5, 7) \times 10^{-3} \text{eV}^2$) and $\sin^2 2\theta_{13} = 0.05$, $E_\mu = 30\text{GeV}$ were used. If we assume that the uncertainty in the overall normalization C is at most 5%, then the correlation $(\bar{\delta}, \bar{C})$ is not so serious, but if we assume that the uncertainty is as large as 20 % then the set of the parameters ($E_\mu \sim 50\text{GeV}$, $L \sim 3000\text{km}$) is not a good option. We will discuss this issue later.

From Figs. 3.17 – 3.21, we see that the correlations of $(\bar{\delta}, \bar{\theta}_{k\ell})$ and $(\bar{\delta}, \bar{\Delta m}_{k\ell}^2)$ are not large for $L \gtrsim 1000\text{km}$, $E_\mu \gtrsim 20\text{GeV}$. As we will show analytically later, the value of $\Delta\chi^2(\theta_{k\ell}, \Delta m_{k\ell}^2, \delta, C; \bar{\theta}_{k\ell}, \bar{\Delta m}_{k\ell}^2, \bar{\delta} = 0, \bar{C})$ increases for $E_\mu \gg 50\text{GeV}$ and $L \ll 1000\text{km}$ unless we minimize it with respect to $\theta_{k\ell}$ and $\Delta m_{k\ell}^2$, but because of strong correlations in $(\bar{\delta}, \bar{\theta}_{13})$, $(\bar{\delta}, \bar{\theta}_{23})$ and $(\bar{\delta}, \bar{\Delta m}_{32}^2)$, the value of $\Delta\chi_{\min}^2$, which is minimized with respect to $\theta_{k\ell}$ and $\Delta m_{k\ell}^2$, decreases for $E_\mu \gg 50\text{GeV}$.

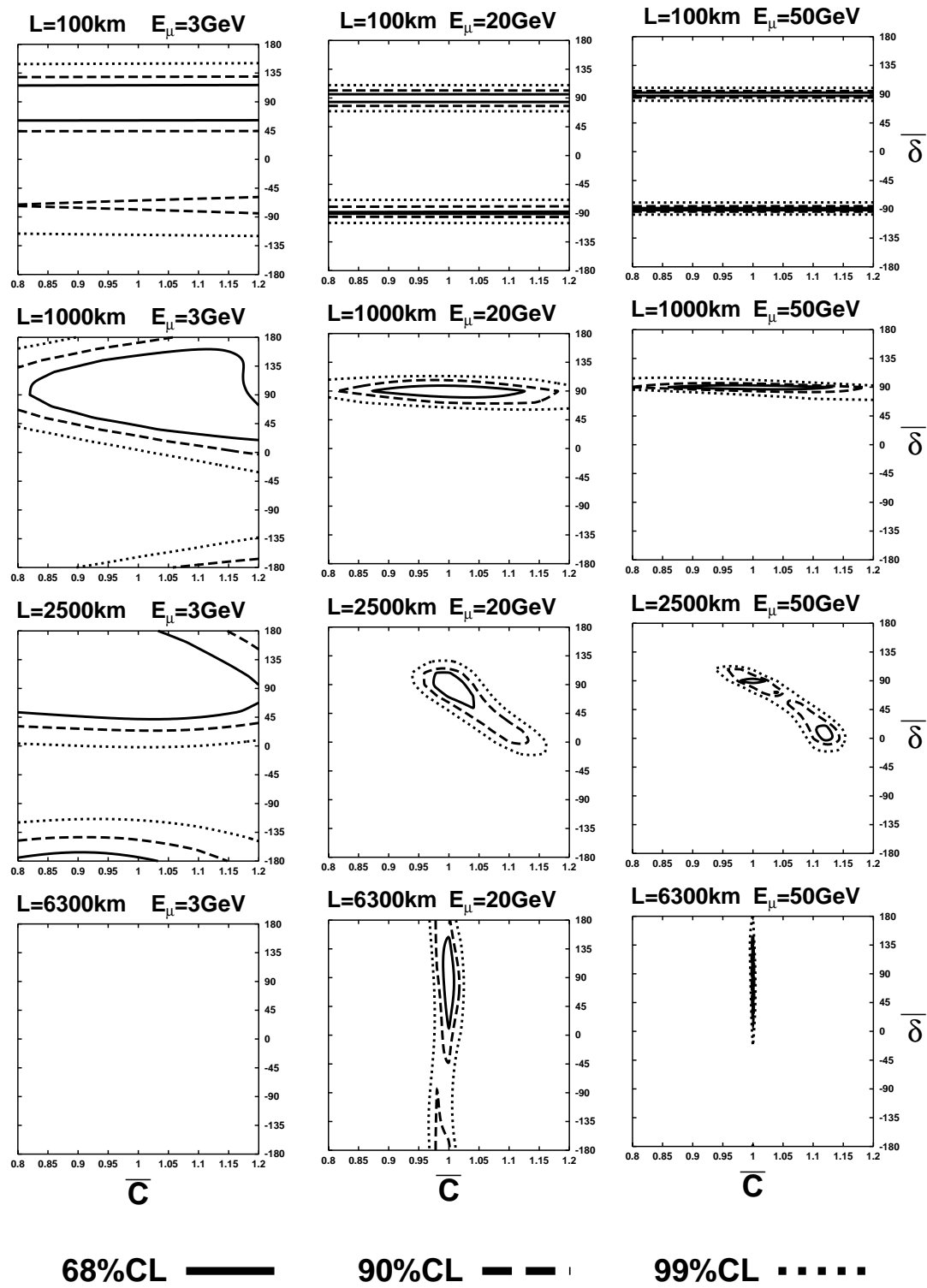
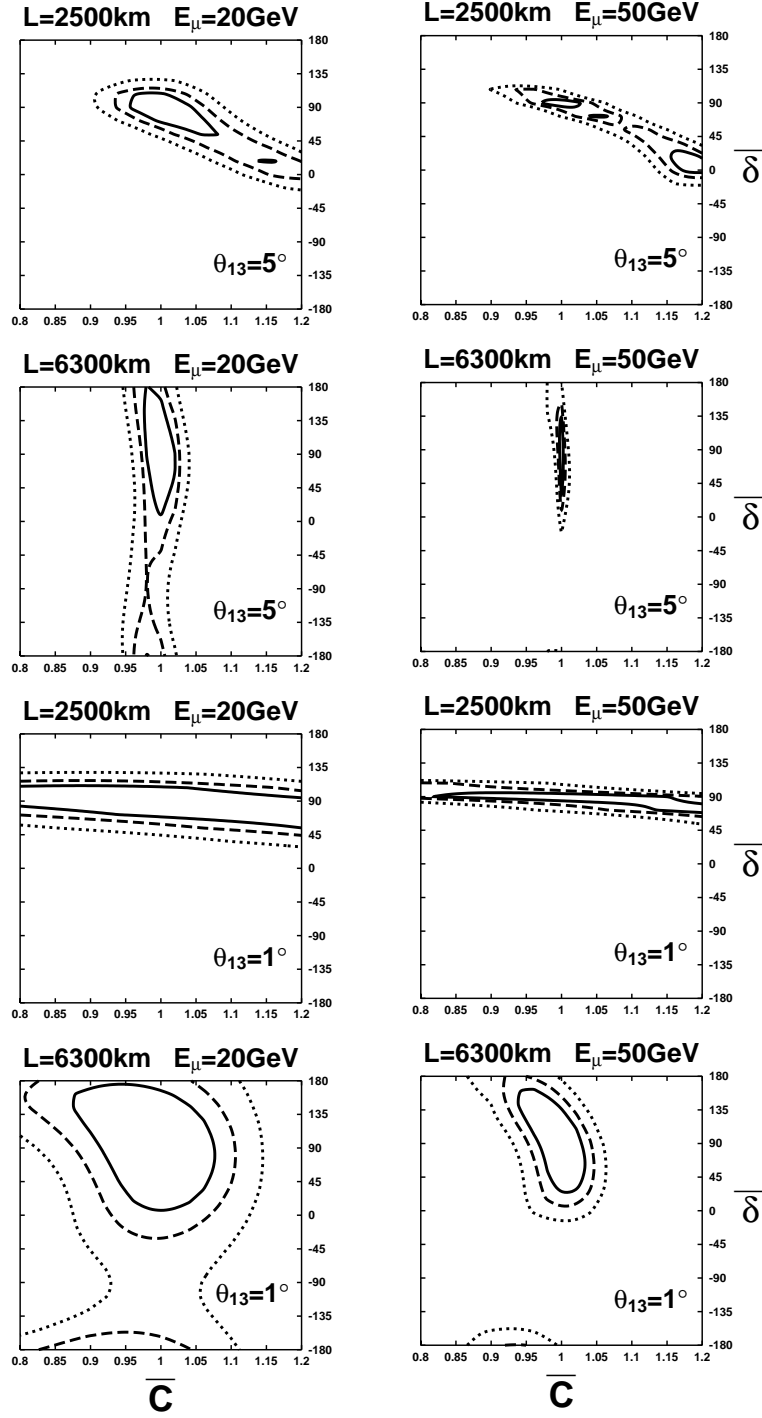


Figure 3.15: Correlations of errors of $\bar{\delta}$ and the normalization \bar{C} for $L=100\text{km}$, 1000km , 2500km , 6300km and for $E_\mu=3\text{GeV}$, 20GeV , 50GeV . $\Delta\chi^2 = 0.18, 0.37, 0.73$ corresponds to $1\sigma\text{CL}$, $90\%\text{CL}$, $99\%\text{CL}$, respectively for two degrees of freedom. The oscillation parameters are $\Delta m_{21}^2 = 1.8 \times 10^{-5}\text{eV}^2$, $\Delta m_{32}^2 = 3.5 \times 10^{-5}\text{eV}^2$, $\sin^2 2\theta_{12} = 0.76$, $\sin^2 2\theta_{23} = 1.0$, $\theta_{13} = 8^\circ$, $\delta = \pi/2$. The number of useful muon decays is $10^{21}\mu \cdot 10\text{kt}$. No backgrounds are taken into consideration in Figs. 3.15 – 3.21.



68%CL ——— 90%CL - - - 99%CL

Figure 3.16: The same correlation as Fig.1a for $\theta_{13} = 5^\circ, 1^\circ$. The oscillation parameters and other reference values are the same as in Fig. 3.15.

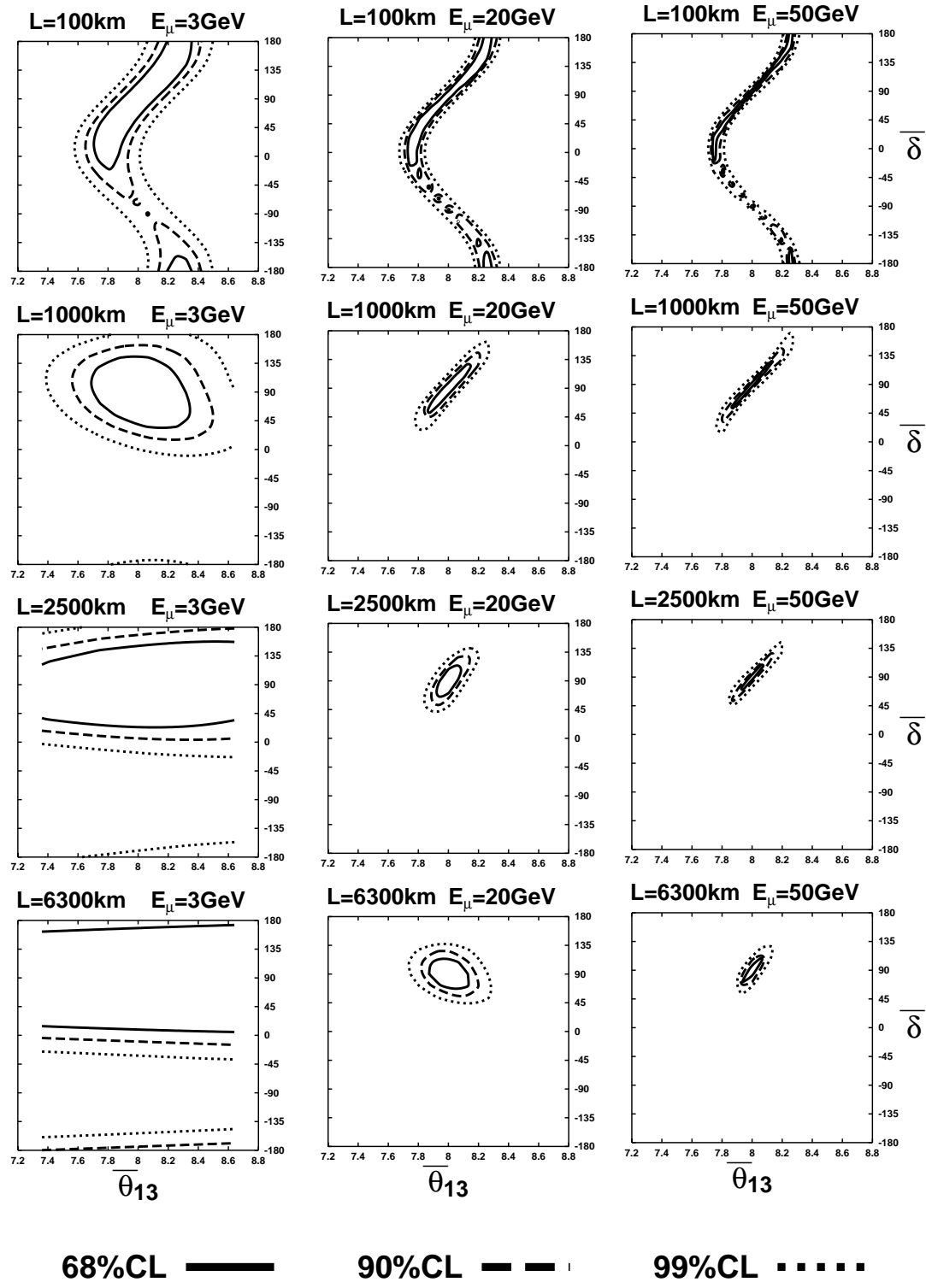


Figure 3.17: Correlations of errors of $\bar{\delta}$ and $\bar{\theta}_{13}$. The oscillation parameters and other reference values are the same as in Fig. 3.15.

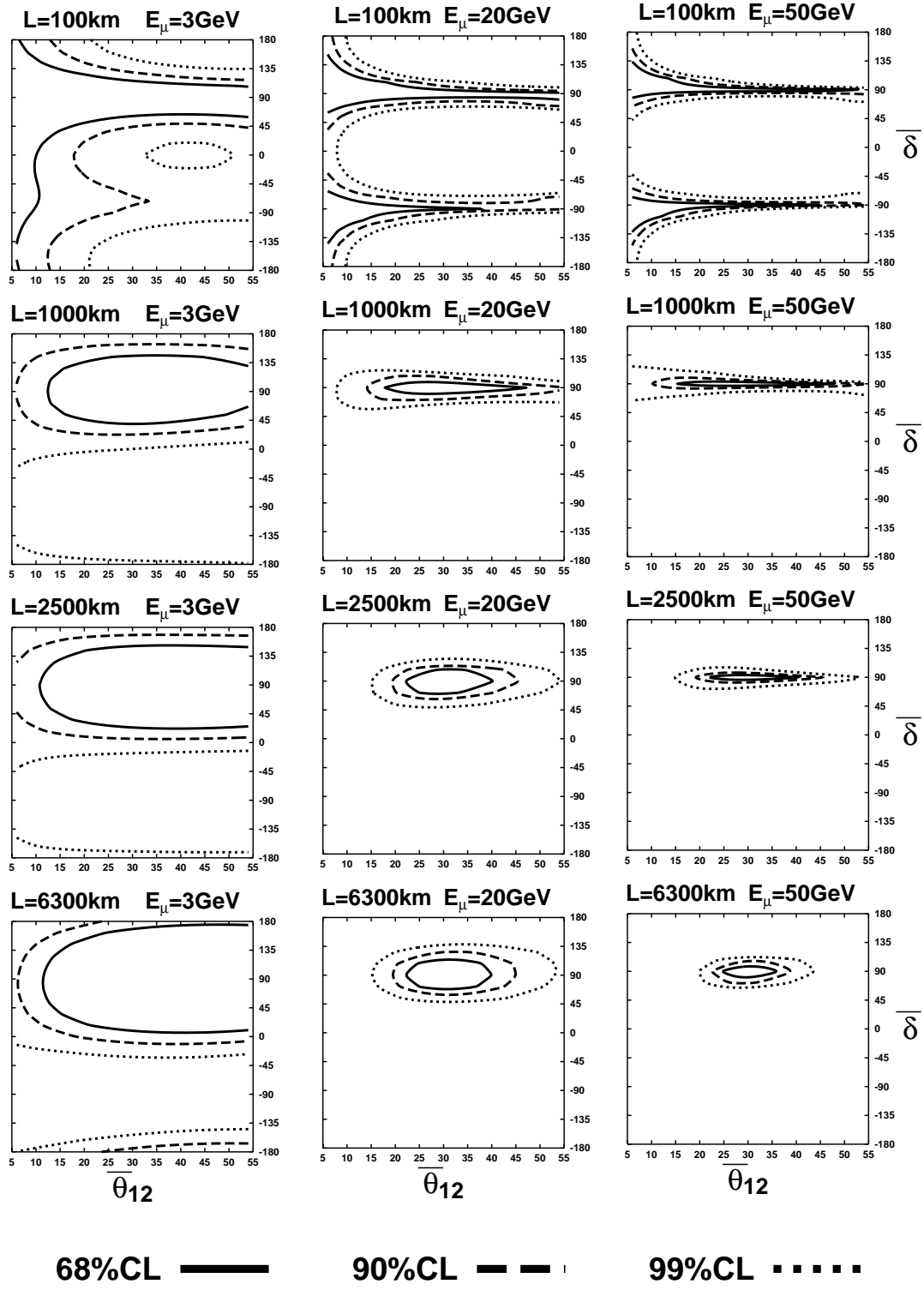


Figure 3.18: Correlations of errors of $\bar{\delta}$ and $\bar{\theta}_{12}$. The oscillation parameters and other reference values are the same as in Fig. 3.15.

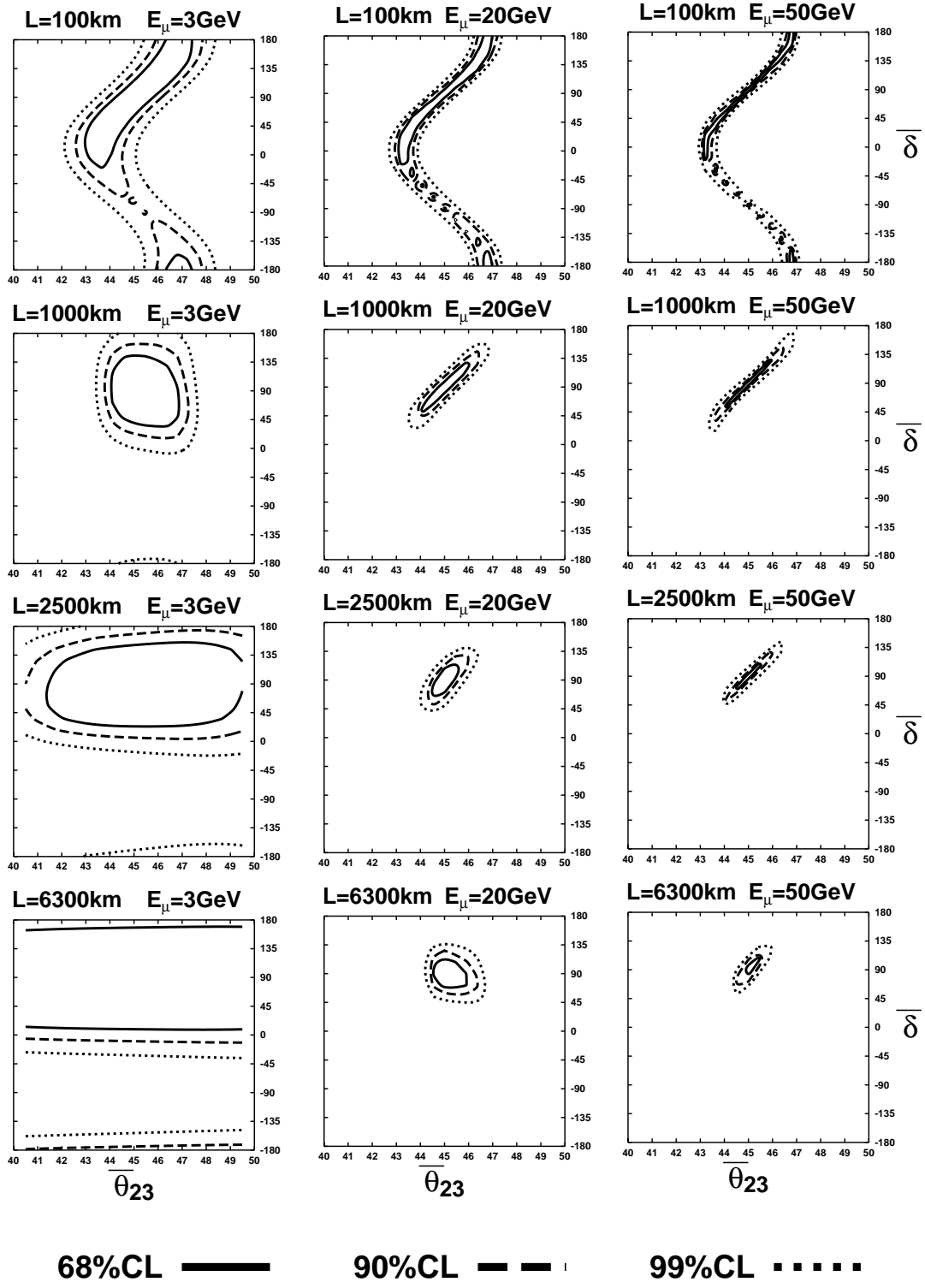


Figure 3.19: Correlations of errors of $\bar{\delta}$ and $\bar{\theta}_{23}$. The oscillation parameters and other reference values are the same as in Fig. 3.15.

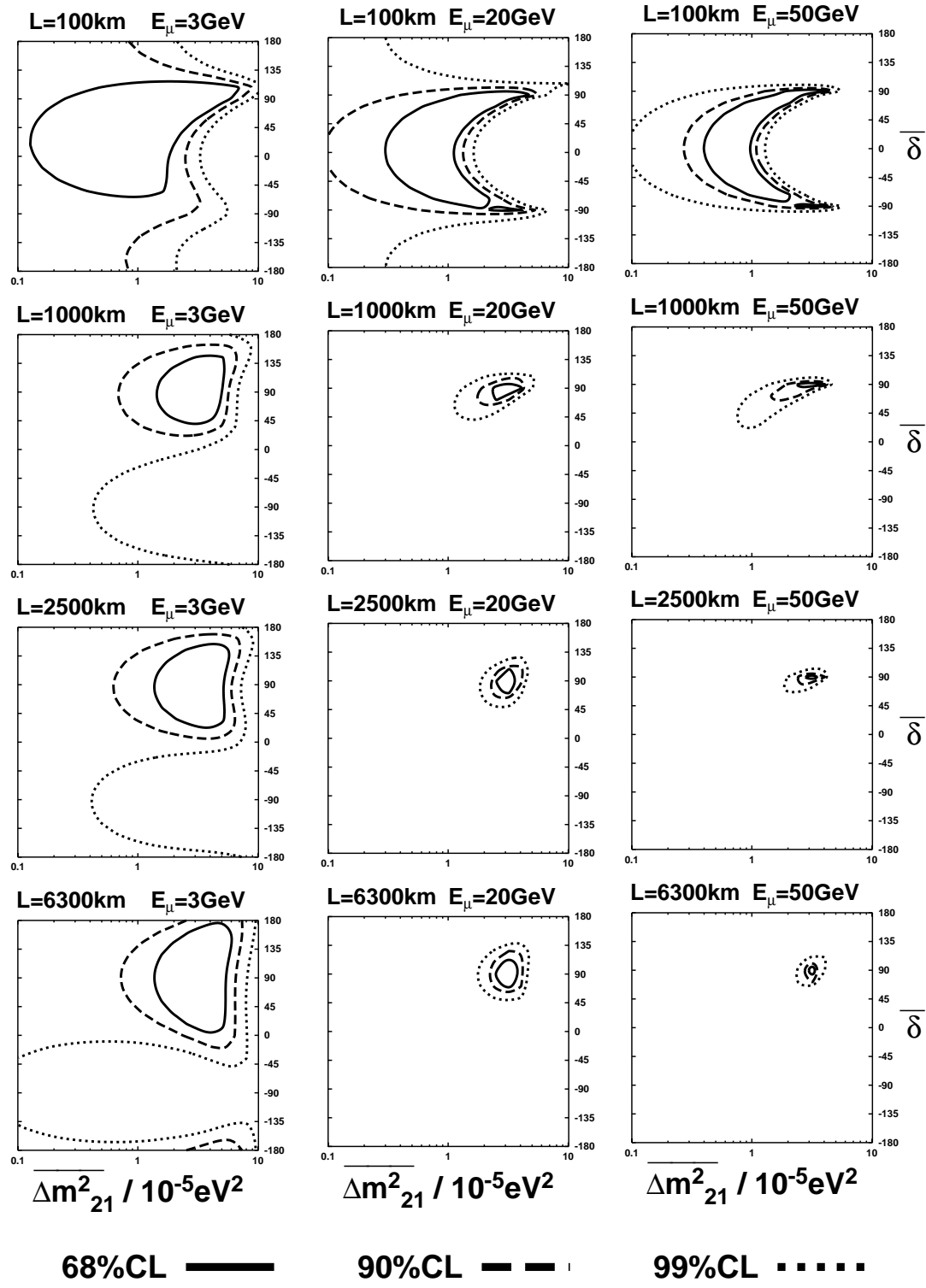


Figure 3.20: Correlations of errors of $\bar{\delta}$ and $\overline{\Delta m^2_{21}}$. The oscillation parameters and other reference values are the same as in Fig. 3.15.

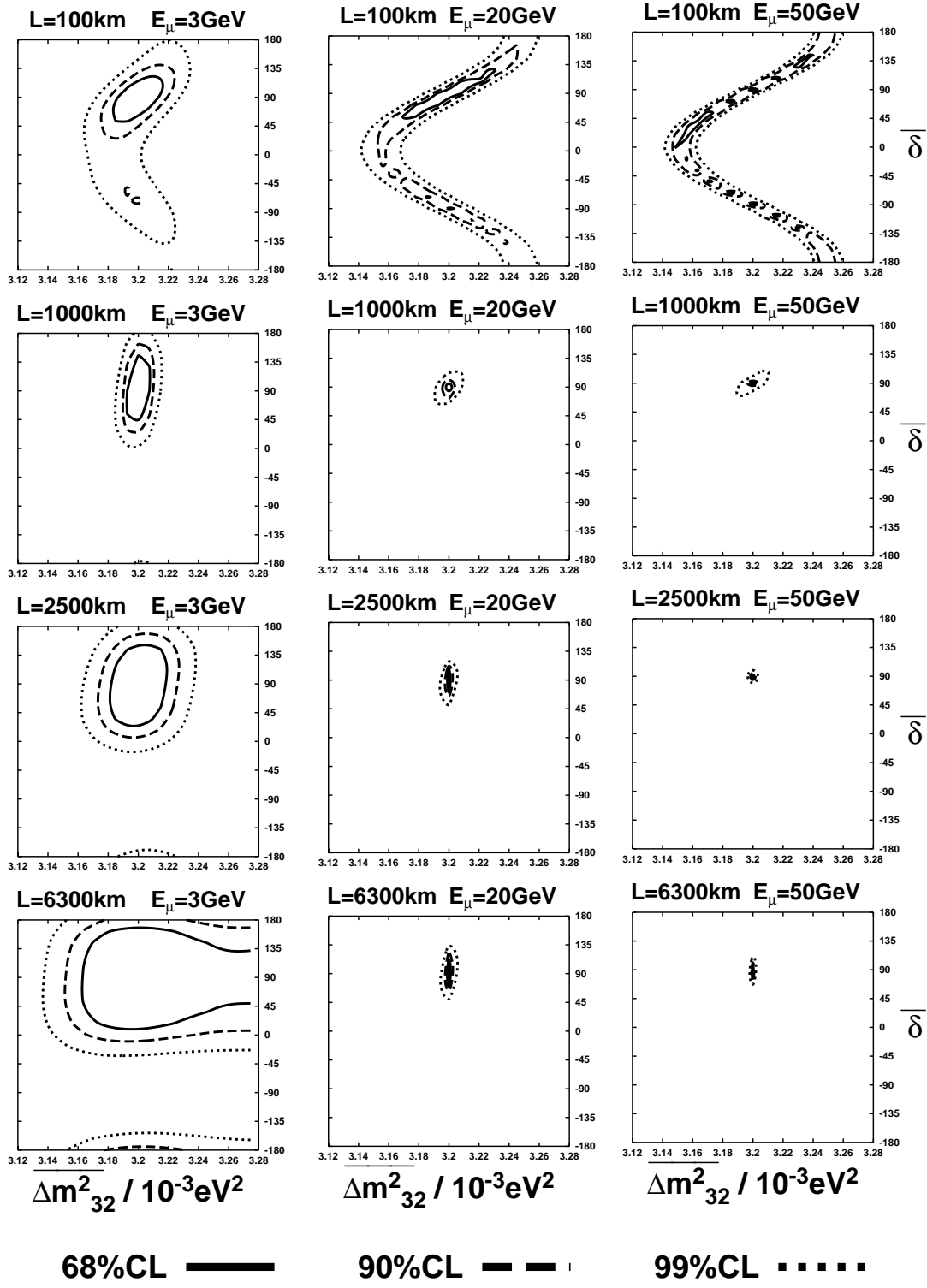


Figure 3.21: Correlations of errors of $\bar{\delta}$ and Δm_{32}^2 . The oscillation parameters and other reference values are the same as in Fig. 3.15.

3.1.5.4 Data size to reject a hypothesis with $\bar{\delta} = 0$

The quantity $\Delta\chi^2_{\min}$ can be regarded as the deviation of χ^2 from the best fit point (the best fit point in eq. (3.2) is of course $\bar{\theta}_{k\ell} = \theta_{k\ell}$, $\overline{\Delta m^2_{k\ell}} = \Delta m^2_{k\ell}$, $\bar{\delta} = \delta$ and $\bar{C} = C$ for which we have $\Delta\chi^2_{\min} = 0$) and for six degrees of freedom the value of $\Delta\chi^2_{\min}$ which corresponds to 3σ (4σ) is 20.1 (28.9). From this we can estimate the necessary data size D to reject a hypothesis $\bar{\delta} = 0$ at 3σ by dividing 20.1 by $\Delta\chi^2_{\min}$ for each value of δ . On the other hand, it is important to include the effect of the backgrounds in the analysis [89, 54, 70]. Here we assume that the fraction f_B of backgrounds to right sign muon events is given by $f_B = 10^{-3}$ or 10^{-5} and that the systematic error of backgrounds is $\sigma_B = 0.1$ as in [70] for simplicity. We also assume the number of muons $10^{21}\mu \cdot 10\text{kt}$ as a reference value. Thus $\Delta\chi^2$ is modified as

$$\begin{aligned} & \Delta\chi^2(\theta_{k\ell}, \Delta m^2_{k\ell}, \delta, C; \bar{\theta}_{k\ell}, \overline{\Delta m^2_{k\ell}}, \bar{\delta}, \bar{C}) \Big|_{f_B} \\ \equiv & \sum_j \frac{[N_j^{\text{wrong}}(\mu^-) - \bar{N}_j^{\text{wrong}}(\mu^-)]^2}{\left[\sqrt{N_j^{\text{wrong}}(\mu^-) + f_B N_j^{\text{right}}(\mu^+) + 1 + \frac{11}{9}} \right]^2 + [\sigma_B f_B N_j^{\text{right}}(\mu^+)]^2} \\ & + \sum_j \frac{[N_j^{\text{wrong}}(\mu^+) - \bar{N}_j^{\text{wrong}}(\mu^+)]^2}{\left[\sqrt{N_j^{\text{wrong}}(\mu^+) + f_B N_j^{\text{right}}(\mu^-) + 1 + \frac{11}{9}} \right]^2 + [\sigma_B f_B N_j^{\text{right}}(\mu^-)]^2} \\ & + \sum_j \frac{[N_j^{\text{right}}(\mu^-) - \bar{N}_j^{\text{right}}(\mu^-)]^2}{N_j^{\text{right}}(\mu^-)} + \sum_j \frac{[N_j^{\text{right}}(\mu^+) - \bar{N}_j^{\text{right}}(\mu^+)]^2}{N_j^{\text{right}}(\mu^+)}, \quad (3.3) \end{aligned}$$

where $\bar{N}_j^{\text{wrong}}(\mu^\pm)$, $\bar{N}_j^{\text{right}}(\mu^\pm)$ stand for $N_j^{\text{wrong}}(\mu^\pm)$, $N_j^{\text{right}}(\mu^\pm)$ with arguments $\bar{\theta}_{k\ell}$, $\overline{\Delta m^2_{k\ell}}$, $\bar{\delta}$, \bar{C} , respectively, and the corrections in the statistical errors are due to the Poisson statistical [70]. Then we minimize $\Delta\chi^2$ with respect $\bar{\theta}_{k\ell}$, $\overline{\Delta m^2_{k\ell}}$ and \bar{C} :

$$\Delta\chi^2_{\min} \Big|_{f_B} \equiv \min_{\bar{\theta}_{k\ell}, \overline{\Delta m^2_{k\ell}}, \bar{C}} \Delta\chi^2(\theta_{k\ell}, \Delta m^2_{k\ell}, \delta, C; \bar{\theta}_{k\ell}, \overline{\Delta m^2_{k\ell}}, \bar{\delta} = 0, \bar{C}) \Big|_{f_B}, \quad (3.4)$$

where the values of oscillation parameters we use in (3.4) are the best fit values in the analyses of the solar and atmospheric neutrinos [42] as in Figs. 3.15 – 3.21, and we take $\theta_{13} = 1^\circ, 5^\circ, 8^\circ$ and $\delta = \pi/2$ as a reference value. In varying the overall normalization C we assume $0.95 \leq C \leq 1.05$. We will mention the results for $|\Delta C| \leq 0.1$ and for $|\Delta C| \leq 0.2$ later. For other oscillation parameters, we vary $(\theta_{12}, \Delta m^2_{21})$ and $(\theta_{23}, \Delta m^2_{32})$ within the allowed region at 90%CL of the solar and the atmospheric neutrino data, i.e.,

$25^\circ \leq \theta_{12} \leq 41^\circ$, $35^\circ \leq \theta_{23} \leq 55^\circ$, $1.5 \times 10^{-5} \text{eV}^2 \leq \Delta m_{21}^2 \leq 2.2 \times 10^{-4} \text{eV}^2$, $1.6 \times 10^{-3} \text{eV}^2 \leq \Delta m_{32}^2 \leq 4 \times 10^{-3} \text{eV}^2$. It should be emphasized that in minimizing $\Delta\chi^2$ in (3.4) all the six parameters are varied at the same time, unlike in Figs. 3.15 – 3.21 which are obtained by varying only one of $\bar{\theta}_{k\ell}$, $\Delta m_{k\ell}^2$, \bar{C} .

The result is given in Fig. 3.22 for a neutrino factory with $0.5 \text{GeV} \leq E_\mu \leq 50 \text{GeV}$, $10 \text{km} \leq L \leq 10000 \text{km}$ and for three values of $\theta_{13} = 1^\circ, 5^\circ, 8^\circ$ and two different values of the background fraction $f_B = 10^{-5}, 10^{-3}$. The behavior of the figures change a little depending on the value of θ_{13} . For $f_B = 10^{-3}$, the sensitivity to CP violation, i.e., the ability to reject a hypothesis with $\bar{\delta} = 0$ is *not* optimized by the set of parameters $(E_\mu, L) \simeq (50 \text{GeV}, 3000 \text{km})$, which has been advocated as the best choice, but rather by $(E_\mu, L) \simeq (20 \text{GeV}, 2000 \text{km})$. This is because with a nonnegligible fraction f_B the contribution of the systematic uncertainty $\sigma_B f_B N_j^{\text{right}}$ to the total error becomes so large for high energy such as $E_\mu \sim 50 \text{GeV}$ and sensitivity to CP violation is lost. For $f_B = 10^{-5}$ and $\theta_{13} = 1^\circ$, on the other hand, the contribution of $\sigma_B f_B N_j^{\text{right}}$ is not so large and the sensitivity is optimized by $(E_\mu, L) \simeq (50 \text{GeV}, 3000 \text{km})$. We note in passing that we have also optimized the sensitivity with respect to the number of energy bins but the conclusion does not depend very much on the number of energy bins. This result disagrees with the claim in [56].

We have also evaluated the data size assuming a larger uncertainty of the matter effect, i.e., $|\Delta C| \leq 0.1$ and $|\Delta C| \leq 0.2$. The results for $\theta_{13} = 8^\circ$ are shown in Fig. 3.23. If we have to assume an uncertainty of the matter effect which is as large as 20%, then the optimum baseline and muon energy become even smaller than the results with $|\Delta C| \leq 0.05$. The situation is less serious for smaller value of θ_{13} , i.e., $\theta_{13} \lesssim 3^\circ$, for which the correlation $(\bar{\delta}, \bar{C})$ is not so strong. It should be noted that we have assumed in our analysis that the detection efficiency does not decrease down to the neutrino energy $E_\nu \sim$ a few GeV, so if this assumption is not satisfied then the optimum muon energy may not be as low as Fig. 3.23 indicates.

In Figs. 3.22 and 3.23 we have taken $\delta = \pi/2$ as a reference value. It is possible to do the same analysis for a value of δ other than $\pi/2$. The results for $\theta_{13} = 8^\circ, 5^\circ$ and 1° are given in Fig. 3.24 for three sets of the parameters $(E_\mu = 50 \text{GeV}, L = 3000 \text{km})$, $(E_\mu = 20 \text{GeV}, L = 1000 \text{km})$ and $(E_\mu = 20 \text{GeV}, L = 2000 \text{km})$. We observe that $(E_\mu = 50 \text{GeV}, L = 3000 \text{km})$ is better than $(E_\mu = 20 \text{GeV}, L = 1000 \text{km})$ for smaller values of θ_{13} , but for larger values of θ_{13} $(E_\mu = 20 \text{GeV}, L = 1000 \text{km})$ can be more advantageous than the other. It should be emphasized that in all cases in Fig. 3.24 we can distinguish the case of $\delta = \pi$ from that of $\delta = 0$, since the necessary data size to reject $\bar{\delta} = 0$ is finite even for $\delta = \pi$. This is because there are both contributions from $\sin \delta$ and $\cos \delta$ for the muon energy $E_\mu \lesssim 50 \text{GeV}$. As we will see in section 4, for extremely high energy $E_\mu \gg 50 \text{GeV}$ we can show analytically that our

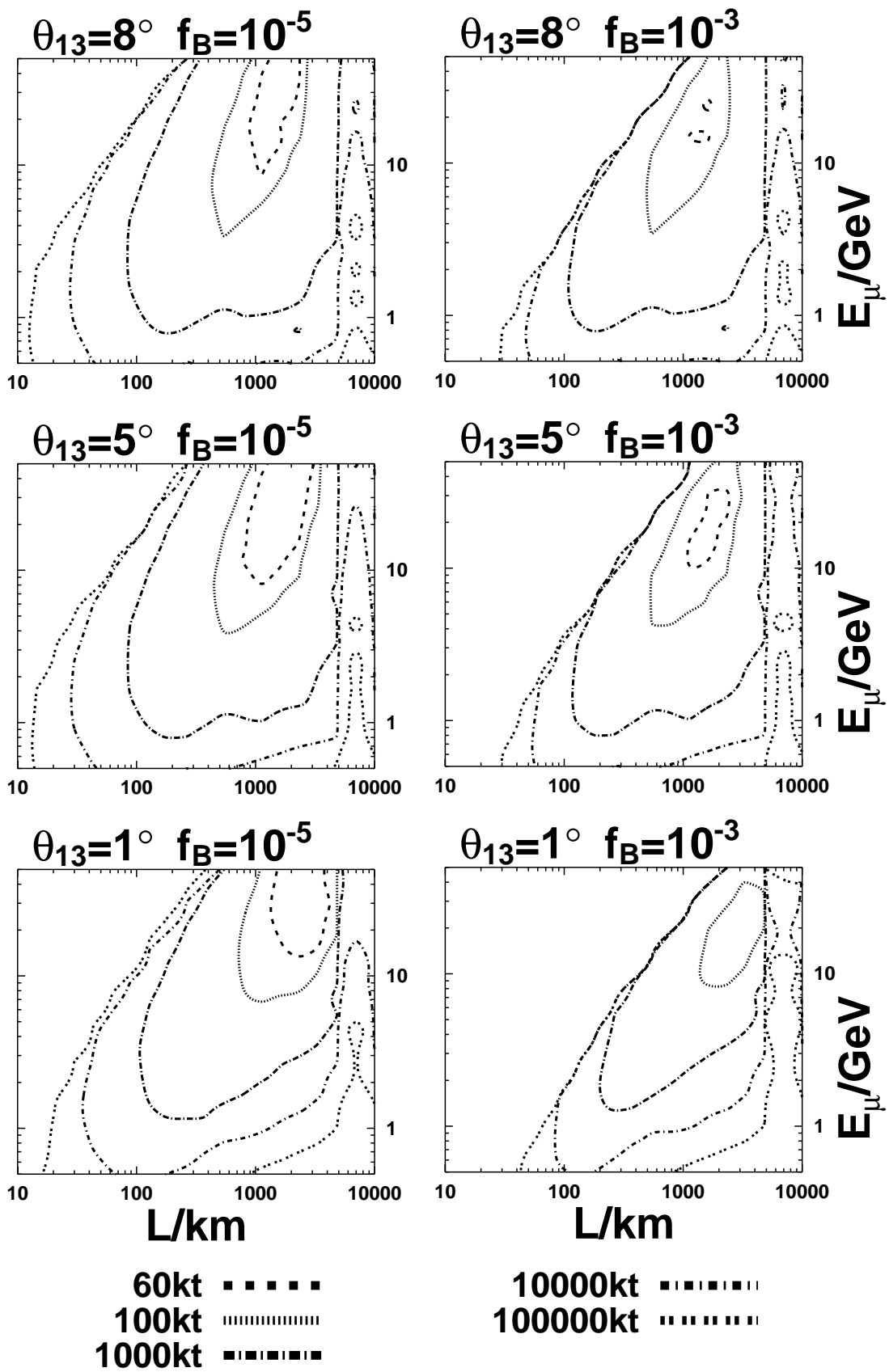


Figure 3.22: The contour plot of equi-number of data size required (in the unit of kt) to reject a hypothesis $\bar{\delta} = 0$ at 3σ using $\Delta\chi^2(\text{CPV})$ (3.4) in the case of a neutrino factory with 10^{21} useful muon decays, the background fraction $f_B = 10^{-5}$ or 10^{-3} , $\theta_{13} = 8^\circ, 5^\circ, 1^\circ$. The other oscillation parameters are the same as in Fig. 3.15.

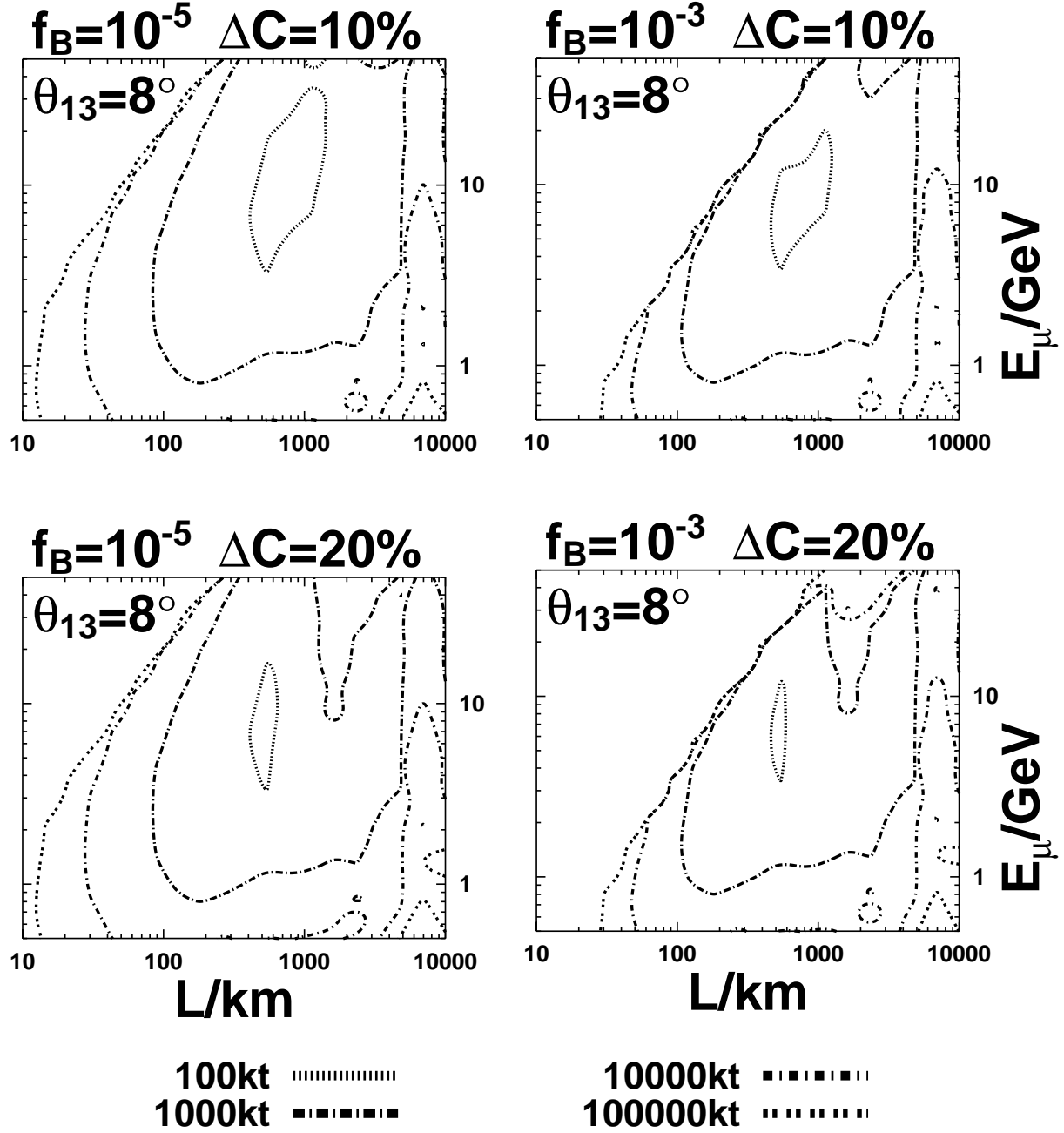


Figure 3.23: The same as Fig. 3.22 with $\theta_{13} = 8^\circ$, except that the uncertainty of the matter effect is assumed to be larger $|\Delta C| \leq 0.1$ or $|\Delta C| \leq 0.2$.

$\Delta\chi^2(\text{CPV})$ becomes proportional to $\sin^2 \delta$ and distinction between $\delta = \pi$ and $\delta = 0$ is no longer possible.

3.1.5.5 Low and high energy behaviors of $\Delta\chi^2$

In this subsection we will show analytically that the sensitivity to CP and T violation decreases as $E_\mu \rightarrow \text{small}$ ($E_\mu \ll 10\text{GeV}$) or $E_\mu \rightarrow \text{large}$ ($E_\mu \gg 50\text{GeV}$). Throughout this section we assume $\sin^2 2\theta_{13} \gtrsim 10^{-3}$ ($\theta_{13} \gtrsim 1^\circ$) so that we are always in the atmospheric regime in the language of [59], i.e., $\sin^2 2\theta_{13}/\sin^2 2\theta_{12} \gg (\Delta m_{21}^2/\Delta m_{31}^2)^2$. In this subsection we will ignore the effects of backgrounds and systematic errors for simplicity.

To examine significance of CP/T violation analytically, we introduce the following simplified quantities:

$$\begin{aligned}\Delta\chi^2(\text{CPV}) &\equiv \min_{\bar{\theta}_{k\ell}, \Delta m_{k\ell}^2, \bar{C}} \Delta\chi^2(\theta_{k\ell}, \Delta m_{k\ell}^2, \delta, C; \bar{\theta}_{k\ell}, \overline{\Delta m_{k\ell}^2}, \bar{\delta} = 0, \bar{C}), \\ \Delta\chi^2(\text{TV}) &\equiv \frac{[\langle P(\nu_e \rightarrow \nu_\mu; \delta) \rangle - \langle P(\nu_\mu \rightarrow \nu_e; \delta) \rangle]^2}{\langle P(\nu_e \rightarrow \nu_\mu; \delta) \rangle},\end{aligned}$$

where

$$\begin{aligned}&\Delta\chi^2(\theta_{k\ell}, \Delta m_{k\ell}^2, \delta, C; \bar{\theta}_{k\ell}, \overline{\Delta m_{k\ell}^2}, \bar{\delta}, \bar{C}) \\ &= \frac{[\langle P(\nu_e \rightarrow \nu_\mu; \theta_{k\ell}, \Delta m_{k\ell}^2, \delta, C) \rangle - \langle P(\nu_e \rightarrow \nu_\mu; \bar{\theta}_{k\ell}, \overline{\Delta m_{k\ell}^2}, \bar{\delta}, \bar{C}) \rangle]^2}{\langle P(\nu_e \rightarrow \nu_\mu; \delta) \rangle}\end{aligned}$$

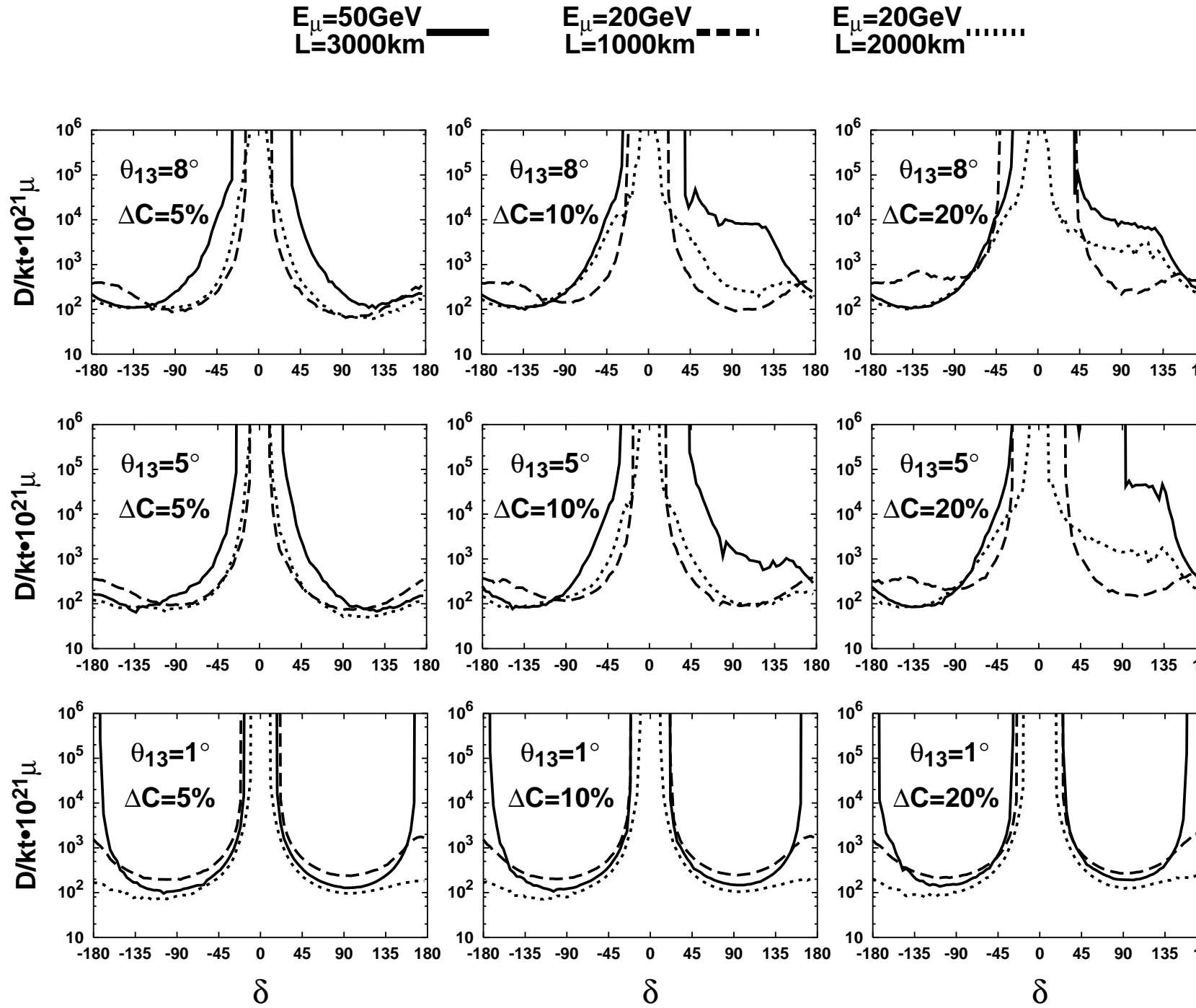
is defined as in (3.2),

$$\begin{aligned}&\langle P(\nu_\alpha \rightarrow \nu_\beta; \delta) \rangle \\ &\equiv \frac{12N_0 E_\mu^2}{\pi L^2 m_\mu^2} \int d\left(\frac{E_\nu}{E_\mu}\right) \left(\frac{E_\nu}{E_\mu}\right)^2 \left(1 - \frac{E_\nu}{E_\mu}\right) \sigma_{\nu N}(E_\nu) P(\nu_\alpha \rightarrow \nu_\beta; \delta) \quad (3.5)\end{aligned}$$

are the number of events $((\alpha, \beta) = (e, \mu) \text{ or } (\mu, e); \text{ in the case of } (\alpha, \beta) = (\mu, e) \text{ we assume perfect polarization as in the previous section so that the number of events is given by the same definition (3.5)})$ and we have ignored effects of the backgrounds and systematic errors and correlations of errors for simplicity in this section. Also we will assume that the cross section is proportional to the neutrino energy E_ν for any E_ν , i.e., $\sigma = \sigma_0 E_\nu$. Strictly speaking this assumption is not accurate, but it is known [66] that $0 < \sigma < \sigma_0 E_\nu$ is satisfied for low energy $E_\nu \ll 1\text{GeV}$, so our approximation is sufficient to give an upper bound on the value of $\Delta\chi^2$ for low energy.

Let us first look at the low energy limit ($E_\nu \ll 10\text{GeV}$). In this case matter effects are negligible and the probability can be replaced by that in

Figure 3.24: The number of data size required to reject a hypothesis $\bar{\delta} = 0$ at 3σ for a neutrino factory using $\Delta\chi^2(\text{CPV})$ (3.4) as a function of the true value of δ for $f_B = 10^{-3}$. All the assumptions except for δ are the same as in Fig. 3.22. The situation is improved for smaller θ_{13} .



vacuum. Thus we have

$$P(\nu_e \rightarrow \nu_\mu; \delta) \simeq s_{23}^2 \sin^2 2\theta_{13} \sin\left(\frac{\Delta E_{31} L}{2}\right) + c_{23}^2 \sin^2 2\theta_{12} \sin\left(\frac{\Delta E_{21} L}{2}\right) \\ + 8\tilde{J} \sin\left(\frac{\Delta E_{21} L}{2}\right) \sin\left(\frac{\Delta E_{31} L}{2}\right) \cos\left(\delta + \frac{\Delta E_{31} L}{2}\right)$$

to the second order in $\mathcal{O}(\theta_{13})$ and $\mathcal{O}(\Delta E_{21}/\Delta E_{31})$, where

$$\tilde{J} \equiv \frac{c_{13}}{8} \sin 2\theta_{12} \sin 2\theta_{13} \sin 2\theta_{23},$$

and $\Delta E_{jk} \equiv \Delta m_{jk}^2/2E \equiv (m_j^2 - m_k^2)/2E$. The number of events are given by

$$\begin{aligned} & \langle P(\nu_e \rightarrow \nu_\mu; \delta) \rangle - \langle P(\nu_e \rightarrow \nu_\mu; \delta = 0) \rangle \\ &= \frac{96N_0 E_\mu^3 \sigma_0 \tilde{J}}{\pi L^2 m_\mu^2} \int dx x^3 (1-x) \sin\left(\frac{\Delta m_{21}^2 L}{4x E_\mu}\right) \\ &\times \sin\left(\frac{\Delta m_{31}^2 L}{4x E_\mu}\right) \left[\cos\left(\delta + \frac{\Delta m_{31}^2 L}{4x E_\mu}\right) - \cos\left(\frac{\Delta m_{31}^2 L}{4x E_\mu}\right) \right] \end{aligned} \quad (3.6)$$

$$\begin{aligned} & \langle P(\nu_e \rightarrow \nu_\mu; \delta) \rangle - \langle P(\nu_\mu \rightarrow \nu_e; \delta) \rangle \\ &= \frac{192N_0 E_\mu^3 \sigma_0 \tilde{J} \sin \delta}{\pi L^2 m_\mu^2} \int dx x^3 (1-x) \\ &\times \sin\left(\frac{\Delta m_{21}^2 L}{4x E_\mu}\right) \sin\left(\frac{\Delta m_{31}^2 L}{4x E_\mu}\right) \sin\left(\frac{\Delta m_{32}^2 L}{4x E_\mu}\right) \end{aligned} \quad (3.7)$$

$$\begin{aligned} & \langle P(\nu_e \rightarrow \nu_\mu; \delta) \rangle \\ &\simeq \frac{12s_{23}^2 \sin^2 2\theta_{13} E_\mu^3 \sigma_0}{\pi L^2 m_\mu^2} \int dx x^3 (1-x) \sin^2\left(\frac{\Delta m_{31}^2 L}{4x E_\mu}\right), \end{aligned} \quad (3.8)$$

where $x \equiv E_\nu/E_\mu$, we have assumed conditions for the atmospheric regime $\sin^2 2\theta_{13}/\sin^2 2\theta_{12} \gg (\Delta m_{21}^2/\Delta m_{21}^2)^2$, and we have put $\bar{\theta}_{k\ell} = \theta_{k\ell}$, $\overline{\Delta m_{k\ell}^2} = \Delta m_{k\ell}^2$, $\bar{C} = C$ in (3.6) instead of optimizing $\langle P(\nu_e \rightarrow \nu_\mu; \delta) \rangle - \langle P(\nu_e \rightarrow \nu_\mu; \delta = 0) \rangle$ with respect to these variables, as that is sufficient to demonstrate that $\Delta\chi^2(\text{CPV})$ decreases as $E_\mu \rightarrow 0$. If we keep L/E_μ fixed while $L, E_\mu \rightarrow 0$, then all the quantities (3.6), (3.7) and (3.8) behave as $\mathcal{O}(E_\mu)$, so $\Delta\chi^2(\text{CPV}) \propto E_\mu$ and $\Delta\chi^2(\text{TV}) \propto E_\mu$ as $E_\mu \rightarrow 0$ with L/E_μ fixed. Thus sensitivity to CP/T violation is asymptotically lost as $E_\mu \rightarrow 0$. This is consistent with our numerical results in previous sections.

Next let us discuss the behavior of $\Delta\chi^2$ in the high energy limit ($E_\mu \gg 50\text{GeV}$). In this case we have to take into account the matter effect and we use the probability which has been obtained in [89] to second order in $\mathcal{O}(\theta_{13})$, $\mathcal{O}(\Delta E_{21}/\Delta E_{31})$, $\mathcal{O}(\Delta E_{21}/A)$ and $\mathcal{O}(\Delta E_{21}L)$:

$$P(\nu_e \rightarrow \nu_\mu; \delta) \simeq s_{23}^2 \sin^2 2\theta_{13} \left(\frac{\Delta E_{31}}{B}\right)^2 \sin^2\left(\frac{BL}{2}\right)$$

$$\begin{aligned}
& + c_{23}^2 \sin^2 2\theta_{12} \left(\frac{\Delta E_{21}}{A} \right)^2 \sin^2 \left(\frac{AL}{2} \right) \\
& + 8\tilde{J} \frac{\Delta E_{21}}{A} \frac{\Delta E_{31}}{B} \sin \left(\frac{AL}{2} \right) \sin \left(\frac{BL}{2} \right) \cos \left(\delta + \frac{\Delta E_{31}L}{2} \right).
\end{aligned} \tag{3.9}$$

Since we assume $\sin^2 2\theta_{13}/\sin^2 2\theta_{12} \gg (\Delta m_{21}^2/\Delta m_{21}^2)^2 = (\Delta E_{21}/\Delta E_{31})^2$ here, we can ignore the second term in (3.9).

It is straightforward to get the following high energy limit of $\Delta\chi^2(\text{TV})$. Using (3.9) we have

$$\begin{aligned}
P(\nu_e \rightarrow \nu_\mu; \delta) - P(\nu_\mu \rightarrow \nu_e; \delta) &= P(\nu_e \rightarrow \nu_\mu; \delta) - P(\nu_e \rightarrow \nu_\mu; -\delta) \\
&\simeq -2\tilde{J} \frac{\Delta m_{21}^2 (\Delta m_{31}^2)^2}{E_\nu^3} \frac{L}{A^2} \sin^2 \left(\frac{AL}{2} \right),
\end{aligned}$$

where we have expanded $\sin(\Delta E_{21}L/2) \simeq \Delta E_{21}L/2$ and have used the fact $B = [(\Delta E_{31} \cos 2\theta_{13} - A)^2 + (\Delta E_{31} \sin 2\theta_{13})^2]^{1/2} \simeq A$ as $E_\nu \rightarrow \text{large}$. Therefore the number of events is given by

$$\begin{aligned}
& \langle P(\nu_e \rightarrow \nu_\mu; \delta) \rangle - \langle P(\nu_\mu \rightarrow \nu_e; \delta) \rangle \\
& \simeq \frac{24N_0\sigma_0\tilde{J} \sin \delta \Delta m_{21}^2 (\Delta m_{31}^2)^2}{\pi m_\mu^2} \frac{1}{A^2 L} \sin^2 \left(\frac{AL}{2} \right) \int dx (1-x) \\
& = \frac{12N_0\sigma_0\tilde{J} \sin \delta \Delta m_{21}^2 (\Delta m_{31}^2)^2}{\pi m_\mu^2} \frac{1}{A^2 L} \sin^2 \left(\frac{AL}{2} \right), \\
& \langle P(\nu_e \rightarrow \nu_\mu; \delta) \rangle \\
& \simeq \frac{3N_0\sigma_0 s_{23}^2 \sin^2 2\theta_{13}}{\pi m_\mu^2} \frac{E_\mu}{A^2 L^2} \sin^2 \left(\frac{AL}{2} \right) \int dx x(1-x) \\
& = \frac{N_0\sigma_0 s_{23}^2 \sin^2 2\theta_{13}}{2\pi m_\mu^2} \frac{E_\mu}{A^2 L^2} \sin^2 \left(\frac{AL}{2} \right).
\end{aligned}$$

Hence we have the behaviors

$$\begin{aligned}
\Delta\chi^2(\text{TV}) &\simeq \frac{N_0\sigma_0}{\pi m_\mu^2} \frac{288 \sin^2 \delta \tilde{J}^2 (\Delta m_{21}^2)^2 (\Delta m_{31}^2)^4}{s_{23}^2 \sin^2 2\theta_{13}} \frac{1}{E_\mu A^2} \sin^2 \left(\frac{AL}{2} \right) \tag{3.10} \\
&\text{as } E_\mu \rightarrow \text{large}.
\end{aligned}$$

(3.10) indicates that the sensitivity to T violation decreases as E_μ becomes very large. Also for a fixed large E_μ , $\Delta\chi^2(\text{TV})$ is optimized for $L \sim \pi/A \sim 3 \times 2000\text{km}/(\rho/2.7\text{g}\cdot\text{cm}^{-3}) \sim 5000\text{km}$. From numerical calculations we see that $\Delta\chi^2(\text{TV})$ is optimized for $(L, E_\mu) \sim (3000\text{km}, 50\text{GeV})$ (see Fig. 3.15), so our analytic treatment is consistent with numerical calculations qualitatively.

The behavior of $\Delta\chi^2(\text{CPV})$ is a little more complicated, as we have to optimize $\Delta\chi^2$ with respect to $\bar{\theta}_{k\ell}$, $\overline{\Delta m_{k\ell}^2}$, \bar{C} . If we put $\bar{\theta}_{k\ell} = \theta_{k\ell}$, $\overline{\Delta m_{k\ell}^2} =$

$\Delta m_{k\ell}^2$, $\bar{C} = C$ as we did in (3.6), we have

$$\begin{aligned}
& P(\nu_e \rightarrow \nu_\mu; \delta) - P(\nu_e \rightarrow \nu_\mu; \delta = 0) \\
& \simeq 2\tilde{J}(\cos \delta - 1) \frac{\Delta m_{21}^2 \Delta m_{31}^2}{E_\nu^2} \frac{1}{A^2} \sin^2 \left(\frac{AL}{2} \right), \\
& \langle P(\nu_e \rightarrow \nu_\mu; \delta) \rangle - \langle P(\nu_e \rightarrow \nu_\mu; \delta = 0) \rangle \\
& = \frac{4N_0\sigma_0\tilde{J}(\cos \delta - 1)\Delta m_{21}^2\Delta m_{31}^2}{\pi m_\mu^2} \frac{E_\mu}{A^2 L^2} \sin^2 \left(\frac{AL}{2} \right),
\end{aligned}$$

so that we naively have the following behavior

$$\Delta\chi^2(\text{naive CPV}) \simeq \frac{N_0\sigma_0}{\pi m_\mu^2} \frac{32(\cos \delta - 1)^2 \tilde{J}^2 (\Delta m_{21}^2)^2 (\Delta m_{31}^2)^2}{s_{23}^2 \sin^2 2\theta_{13}} \frac{E_\mu}{A^2 L^2} \sin^2 \left(\frac{AL}{2} \right). \quad (3.11)$$

It turns out that it is sufficient to consider the correlation of two variables $(\bar{\delta}, \bar{X})$, where X is $\theta_{k\ell}$, $\Delta m_{k\ell}^2$ or C , to demonstrate $\Delta\chi^2(\text{CPV}) \propto 1/E_\mu$. Except for the correlations $(\bar{\delta}, \bar{\theta}_{12})$ and $(\bar{\delta}, \bar{\Delta m_{21}^2})$, we can ignore terms of order $\mathcal{O}((\Delta E_{21}/\Delta E_{31})^2)$. From the assumption $\sin^2 2\theta_{13}/\sin^2 2\theta_{12} \gg (\Delta m_{21}^2/\Delta m_{31}^2)^2$, (3.9) is approximately given by

$$\begin{aligned}
P(\nu_e \rightarrow \nu_\mu; \delta) & \simeq \left[s_{23} \sin 2\theta_{13} \frac{\Delta E_{31}}{A} \sin \left(\frac{AL}{2} \right) \right. \\
& \quad \left. + \frac{4\tilde{J}}{s_{23} \sin 2\theta_{13}} \frac{\Delta E_{21}}{A} \sin \left(\frac{AL}{2} \right) \cos \left(\delta + \frac{\Delta E_{31}L}{2} \right) \right]^2,
\end{aligned}$$

where we have used $A - \Delta E_{31} \simeq A$ for $E_\nu \rightarrow \text{large}$, and we have ignored terms of order $\mathcal{O}((\Delta E_{21}/\Delta E_{31})^2)$. In the case of the two variable correlation $(\bar{\delta}, \bar{\theta}_{13})$, to minimize the square of

$$\begin{aligned}
& P(\nu_e \rightarrow \nu_\mu; \theta_{13}, \delta) - P(\nu_e \rightarrow \nu_\mu; \bar{\theta}_{13}, \bar{\delta}) \\
& \simeq \left[s_{23} \sin 2\theta_{13} \frac{\Delta E_{31}}{A} \sin \left(\frac{AL}{2} \right) + \frac{4\tilde{J}}{s_{23} \sin 2\theta_{13}} \frac{\Delta E_{21}}{A} \sin \left(\frac{AL}{2} \right) \cos \left(\delta + \frac{\Delta E_{31}L}{2} \right) \right]^2 \\
& - \left[s_{23} \sin 2\bar{\theta}_{13} \frac{\Delta E_{31}}{A} \sin \left(\frac{AL}{2} \right) + \frac{4\tilde{J}}{s_{23} \sin 2\bar{\theta}_{13}} \frac{\Delta E_{21}}{A} \sin \left(\frac{AL}{2} \right) \cos \left(\bar{\delta} + \frac{\Delta E_{31}L}{2} \right) \right]^2,
\end{aligned} \quad (3.12)$$

it is sufficient to take³

$$\sin 2\bar{\theta}_{13} = \sin 2\theta_{13} - \frac{4\tilde{J}}{s_{23}^2 \sin 2\theta_{13}} \frac{\Delta m_{21}^2}{\Delta m_{31}^2} (\cos \bar{\delta} - \cos \delta), \quad (3.13)$$

³Here we do not discuss the other solution of the quadratic equation which was discussed by [59], since we are mainly interested in rejecting $\bar{\delta} = 0$ rather than determining the precise value of δ .

where we have used in (3.12) and (3.13) the fact $\tilde{J}/\sin 2\theta_{13} = \cos \theta_{13} \times$ (independent of θ_{13}) $\simeq \cos \bar{\theta}_{13} \times$ (independent of θ_{13}) which holds because $\sin^2 \theta_{13} \ll 1$. Notice that the phase $\Delta E_{31}L/2$ which appears together with δ in cosine in (3.12) disappears as $E_\nu \rightarrow \text{large}$. Plugging (3.13) in (3.12), we find

$$\begin{aligned}
& P(\nu_e \rightarrow \nu_\mu; \theta_{13}, \delta) - P(\nu_e \rightarrow \nu_\mu; \bar{\theta}_{13}, \bar{\delta}) \\
& \simeq s_{23}^2 \left(\frac{\Delta E_{31}}{A} \right)^2 \sin^2 \left(\frac{AL}{2} \right) (\sin^2 2\theta_{13} - \sin^2 2\bar{\theta}_{13}) \\
& + 8\tilde{J} \frac{\Delta E_{21} \Delta E_{31}}{A^2} \sin^2 \left(\frac{AL}{2} \right) \left[\cos \left(\delta + \frac{\Delta E_{31}L}{2} \right) - \cos \left(\bar{\delta} + \frac{\Delta E_{31}L}{2} \right) \right] \\
& \simeq 8\tilde{J} \frac{\Delta E_{21} \Delta E_{31}}{A^2} \sin^2 \left(\frac{AL}{2} \right) \\
& \times \left[\cos \left(\delta + \frac{\Delta E_{31}L}{2} \right) - \cos \left(\bar{\delta} + \frac{\Delta E_{31}L}{2} \right) - \cos \delta + \cos \bar{\delta} \right], \\
& \simeq 8\tilde{J} \frac{\Delta E_{21} \Delta E_{31}}{A^2} \sin^2 \left(\frac{AL}{2} \right) (\sin \bar{\delta} - \sin \delta) \frac{\Delta E_{31}L}{2}, \tag{3.14}
\end{aligned}$$

where we have expanded $\sin(\Delta E_{31}L/2) \simeq \Delta E_{31}L/2$, $\cos(\Delta E_{31}L/2) - 1 \simeq -(\Delta E_{31}L)^2/2 \simeq 0$ in the last step in (3.14). Hence we get

$$\begin{aligned}
& \langle P(\nu_e \rightarrow \nu_\mu; \theta_{13}, \delta) - P(\nu_e \rightarrow \nu_\mu; \bar{\theta}_{13}, \bar{\delta} = 0) \rangle \\
& \simeq -\frac{6N_0\sigma_0}{\pi m_\mu^2} \tilde{J} \sin \delta \frac{\Delta m_{21}^2 (\Delta m_{31}^2)^2}{A^2 L^2} \sin^2 \left(\frac{AL}{2} \right) \int dx (1-x) \\
& = \frac{3N_0\sigma_0}{\pi m_\mu^2} \tilde{J} \sin \delta \Delta m_{21}^2 (\Delta m_{31}^2)^2 \frac{\sin^2 (AL/2)}{A^2 L^2}. \tag{3.15}
\end{aligned}$$

We see from (3.15) that if we optimize $\Delta\chi^2(\text{CPV})$ with respect only to $\bar{\theta}_{13}$ then $\Delta\chi^2(\text{CPV})$ behaves as

$$\Delta\chi^2(\text{CPV}; (\delta, \theta_{13})) \simeq \frac{18N_0\sigma_0}{\pi m_\mu^2} \frac{\tilde{J}^2 \sin^2 \delta (\Delta m_{21}^2)^2 (\Delta m_{31}^2)^2 \sin^2 (AL/2)}{s_{23}^2 \sin^2 2\theta_{13} E_\mu A^2}. \tag{3.16}$$

Note that the behavior of $\Delta\chi^2(\text{CPV}; (\delta, \theta_{13}))$ which is optimized with respect to $\bar{\theta}_{13}$ is quite different from that of $\Delta\chi^2(\text{naive CPV})$ in (3.11). We observe that the dependence of $\Delta\chi^2(\text{CPV}; (\delta, \theta_{13}))$ on E_μ is the same as that of $\Delta\chi^2(\text{TV})$. It should be also emphasized that $\Delta\chi^2(\text{CPV}; (\delta, \theta_{13}))$ is proportional to $\sin^2 \delta$ and does not depend on $\cos \delta$ unlike $\Delta\chi^2(\text{naive CPV})$ in (3.11).

We can play the same game for θ_{23} , Δm_{32}^2 and C . In the case of the two variable correlation $(\bar{\delta}, \bar{\theta}_{23})$,

$$\sin \bar{\theta}_{23} = \sin \theta_{23} - \frac{4\tilde{J}}{s_{23} \sin^2 2\theta_{13}} \frac{\Delta m_{21}^2}{\Delta m_{31}^2} (\cos \bar{\delta} - \cos \delta) \tag{3.17}$$

minimizes $\Delta\chi^2(\text{CPV}; (\delta, \theta_{23}))$ and we have

$$\Delta\chi^2(\text{CPV}; (\delta, \theta_{23})) \simeq \frac{18N_0\sigma_0}{\pi m_\mu^2} \frac{\tilde{J}^2 \sin^2 \delta (\Delta m_{21}^2)^2 (\Delta m_{31}^2)^2 \sin^2 (AL/2)}{s_{23}^2 \sin^2 2\theta_{13}} \frac{1}{E_\mu A^2},$$

which is the same as $\Delta\chi^2(\text{CPV}; (\delta, \theta_{13}))$. In the case of the two variable correlation $(\bar{\delta}, \overline{\Delta m_{32}^2})$, using

$$\begin{aligned} & P(\nu_e \rightarrow \nu_\mu; \delta) \\ & \simeq \left[s_{23} \sin 2\theta_{13} \frac{\Delta E_{31}}{A} \sin\left(\frac{AL}{2}\right) + \frac{4\tilde{J}}{s_{23} \sin 2\theta_{13}} \frac{\Delta E_{21}}{A} \sin\left(\frac{AL}{2}\right) \cos \delta \right]^2, \end{aligned}$$

we find

$$\overline{\Delta m_{31}^2} = \Delta m_{31}^2 - \frac{4\tilde{J}}{s_{23}^2 \sin^2 2\theta_{13}} \Delta m_{21}^2 (\cos \bar{\delta} - \cos \delta) \quad (3.18)$$

minimizes $\Delta\chi^2(\text{CPV}; (\delta, \Delta m_{31}^2))$. We obtain

$$\Delta\chi^2(\text{CPV}; (\delta, \Delta m_{31}^2)) \simeq \frac{18N_0\sigma_0}{\pi m_\mu^2} \frac{\tilde{J}^2 \sin^2 \delta (\Delta m_{21}^2)^2 (\Delta m_{31}^2)^2 \sin^2 (AL/2)}{s_{23}^2 \sin^2 2\theta_{13}} \frac{1}{E_\mu A^2},$$

which again is the same as $\Delta\chi^2(\text{CPV}; (\delta, \theta_{13}))$. In the case of the two variable correlation $(\bar{\delta}, \bar{C})$,

$$\frac{\sin(\bar{A}L/2)}{\bar{A}} = \frac{\sin(AL/2)}{A} \left[1 - \frac{4\tilde{J}}{s_{23}^2 \sin^2 2\theta_{13}} \frac{\Delta m_{21}^2}{\Delta m_{31}^2} (\cos \bar{\delta} - \cos \delta) \right] \quad (3.19)$$

minimizes $\Delta\chi^2(\text{CPV}; (\delta, C))$ and we get

$$\Delta\chi^2(\text{CPV}; (\delta, C)) \simeq \frac{18N_0\sigma_0}{\pi m_\mu^2} \frac{\tilde{J}^2 \sin^2 \delta (\Delta m_{21}^2)^2 (\Delta m_{31}^2)^2 \sin^2 (AL/2)}{s_{23}^2 \sin^2 2\theta_{13}} \frac{1}{E_\mu A^2},$$

which once again is the same as $\Delta\chi^2(\text{CPV}; (\delta, \theta_{13}))$. The expressions (3.13), (3.17), (3.18) and (3.19) for the optimal values for $\bar{\theta}_{13}$, $\bar{\theta}_{23}$, $\overline{\Delta m_{31}^2}$ and \bar{C} explain why the correlation has a cosine curve for large E_μ and small L in Figs. 1, 2, 4 and 6.

In the case of the correlations $(\bar{\delta}, \bar{\theta}_{12})$, and $(\bar{\delta}, \overline{\Delta m_{21}^2})$, we have to take into account of terms of order $\mathcal{O}((\Delta E_{21}/\Delta E_{31})^2)$. For $(\bar{\delta}, \bar{\theta}_{12})$, we have

$$\begin{aligned} \sin 2\bar{\theta}_{12} &= -\frac{4\tilde{J}}{c_{23}^2} \frac{\Delta m_{31}^2}{\Delta m_{21}^2} \cos \bar{\delta} + \left[\left(\frac{4\tilde{J}}{c_{23}^2} \frac{\Delta m_{31}^2}{\Delta m_{21}^2} \right)^2 \cos^2 \bar{\delta} \right. \\ &\quad \left. + \frac{8\tilde{J}}{c_{23}^2} \frac{\Delta m_{31}^2}{\Delta m_{21}^2} \cos \delta \sin 2\theta_{12} + \sin^2 2\theta_{12} \right]^{\frac{1}{2}}, \end{aligned} \quad (3.20)$$

and this optimizes $\Delta\chi^2(\text{CPV})$. We find

$$\begin{aligned}
& P(\nu_e \rightarrow \nu_\mu; \theta_{12}, \delta) - P(\nu_e \rightarrow \nu_\mu; \bar{\theta}_{12}, \bar{\delta}) \\
& \simeq \frac{8\tilde{J}}{\sin 2\theta_{12}} \frac{\Delta E_{21}\Delta E_{31}}{A^2} \sin^2\left(\frac{AL}{2}\right) \left[\sin 2\theta_{12} \cos\left(\delta + \frac{\Delta E_{31}L}{2}\right) \right. \\
& \quad \left. - \sin 2\bar{\theta}_{12} \cos\left(\bar{\delta} + \frac{\Delta E_{31}L}{2}\right) - \sin 2\theta_{12} \cos \delta + \sin 2\bar{\theta}_{12} \cos \bar{\delta} \right] \\
& \simeq \frac{8\tilde{J}}{\sin 2\theta_{12}} \frac{\Delta E_{21}\Delta E_{31}}{A^2} \sin^2\left(\frac{AL}{2}\right) (\sin \bar{\delta} \sin 2\bar{\theta}_{12} - \sin \delta \sin 2\theta_{12}) \frac{\Delta E_{31}L}{2},
\end{aligned}$$

where we have expanded $\sin(\Delta E_{31}L/2) \simeq \Delta E_{31}L/2$. By putting $\bar{\delta} = 0$, we obtain

$$\Delta\chi^2(\text{CPV}; (\delta, \theta_{12})) \simeq \frac{18N_0\sigma_0}{\pi m_\mu^2} \frac{\tilde{J}^2 \sin^2 \delta (\Delta m_{21}^2)^2 (\Delta m_{31}^2)^2 \sin^2(AL/2)}{s_{23}^2 \sin^2 2\theta_{13} E_\mu A^2},$$

which once again is the same as $\Delta\chi^2(\text{CPV}; (\delta, \theta_{13}))$. For $(\bar{\delta}, \overline{\Delta m_{21}^2})$, we have

$$\begin{aligned}
\overline{\Delta m_{21}^2} &= -\frac{4\tilde{J}}{c_{23}^2 \sin^2 2\theta_{12}} \Delta m_{31}^2 \cos \bar{\delta} + \left[\left(\frac{4\tilde{J}}{c_{23}^2 \sin^2 2\theta_{12}} \right)^2 \cos^2 \bar{\delta} (\Delta m_{31}^2)^2 \right. \\
&\quad \left. + \frac{8\tilde{J}}{c_{23}^2 \sin^2 2\theta_{12}} \Delta m_{21}^2 \Delta m_{31}^2 \cos \delta + (\Delta m_{21}^2)^2 \right]^{\frac{1}{2}} \quad (3.21)
\end{aligned}$$

which leads to

$$\begin{aligned}
& P(\nu_e \rightarrow \nu_\mu; \Delta m_{21}^2, \delta) - P(\nu_e \rightarrow \nu_\mu; \overline{\Delta m_{21}^2}, \bar{\delta}) \\
& \simeq 8\tilde{J} \frac{\Delta E_{21}\Delta E_{31}}{A^2} \sin^2\left(\frac{AL}{2}\right) (\sin \bar{\delta} - \sin \delta) \frac{\Delta E_{31}L}{2}.
\end{aligned}$$

Thus we get

$$\Delta\chi^2(\text{CPV}; (\delta, \Delta m_{21}^2)) \simeq \frac{18N_0\sigma_0}{\pi m_\mu^2} \frac{\tilde{J}^2 \sin^2 \delta (\Delta m_{21}^2)^2 (\Delta m_{31}^2)^2 \sin^2(AL/2)}{s_{23}^2 \sin^2 2\theta_{13} E_\mu A^2},$$

which once again is the same as $\Delta\chi^2(\text{CPV}; (\delta, \theta_{13}))$. Unlike the cases for $(\bar{\delta}, \bar{\theta}_{13})$, $(\bar{\delta}, \bar{\theta}_{23})$, $(\bar{\delta}, \overline{\Delta m_{31}^2})$ and $(\bar{\delta}, \bar{C})$, the optimal values (3.20) and (3.21) have nontrivial behaviors even for large E_μ and small L , as we can see from Figs. 3 and 5.

We have seen analytically that two variable correlations give us the behavior $\Delta\chi^2(\text{CPV}) \propto \sin^2 \delta / E_\mu$ and this behavior is the same as $\Delta\chi^2(\text{TV})$. Although it is difficult to discuss correlations of more than two variables analytically, the discussions above are sufficient to demonstrate that sensitivity to CP violation decreases as E_μ becomes larger. In fact we have verified

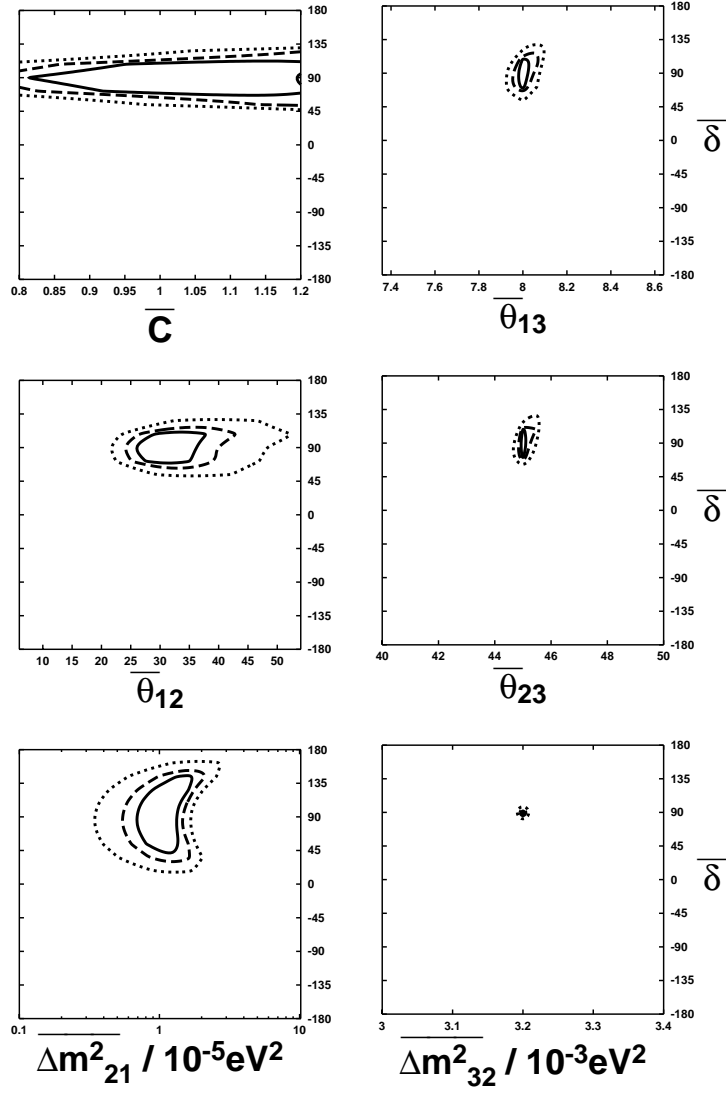
numerically that $\Delta\chi^2(\text{CPV})$ decreases as the muon energy increases ($E_\mu \gtrsim 100\text{GeV}$). The conclusion in this subsection is qualitatively consistent with the work [71] by Lipari who claims that sensitivity to CP violation decreases as E_μ becomes large. However it may not be quantitatively consistent with [71] in which it was suggested that sensitivity starts getting lost for $E_\nu \gtrsim$ a few GeV. In our discussion here it was necessary to have $|\Delta E_{31}L| \ll 1$ which may not be attained for $L \sim 3000\text{km}$ and $E_\mu \lesssim 50\text{GeV}$. Our numerical calculations in the previous section indicate that the sensitivity is optimized for $20\text{GeV} \lesssim E_\mu \lesssim 50\text{GeV}$ which is quantitatively consistent with the results in [6, 89, 47, 48, 49, 50, 51, 52, 53, 54, 56, 57]. This interval for E_μ is the intermediate energy region which cannot be treated analytically using our arguments in this section. In fact it seems difficult to explain analytically the strong correlation of $(\bar{\delta}, \bar{C})$ for $E_\mu \simeq 50\text{ GeV}$ and $L \simeq 3000\text{km}$. (cf. Fig. 3.15)

3.1.5.6 JHF experiment

The JHF project [4] has been proposed to perform precise measurements of the oscillation parameters. The possible extension of this project includes the upgrade of the power to 4MW and the construction of a mega-ton detector [67]. The possibility to measure CP violation at the JHF project has been discussed by [72, 70, 73]. Here we briefly discuss the possibility of measurements of CP violation at the JHF experiment with power 4MW and a 1 Mton detector as a comparison with neutrino factories. As in previous subsections, we will take into consideration the correlations of all the oscillation parameters. In the case of the JHF experiment, which has the baseline $L \simeq 300\text{km}$, the matter effect is almost negligible and it is possible to compare the numbers of events for $\nu_\mu \rightarrow \nu_e$ and $\bar{\nu}_\mu \rightarrow \bar{\nu}_e$ directly by taking into account the difference of the cross sections between $\sigma_{\nu N}$ and $\sigma_{\bar{\nu} N}$. However, we use the same $\Delta\chi^2$ as in section 2, as discussions with the same criterion gives more transparent comparisons between neutrino factories and the superbeam at JHF.

The correlations of two variables (δ, X) , where X is $\theta_{k\ell}$, $\Delta m_{k\ell}^2$ or C , are shown in Fig. 3.25, where the central values for these parameters are those of the best fit point, i.e., $\sin^2 2\theta_{12} = 0.75$, $\Delta m_{21}^2 = 3.2 \times 10^{-5}\text{eV}^2$; $\sin^2 2\theta_{23} = 1.0$, $\Delta m_{32}^2 = 3.2 \times 10^{-3}\text{eV}^2$, $C=1.0$ and we have used a reference value $\theta_{13} = 8^\circ$. In this calculation the narrow band beam (NBB) (the flux referred to as LE2 π in [4]) is used, and it is assumed for simplicity that there are no backgrounds and the detection efficiency is 70% in Fig. 3.25. Note that for the purpose of measurements of CP violation NBB is more advantageous than the wide band beam, as the former has better energy resolution.

As in the previous subsections, we have evaluated numerically the data size required to reject a hypothesis with $\bar{\delta} = 0$. Of course the data size



68%CL ——— 90%CL - - - 99%CL

Figure 3.25: The correlations of errors of $(\bar{\delta}, \bar{C})$, $(\bar{\delta}, \bar{\theta}_{13})$, $(\bar{\delta}, \bar{\theta}_{12})$, $(\bar{\delta}, \bar{\theta}_{23})$, $(\bar{\delta}, \Delta m^2_{21})$, $(\bar{\delta}, \Delta m^2_{32})$ in the case of the JHF experiment with 4MW power, a 1 mega ton detector and NBB. No backgrounds are taken into consideration in these figures. The oscillation parameters used are the same as in Fig. 3.15.

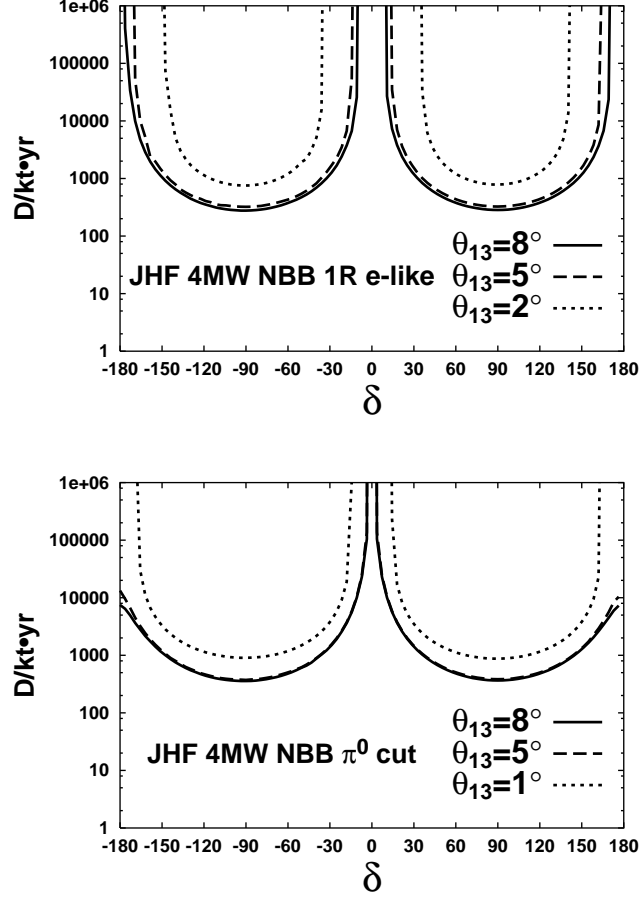


Figure 3.26: The number of data size required (in the unit of kt) to reject a hypothesis $\bar{\delta} = 0$ at 3σ for the JHF experiment with 4MW power, a 1 mega ton detector and NBB using $\Delta\chi^2(\text{CPV})$ (3.4) as a function of the true value of δ . Unlike in the case of Fig. 3.25, the effects of backgrounds are taken into account in this figure. The oscillation parameters used are the same as in Fig. 3.15, and two ways of cuts (1-ring e-like and π^0 cut) [72] are used. In the case of the 1-ring e-like selection, $\theta_{13} = 1^\circ$ does not have a solution because the systematic errors become so large.

depends on the true value δ and the results obtained by varying the six variables $(\theta_{k\ell}, \Delta m_{k\ell}^2, C)$ are plotted in Fig. 3.26, where we have taken the best fit values for $(\theta_{12}, \Delta m_{21}^2)$, $(\theta_{23}, \Delta m_{32}^2)$, $\theta_{13} = 8^\circ, 5^\circ, 1^\circ (2^\circ)$, and the NBB is used. The vertical axis of Fig. 3.26 stands for the data size required per $\text{kt} \times (\nu_\mu \text{ 1 year} + \bar{\nu}_\mu \text{ 2 years})$. We have used two ways of ν_e selections, one is 1-ring e-like selection which has the background fraction $f_B = 1.8 \times 10^{-2}$, the detection efficiency 70.4%, and the other one is π^0 cut selection which has the background fraction $f_B = 2 \times 10^{-3}$, the detection efficiency 50.4% [72]. In the case of the 1-ring e-like selection, for $\theta_{13} = 1^\circ$ the systematic error becomes so large that the data size required to reject $\bar{\delta} = 0$ becomes infinite. Also in this case the number of events for $\delta = \pi$ becomes almost the same as that for $\delta = 0$ up to the systematic errors and there is no way to distinguish the case of $\delta = \pi$ and that of $\delta = 0$. However, as long as the value of δ is not close to 0 or π and $\theta_{13} \gtrsim 3^\circ$, the JHF with 4MW power and a 1 mega ton detector will be able to demonstrate $\bar{\delta} \neq 0$ at $3\sigma\text{CL}$.

3.1.5.7 discussions

The bottom line of the present subsection is that either the high ($E_\mu \sim 50\text{GeV}$) or medium ($E_\mu \sim 20\text{GeV}$) energy option is certainly better than the low energy ($E_\nu \ll 10\text{GeV}$) option which has been advocated by some people [56, 62, 63]. We have arrived at this conclusion on the assumption that the energy threshold is as low as 0.1 GeV, and the detection efficiency is independent of the neutrino energy. In practice, it may be very difficult to have such a low threshold and to keep such a good detection efficiency down to 0.1 GeV, so it is expected that the low energy option becomes less and less advantageous.

If $\theta_{13} \gtrsim 3^\circ$ and if the value of δ is not close to 0 or π , then the JHF experiment with 4MW power and a 1 mega ton detector will be able to demonstrate $\bar{\delta} \neq 0$ at $3\sigma\text{CL}$. On the other hand, if $\theta_{13} \lesssim 3^\circ$, then neutrino factories seem to be the only experiment which can demonstrate $\bar{\delta} \neq 0$. In that case, depending on the situation such as the fraction of backgrounds, the uncertainty of the matter effect and the magnitude of θ_{13} , the option with ($E_\mu \simeq 50\text{GeV}$, $L \simeq 3000\text{km}$) may be advantageous (or disadvantageous) over ($E_\mu \simeq 20\text{GeV}$, $L \simeq 1000\text{km}$). In both a neutrino factory with ($20\text{GeV} \lesssim E_\mu \lesssim 50\text{GeV}$, $1000\text{km} \lesssim L \lesssim 3000\text{km}$) and the JHF experiment, our $\Delta\chi^2(\text{CPV})$ depends not only on $\sin\delta$ but also $\cos\delta$,⁴ so that we can in principle distinguish $\delta = \pi$ from $\delta = 0$ as long as the statistical significance overcomes the systematic errors. This is not the case for a neutrino factory with large systematic errors for small θ_{13} , i.e., for $E_\mu = 50\text{GeV}$ and

⁴If we evaluate $\Delta\chi^2(\text{CPV}; (\delta, \theta_{13}))$ in (3.16) to the next leading order in $\Delta m_{31}^2 L/E_\mu$ then $\bar{J}^2 \sin^2 \delta$ in (3.16) is replaced by $\bar{J}^2 (\sin\delta + \text{const.} (\Delta m_{31}^2 L/E_\mu) \cos\delta)^2$, and $\Delta m_{31}^2 L/E_\mu$ is not necessarily negligible in either case.

$\theta_{13} = 1^\circ$ (cf. Fig. 3.24), and for the JHF experiment with less S/N ratio i.e., when the 1-ring e-like selection is adopted, or when $\theta_{13} = 8^\circ$ and the π^0 cut selection is adopted (cf. Fig. 3.26). From Fig. 3.24 we find that the high energy option $E_\mu \sim 50\text{GeV}$, which has been advocated as the best choice, is not always the best, when the background effect is taken into account. In fact, if UNO type detectors with the detector mass ~ 1 mega ton and the background fraction $f_B \sim 10^{-3}$ can be built, then $E_\mu \sim 20\text{GeV}$, $L \sim 1000\text{km}$ is probably the best parameter set for measurements of CP violation for generic values of θ_{13} and ΔC .

In order to be more concrete, we need the knowledge on the uncertainty of the matter effect A . The error of $A = \sqrt{2}G_F Y_e \rho$ comes from those of Y_e and ρ . The error of Y_e has been discussed by [74] and it is about 2% and geophysicists [75, 76] agree with it. Without any uncertainty of the matter effect, it has been claimed that a medium baseline experiment ($L \sim 3000\text{km}$, $E_\mu \sim 50\text{GeV}$) is best for measurements of CP violation. In that case the depth of the neutrino path is at most 200km and most of the neutrino path is in the upper mantle. It is known in geophysics [77] that the crust has relatively large latitude-longitude dependent fluctuations around constant density. On the other hand, in the case of the upper mantle, some geophysicists claim that fluctuations around constant density are a few % [78, 75, 76] while another [79] says that they may be as large as 5 %. However, such discussions are based on normal mode studies in seismology which are confined to long wavelength features, and it was pointed out [76, 79] that the fluctuations in the density in the analysis of neutrino factories may be larger than 5 %, since the width of the neutrino beam is much smaller than typical wavelengths in seismological studies. If that is the case, then it follows from Fig. 3.23 that the case $L \simeq 1000\text{km}$ is better than the case $L \simeq 3000\text{km}$, since the former is insensitive to the uncertainty of the matter effect. In this section we adopted simplified assumptions such as that the detection efficiency is independent of the neutrino energy, that the threshold energy can be taken as low as 0.1GeV, and that the uncertainty of the matter effect is at most 5 %. We need much more detailed experimental information as well as seismological discussions to obtain the optimal baseline and the muon energy in neutrino factories.

3.1.6 Statistical Evaluation

In the following, a different approach of statistics needed is shown.

3.1.6.1 Determination of U_{e3}

In this subsection, it is estimated how large data sample is needed to see that $\sin \theta_{13} \neq 0$. As long as the solar neutrino deficit is explained by the SMA or

VO solution the appearance events immediately implies that $\sin \theta_{13} \neq 0$. The sensitivity to the observation of non-zero $\sin \theta_{13}$ depends simply on $\sin^2 \theta_{13} E_\mu$ as given in the section 2. Thus higher muon energy will be better.

On the other hand, if the solar neutrino problem is attributed to the LMA solution, then even if $\sin \theta_{13} = 0$, we can observe the appearance event. Indeed at the high energy region the oscillation effect due to the solar mixings mimics that due to $\sin \theta_{13}$. Therefore we estimate the data size in the LMA case since we can expect that there is a difficulty to see that $\sin \theta_{13} \neq 0$.

We employ the following test statistics.

$$T_{13}^2 = \sum_i^n \frac{[\bar{N}_i^{\text{th}}(0; \tilde{x}_j) N_i^{\text{ex}} + N_i^{\text{th}}(0; \tilde{x}_j) \bar{N}_i^{\text{ex}} - 2 N_i^{\text{th}}(0; \tilde{x}_j) \bar{N}_i^{\text{th}}(0; \tilde{x}_j)]^2}{\{N_i^{\text{th}}(0; \tilde{x}_j)\}^2 N_i^{\text{ex}} + \{N_i^{\text{th}}(0; \tilde{x}_j)\}^2 \bar{N}_i^{\text{ex}}}. \quad (3.22)$$

Here $N_i^{\text{ex}}(\bar{N}_i^{\text{ex}})$ denotes the appearance event rate for $\nu_e \rightarrow \nu_\mu$ ($\bar{\nu}_e \rightarrow \bar{\nu}_\mu$) at energy bin i . Here, since we do not have any real data, we replace them with theoretically calculated event rate $N_i^{\text{th}}(\theta_{13}; x_j)$ using the theoretical parameters $\{x_i\} \equiv \{\theta_{12}, \theta_{23}, \delta m_{ij}^2, \delta, a\}$. By varying \tilde{x}_j 's with $\theta_{13} = 0$ we search the minimum of T_{13}^2 ,

$$\chi_{13}^2 \equiv \min_{\tilde{x}_j, n} T_{13}^2 \quad (3.23)$$

and from χ_{13}^2 we estimate the necessary data size. See ref.[109] for details.

We plot in Fig.3.27 the required data size in the unit 10^{21} for parent muon number and 100kt for the detector mass. Here $\{\theta_{12}, \theta_{23}, m_{31}^2, m_{21}^2, \delta\} = \{\pi/4, \pi/4, 3 \times 10^{-3} \text{eV}^2, 10^{-4} \text{eV}^2, 0\}$. As we expected, while for small $\sin \theta_{13}$ the sensitivity depends on $\sin^2 \theta_{13} E_\mu$, the sensitivity is drastically worse for small $\sin \theta_{13}$.

In conclusion we can observe the effect by $\sin \theta_{13}$ very precisely if it is larger than 0.03. If it is smaller than 0.03, we need a very precise information about mixing angle and the mass square difference for the solar neutrino deficit.

3.1.6.2 Determination of the Sign of Δm^2

Here we estimate how large data size we need to see the sign of Δm_{31}^2 . Since to see the sign is essentially same as to see the fake CP asymmetry due to the matter effect we employ the following test statistics.

$$T_m^2 = \sum_i^n \frac{[\bar{N}_i^{\text{th}}(-\Delta m_{31}^2; \tilde{x}_j) \times N_i^{\text{ex}} - N_i^{\text{th}}(-\Delta m_{31}^2; \tilde{x}_j) \times \bar{N}_i^{\text{ex}}]^2}{\{\bar{N}_i^{\text{th}}(-\Delta m_{31}^2; \tilde{x}_j)\}^2 N_i^{\text{ex}} + \{N_i^{\text{th}}(-\Delta m_{31}^2; \tilde{x}_j)\}^2 \bar{N}_i^{\text{ex}}}. \quad (3.24)$$

Here $N_i^{\text{ex}}(\bar{N}_i^{\text{ex}})$ denotes the appearance event rate for $\nu_e \rightarrow \nu_\mu$ ($\bar{\nu}_e \rightarrow \bar{\nu}_\mu$) at energy bin i . Here, since we do not have any real data, we replace them

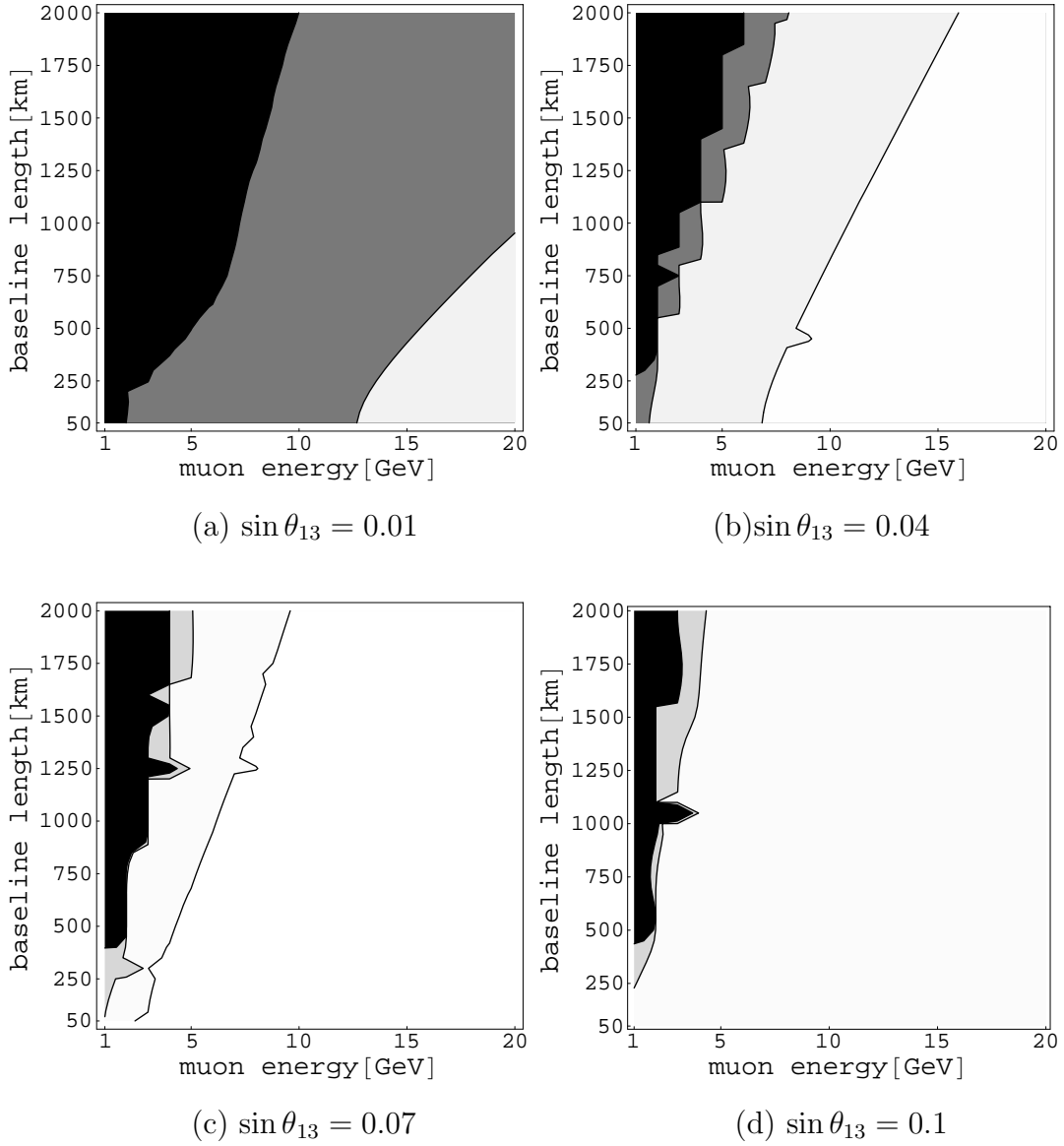


Figure 3.27: Required data size in the unit $[10^{21}/100\text{kt}]$ to observe that $\sin \theta_{13} \neq 0$ as a function of muon energy E_μ and baseline length L . $\sin \theta_{13} =$ (a) 0.01, (b) 0.04, (c) 0.07, (d) 0.1 .

with theoretically calculated event rate $N_i^{\text{th}}(\Delta m_{31}^2; x_j)$ using the theoretical parameters $\{x_i\} \equiv \{\theta_{ij}, \delta, \Delta m_{21}^2, a\}$. By varying the bin number n and \tilde{x}_j 's

with $-\Delta m_{31}^2$ search the minimum of T_m^2 ,

$$\chi_m^2 \equiv \min_{n, \tilde{x}_j, -\Delta m_{31}^2} \frac{T^2}{\chi_\alpha^2(n)} \quad (3.25)$$

and from χ_m^2 we estimate the necessary data size to the sign of Δm_{31}^2 at α level of significance. See the appendix of ref.[109] for details. Hereafter we set $\alpha = 0.01$ which naively corresponds to 99% confidence level.

In Fig.3.28 We show the required data size to see the sign in the unit 10^{21} for parent muon number and 100kt for the detector mass. There we plot it for various $\sin \theta_{13}$ and $\{\sin \theta_{12}, \sin \theta_{23}, \Delta m_{31}^2, \Delta m_{21}^2\} = \{\pi/4, \pi/4, 3 \times 10^{-3} \text{eV}^2, 10^{-4} \text{eV}^2\}$.⁵ From these graphs we find that it is difficult to observe the sign at shorter baseline. Indeed the asymmetry due to the matter effect takes the form

$$\frac{2}{3} \sin^2 \theta_{23} \sin^2 2\theta_{13} \cos 2\theta_{13} \frac{a(L)L}{4E_\nu} \left(\frac{\Delta m_{31}^2 L}{4E_\nu} \right)^3. \quad (3.26)$$

As a event rate it increased with L^2 and hence the sensitivity to the sign increases with L^4 . Thus the longer baseline is much more suitable for the observation of the sign.

Next we show in Fig.3.29 how large data size is required to see the sign for various values of $\sin \theta_{13}$ at $L = 2000 \text{km}$ with $E_\mu = 20 \text{GeV}$. The required data size depends on $\sin^2 \theta_{13}$ for rather large $\sin \theta_{13}$. It is easily understood; From Eq.3.26 the numerator of Eq.3.24 depends on $\sin^4 \theta_{13}$ while the denominator depends on $\sin \theta_{13}$. On the other hand, the dependence on smaller $\sin \theta_{13}$ is rather complicated. In the numerator of Eq.3.24 there is also a contribution from the true CP-violation effect and its ambiguity can mimic the fake asymmetry due to the matter effect. Therefore the sensitivity to the sign becomes drastically worse. In the reference value of the theoretical parameters considered here, we find in Fig.3.29 that for $\sin \theta_{13} < 0.03$ the matter effect can hidden and hence the sensitivity becomes worse.

To raise the sensitivity to the sign we should make an experiment with longer baseline.

3.1.6.3 Measurement of CP asymmetry

Here we estimate how large data size we need to see the CP-violation effect as the asymmetry between neutrinos and anti-neutrinos. We employ the following test statistics.

$$T^2 = \sum_i^n \frac{[\bar{N}_i^{\text{th}}(\delta_0; \tilde{x}_j) \times N_i^{\text{ex}} - N_i^{\text{th}}(\delta_0; \tilde{x}_j) \times \bar{N}_i^{\text{ex}}]^2}{\{\bar{N}_i^{\text{th}}(\delta_0; \tilde{x}_j)\}^2 N_i^{\text{ex}} + \{N_i^{\text{th}}(\delta_0; \tilde{x}_j)\}^2 \bar{N}_i^{\text{ex}}}. \quad (3.27)$$

⁵Matter density is approximated to be constant and calculated by PREM. Thus the matter effect has a dependence on the baseline length, $a(L)$.

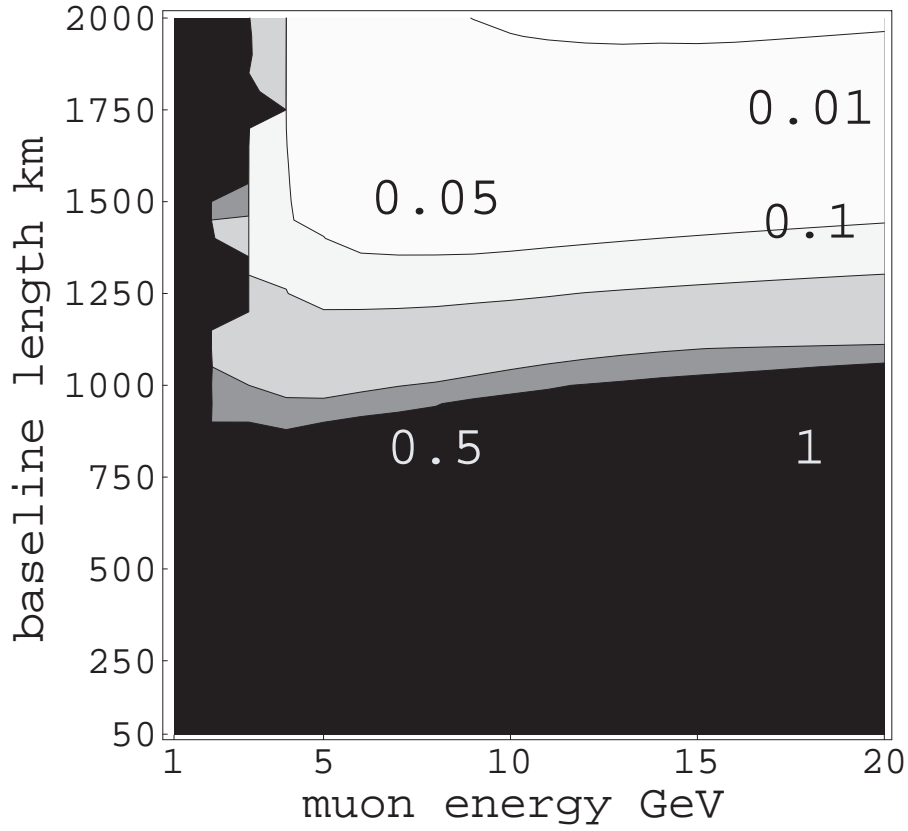


Figure 3.28: Required data size to observe the sign of Δm_{31}^2 as function of muon energy E_μ and baseline length L .

Here $N_i^{\text{ex}}(\bar{N}_i^{\text{ex}})$ denotes the appearance event rate for $\nu_e \rightarrow \nu_\mu$ ($\bar{\nu}_e \rightarrow \bar{\nu}_\mu$) at energy bin i . Here, since we do not have any real data, we replace them with theoretically calculated event rate $N_i^{\text{th}}(\delta; x_j)$ using the theoretical parameters $\{x_i\} \equiv \{\theta_{ij}, \Delta m_{ij}^2, a\}$. By varying the bin number n and \tilde{x}_j 's with $\{\delta_0\} = \{0, \pi\}$ we search the minimum of T^2 ,

$$\chi^2 \equiv \min_{n, \tilde{x}_j, \delta_0} \frac{T^2}{\chi_\alpha^2(n)} \quad (3.28)$$

and from χ^2 we estimate the necessary data size to see the CP-violation effect at α level of significance. See the appendix of ref.[109] for details. Hereafter we set $\alpha = 0.01$ which naively corresponds to 99% confidence level.

In Fig.3.30 We show the required data size to see the CP-violation effect in the unit 10^{21} for parent muon number and 100kt for the detector mass. There we plot it for various δ and Δm_{21}^2 and $\{\sin \theta_{13}, \sin \theta_{12}, \sin \theta_{23}, \Delta m_{31}^2\} =$

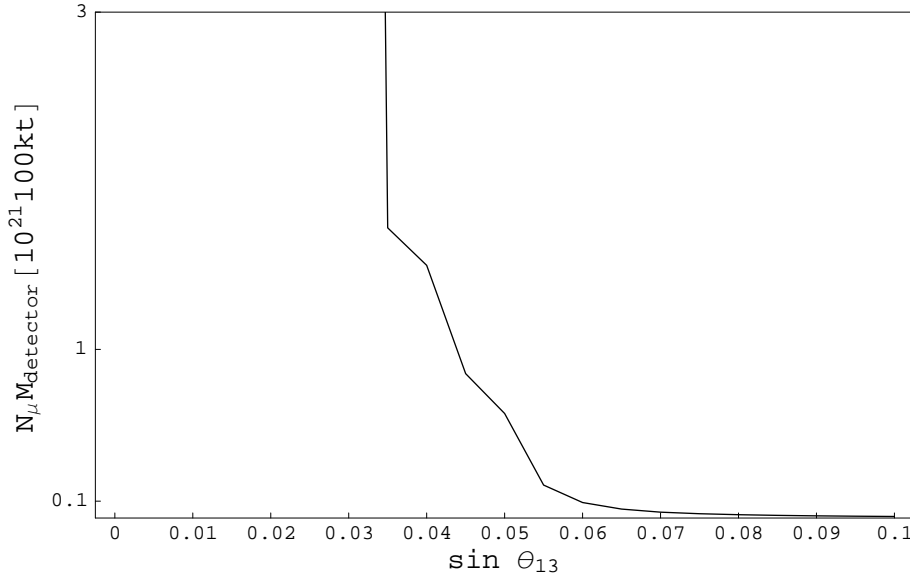


Figure 3.29: Required data size to observe the sign of Δm_{31}^2 as a function of $\sin \theta_{13}$ at $L = 2000\text{km}$ and $E_\mu = 20 \text{ GeV}$.

$\{0.1, \pi/4, \pi/4, 3 \times 10^{-3} \text{eV}^2\}$.⁶ From these graphs we find that it is difficult to observe the CP asymmetry with longer baseline. Since the neutrino propagates in the earth, there is not only the pure asymmetry due to the CP-violation effect but also that due to the matter effect. We have to distinguish them. The CP asymmetry is almost proportional to

$$J_{/\delta} \equiv \frac{\Delta m_{21}^2}{\Delta m_{31}^2} \sin 2\theta_{12} \sin 2\theta_{23} \sin 2\theta_{13} \cos \theta_{13} \sin \delta \quad (3.29)$$

and the matter asymmetry is proportional to

$$\frac{2}{3} \sin^2 \theta_{23} \sin^2 2\theta_{13} \cos 2\theta_{13} \frac{a(L)L}{4E_\nu}. \quad (3.30)$$

From these Eqs.3.29 and 3.30 we find that at a longer length it become difficult to see the CP-violation effect as the asymmetry. Moreover it is easy to understand for smaller Δm_{21}^2 and $\sin \delta$ the shorter baseline becomes better.

Next we study the sensitivity to the asymmetry at $L = 1000\text{km}$. In Fig3.31 we plot the required data size for various $\sin \theta_{13}$ with (a) E_μ . From these graphs we find that the sensitivity depends very weakly on $\sin \theta_{13}$. It is easily understood from Eq.3.29. Since the asymmetry is proportional to $\sin \theta_{13}$, in the test statistics Eq.3.22 the dependence on $\sin \theta_{13}$ almost cancels. It is also easy to understand that the sensitivity is slightly worse in the larger $\sin \theta_{13}$ region. Since for larger $\sin \theta_{13}$ the matter effect is stronger as seen in Eq.3.30, the sensitivity is slightly worse.

⁶Matter density is approximated to be constant and calculated by PREM. Thus the matter effect has a dependence on the baseline length, $a(L)$.

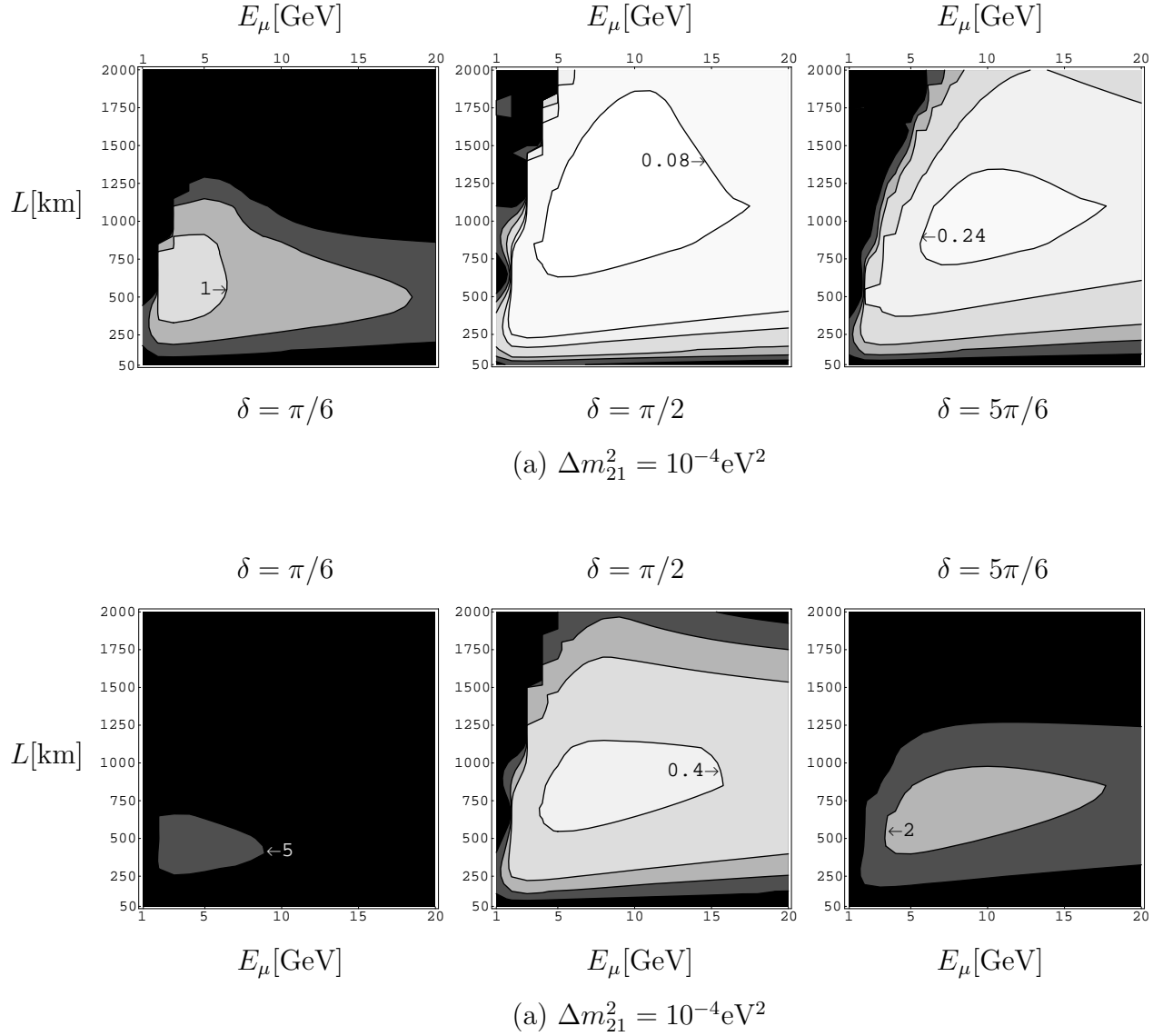


Figure 3.30: Required data size in the unit $[10^{21} 100\text{kt}]$ to observe the CP-violation effect as a function of muon energy E_μ and baseline length L for various δ and Δm_{21}^2 . (a) $\Delta m_{21}^2 = 10^{-4} \text{eV}^2$. (b) $\Delta m_{21}^2 = 5 \times 10^{-5} \text{eV}^2$.

In conclusion, if we want to see the CP-violation effect as the difference between neutrino and anti-neutrino we have to make an experiment at shorter distance as long as the theoretical parameters have ambiguities.

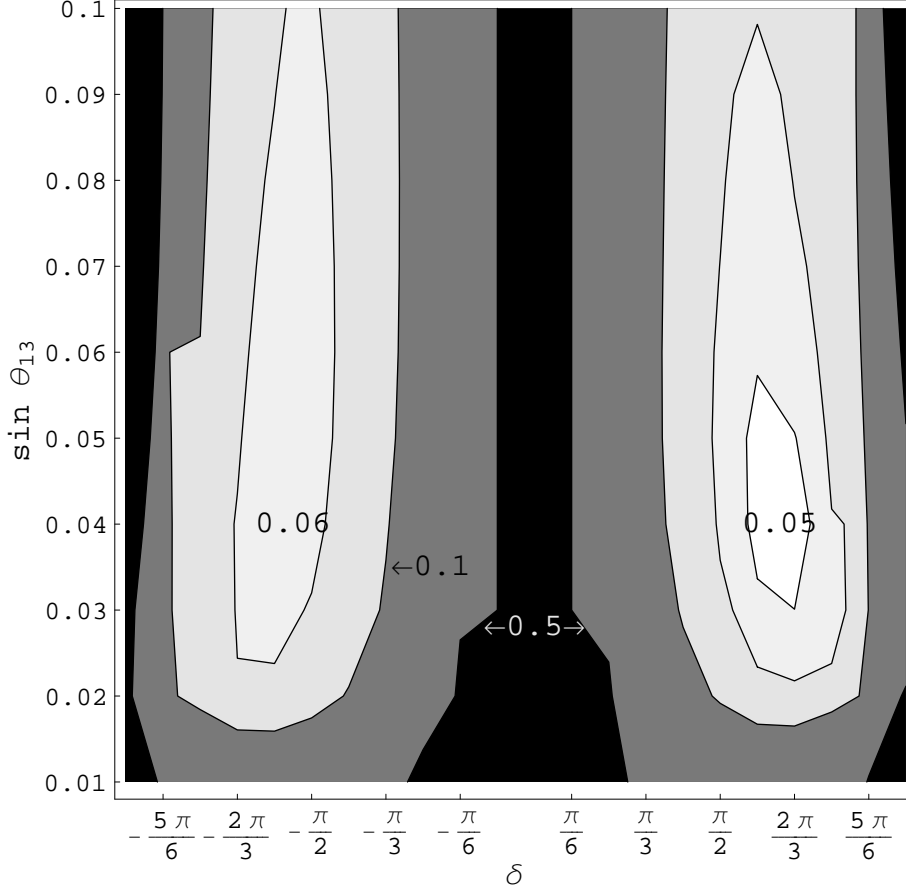


Figure 3.31: Required data size at $L = 1000\text{km}$ and $E_\mu = 10\text{ GeV}$ in the unit $[10^{21}/100\text{kt}]$ for various $\sin\theta_{13}$.

3.1.7 Possibility of Search for T violation

The other way to study the imaginary phase, δ , in neutrino oscillation is to compare the T-reversed transitions, such as $\nu_e \rightarrow \nu_\mu$ and $\nu_\mu \rightarrow \nu_e$. By the CPT theorem, in vacuum, T-violation implies CP-violation. Even in a terrestrial oscillation experiment, it is known that an asymmetric matter distribution does not introduce sizable CP-odd fake effects [?]. For instance, an asymmetric matter density distribution of about 10 % introduce a fake effect of a few % in magnitude compared with the genuine CP violation. In this subsection, a possibility of T-violation is discussed.

As was discussed, it is believed that the oscillation of $\nu_\mu \rightarrow \nu_e$ (or their anti-particles) is difficult to observe at a neutrino factory. It is due to the following fact. Since μ^- decays produce $\bar{\nu}_e$ as well as ν_μ , after the neutrino oscillation of $\nu_\mu \rightarrow \nu_e$, there will be $\bar{\nu}_e$ and ν_e . They will produce after charged-current interaction e^+ s and e^- s, respectively. However, in a large-mass detector, it is difficult to distinguish e^+ s from e^- s after their conversion to showers.

There is an idea to use the muon polarization to discriminate the oscillating and non-oscillating events. For instance, if the muon polarization

$P_\mu = -1$, no electron neutrino, $\bar{\nu}_e$, in the very forward direction of the muon would appear, resulting in that it is easy to observe $\nu_\mu \rightarrow \nu_e$. In reality, it would be hard to prepare 100 % muon polarization. Therefore, the most-practical way might be to do observation with different value of muon polarization and to extrapolate to -100 % for the muon (μ^-) polarization. The idea is not terribly new, but this is the first time to do detailed analysis.

3.1.7.1 Principle

The neutrino flux in the forward direction of a μ^- beam with its muon spin polarization P_μ is given by

$$\Phi_{\bar{\nu}_e} \propto (1 + P_\mu)y^2(1 - y) \quad (3.31)$$

$$\Phi_{\nu_\mu} \propto y^2(3 - 2 * y) + P_\mu y^2(1 - 2y), \quad (3.32)$$

where $y \equiv E_\nu/E_\mu$, and E_μ is the μ^- energy E_μ and E_ν is the neutrino energy. Thus, the non-oscillating event rate of $\bar{\nu}_e \rightarrow \bar{\nu}_e$ ($N_{\bar{\nu}_e \rightarrow \bar{\nu}_e}$) and the appearance event rate of $\nu_\mu \rightarrow \nu_e$ ($N_{\nu_\mu \rightarrow \nu_e}$) are given by

$$N_{\bar{\nu}_e \rightarrow \bar{\nu}_e} = (1 + P_\mu)N_3, \quad (3.33)$$

$$N_{\nu_\mu \rightarrow \nu_e} = N_1 + P_\mu N_2, \quad (3.34)$$

respectively. From these, the total rate of e -like events is given by

$$N_{e\text{-like}} = \beta_0 + P_\mu \beta_1. \quad (3.35)$$

$$\beta_0 \equiv N_1 + N_3 \quad (3.36)$$

$$\beta_1 \equiv N_1 + N_2 \quad (3.37)$$

Note that from eq.(3.33), for $P_\mu = -1$, $N_{e\text{-like}}$ is equal to $N_{\nu_\mu \rightarrow \nu_e}$. The e -like event rate at $P_\mu = -1$ is essentially the same as that of $N_{\nu_\mu \rightarrow \nu_e}$. It is illustrated in Fig. 3.32.

3.1.7.2 Procedure

The procedure is to estimate $N_{\nu_\mu \rightarrow \nu_e}$ at $P_\mu = -1$ by the extrapolation from the measured rates of different values of muon polarization.

Suppose that the measurements of e -like events of y_i with $N_i (\equiv N_{\mu^-}/f_i)$ appearance events for the μ^- polarization of $P_\mu = P_{\mu_i}$, ($i = 1 \cdots n$) are made. Here, N_{μ^-} is a total number of the muons with $P_\mu = 100\%$. Eq.(3.35) can be rewritten by,

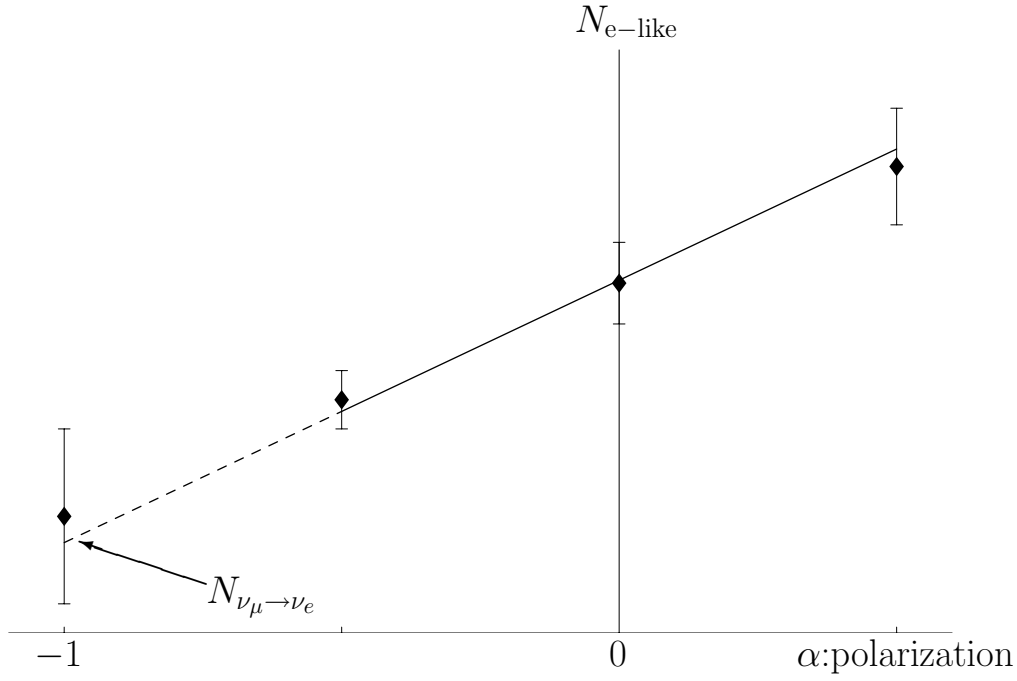


Figure 3.32: Graphical view of the idea. We have observations of e-like event with partially polarized muon beams and from them we estimate the event rate at $P_\mu = -1$.

$$N_{\text{e-like}} = \beta_0^* + P_\mu^* \beta_1, \quad (3.38)$$

$$\beta_0^* \equiv \beta_0 + \bar{P}_\mu \beta_1, \quad (3.39)$$

$$P_\mu^* \equiv P_\mu - \bar{P}_\mu, \quad (3.40)$$

$$\bar{P}_\mu \equiv \frac{1}{F} \sum_i \frac{P_{\mu_i}}{f_i}, \quad (3.41)$$

$$F \equiv \sum_i \frac{1}{f_i}. \quad (3.42)$$

The expectation values of y_i , \bar{y}_i is given by⁷

$$f_i \bar{y}_i = \beta_0 + P_{\mu_i}^* \beta_1. \quad (3.43)$$

It is assumed that y_i 's are large enough so that it would obey the normal distribution of $N(\bar{y}_i, \bar{y}_i)$. In this case, the likelyhood function to estimate β_0

⁷In the following we denote β_0^* by β_0 .

and β_1 is given by^{8 9}

$$-\log L = \sum_i \frac{\left\{ f_i y_i - (\beta_0 + P_{\mu_i}^* \beta_1) \right\}^2}{2 f_i^2 y_i}. \quad (3.44)$$

From this likelihood function we get the equations for the estimates of β_0 and β_1 as follows;

$$-\frac{\partial \log L}{\partial \beta_0} = \beta_0 \sum_i \frac{1}{f_i^2 y_i} + \beta_1 \sum_i \frac{P_{\mu_i}^*}{f_i^2 y_i} - \sum_i \frac{1}{f_i} \quad (3.45)$$

$$\begin{aligned} -\frac{\partial \log L}{\partial \beta_1} &= \beta_0 \sum_i \frac{P_{\mu_i}^*}{f_i^2 y_i} + \beta_1 \sum_i \frac{(P_{\mu_i}^*)^2}{f_i^2 y_i} - \sum_i \frac{P_{\mu_i}^*}{f_i} \\ &= \beta_0 \sum_i \frac{P_{\mu_i}^*}{f_i^2 y_i} + \beta_1 \sum_i \frac{(P_{\mu_i}^*)^2}{f_i^2 y_i}. \end{aligned} \quad (3.46)$$

Here we used the definitions of P_{μ}^* , eq.(3.40), and \bar{P}_{μ} , eq.(3.41) and drop the last term in the first line of eq.(3.46). Using these eqs.(3.45) and (3.46), we can estimate β_0 and β_1 in terms of y_i as follows:

$$\beta_0 = \frac{F}{D} \sum_i \frac{(P_{\mu_i}^*)^2}{f_i^2 y_i}, \quad (3.47)$$

$$\beta_1 = -\frac{F}{D} \sum_i \frac{P_{\mu_i}^*}{f_i^2 y_i}. \quad (3.48)$$

Here

$$D \equiv \left(\sum_i \frac{1}{f_i^2 y_i} \right) \left(\sum_i \frac{(P_{\mu_i}^*)^2}{f_i^2 y_i} \right) - \left(\sum_i \frac{P_{\mu_i}^*}{f_i^2 y_i} \right)^2. \quad (3.49)$$

Thus $N_{\nu_{\mu} \rightarrow \nu_e}$ (at $P_{\mu} = -1$) is estimated using eqs.(3.47) and (3.48) as

$$N_{\nu_{\mu} \rightarrow \nu_e} = \beta_0 + (-1 - \bar{P}_{\mu}) \beta_1. \quad (3.50)$$

⁸Exactly speaking, the denominator of eq.(3.44) is $f_i^2 \bar{y}_i$. However for simplicity, under the assumption that y_i 's are large, it can be replaced with $f_i^2 y_i$. This is justified since the non-oscillating event rates $N_{\bar{\nu}_e \rightarrow \bar{\nu}_e}$ at any polarization are large. (It does not depend on whether there are enough appearance event rate $N_{\nu_{\mu} \rightarrow \nu_e}$ as long as the polarization is not very close to -1.)

⁹We can construct the likelihood function with Poisson distribution. By this construction we get the same function as eq.(3.44) if we can assume that y_i 's are large enough.

How large statistical error does the estimate value have? Formally the variance of the estimate is given by

$$V(N_{\nu_\mu \rightarrow \nu_e}) = V(\beta_0 + (-1 - \bar{P}_\mu)\beta_1) \quad (3.51)$$

$$= V(\beta_0) + (-1 - \bar{P}_\mu)^2 V(\beta_1) + 2(-1 - \bar{P}_\mu)V(\beta_0, \beta_1) \quad (3.52)$$

where $V(\beta)$ is the variance of β , $V(\beta_0, \beta_1)$ is the covariance of β_0, β_1 .

It is impossible to evaluate the variance of $N_{\nu_\mu \rightarrow \nu_e}$ using eqs.(3.47) and (3.48) directly. Therefore we approximate it by the inverse matrix of the expectation value of Fisher's information.¹⁰ Fisher's information-matrix is given by

$$-\frac{\partial^2}{\partial \beta_i \partial \beta_j} \log L = \begin{pmatrix} \sum_i \frac{1}{f_i^2 y_i} & \sum_i \frac{P_{\mu_i}^*}{f_i^2 y_i} \\ \sum_i \frac{P_{\mu_i}^*}{f_i^2 y_i} & \sum_i \frac{(P_{\mu_i}^*)^2}{f_i^2 y_i} \end{pmatrix}, \quad (3.53)$$

and hence the variance matrix is given by

$$\frac{1}{D} \begin{pmatrix} \sum_i \frac{(P_{\mu_i}^*)^2}{f_i^2 y_i} & -\sum_i \frac{P_{\mu_i}^*}{f_i^2 y_i} \\ -\sum_i \frac{P_{\mu_i}^*}{f_i^2 y_i} & \sum_i \frac{1}{f_i^2 y_i} \end{pmatrix} \quad (3.54)$$

Thus, the estimate of $N_{\nu_\mu \rightarrow \nu_e}$ has its variance of

$$\begin{aligned} V(N_{\nu_\mu \rightarrow \nu_e}) &= \frac{1}{D} \left\{ \sum_i \frac{(P_{\mu_i}^*)^2}{f_i^2 y_i} + (-1 - \bar{P}_\mu)^2 \sum_i \frac{1}{f_i^2 y_i} - 2(-1 - \bar{P}_\mu) \sum_i \frac{P_{\mu_i}^*}{f_i^2 y_i} \right\} \\ &= \frac{1}{F} \left[2N_{\nu_\mu \rightarrow \nu_e} + N_{\bar{P}_\mu} \left\{ (-1 - \bar{P}_\mu)^2 \frac{\sum_i 1/f_i^2 y_i}{\sum_i (P_{\mu_i}^*)^2 / f_i^2 y_i} - 1 \right\} \right]. \end{aligned} \quad (3.56)$$

Here $N_{\bar{P}_\mu}$ is the estimate of event rate at $P_\mu = \bar{P}_\mu$ when we make use of N_{μ^-} .

3.1.7.3 Numerical check

Until here we have made several assumption: E.g. The likelihood function for the β 's is given by eq.(3.44), The variance of the estimate is given by the inverse of the Fisher's information matrix, and so on. Here we make

¹⁰Strictly speaking, the inverse matrix of the expectation value of Fisher's information gives the lower limit of the corresponding variance. However if the likelihood function is constructed well then it coincide with the variance and hence we use this approximation. We also approximate the expectation value of the Fisher's information by eq.(3.53) since we can assume that y_i 's are large number enough.

a following numerical calculation to check the theoretical argument. We calculate the extrapolated value at $P_\mu = -1$ which indeed coincides with the theoretical expectation value $\bar{y}|_{P_\mu=-1}$ and the variance of it which is actually given by eq.(3.56).¹¹

The algorithm for this check is as follows:

0. Select several values of the polarization P_{μ_i} where we make an experiment.
1. Fix all parameters, say, the theoretical parameters (e.g. mixing angle), muon energy and so on, and then calculate the expectation of event rates in each points (\bar{y}_i).
2. Generate the “actual” event rates y_i according to Poisson distribution with its expectation value \bar{y}_i
3. Substitute this event set into eqs.(3.47),(3.48), and using these β ’s find the extrapolated value at $P_\mu = -1$ from eq.(3.50).
4. Repeat “2” and “3” for very many times and find the type of distribution of the extrapolated value.

We made this virtual experiment for various parameters and found that the extrapolated value obeys the normal distribution with its mean value $\bar{y}|_{P_\mu=-1}$ and its variance given by eq.(3.56).

3.1.7.4 Sensitivity for T Violation

In this section we see the sensitivity to T-violation using the idea studied previously. We define the statistics to see T-violation effect

$$\chi^2 = \frac{(N_0\bar{N} - \bar{N}_0N)^2}{N_0^2V + \bar{N}_0^2N}, \quad (3.57)$$

where

$$\begin{aligned} N &: N_{\nu_e \rightarrow \nu_\mu}, \\ \bar{N} &: N_{\nu_\mu \rightarrow \nu_e}, \end{aligned}$$

and the subscript 0 indicates the estimate of the event rate with CP violating phase $\delta = \delta_0, \delta_- = \{0, \pi\}$. Note that in the denominator of χ^2 there is V . Though V is given by eq.(3.56) theoretically, in the following sensitivity plot we calculate it using the numerical method explained in sec.3.1.7.3.

For simplicity we assume that $N_i = N_{\mu+}$ and show how many muons decays we will need to observe T-violation effect In the next subsection we

¹¹We only checked the case $f_i = f = \text{const.}$

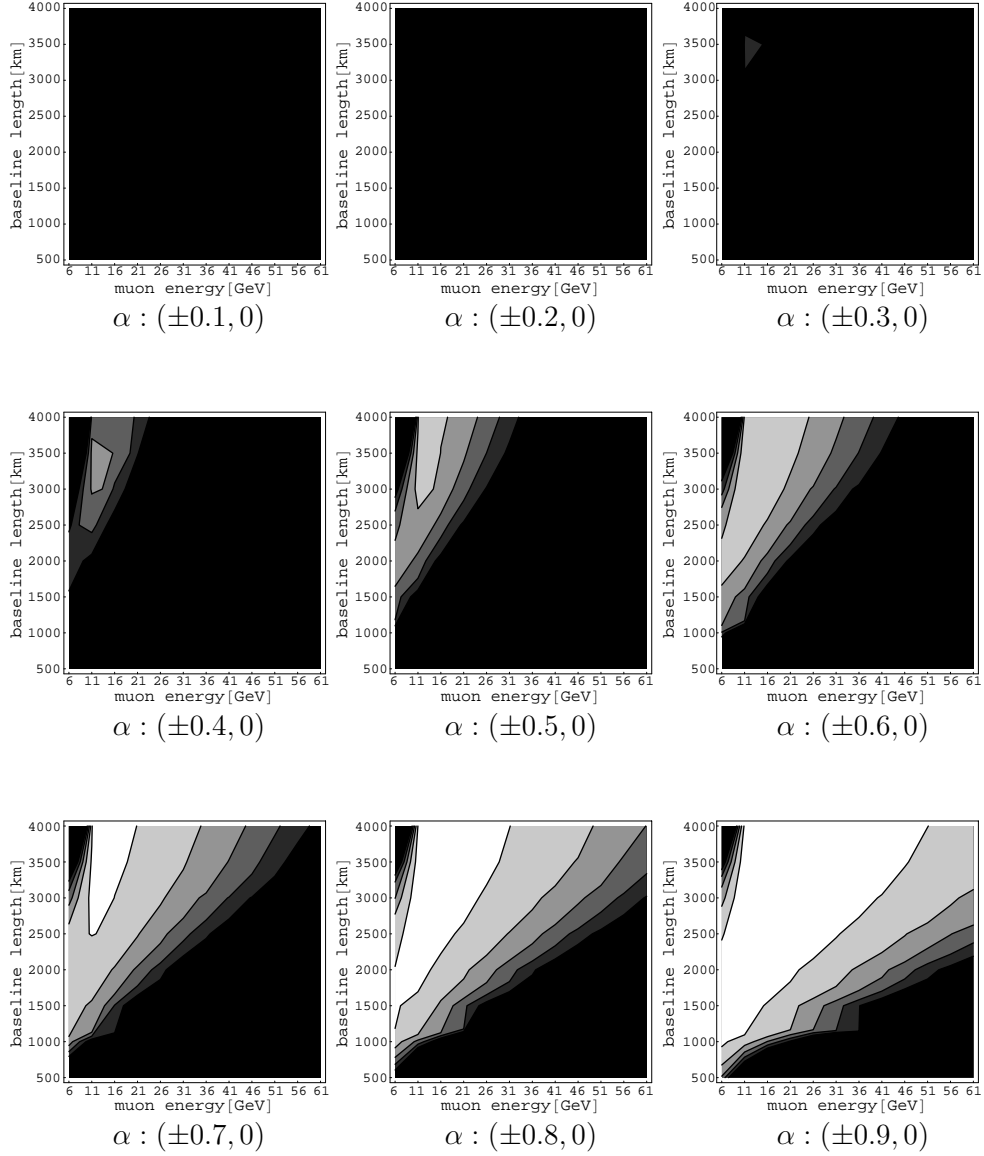


Figure 3.33: Sensitivity plot as a function of the polarization P_μ . In this plot the necessary data sizes (in the unit $10^{21} \times 100\text{kt}$) are plotted as a function of the muon energy and the baseline length.

discuss how we should distribute the polarizations of muons and how the sensitivity plot changes with the change of the distribution. For graphs we use the theoretical parameter, $\sin \theta_{12} = 0.5, \sin \theta_{23} = 1/\sqrt{2}, \sin \theta_{13} = 0.1, \delta m_{31}^2 = 3 \times 10^{-3} \text{eV}^2, \delta m_{21}^2 = 10^{-4} \text{eV}^2, \delta = \pi/2$. The sensitivity is almost proportional to

$$(\sin \delta \sin 2\theta_{12} \sin 2\theta_{23} \cos \theta_{13} \frac{\delta m_{21}^2}{\delta m_{31}^2})^2. \quad (3.58)$$

We find that we need at worst $\alpha = \pm 0.3$ to observe T-violation effect with total 10^{21} μ and 100kt detector. On the other hand, on the contrary to the sensitivity of CP-violation effect usually discussed, since the V will convey the largest error among other uncertainties like other statistical errors, systematic errors, even if we include other errors in the statistical analysis the sensitivity will not change drastically.

In the remaining of this section, we see what we can learn from the theoretical analysis.

3.1.7.5 How to distribute μ^+ and μ^- ?

To see the most efficient ratio between the numbers of $\mu^+(N_{\mu^+})$ and $\mu^-(N_{\mu^-})$ for a fixed distribution of N_{μ^-} at each polarization f_i , we rewrite the χ^2 to factor out the sensitivity to the numbers:

$$\begin{aligned} N &\rightarrow N_{\mu^+} N, \\ \bar{N} &\rightarrow N_{\mu^-} \bar{N} \\ V &\rightarrow N_{\mu^-} V \end{aligned}$$

$$\chi^2 \rightarrow \frac{(N_0 \bar{N} - \bar{N}_0 N)^2}{N_0^2 V / N_{\mu^-} + \bar{N}_0^2 N / N_{\mu^+}}. \quad (3.59)$$

If the total numbers of muon is fixed, then

$$\sum N_i + N_{\mu^+} = \sum_i \frac{N_{\mu^-}}{f_i} + N_{\mu^+} = F N_{\mu^-} + N_{\mu^+} = N \quad (3.60)$$

is a fixed number. Here F is given by eq.(3.42). Under the condition the most efficient ratio of the numbers of $\mu^+(N_{\mu^+})$ and $\mu^-(N_{\mu^-})$ is given by

$$\frac{N_{\mu^+}}{\sum N_i} = \frac{\bar{N}_0}{N_0} \sqrt{\frac{N}{A}}, \quad (3.61)$$

where A is given by eq.(3.56) $\times F$.

Since the oscillation probability is at most a few % while $N_{\bar{P}_\mu}$ in eq.(3.56) is essentially given by non-oscillation event, using the fact that $N/N_{\bar{P}_\mu} \sim O(0.01)$ and $(\sum_i 1/f_i^2 y_i)/(\sum_i (P_{\mu_i}^*)^2/f_i^2 y_i)$ in eq.(3.56) is much larger than 1 in a realistic case, we find that we need much larger number of μ^- . Therefore by tuning the ratio of the numbers of μ^+ and μ^- we will get higher sensitivity to T-violation effect by several tens %.

3.1.8 The dependence of polarization pattern

In general, muons are produced with a polarization distribution. In this subsection we discuss the dependence on the distribution of the polarization assuming that we can make use of the full information on the polarization.¹²

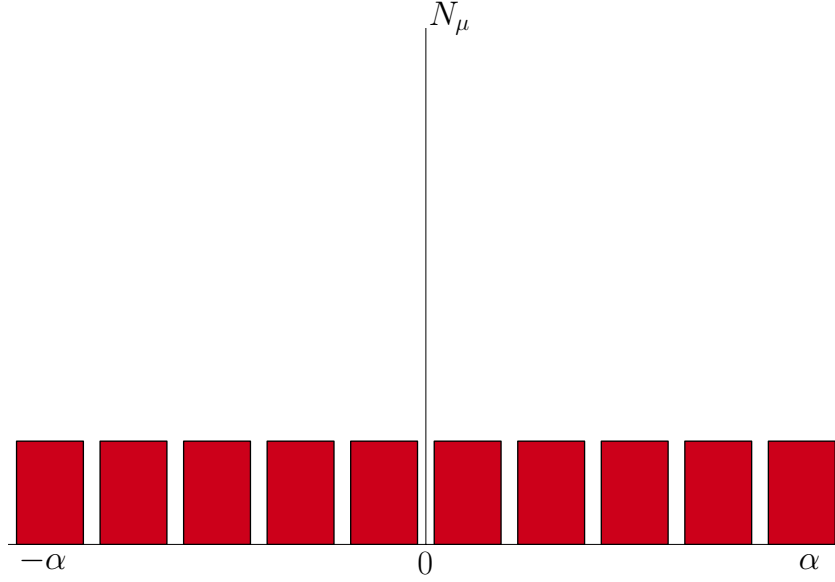


Figure 3.34: Distribution assumed in this subsection of the polarization of muon just after generated from pion. It distributes from $-P_\mu$ to $+P_\mu$ uniformly.

Here We assume for simplicity that the produced muon has a uniform distribution of the polarization from $-P_\mu$ to $+P_\mu$ as shown in fig.3.34.

Let's consider the case that we produce muon beam with its polarization at $\pm P_\mu$ as shown in fig.3.35.

Though the fact that we have a polarized muon with its polarization P_μ will mean that we use muons at the $(1/M)$ edge of the distribution, first we assume that we can make a polarized beam at $\pm P_\mu$ without loss of the muon number. In this case the variance (3.56) of extrapolated appearance number has the dependence, in the case of the polarization shown in fig.3.34,¹³

$$\frac{1}{F} \frac{\sum_i 1/f_i^2 y_i}{\sum_i (P_{\mu_i}^*)^2 / f_i^2 y_i} - 1 \propto \frac{3}{P_\mu^2} - 1, \quad (3.62)$$

¹²For example, we make a long length (say 100m) beam circulated in beam line where we know the distribution of the polarization. If we have very good time resolution, that is, we can measure which part of the beam neutrino comes, then we can know the polarization of the muon in decay.

¹³Here we assume that we do not have very large polarization. It means that y_i 's are almost constant.

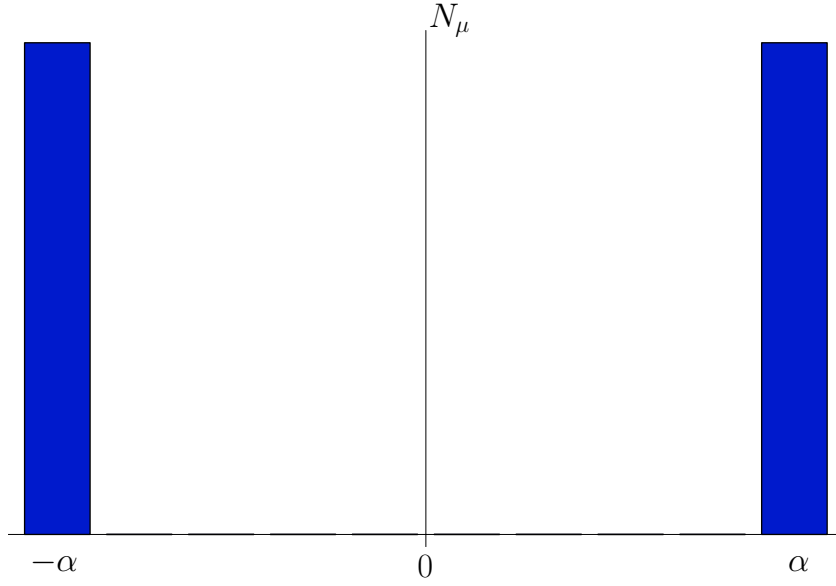


Figure 3.35: Distribution of the polarization of μ . There are only muons with their polarization around $-P_\mu$ and $+P_\mu$.

while in fig.3.35,

$$\frac{1}{F} \frac{\sum_i 1/f_i^2 y_i}{\sum_i (P_{\mu_i}^*)^2 / f_i^2 y_i} - 1 \propto \frac{1}{P_\mu^2} - 1. \quad (3.63)$$

Therefore we have higher sensitivity by three times.

However, as mentioned above, if to produce muon beam shown in fig.3.35 means merely that we make use of only the $(1/M)$ edge of of the distribution, then the sensitivity is proportional to

$$\frac{1}{F} \frac{\sum_i 1/f_i^2 y_i}{\sum_i (P_{\mu_i}^*)^2 / f_i^2 y_i} - 1 \propto \frac{M}{P_\mu^2} - 1. \quad (3.64)$$

Then the sensitivity is better by $3/M$.

To discuss the sensitivity as function of the distribution of the polarization, we need the experimental setup. The extension of the discussion here for each experimental setup is quite straightforward.

Appendix A

PRISM

A.1 PRISM Overview

PRISM is the project to produce a high-intensity low-energy muon beam with narrow beam energy spread and small beam contamination. PRISM stands for “*Phase Rotated Intense Slow Muon source*”. The beam intensity of PRISM is about $10^{11} - 10^{12} \mu^\pm/\text{sec}$. which is about four orders of magnitude that presently available. Phase rotation is used to make the spread of beam energy narrower. It is critical to carry out stopped muon experiments.

One of the most important physics topics expected with PRISM is searches for muon lepton flavor violation [21]. In particular, search for $\mu^- - e^-$ conversion in a muonic atom is the most promising with PRISM for further improvement. In an experiment of $\mu^- - e^-$ conversion, μ^- s are stopped in a target material and a conversion e^- of its energy of a muon mass (~ 106 MeV) is detected. To reduce energy loss in the muon-stopping target, it should be as thin as possible. The aimed sensitivity is about 10^{-18} [10].

PRISM is based on the following components.

- large-solid angle pion capture (with a high solenoid field)
- a ($\pi \rightarrow \mu$) decay section,
- phase rotation.

In the solenoid pion capture section, low-energy pions and muons are trapped in a high solenoidal magnetic field (such as 10 T or more) to achieve high intensity. In the phase rotation section, slow muons are accelerated, and fast muons are decelerated by a strong radio-frequency (RF) electric field to yield a narrow longitudinal momentum spread. A schematic view of the basic concepts of solenoid capture and phase rotation is shown in Fig.A.1, where the solenoid capture section followed by the phase rotation section is seen.

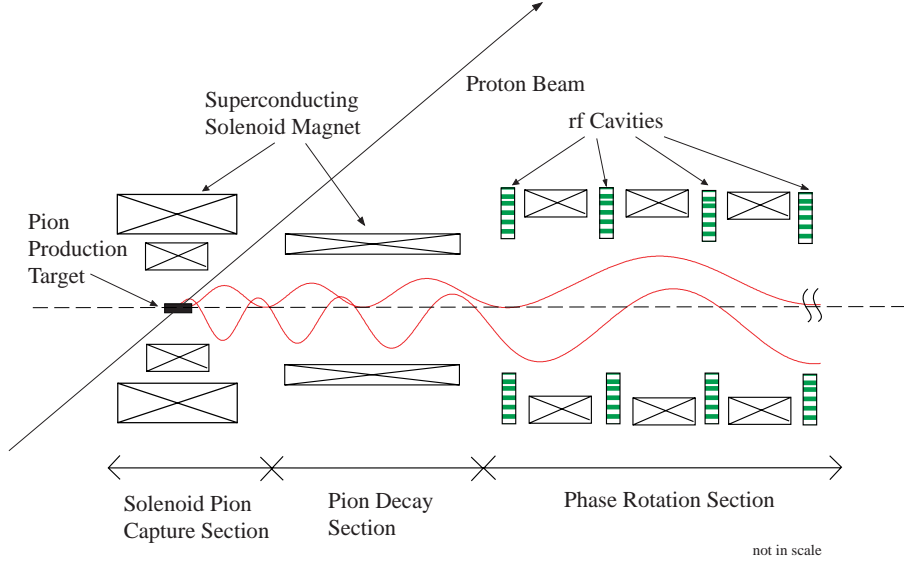


Figure A.1: Conceptual layout of a high intensity muon source

Schematic layout of PRISM is shown in Fig.A.2. It combines high-field pion capture of about 10-12 T, the $\pi - \mu$ decay section of a 10-m long superconducting solenoid magnet, and phase rotation. One of the features of PRISM is to do phase rotation at a Fixed-Field Alternating Gradient synchrotron (FFAG), which has several advantages, such as a large momentum acceptance. The parameters of PRISM is shown in Table A.1.

Table A.1: FFAG-based PRISM parameters

item	value
Intensity	$10^{11} - 10^{12} \mu^\pm/\text{sec}$
Beam kinetic energy	20 MeV ($\sim 67 \text{ MeV}/c$)
Beam energy spread	a few % (after phase rotation)
Beam repetition	more than 1 kHz
Pion extraction	backward
Pion capture field	6 – 12 T ($P_T < 90 \text{ MeV}/c$)*

* The pion capture scheme is more modest than that for a neutrino factory.

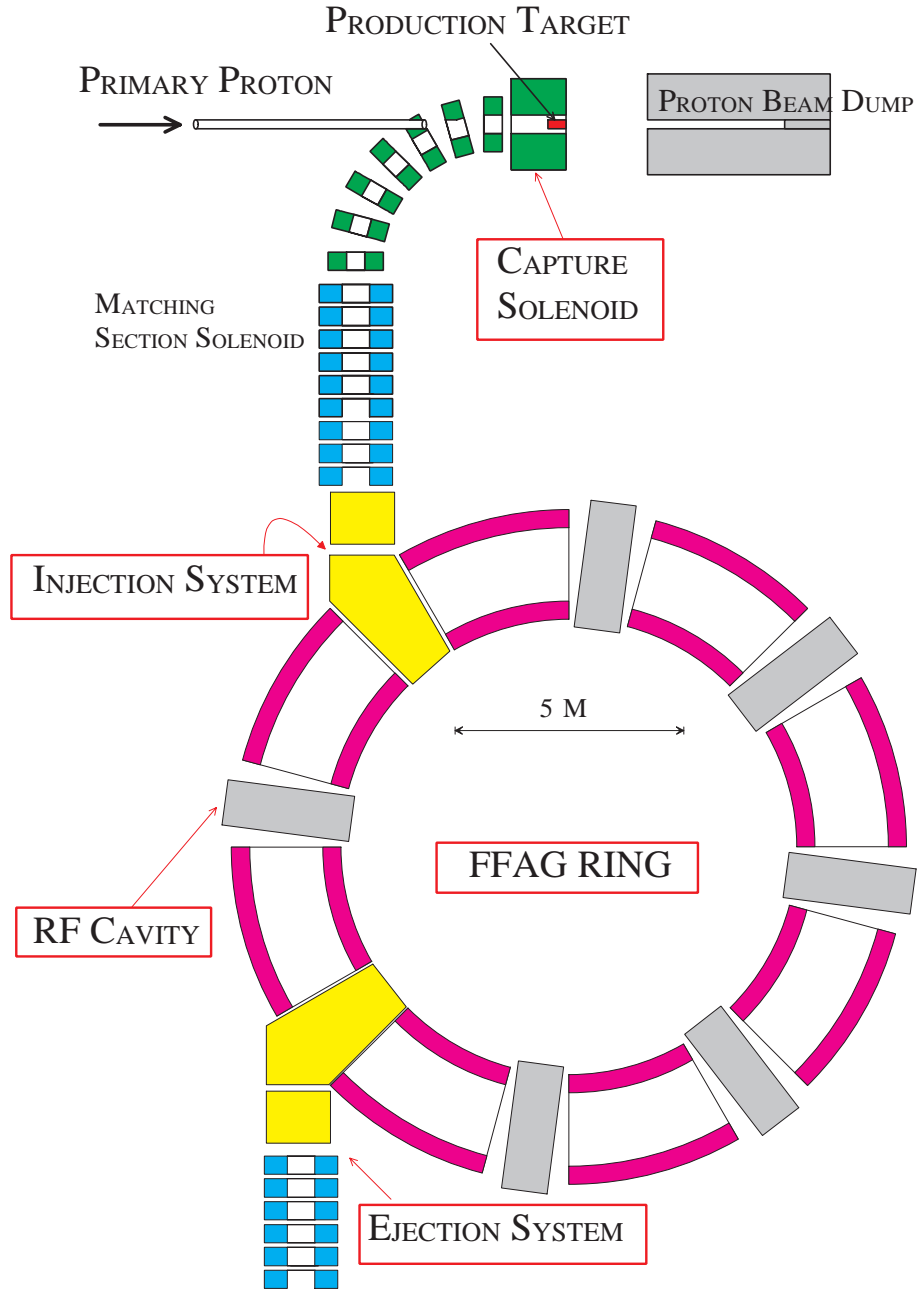


Figure A.2: Schematic layout of FFAG-based PRISM

A.2 Solenoid Pion Capture

The pion production is estimated from the MARS Monte Carlo simulation developed at Fermilab. Fig.A.3 shows the distribution of the longitudinal momentum (P_L) of pions for different total momentum region (P_{total}) when

a proton beam of 50 GeV (which is expected from the 50-GeV PS) is impinge into a Pt target. For the low momentum region of interest ($P_{total} < 0.1$ GeV/ c) the distribution of pions is almost uniform, whereas at higher momentum region pions are emitted forward. At PRISM, to reduce energetic pions in a beam, backward extraction has been adopted, in which the pion yield of interest is the same as that of forward taking.

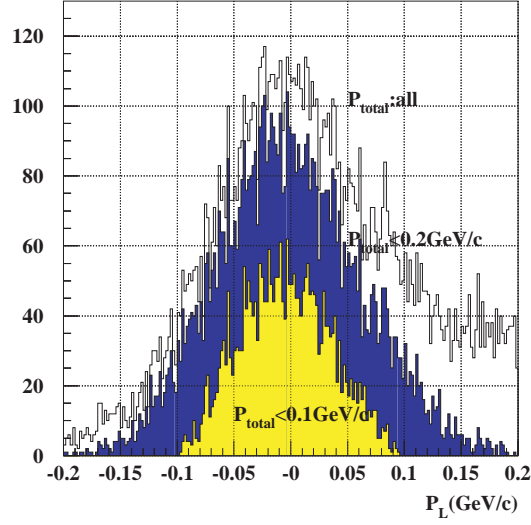


Figure A.3: Longitudinal momentum distribution of pions for different total momentum regions. At low energy, the distribution is almost uniform.

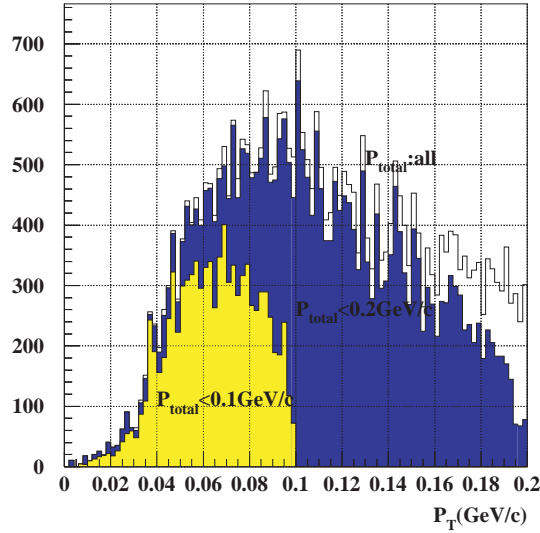


Figure A.4: Transverse momentum distribution of pions produced for the different total momentum regions.

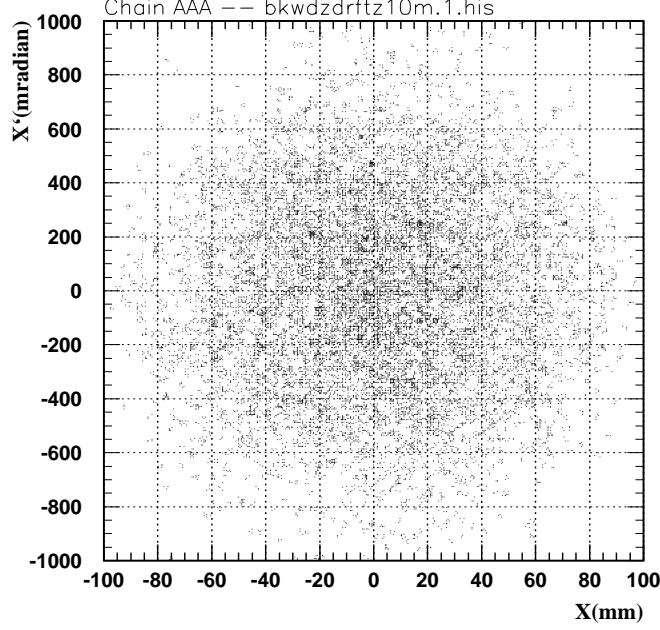


Figure A.5: Phase space distribution of muons at the exit of the decay solenoid channel.

When the clear inner bore of a superconducting magnet is R and a magnetic field of B , the maximum transverse momentum (P_T) is given by

$$P_T(\text{MeV}/c) \leq P_T^{max} = 0.3 \times B(\text{kG}) \times \frac{R(\text{cm})}{2}. \quad (\text{A.1})$$

For instance, $B=10$ T, $R=6$ cm gives $P_T \leq 90$ MeV/ c . Fig.A.4 shows the transverse momentum distribution for the different total momentum regions. For $P_{total} \leq 100$ MeV/ c , the pion yield of 0.2 / proton is obtained. Since the proton intensity of the 50-GeV PS is 10^{14} protons/sec, it is naively estimated that about 2×10^{13} pions /sec can be captured.

The pions thus captured are injected into the $\pi \rightarrow \mu$ decay section, which consists of a long superconducting solenoid magnet. The phase space distribution at the exit of the decay solenoid is given in Fig.A.5.

A.3 Phase Rotation

The phase rotation is to accelerate slow muons and to decelerate fast muons by a strong radio-frequency (RF) electric field, yielding a narrow longitudinal

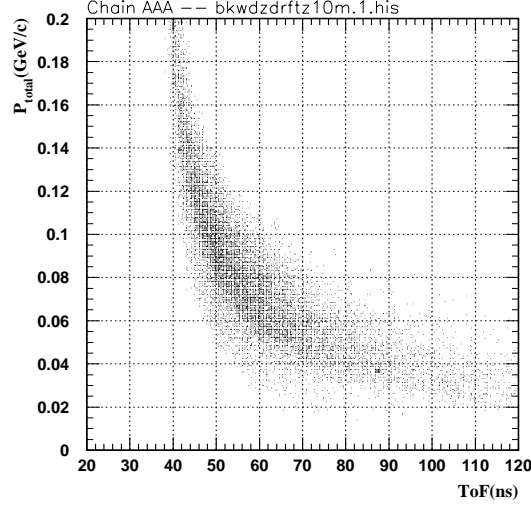


Figure A.6: Distribution of P_{total} versus ToF for pions at low energy.

momentum spread. To identify fast and slow muons by their time of flight from the production time, a very narrow pulsed proton beam must be used.

After a long drift, slow pions come late and fast pions come early. The distribution in P_{total} vs. a time of flight (ToF) is shown in Fig.A.6.

One of the features of PRISM is to do phase rotation at a Fixed-Field Alternating Gradient synchrotron (FFAG), which has several advantages such as a large momentum acceptance and large emittance. The present design of the FFAG ring has a diameter of about 10 m. About five turns of muons in the FFAG ring will complete phase rotation. Since PRISM is focused on experiments with stopped muons, the central muon momentum of the FFAG ring is set to 68 MeV/c (corresponding to a kinetic energy of 20 MeV). The simulation of phase rotation at FFAG with a sinusoidal wave form of rf is shown in Fig.A.7, where the non-linear relation between energy and time makes the phase rotation worse. In Fig.A.8, a saw-tooth wave form is tried, where the original momentum spread of $\pm 20\%$ is reduced down to $\pm 2\%$ after phase rotation.

A.4 Time Structure

The ideas of high-field pion capture and phase rotation have emerged in studies of a $\mu^+\mu^-$ collider at the high-energy frontier. Although there are many common R&D items between a low-energy muon source and a $\mu^+\mu^-$ collider, there are discussions on whether the front-end muon collider (FMC) could be

directly used in experiments with muons. The FMC will run with a pulsed beam of slow repetition (at typically 15 Hz). However, most experiments with muons require a beam with a high duty factor, because of the reduction of the instantaneous rate. The precise requirement on the beam time structure depends on the type of experiments. For instance, searches for $\mu^+ \rightarrow e^+ \gamma$ and $\mu^+ \rightarrow e^+ e^+ e^-$ must use a continuous beam to reduce the instantaneous rate, whereas searches for $\mu^- - e^-$ (or $\mu^- - e^+$) conversion, $\text{Mu} - \overline{\text{Mu}}$ conversion and a measurement of the muon lifetime need a pulsed beam with a pulse separation of an order of the muon lifetime ($\sim \mu\text{sec}$). Thus, independent R&D items, in particular concerning phase rotation, exist in a low-energy muon source, such as in PRISM.

Its R&D program starts from a relatively low repetition rate ($\sim \text{kHz}$), and aims at a higher repetition in the future. This repetition rate is limited at present by that of a kicker magnet for injection and extraction of a beam to FFAG.

A.5 PRISM at the 50-GeV PS Experimental Hall

The size of the PRISM-FFAG ring is about 10 m in diameter. Together with space for power supplies of rf cavities and magnets, an area of $20 \times 20 \text{ m}^2$ is needed. Also, a 10-m long solenoid magnet for $\pi \rightarrow \mu \nu$ decay is needed. The size of the experimental area is about $10 \times 10 \text{ m}^2$ is sufficient. A possible layout of PRISM in the 50-GeV PS experimental hall is shown in Fig.A.9.

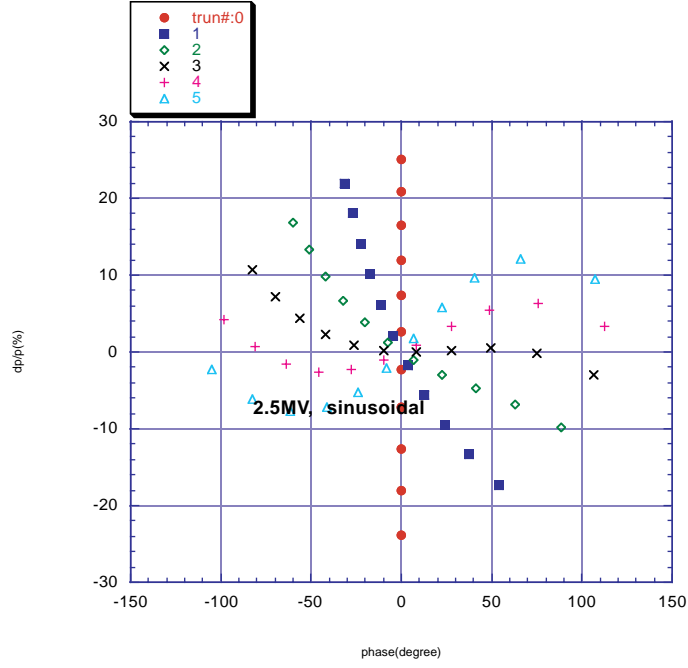


Figure A.7: Simulation of phase rotation at FFAG with sinusoidal wave form. A nonlinear relation between energy and arrival time affects the phase rotation performance bad.

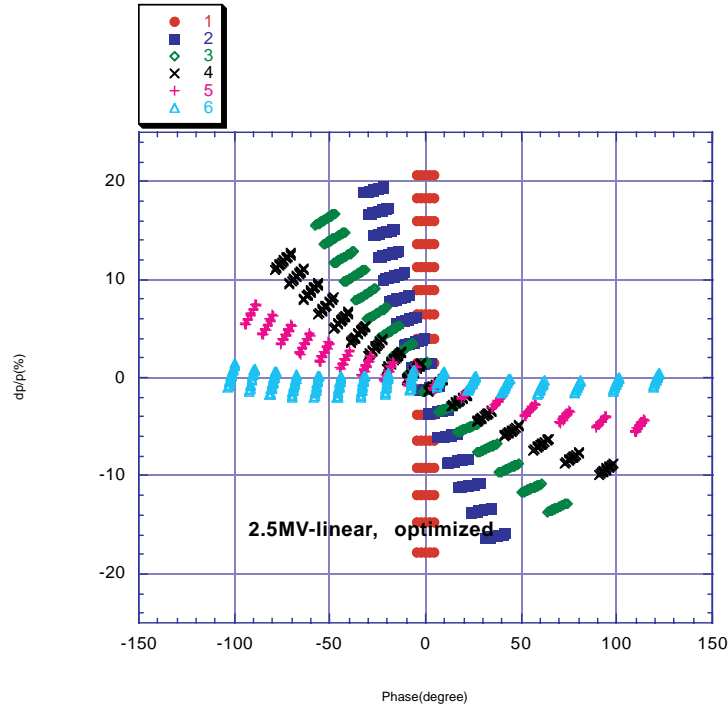


Figure A.8: Simulation of phase rotation at FFAG with a saw-tooth rf wave form. After 5 turns, an energy spread becomes \pm a few %.

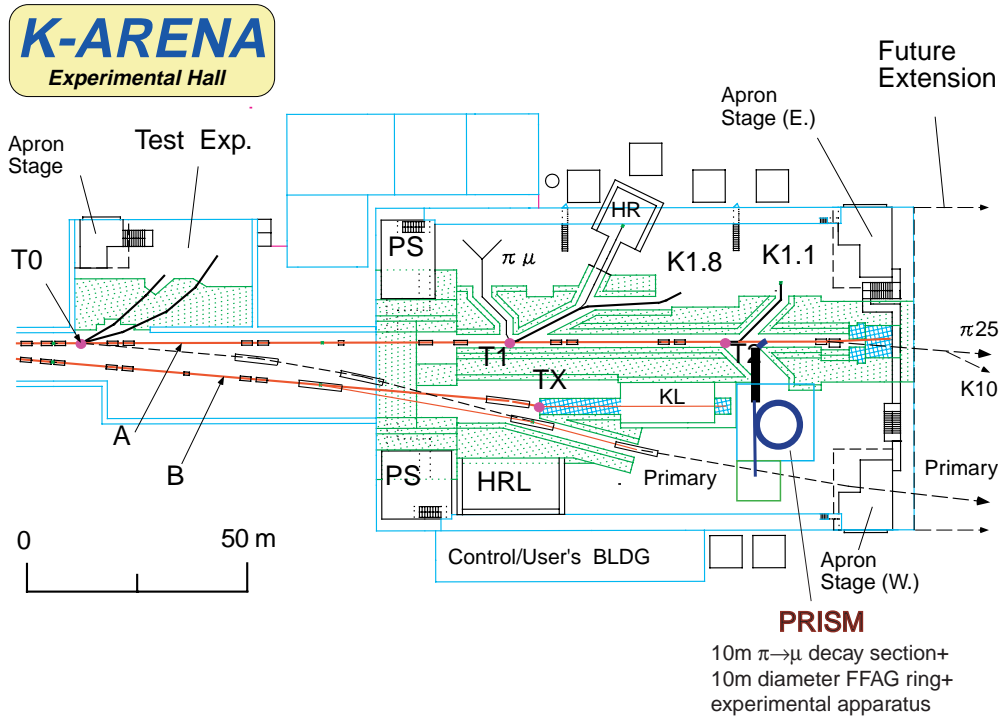


Figure A.9: PRISM in the experimental hall of the 50-GeV PS in the KEK/JAERI joint project.

Appendix B

FFAG Principle

B.1 FFAG and Other Accelerators

Let us mention a little about a Fixed Field Alternating Gradient (FFAG) synchrotron. As the name stands for, the most difference from an ordinary Alternating Gradient (AG) synchrotron (hereafter, just a synchrotron) comes out of DC operation of magnets.

Magnets of a synchrotron are AC operated in accordance with beam momentum such that the average radius, and therefore the path length, is constant. As a consequence, when a light rest mass particle such as an electron is accelerated in a synchrotron, speed of a particle reaches speed of light quickly so that the revolution frequency becomes constant. However, speed of a heavy particle such as a proton is slowly increased. Unless a particle is accelerated to high enough, say a few hundred GeV, revolution frequency varies with momentum although the path length is constant.

To the contrary, the average radius in a FFAG synchrotron increases (or decreases in some peculiar field configurations) as a particle is accelerated just like a cyclotron. However, unlike a cyclotron, different momentum particles have different revolution frequencies. In other words, isochronous condition is violated purposely. That makes longitudinal focusing and synchrotron oscillations. Of course, the rf frequency of an accelerating cavity has to follow the speed of a particle. But unlike proton synchrotrons, in which the rf frequency is determined with the excitation of bending magnets, the rf frequency pattern and therefore the momentum pattern in time is made solely by itself free from other references. Table B.1 shows the function of magnets and rf in various accelerators.

Table B.1: Operation of magnet and rf in different accelerators

	constant frequency	variable frequency
constant bending field	cyclotron	FFAG synchrotron
variable bending field	electron synchrotron	proton synchrotron

B.2 Zero Chromaticity

In transverse directions, it has alternating gradient (or strong) focusing. Free from the isochronous condition which was required in a cyclotron, a field index of each gradient magnet can be large determined only by the transverse stability of betatron oscillations. Careful optimization of transverse tunes avoiding strong resonances are possible. That strong focusing is valid for wide range, for example a factor of 3 as a ratio of the highest momentum to the lowest one. In principle, the transverse tune is constant for that whole range. That is called, in terms of accelerator terminology, zero chromaticity. A FFAG with zero chromaticity satisfied is called "a scaled machine". Zero chromaticity is desirable to accelerate a beam from injection to extraction with constant field magnets. It is also ideal to accumulate a wide spread momentum beam.

The first principle of FFAG with zero chromaticity can be described with the following two conditions.

$$\frac{\partial}{\partial p} \left(\frac{K}{K_0} \right) \Big|_{\vartheta=const.} = 0, \quad (\text{B.1})$$

where K_0 is average curvature and K is local curvature. θ is generalized azimuth. That imposes geometrical similarity. In addition

$$< \frac{\partial n}{\partial p} \Big|_{\vartheta=const.} = 0, \quad (\text{B.2})$$

where n is field index of magnet and constancy of n at corresponding orbit points is assured. The magnet which has the following function satisfied those conditions.

$$B = B_0 \left(\frac{r}{r_0} \right)^k \quad (\text{B.3})$$

In fact, there is a FFAG with non zero chromaticity or a non scaled one, in which transverse tunes varies as a particle gets accelerated. That occurs because the magnetic field distribution in a real magnet is not perfect as described. In order to simplify magnet design, sometimes non scaled machine is introduced purposely.

Those non scaling machines may be adequate for muon applications since there is only a few turns in each acceleration process.

B.3 Large Acceptance

In a synchrotron, acceptable momentum spread is limited by two factors. One is a bucket height in longitudinal phase space determined by rf voltage. Above that, a particle is not bounded and no synchrotron oscillations is expected. The other is momentum acceptance. A higher momentum particle has larger bending radius so that it circulates (usually) outer orbit. Dispersion function is the measure of displacement due to momentum spread. Since the vacuum pipe has a limited radius in transverse plane, a higher or lower particle hits the wall of pipe even though a betatron amplitude is zero. The momentum acceptance is a few percent in terms of dp/p in an ordinary synchrotron.

FFAG, on the other hand, has a potential of acceleration of a beam with much higher momentum spread. As we have mentioned already, the magnets are DC operated and it covers focusing from injection to extraction. The momentum ratio through a cycle is 3 for our design. In other words, the momentum acceptance is $\pm 50\%$ if we take the central momentum of a beam matched to the mean value of injection and extraction momentum. As for the bucket height, higher voltage makes higher bucket height. The bucket height is proportional to the square root of the voltage.

B.4 Radial and Spiral Type

Depending on the magnet profile in θ direction, there are mainly two kinds of FFAG; one is radial sector type and the other is spiral sector one. A radial sector type has a magnet whose entrance and exit faces are on radial line drawn from the machine center. There are normal and reverse bending magnets with nonlinear gradient which provide focus and defocus property in each transverse plane. Focusing and defocusing actions come also from an angle between entrance and exit orbit and the magnet face.

A spiral sector type has no reversed bending magnets. The alternating gradient focusing action comes mainly from the edge angle. That edge focusing acts in alternative way at the entrance and at the exit in addition to the main body field which has the same field variation in a radial direction as that of radial sector type. Higher momentum particle needs stronger focusing action so that the edge angle becomes larger at outer radius resulting in spiral shape of magnets.

B.5 Historical Background

The FFAG idea was first introduced by several people independently in early 1950's right after the AG principle was found. Electron models, both radial and spiral sector types, to prove the principle were made. They are a few meter in size and the output energy is less than 1 MeV. Extensive study was carried out at Midwestern University Research Associate (MURA) and a proposal to construct a few 10 GeV machine was made. However, an ordinary synchrotron was chosen for pursuing the energy frontier and the development as well as MURA itself died out in early 1960's. By the way, a lot of inventions which are nowadays common to the community were first emerged in the MURA era. Those are rf stacking, adiabatic capture, and concept of separatrix, among others.

In 1980's, demands of high intensity machine draw people's attention to a FFAG accelerator. It is true that FFAG was not the right choice to explore the energy frontier because of relatively large magnets due to orbit excursion between injection and extraction momenta. However, large acceptance and possible high repetition cycle are best for high intensity with medium energy machine. There were several study mostly in Europe and Japan but no real machine was constructed. Some difficulties still exist to realize a real scale FFAG. One is the modeling of a magnet. The magnet for FFAG requires nonlinear gradient as described in Eq. B.3. Shaping of magnet pole to make a design field needed iterative efforts. The other difficulty, that is most essential, is the rf cavity which works in wide frequency range with large physical aperture, especially in horizontal direction.

Both items are overcome, recently. As for the magnet shaping, design is now efficiently done with a help of 3D magnetic field computation code like TOSCA. More fundamental breakthrough comes with a new type of a rf cavity equipped with magnetic alloy (MA). Because of the very high permeability, a MA cavity has both high shunt impedance and wide band frequency range at the same time. From the fabrication point of view, MA is a tape in its original form so that any kind of core shape is possible.

With those recent development, another proof of principle machine, this time the proof of proton acceleration with 1 kHz repetition rate, was constructed at KEK. The first beam is commissioned in June 2000 and the design procedure is established. About the status of the PoP machine and the larger machine followed will be described in the next appendix.

Appendix C

R&D Status of POP FFAG

C.1 Overview

Recently, the demand of high intensity accelerators has been recognized in various scientific field, and a FFAG accelerator has attracted attention as one of the promising candidates of such. However, after the proposal of the FFAG principle and the very initial R&D activity done by the MURA project that was the electron FFAG ring, no proton FFAG accelerator has not been developed. At the time when the FFAG principle was proposed, there were two major bottle-necks in the design of FFAG. They are

- *Lack of reliable numerical magnetic field-calculation codes,*
The FFAG machine obtains its focusing force through the strong non-linear field. In order to design the magnets with such a non-linear field, numerical calculations are indispensable. However, in 1960's, there were no reliable code to do them.
- *Lack of a high gradient RF cavity to make fast beam acceleration possible*

Now, those difficulties has overcome. The high-gradient cavity using magnetic alloy (MA) core has been developed at KEK, and it has solved the difficulty associated with RF acceleration. Also, we have now a developed 3D field calculation code, such as TOSCA, which offers a tool of numerical field calculations. Therefore, a time to build FFAG machines has come. We could re-establish the FFAG principle with advanced accelerator techniques. Under the above motivations, the POP(Proof Of Principle) FFAG machine was developed at KEK,

- to establish the FFAG principle,
- to prove the fast acceleration by FFAG synchrotron, and

- to demonstrate the large acceptance of FFAG synchrotron.

It should be noted that it is the first **proton** FFAG accelerator in the world. The schematic layout and the picture of the POP FFAG are shown in Figs. C.1 and C.2, respectively.

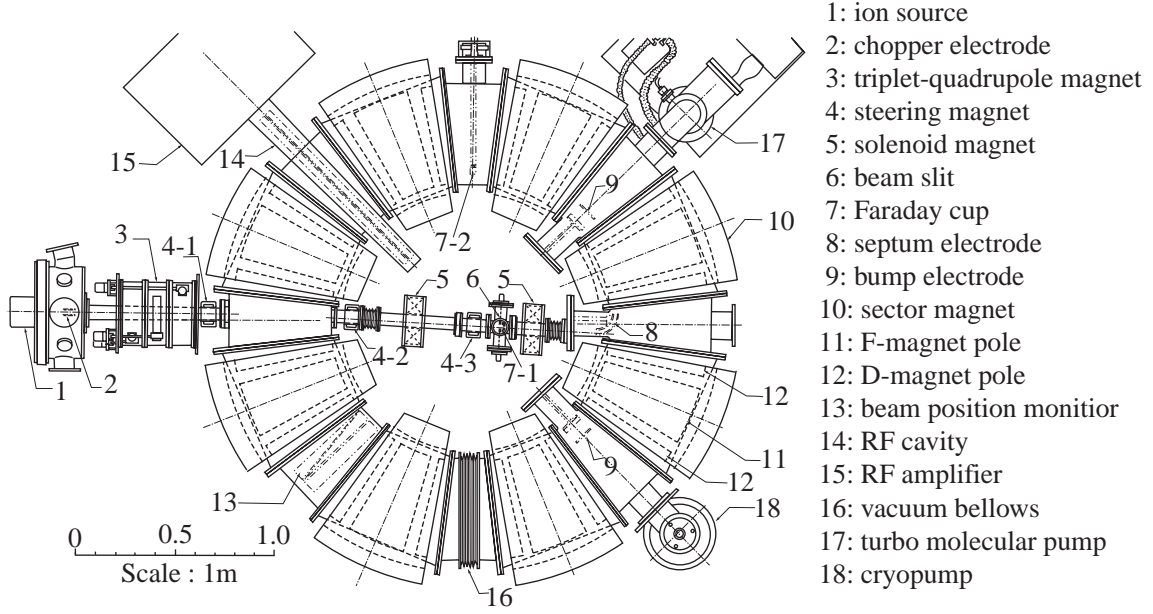


Figure C.1: Layout of the POP FFAG

Table C.1 summarizes the main design parameters.

Table C.1: FFAG POP model parameters

Type of magnet	Radial sector type(Triplet)
No. of sectors	8
Field index(k -value)	2.5
Energy	50keV(injection) - 500keV
Repetition rate	1kHz
Magnetic field	Focus-mag. : 0.14~0.32 Tesla Defocus-mag. :0.04~0.13 Tesla
Radii of closed orbit	0.81 ~ 1.14
Betatron tune	Horizontal : 2.17~2.22 Vertical : 1.24~1.26
rf frequency	0.61 ~ 1.38MHz
rf voltage	1.3 ~ 3.0 kVp

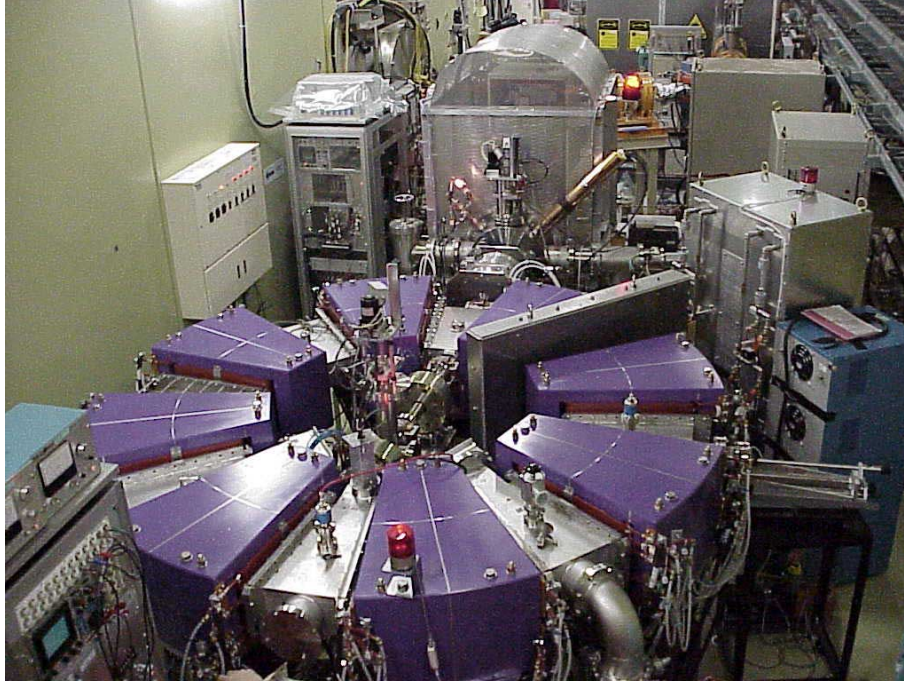


Figure C.2: Top-view of the POP FFAG

C.2 Experimental status

Since the construction of POP FFAG was complete, intensive accelerator studies were carried out in order to make the characteristics of FFAG accelerator clear. The major items of the accelerator study are as follows.

- Demonstration of the fast acceleration,
- Betatron tune and synchrotron tune in various condition,
- Beam position in various energies, and
- Beam acceptance.

In the following, the results of accelerator studies are briefly reviewed.

C.2.1 Beam acceleration

Compared to ordinary synchrotron, the acceleration time of the FFAG synchrotron is not restricted by a ramping time of a pulsed magnet. Thus, the higher the acceleration field is, the quicker the acceleration is completed. It is one of the prominent merits of the FFAG synchrotron. To demonstrate this feature of FFAG accelerator is one of the strong motivation to develop POP FFAG.

In the case that a synchronous phase is set to be 20 degree, the rf voltage should be at least 1.3 kV during acceleration. We have developed a rf cavity using two rectangular FINEMET¹ which has a core of 1.1 m (width) \times 0.7 m (height). The thickness of the core is 30mm. A 55kW rf amplifier which consists of two tetrodes (Eimac 4CW25,000) was used.

Fig.C.2.1 shows a typical beam signal observed by the inner and outer electrodes of the beam position monitor during acceleration of a proton beam. As seen in Fig.C.2.1, it indicates that, as it is accelerated, the beam moves outward. In the case of Fig.C.2.1, a flat-top energy is about 350 keV. The acceleration time is about 600 μ sec. At present, the acceleration up to 500 keV completes within 1 msec, and the beam characteristics in different energies were measured. Some of them are presented in the following sections.

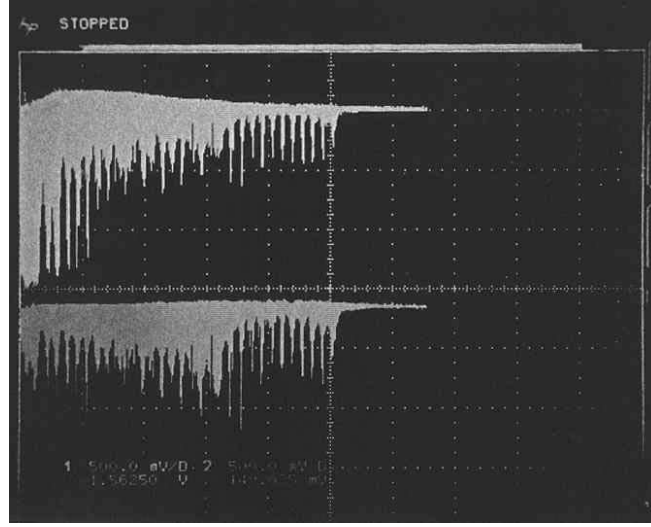


Figure C.3: Typical BPM signal during acceleration in POP FFAG, Upper signal: inside, Lower signal: outside

C.2.2 Tune survey

Firstly, a betatron tune was measured in injection orbit in various field condition. In the FFAG machine, the betatron tune can be changed by varying the relative field strength between the focusing magnet and the defocusing magnet, which is called “F/D ratio”. Fig.C.2.2 shows the betatron tune in various different F/D ratio. The results were consistent with the expectation from the computer simulation.

¹For the details of FINEMET, see [20]

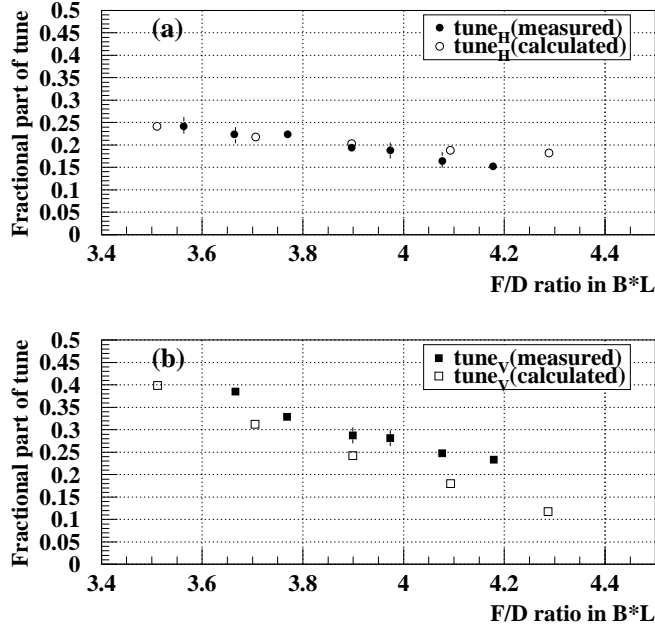


Figure C.4: Betatron tune in various field setting, (a) Horizontal tune, (b) Vertical tune

The synchrotron tune was measured in the energy range from 50 keV to 500 keV. The result in Fig.C.2.2 shows good agreement with the expected tune.

C.2.3 Beam position

In FFAG, the orbit position changes as the beam energy increases. The consistency of the beam position with the calculation is one of the measure to verify the current design strategy.

The beam position was measured with energy from 100 keV to 400 keV. The results were summarized in Fig.C.2.3, and it is consistent with the simulation within the systematics error.

C.3 Aperture survey

It is known that one of the outstanding advantages of the FFAG accelerator is its large transverse acceptance. It would be a key issue to realize a FFAG-based neutrino factory.

POP FFAG adopted the multi-turn injection scheme by using a DC septum and a pair of bump electrodes. Thus, by tuning the injection condition, it can inject a single bunch with a large injection error. Making use of this feature, the capability of storage and acceleration of a large emittance beam

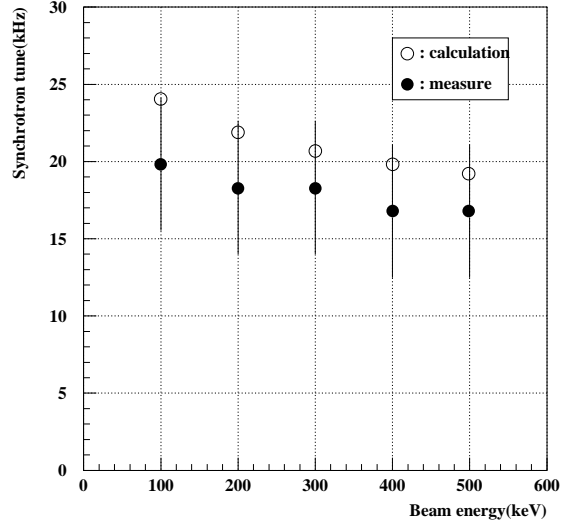


Figure C.5: Synchrotron tune in various energies

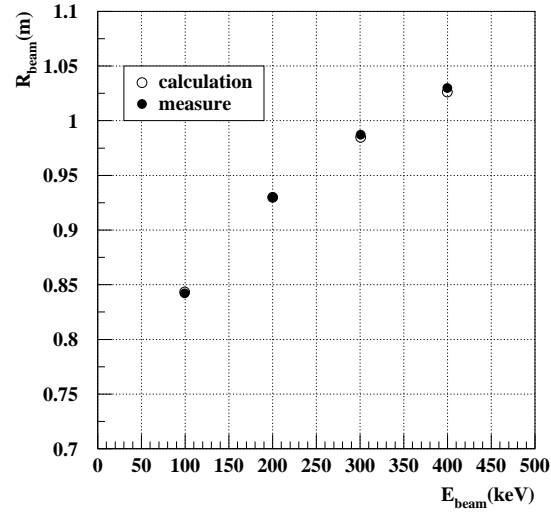


Figure C.6: Radial position of the circulating beam observed by the Faraday cup in the ring in various energies

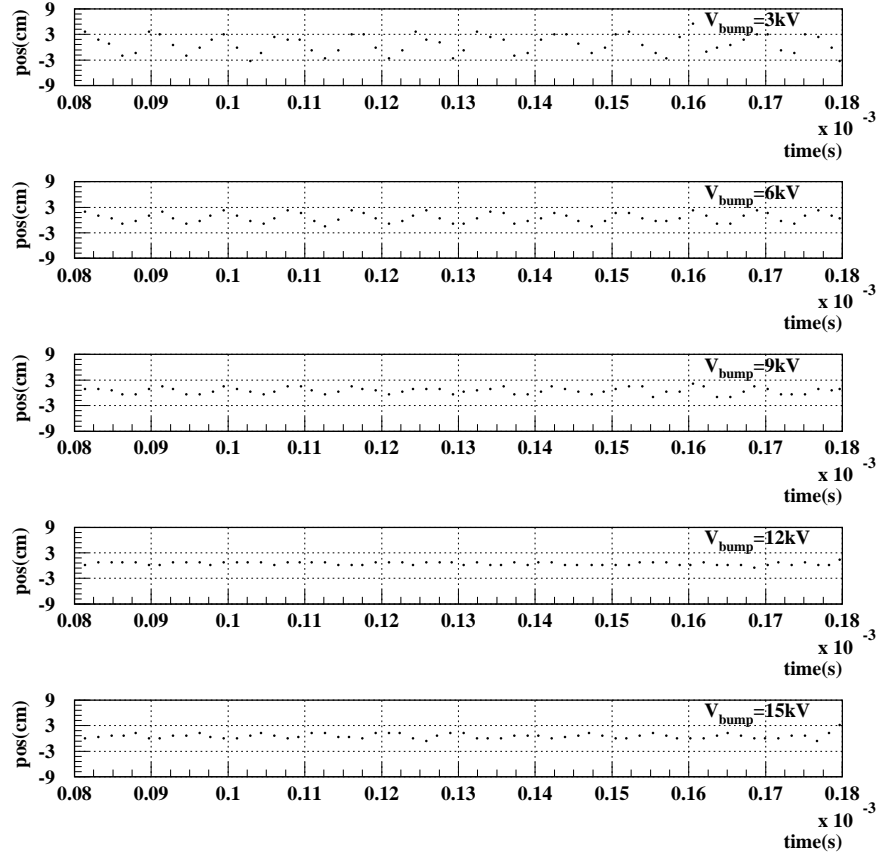


Figure C.7: Beam position observed by the beam position monitor in various injection error

in the FFAG ring has been successfully demonstrated. Fig.C.3 shows a typical change of the horizontal beam position observed by the beam position monitor, changing the amplitude of injection errors. It indicates that the beam with more than 3 cm in amplitude was circulated in the FFAG ring. The beam with such a large amplitude was successfully accelerated to the final energy. It means that the horizontal acceptance is at least more than $5000 \pi \text{mm} \cdot \text{mrad}$. At present, the acceptance presented here is no more than a lower limit, since the maximum injection error is restricted by the distance between the injection septum and the injection orbit. Thus, at present, a trial to move the injection orbit outward is undertaken.

C.4 Summary of POP FFAG R&D

From the accelerator study of POP FFAG, the following results have been demonstrated.

- Fast beam acceleration, *i.e.* from 50 keV to 500 keV within 1 msec.
- Large horizontal acceptance, typically more than 5000 π mm·mradian.
- Good agreement between the betatron tune, the synchrotron tune and the orbit position with the numerical calculations.

They give strong supports for the application of FFAG to accelerate a beam of short-lived particles with large emittance. At present, further accelerator studies are going on. In addition, a plan of beam extraction from the POP FFAG ring is under the investigation.

Appendix D

R&D Status of 150 MeV FFAG

D.1 Overview

After the success of the POP FFAG commissioning, a new proposal to construct a larger FFAG accelerator was approved in Japanese fiscal year (JFY) 2000. In this project, a FFAG synchrotron to accelerate protons up to 150 MeV will be constructed. The main parameters are summarized in Table D.1. The schematic view of this 150MeV FFAG accelerator is shown in Fig. D.1

Table D.1: 150MeV FFAG main parameters

Type of magnet	Radial sector type(Triplet)
No. of sectors	12
Field index(k -value)	7.5
Energy	10MeV - 125MeV or 12MeV -150MeV
Repetition rate	250Hz
Magnetic field	Focus-mag. : 0.34~1.63 Tesla Defocus-mag. :0.15~0.78 Tesla
Radii of closed orbit	4.4m ~ 5.3m
Betatron tune	Horizontal : ~3.8 Vertical : ~2.2
rf frequency	1.5 ~ 4.6MHz

D.2 Main Features of 150-MeV FFAG

Compared to POP FFAG, 150-MeV FFAG has three new features for R&D works. They are (1) adoption of yoke-free magnets, (2) beam extraction from

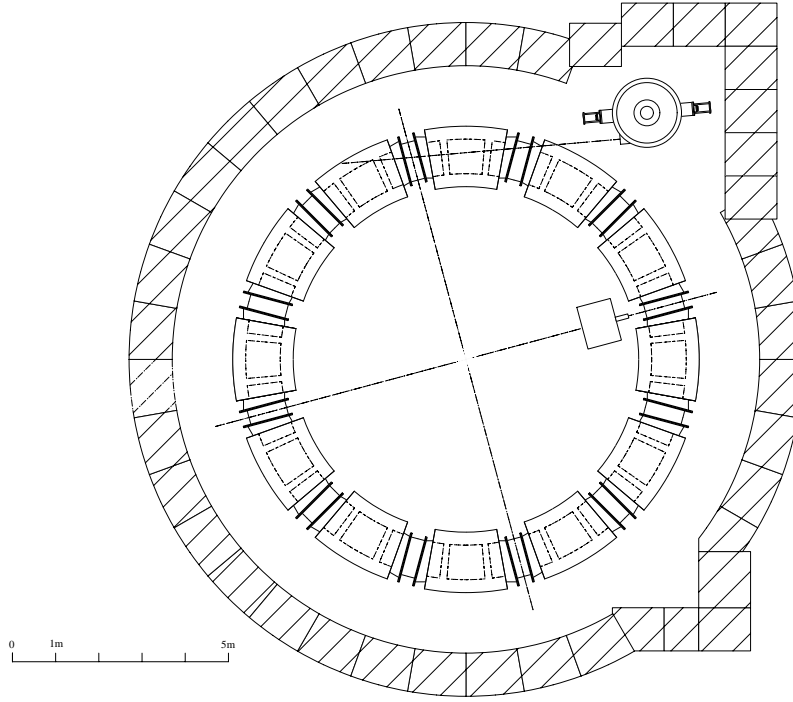


Figure D.1: Schematic view of the 150MeV FFAG

the FFAG ring, and (3) operation with high repetition.

As the first item, yoke-free magnets are one of the key issues for future developments of the FFAG-based neutrino factory. If it is successful, it could allow easy access of injection and extraction of the beam and also could offer large degree of freedom for possible configuration of beam apparatus. Thus, the demonstration of yoke-free magnet is useful.

As the second item, it is now being considered to employ the following scheme. The beam in the FFAG ring is bent by a kicker magnet installed in the middle of the straight section. A typical field strength for 150-MeV FFAG is about 600 gauss. A decay time of the magnetic field is less than 150 ns. In the next straight section, a DC septum magnet is installed to give further horizontal kick to the beam. The required field strength is about 2 kgauss. Finally, the beam is extracted from the ring. Fig.D.2 shows a typical beam extraction orbit.

As the third item, in some sense it could be said that the capability of high-repetition operation has been already demonstrated at POP FFAG and, as shown before, it has proved that it can accelerate a beam within 1 msec. However, in POP FFAG, the actual repetition rate is 1 Hz due to limitation of the power consumption. Thus, in 150-MeV FFAG, a real high repetition

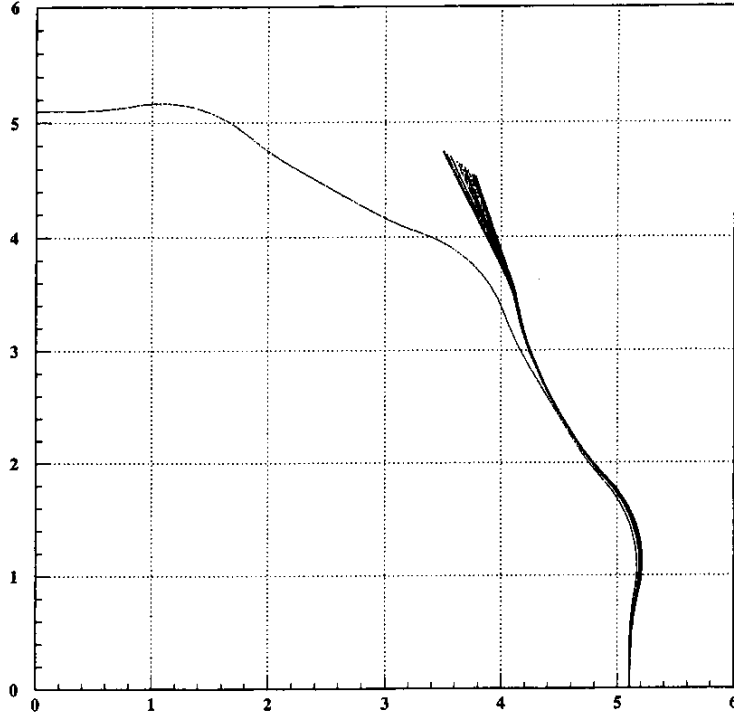


Figure D.2: Typical extraction orbit of 150MeV FFAG

operation has to be demonstrated. A repetition rate of 250 Hz is planned. A fast kicker magnet will also be needed for a neutrino factory.

D.3 R&D status and Construction Schedule

At present, the ring design and the beam-extraction scheme has been almost fixed. The fabrication of sector magnets and extraction elements is undergoing. Until the end of JFY 2001, most of the components will be ready, and the construction/commissioning will start at the beginning of JFY 2002.

Acknowledgment

We would like to thank KEK Director General Hirotaka Sugawara for initiating this study and his continued encouragement. We thank Profs. Shoji Nagamiya (a head of the KEK/JAERI Joint Project Office) and Kenzo Nakamura (a division head of the KEK-PS group) for their support through the study. We would also like to thank the members of the PRISM working group and the NufactJ working group, in particular, Prof. Noboru Sasao and Masaharu Aoki. We thank the following students for their contribution to this works : Masamitsu Aiba, Masahiro Yoshimoto, and Ryuichi Ueno. We also thank Prof. Koji Yoshimura for his assistance. Finally, we would like to thank our friends in U.S. and Europe for their discussions and encouragement.

Bibliography

- [1] Z. Maki, M. Nakagawa, and S. Sakata, Prog. Theor. Physics **28** (1962) 870.
- [2] FNAL report "A Feasibility Study of a neutrino Source Based on a Muon Storage Ring" edited by N. Holtkamp and D. Finley : "Physics at a Neutrino Factory", FERMILAB-FN-692, April, 2000.
- [3] CERN report 99-02 and ECFA 99-197, "Prospective Study of muon Storage Rings at CERN", edited by B. Autin, A. Blondel and J. Ellis.
- [4] Y. Itow et al., Letter of Intent,
http://www-jhf.kek.jp/JHF_WWW/LOI/jhfnu.loi.ps.
- [5] V. Barger, S. Geer, R. Raja, and K. Whisnant, hep-ph/0012017.
- [6] V. Barger, S. Geer and K. Whisnant, Phys. Rev. **D61** (2000) 053004.
- [7] P.F.Harrison and W.G. Scott, Phys. Lett. B **476** (2000) 349 ; H.Yokomakura, K.Kimura and A. Takamura, Phys. Lett. B **496** (2000) 175 ; S.J. Park, T. Weiler, hep-ph/0011247
- [8] A. . Cervera , A. Donini, M.B. Gavela, J.J. Gomez Cadenas, P. Hernandez, O. Mena and S. Rigolin, hep-ph/0002108.
- [9] JAERI/KEK Joint Project Proposal, 1999, unpublished.
- [10] Y. Kuno *et al.*, in Proceedings of Workshop on "High Intensity Muon Sources", December, 1999, World Scientific.
- [11] R.Palmer, C.Johnson, E.Keil: CERN-SL-99-070-AP, 1999.
- [12] C.Ohkawa: Bulletin of Physical Society of Japan, 1953.
- [13] K.R.Symon et al.: Phys. Rev., 103,(1956)1837.
- [14] Y. Mori and FFAG group at KEK: Proc. European Particle Accelerator Conference, 2000, Vienna, Austria, pp581.

- [15] JHF Project Office: "Proposal of High Intensity Proton Accelerators", 2000.
- [16] H. Shonauer, Workshop on FFAG accelerator, FFAG00, KEK, 2000
- [17] W.D.Kilpatrick, et al., "Criterion for Vacuum Sparking Designed to Include Both rf and dc", The Review of Scientific Instruments, Vol. 28, No.10, 824-826, 1957
- [18] K. W. Shepard and W.C. Sellyey: "A Low-Frequency RFQ for a Low-Charge-State Injector for ATLAS", Proc. of the 18th International Linac Conf. 26-30 Aug. 1996, Geneva, Switzerland, pp.68-70
- [19] J. Boucheron, R. Garoby, D. Grier, M. Paoluzzi, F. Pedersen: "A 1 MV 9.5MHz RF System for the CERN Antiproton Collector", Proc of the European Particle Accelerator Conference", 11-16 June, 1990, Nice, France, pp.958-960
- [20] Y. Mori et al., Proceedings of EPAC, 1998, p.299-301
- [21] Y. Kuno and Y. Okada, Review of Modern Physics, **73** (2001) 151.
- [22] B.T. Cleveland et al., Nucl. Phys. B (Proc. Suppl.) **38**, 47 (1995).
- [23] K.S. Hirata et al., Phys. Rev. Lett. **63**, 16 (1989); *ibid.* **65**, 1297 (1990); *ibid.* **65**, 1301 (1990); *ibid.* **66**, 9 (1991); Phys. Rev. **D44**, 2241 (1991); Y. Fukuda et al., Phys. Rev. Lett. **77**, 1683 (1996).
- [24] Y. Fukuda et al., Phys. Rev. Lett. **81**, 1158 (1999); *ibid.* **82**, 1810 (1999); *ibid.* **82**, 2430 (1999).
- [25] VA. I. Abazov et al., Phys. Rev. Lett. **67**, 3332 (1991); J. N. Abdurashitov et al., Nucl. Phys. B (Proc. Suppl.) **38**, 60 (1995); Nucl. Phys. B (Proc. Suppl.) **77**, 20 (1999).
- [26] P. Anselmann et al., Phys. Lett. **B285**, 376 (1992); *ibid.* **B314**, 445 (1993); *ibid.* **327**, 377 (1994); *ibid.* **B342**, 440 (1995); *ibid.* **B357**, 237 (1995); *ibid.* **B388**, 384 (1996); Nucl. Phys. B (Proc. Suppl.) **77**, 26 (1999).
- [27] M. Altmann et al., Phys. Lett. **B490**, 16 (2000).
- [28] K.S. Hirata et al., Phys. Lett. **B205**, 416 (1988); Phys. Lett. **B280**, 146 (1992); Y. Fukuda et al., Phys. Lett. **B335**, 237 (1994); S. Hatakeyama et al., Phys. Rev. Lett. **81**, 2016 (1998).
- [29] D. Casper et al., Phys. Rev. Lett. **66**, 2561 (1989); R. Becker-Szendy et al., Phys. Rev. **D46**, 3720 (1992).

- [30] Y. Fukuda et al., Phys. Lett. **B433**, 9 (1998); Phys. Lett. **B436**, 33 (1998); Phys. Rev. Lett. **81**, 1562 (1998); Phys. Rev. Lett. **82**, 2644 (1999); Phys. Rev. Lett. **82**, 5194 (1999); Phys. Lett. **B467**, 185 (1999); Phys. Rev. Lett. **85**, 3999 (2000); C. McGrew, talk at *The 2nd Workshop on "Neutrino Oscillations and Their Origin"*, December 6-8, 2000, University of Tokyo, Tokyo, Japan (<http://www-sk.icrr.u-tokyo.ac.jp/noon/2/transparency/1207/08/index.html>).
- [31] W.W.M. Allison et al., Phys. Lett. **B391**, 491 (1997); Phys. Lett. **B449**, 137 (1999).
- [32] F. Ronga, Nucl. Phys. B (Proc. Suppl.) **77**, 117 (1999).
- [33] C. Athanassopoulos *et al.*, (LSND Collaboration), Phys. Rev. Lett. **77**, 3082 (1996); Phys. Rev. C **54**, 2685 (1996); Phys. Rev. Lett. **81**, 1774 (1998); Phys. Rev. C **58**, 2489 (1998); D.H. White, Nucl. Phys. Proc. Suppl. **77** 207 (1999); G. Mills, talk at *19th International Conference on Neutrino Physics and Astrophysics* (Neutrino 2000), Sudbury, Canada, June 16-22, 2000 (<http://nu2000.sno.laurentian.ca/G.Mills/>).
- [34] B. M. Pontecorvo, Sov. Phys. JETP **34**, 247 (1958).
- [35] Z. Maki, M. Nakagawa and S. Sakata, Prog. Theor. Phys. **28**, 870 (1962).
- [36] Y. Suzuki, talk at *19th International Conference on Neutrino Physics and Astrophysics* (Neutrino 2000), Sudbury, Canada, June 16-22, 2000 (<http://nu2000.sno.laurentian.ca/Y.Suzuki/>).
- [37] O. Yasuda, Acta Phys. Pol. **B30**, 3089 (1999).
- [38] M.C. Gonzalez-Garcia, M. Maltoni, C. Pena-Garay, J.W.F. Valle, Phys. Rev. **D63**, 033005 (2001).
- [39] G.L. Fogli, E. Lisi, A. Marrone, D. Montanino and A. Palazzo, hep-ph/0104221.
- [40] M. Apollonio *et al.*, Phys. Lett. B **338**, 383 (1998); Phys. Lett. B **466**, 415 (1999).
- [41] G.L. Fogli, E. Lisi, A. Marrone and D. Montanino, hep-ph/0009269; M.C. Gonzalez-Garcia, M. Maltoni, C. Pena-Garay and J.W.F. Valle, Phys. Rev. **D63**, 033005 (2001).
- [42] M.C. Gonzalez-Garcia and C. Pena-Garay, hep-ph/0009041.
- [43] G.L. Fogli, E. Lisi, D. Montanino, and A. Palazzo, Phys. Rev. **D62** (2000) 113003.

- [44] A.Yu. Smirnov, talk at Europhysics Neutrino Oscillation Workshop (NOW2000), Conca Specchiulla (Otranto, Italy), September 9-16, 2000 (<http://www.ba.infn.it/~now2000/views/slides/Smirnov/>) and private communication.
- [45] J.G. Learned, hep-ex/0007056.
- [46] B. Autin et al., CERN-SPSC-98-30; Neutrino Factory and Muon Collider Collaboration (D. Ayres *et al.*), physics /9911009; C. Albright *et al.*, hep-ex/0008064.
- [47] V. Barger, S. Geer, R. Raja and K. Whisnant, Phys. Rev. **D62**, 013004 (2000); Phys. Lett. **B485** (2000) 379; hep-ph/0007181.
- [48] V. Barger, S. Geer, R. Raja and K. Whisnant, Phys. Rev. **D62**, 073002 (2000);
- [49] A. De Rujula, M. B. Gavela and P. Hernandez, Nucl. Phys. **B547**, 21 (1999).
- [50] A. Donini, M. B. Gavela, P. Hernandez and S. Rigolin, Nucl. Phys. **B574**, 23 (2000).
- [51] A. Romanino, Nucl. Phys. **B574**, 675 (2000).
- [52] K. Dick, M. Freund, M. Lindner, and A. Romanino, Nucl. Phys. **B562**, 29 (1999).
- [53] M. Freund, M. Lindner, S.T. Petcov and A. Romanino, Nucl. Phys. **B578**, 27 (2000).
- [54] M. Campanelli, A. Bueno and A. Rubbia, hep-ph/9905240; A. Bueno, M. Campanelli and A. Rubbia, Nucl. Phys. **B573**, 27 (2000); Nucl. Phys. **B589**, 577 (2000).
- [55] M. Freund, P. Huber and M. Lindner, Nucl. Phys. **B585**, 105 (2000).
- [56] J. Sato, Nucl. Instrum. Meth. **A451**, 36 (2000); hep-ph/0006127, hep-ph/0008056; M. Koike and J.Sato, Phys. Rev. **D61**, 073012 (2000); talk at International Workshop on Muon Storage Ring for a Neutrino Factory (NUFACT'00), Monterey, California, 22 – 26 May 2000; talk at the Joint U.S./Japan Workshop On New Initiatives In Muon Lepton Flavor Violation and Neutrino Oscillation With High Intense Muon and Neutrino Sources, Honolulu, Hawaii, Oct. 2–6, 2000; talk at JSPS-KOSEF Joint Workshop on "New Developments in Neutrino Physics", Korea Institute for Advanced Study, Seoul, Korea, 16 - 20 October 2000; T. Ohta and J. Sato, Phys. Rev. **D63**, 093004 (2001); M. Koike, T. Ohta and J. Sato, hep-ph/0011387.

- [57] O. Yasuda, talk at KEK International Workshop On High Intensity Muon Sources (HIMUS 99), Tsukuba, Japan, 1 – 4 December 1999, hep-ph/0005134.
- [58] T. Miura, E. Takasugi, Y. Kuno, M. Yoshimura, hep-ph/0102111.
- [59] J. Burguet-Castell, M.B. Gavela, J.J. Gomez-Cadenas, P. Hernandez, O. Mena, hep-ph/0103258.
- [60] M. Freund, P. Huber and M. Lindner, hep-ph/0105071.
- [61] J. Pinney and O. Yasuda, hep-ph/0105087
- [62] A. Konaka, talk at the 1st Tokutei-RCCN Workshop on Neutrinos, ICRR, Univ. of Tokyo, Kashiwa, Japan, May 12, 2000.
- [63] H. Minakata and H. Nunokawa, Phys. Lett. **B495**, 369 (2000).
- [64] B. Richter, hep-ph/0008222.
- [65] M. Nakahata et. al., J. Phys. Soc. Japan, **55**, 3786 (1986).
- [66] P. Lipari, M. Lusignoli and F. Sartogo, Phys. Rev. Lett. **74**, 4384 (1995).
- [67] K. Nakamura, talk at the Joint U.S./Japan Workshop On New Initiatives In Muon Lepton Flavor Violation and Neutrino Oscillation With High Intense Muon and Neutrino Sources, Honolulu, Hawaii, Oct. 2–6, 2000,
http://meco.ps.uci.edu/lepton_workshop/talks/nakamura.pdf.
- [68] D. Casper, talk at Joint U.S. / Japan Workshop on New Initiatives in Lepton Flavor Violation and Neutrino Oscillation with High Intense Muon and Neutrino Sources, Honolulu, Hawaii, 2-6 Oct 2000,
http://meco.ps.uci.edu/lepton_workshop/talks/casper/uno.pdf.
- [69] F. Stacey, *Physics of the Earth, 2nd ed.* (J. Wiley and Sons, Chichester, 1977).
- [70] V. Barger, S. Geer, R. Raja and K. Whisnant, hep-ph/0012017.
- [71] P. Lipari, hep-ph/0102046.
- [72] Y. Obayashi, talk at the Joint U.S./Japan Workshop On New Initiatives In Muon Lepton Flavor Violation and Neutrino Oscillation With High Intense Muon and Neutrino Sources, Honolulu, Hawaii, Oct. 2–6, 2000,
http://meco.ps.uci.edu/lepton_workshop/talks/obayashi.pdf.
- [73] T. Kobayashi, talk at the 5th Tokutei-RCCN Workshop on Neutrinos, ICRR, Univ. of Tokyo, Kashiwa, Japan, Feb. 23–24, 2001.

- [74] M. Maris and S.T. Petcov, Phys. Rev. **D56**, 7444 (1997).
- [75] D.L. Anderson, private communication.
- [76] T. Tanimoto, private communication.
- [77] T. Tanimoto, J. Phys. Earth **38**, 493 (1990).
- [78] J. Resovsky, private communication.
- [79] R. Geller, private communication.
- [80] Super-Kamiokande Collaboration, Y. Fukuda *et al.*, Phys. Rev. Lett. **81** (1998) 1562; Phys. Lett. **B433** (1998) 9; Phys. Lett. **B436** (1998) 33; Phys. Rev. Lett. **82** (1999) 2644.
- [81] GALLEX Collaboration, W. Hampel *et al.*, Phys. Lett. B **447** (1999) 127.
- [82] SAGE Collaboration, J. N. Abdurashitov *et al.*, astro-ph/9907113.
- [83] Kamiokande Collaboration, Y. Suzuki, Nucl. Phys. B (Proc. Suppl.) **38** (1995) 54.
- [84] Homestake Collaboration, B. T. Cleveland *et al.*, Astrophys. J. **496** (1998) 505.
- [85] Super-Kamiokande Collaboration, Y. Fukuda *et al.*, Phys. Rev. Lett. **82** (1999) 1810; *ibid.* **82** (1999) 2430.
- [86] G. L. Fogli, E. Lisi, D. Marrone and G. Scioscia, Phys. Rev. D **59** (1999) 033001; G. L. Fogli, E. Lisi, D. Montanino and A. Palazzo Phys. Rev. D **62** (2000) 013002.
- [87] M. Apollonio *et al.*, Phys. Lett. **B420**, 397 (1998); Phys. Lett. B466, 415 (1999).
- [88] S. Geer, Phys. Rev. **D57**, 6989 (1998), erratum *ibid.* **D59** (1999) 039903.
- [89] A. Cervera , A. Donini, M.B. Gavela, J. J. Gomez Cadenas, P. Hernandez, O. Mena and S. Rigolin, Nucl. Phys. **B579** (2000) 17.
- [90] A. De Rujula, M. B. Gavela and P. Hemandez, Nucl. Phys. **B547**, 21 (1999); A. Donini, M. B. Gavela, P. Hemandez and S. Rigolin, Nucl. Phys. **B574** (2000) 23.
- [91] K. Dick, M. Freund, M. Lindner, and A. Romanino, Nucl. Phys. **B562** (1999) 29; A. Romanino, Nucl. Phys. **B574** (2000) 675; M. Freund, P. Huber and M. Lindner, Nucl. Phys. **B585** (2000) 105.

- [92] Neutrino Factory and Muon Collider Collaboration (D. Ayres *et al.*), physics/9911009; C. Albright *et al.* hep-ex/0008064.
- [93] J. Sato, hep-ph/0006127; M. Koike and J.Sato, Phys. Rev. **D61** (2000) 073012.
- [94] O. Yasuda, hep-ph/0005134.
- [95] N. Cabibbo, Phys. Lett. **72B**, 333 (1978).
- [96] V. Barger, K. Whisnant and R. J. N. Phillips, Phys. Rev. Lett. **45**, 2084 (1980).
- [97] M. Tanimoto, Phys. Rev. D **55**, 322 (1997); M. Tanimoto, Prog. Theor. Phys. **97**, 901 (1997).
- [98] J. Arafune and J. Sato, Phys. Rev. D **55**, 1653 (1997).
- [99] J. Arafune, M. Koike and J. Sato, Phys. Rev. D **56**, 3093 (1997); erratum *ibid.* **60**, 119905 (1999).
- [100] H. Minakata and H. Nunokawa, Phys. Rev. D **57** 4403 (1998).
- [101] H. Minakata and H. Nunokawa, Phys. Lett. B **413**, 369 (1997).
- [102] M. Bilenky, C. Giunti, and W. Grimus, Phys. Rev. D **58**, 033001 (1998).
- [103] M. Kobayashi and T. Maskawa, Prog. Theor. Phys. **49**, 652 (1973).
- [104] L. Wolfenstein, Phys. Rev. **D17** (1978) 2369; S. P. Mikheev and A. Yu. Smirnov, Sov. J. Nucl. Phys. **42** (1985) 913.
- [105] J. Sato, hep-ph/0008056.
- [106] T. Ota and J. Sato, hep-ph/0011234.
- [107] A. M. Dziewonski and D. L. Anderson, *Phys. Earth Planet. Inter.* **25**, 297 (1981)
- [108] P. F. Harrison and W. G. Scott, Phys. Lett. **B476** (2000) 349.
- [109] M. Koike, T. Ota and J.Sato, hep-ph/0011387.